Segregation to Oxide Grain Boundaries in High Temperature FeCrAlRE Alloys

UNIVERSITY OF LIVERPOOL

Thesis submitted in accordance with the requirements of the University of Liverpool for the degree of Doctor in Philosophy

by

Dinesh Lalmani Ram

10/2007

Materials Science and Engineering

Department of Engineering, Faculty of Engineering

ABSTRACT

Segregation to Oxide Grain Boundaries in High Temperature FeCrAlRE Alloys

Dinesh Lalmani Ram

FeCrAl alloys are technologically important and extensive previous research has established that the oxidation of these alloys at temperatures ≥1000°C results in the formation of α-Al_2O_3 oxide scales. Additionally, it has been demonstrated that the scale performance may be modified dramatically by the segregation of minor alloy constituents (particularly Reactive Elements (RE) such as Y, Hf, Zr, etc.) or non-metallic impurities (such as S, N, etc.) to the oxide grain boundaries and/or the oxide - alloy interface. REs can change the oxide growth mechanism, reduce the mechanical failure by reducing cracking and spallation and enhance alloy lifetimes governed ultimately by scale chemical failure leading to breakaway attack. Knowledge of segregation behaviour of these REs is thus central to mechanistic understanding of the oxidation behaviour of this range of alloys.

The aim of this work is to understand the effect of segregation of the REs to the oxide grain boundaries. Studies of segregation have only been possible previously using Scanning Transmission Electron Microscopy (STEM) and energy dispersive X-ray analysis (EDX). However the new SuperSTEM microscope at the Daresbury Laboratory offers considerable potential for more detailed study of the segregation to oxide grain boundaries at the atomic level. This microscope has an aberration corrector fitted to the objective lens, allowing the formation of sub-Angstrom probe for simultaneous ultra-high resolution high angle annular dark field (HAADF) imaging and atomic-column electron energy loss spectroscopy (EELS).

Model FeCrAlRE alloys containing controlled additions of reactive elements, such as yttrium and hafnium were oxidized at 1250°C and 1200°C, in air, for 50 and 100 hours. The oxide was then detached from the underlying alloy using a ferritic stainless steel etch and ion thinned to electron transparency. After an initial examination using conventional TEM, STEM analysis was carried out in conjunction with EDX. Finally, lattice imaging and EELS analysis were then carried out in the SuperSTEM, which showed the segregation of the reactive elements at the grain boundaries and the formation of hafnium rich particles at the boundaries and within the scales. Atomic resolution imaging was carried out, in order to investigate the possible links between the segregation sites and the orientation of grains and grain boundaries.

Contents

LIST OF FIGURES

ACKNOWLEDGEMENTS

Firstly, I would like to express my gratitude to Prof. G.J. Tatlock, who fulfilled and exceeded his brief as my supervisor and made it possible for me embark upon and complete this work.

I thank Prof. P.J. Goodhew for the provision of the facilities of the department and SuperSTEM, and the EPSRC for providing me with the grant.

I would like to acknowledge the help of Dr. R. Murray for getting me off on the right foot; Dr. A. Papworth, Dr. A. Bleloch, Dr. U. Falke, Dr. P.G. Beahan, and Dr. H. Al Badairy for the assistance throughout the project. Thanks to the various residents of the High Temperature Oxidation Group and SuperSTEM group for help and encouragement, and thanks to the colleagues, friends, academic and technical staff, whose assistance over the years is very much appreciated.

Chapter 1

Introduction to FeCrAl alloys

1.1. High temperature oxidation

Material degradation at high temperature is a serious problem in several high-technology industries. Gas turbines, catalytic convertors and heating elements are a few of the examples where oxidation/corrosion either limits their use, reduces their life or reduces operating temperature and hence efficiency.

Oxidation of pure metals could be broadly categorized into two categories; one in which the metal resists oxidation by forming a thin stable oxide film over the surface which may protect the substrate beneath from subsequent oxidation. Elements like Fe, Al, Cr, Ti and Zn form oxides such as Fe_2O_3, Al_2O_3, Cr_2O_3, TiO_2 and ZnO respectively. The oxidation stages in these types of elements can be described by adsorption, dissociation, chemisorption and ionization of oxygen. This would lead to a constant reaction rate, if rate controlling as represented by Equation 1-1[1].

$$O_2(g) \rightarrow O_2(ad) \rightarrow 2O(ad) = 2O^{\cdot}(chem) \rightarrow 2h^{\cdot} \rightarrow 2O^{2\cdot}(latt) + 4h^{\cdot} \quad \text{---------- 1-1}$$

However these processes are so rapid that the oxidation period over which they control the reaction rate is rarely observed. This early period is extremely difficult to observe and under the condition the oxide scale formed is thick enough for ionic diffusion through the scale to be rate controlling[2].

In the second category, the metal resists oxidation by its chemical inertness. Elements which fall in to this category are known as noble elements, such as Au and Pt. Oxidation of an alloy is much more complex than that of the pure elements, due to the following[3].

- The metals in the alloy will each have a different affinity towards oxygen controlled by different free energies of formation of the oxides.
- A degree of solid solubility may exist between the oxides.
- The various metal ions present in the alloy will have different mobility and diffusivity in the oxide and alloy.

An example for the above would be NiCrAl alloys which form a chromia scale below 1000°C and alumina scale above 1000°C.

1.2. FeCrAl alloys

FeCrAl alloys are technologically important today because of their wide spread application in various industries where operation in an oxidizing atmosphere at high temperature is required. They are used in industrial furnaces for making heating elements, in oil and gas industries to make oil rig flares, in the automotive industries to make catalytic convertors and in aerospace industries to make abradable honeycomb seals. Today nearly all cars are fitted with lambdaprobe-controlled three-way catalytic convertors which are made using 50 micron thick foils of FeCrAl alloys with additions of reactive elements (RE)[4]. Due to a huge demand in industrial application, these alloys have been studied extensively in the past few decades and are still studied today as further performance enhancement is desirable.

FeCrAl alloys are used extensively because they form a chromia (Cr_2O_3) or alumina (Al_2O_3) scale depending upon the oxidation temperature, and these act as a good barrier and provide corrosion resistance at higher temperature. Above 1000 °C, only alpha alumina is stable. This oxide scale grows by inward diffusion of oxygen and outward diffusion of Cr/Al[5]. During the production of these alloys, tramp impurities like sulphur, carbon and phosphorus are incorporated within it. One of the problems with these alloys is that the scales formed on them are usually wavy/undulated in structure because of different coefficients of thermal expansion and the impurities segregate to these free surfaces and enhance the failure of the scale thus reducing lifetime of the alloy [6, 7]. The impurities could be removed by annealing in the presence of H_2 to reduce the content of impurities below 10 ppm, but this is usually uneconomical. Another factor responsible for premature failure of oxide is due to the fact that the scale grows by inward diffusion of oxygen and outward diffusion of aluminium/chromium.

After the complete layer of scale has formed, subsequent chromia/alumina grows within the previously formed chromia/alumina and finally chromium or aluminium content is reduced below that necessary to sustain the oxide growth. This Al or Cr may not be a limiting factor for thicker alloys but may play an important role when thin strips are oxidized, as will be the case for the future catalytic convertors. To cope with the demands of the future catalytic convertors, the thickness of these foils must be reduced from 50 micron towards 30 micron. However, the thinner the foil, the greater is the risk of breakaway oxidation[8-12].

Hence to increase the lifetime of the alloy, it is important to protect the scale from spallation or the onset of breakaway oxidation. This may be achieved by addition of reactive elements which change the growth mechanism of the scale and enhance the lifetime of alloy[13-15]. It is this effect which is the core of this project and remains of active interest to industries.

1.3. Objectives of this work

The purpose of this work was to look at the segregation of reactive elements to the oxide grain boundaries and to measure the segregation of different reactive elements to them, as they play an important role in oxide scale growth.

With the aid of scanning transmission electron microscopy (STEM) and energy dispersive spectroscopy (EDX), the segregation to oxide grain boundaries was studied with a view to understanding the build-up of reactive elements and trying to quantify the amount of segregant present.

With the help of SuperSTEM and electron energy loss spectroscopy (EELS), the segregation to the grain boundaries was assessed and lattice imaging carried out in order to see if there was any link between segregation and the orientation of the grains and grain boundaries, and to see whether it was possible to identify the sites occupied by reactive elements at the grain boundary.

Although much of the work is relatively fundamental in nature, the practical implication of the findings will be considered along with suggestions for future work.

Chapter 2

Literature Review

2.1. FeCrAl alloys

The high temperature oxidation of FeCrAl alloys forming chromia and alumina scales have been studied for many years. FeCrAl alloys for high-temperature applications rely on the formation of a protective, continuous, adherent and slow growing chromia/aluminum oxide scale. Cr_2O_3 scale is formed on the alloys when oxidation is carried below 1000°C, whereas Al_2O_3 scale is formed above 1000°C. In the following work only alumina scale formation was considered. This Al_2O_3 scale protects the metal from corrosion and is thermodynamically very stable and has a high melting point. The transport processes through these scales are very slow and thus they remain protective up to 1350 °C in strongly oxidizing atmospheres. The nucleation and initial growth of alumina scales is strongly affected by segregation or adsorption on the surface of the base metals. The growth mechanism is modified by segregation to the grain boundary in the growing oxides and oxide adherence is affected by segregation and accumulation at the metal-oxide interface[16, 17]. Non-metallic impurities like sulphur, phosphorus, carbon etc. play an important role in the oxidation of these alloys along with reactive elements such as yttrium, hafnium, cerium etc. The non-metallic impurities become incorporated into the alloys during the routine manufacturing processes and tend to segregate to the metal-oxide interface, lowering the scale adhesion[14]. Reactive elements can be added to substrates in many ways: 1) added as pure element in the alloys, 2) as an oxide dispersion, 3) as ion implantation or 4) as a surface coating[18, 19]. The presence of chromium in the alloy provides a third element effect and tends to stabilize the alpha-alumina. The presence of chromium also reduces the oxygen diffusion into the alloy thereby promoting the formation of an alumina scale[20]. To develop and maintain a protective Al_2O_3 scale on FeCrAl alloys a critical aluminum reservoir is required. In a thick foil the alumina scale may grow and protect the alloy as long as the Al present in the alloy does not drop below a critical level. The oxide scale may spall under stress and a subsequent healing layer of alumina grows at the spalled

site. The critical aluminum content of the alloy required to form the alumina healing layer is about 2-2.5 wt. % on strong alloys but less on weak ones[21, 22]. As far as the FeCrAl alloys are concerned strong usually refers to those alloys that have been oxide dispersion strengthened, such as PM2000 or MA956. Some other mechanically alloyed materials are also usually strong. The rest are very weak and creep rapidly at high temperatures, so that any stress generated during oxidation is accommodated. There is a much lower chance that the oxide will crack and spall when the alloys are weak; hence most oxides on weak alloys remain protective even when the Al content is well below 2%.

In the thin foils the failure of scale occurs after the formation of a chromia-rich layer at the base of the protective alumina scale and failure leads to break away oxidation in a more classic pattern by the formation of voluminous iron and chromium-rich oxides[23]. In the sections to follow, the growth mechanism, scale spallation and failure mechanism are considered with and without the presence of reactive element additives.

2.2. Mechanism of oxidation

The oxidation of a metal may be represented as, [24]

$$xM + \frac{y}{2}O_2 = M_xO_y \qquad \text{----------2 - 1}$$

where M is the reacting metal and M_xO_y the metal oxide.

For alumina the above Equation 2-1 can be written as,

$$2Al + \frac{3}{2}O_2 = Al_2O_3 \qquad \text{----------2 - 2}$$

From a thermodynamic point of view, the driving force for the above reaction is the change in the Gibbs free energy. The change in Gibbs free energy (ΔG) is described by the second law of thermodynamics as:

$$\Delta G = \Delta H - T\,\Delta S \qquad \text{----------2 - 3}$$

where, ΔH is change in the enthalpy of reaction, T is the absolute temperature and ΔS is the change in entropy.

The reaction is said to be thermodynamically favorable when ΔG is negative and unfavorable when ΔG is positive and is said to be in equilibrium when ΔG is equal to zero.

In the Figure 2-1 below, MO separates the two reactants as follow

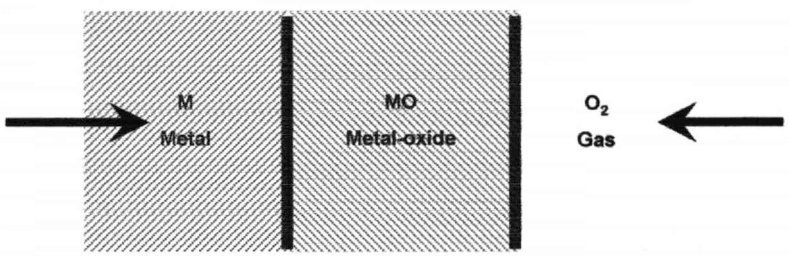

Figure 2- 1: Schematic of an oxidation reaction, where the reaction product separates both the reactants.

One or both the reactants must penetrate the scale for the reaction to proceed further, i.e. either metal must be transported through the oxide scale to the oxide-gas interface and react there or oxygen must be transported through the oxide to oxide-metal interface. When both the reactants, that is metal as well as oxygen, are transported through the oxide, they can react within the oxide and form oxide within oxide.

Quantitatively the driving force for Equation 2-1 is given by the change in the standard Gibbs free energy, ΔG[24],

$$\Delta G = \Delta G^0 + RT \ln\left(\frac{a_{MxOy}}{a_M^x P_{O_2}^{y/2}}\right) \qquad \text{----------2 - 4}$$

where ΔG^0 is the free energy change when all the species present are in their standard states, a_i is the chemical activity of component i, P_{O_2} the oxygen partial pressure within the scale, R the universal gas constant and T the absolute temperature. At equilibrium,

$$\Delta G = 0$$

$$-\Delta G^0 = RT \ln\left(\frac{a_{MxOy}}{a_M^x P_{O_2}^{y/2}}\right) \approx RT \ln[K] \qquad \text{----------2 - 5}$$

where K is the equilibrium constant. Rearranging the Equation 2-4 gives,

$$K = \left(\frac{a_{MxOy}}{a_M^x P_{O_2}^{y/2}}\right) = \exp\left(\frac{-\Delta G^0}{RT}\right) \qquad \text{----------2 - 6}$$

Equation 2-5 can be rearranged to yield the minimum oxygen potential required to form the metal oxide, as shown below

$$P_{O_2}^{y/2} = \frac{a_{MxOy}}{a_M^x} \cdot \exp\left(\frac{\Delta G^0}{RT}\right) \qquad \text{----------2 - 7}$$

$P_{O_2}^{y/2}$ is the equilibrium dissociation pressure of M_xO_y. The reaction will not proceed unless the ambient oxygen pressure exceeds $P_{O_2}^{y/2}$. The standard Gibbs free energy of formation of selected oxides as a function of temperature is summarized in an Ellingham diagram (Figure 2-2).

Once the surface of a metal is completely covered with oxide and there is sufficient oxygen at the scale surface, solid state diffusion of reactants through the oxide scale is the rate-determining step. Solid state diffusion occurs via the grain boundaries, lattice and/or other short-circuit paths within the oxide. A parabolic rate law is established as the scale grows thicker, which can be expressed as[6, 25],

$$\frac{dX}{dt} = \frac{k_P}{X} \qquad \text{----------2 - 8}$$

where X is the scale thickness, t is the time and k_p is the parabolic rate constant and upon integration Equation 2-8 yields,

$$X^2 = 2k_p t + C \qquad \text{----------2 - 9}$$

At the start of oxidation, X = 0, when t = 0 implies C = 0.

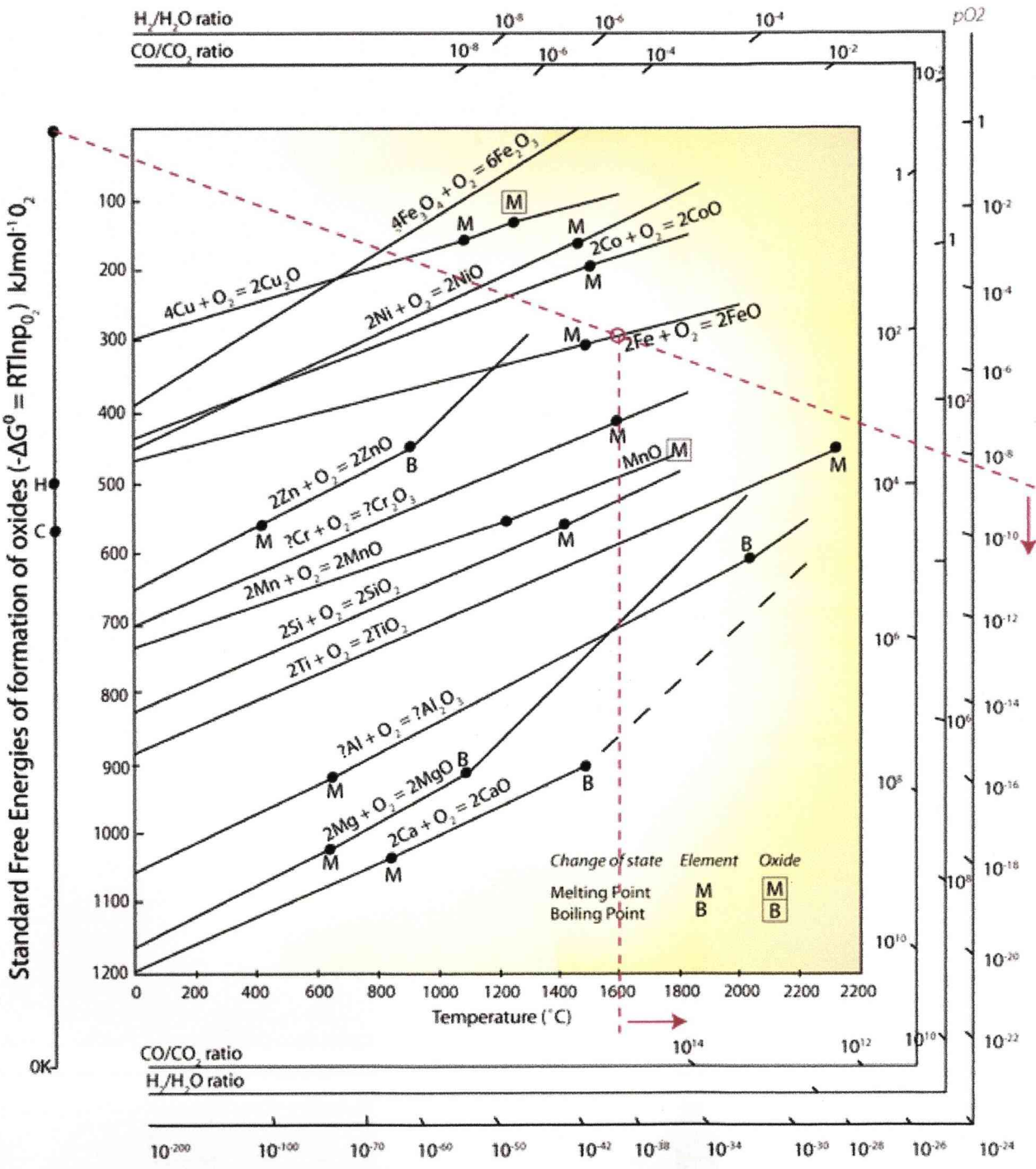

Figure 2- 2: Standard free energy of formation of selected oxides as a function of temperature[26].

Sometimes the growth of scales is limited by gas-phase diffusion, when oxide scales contains microcracks and pores within them. Microcracks in the scale provide direct access for oxygen and thus a linear rate law is followed by the oxidation process given by,

$$x = k_l t \qquad \text{----------2 - 10}$$

where k_l is known as the linear rate constant.

2.2.1. Diffusion in oxides

Diffusion plays an important role in the oxidation of metals and alloys and is described by Fick's first law, which is used to define steady-state diffusion and is given as,

$$J = -D\left[\frac{dc}{dx}\right] \qquad \text{----------2 - 11}$$

where, J is the diffusion flux or mass diffusing through a unit cross section in the concentration gradient (atom/cm^2.s), dc/dx is the concentration gradient (atom/cm^4) and D is the diffusion coefficient or diffusivity (cm^2/s) which increases exponentially with temperature and is given by the Arrhenius equation as,

$$D = D_0 \exp\left(\frac{-Q}{RT}\right) \qquad \text{----------2 - 12}$$

where, D_0 is a constant for a given system, Q is the activation energy for diffusion, R is the gas constant and T the absolute temperature.

2.3. Growth mechanism of Al_2O_3 scale

When a FeCrAl alloy is oxidized above 1000 °C, it forms a protective scale of alumina. During the initial stages of the scale growth, a transient oxide scale is formed. This transient oxide which is metastable oxide contains all the oxides of the different elements present in FeCrAl alloy, viz. Fe_2O_3, Cr_2O_3 and Al_2O_3. But as the oxidation progresses only Al_2O_3 is stable at this

temperature and it can be seen from the Ellingham diagram (Figure 2-2) that alumina is more stable than chromia and iron oxide. In binary alloys of Fe-Al, it is possible to develop alumina scale, provided it has sufficient aluminium concentration[27, 28]. It has been found by many authors that it is much easier to establish and maintain an alumina scale on FeCrAl alloy than on binary alloys. This is due to the effect of chromium, which tends to reduce oxygen ingress into alloys and thereby enhancing the external layer of alumina[29].It was also found that oxidation rate decreased by an order of magnitude when chromium content was increased from 15 to 18%. It has also been shown that the chromium or chromia particles acted as nuclei for the formation of α-Al_2O_3 were by suppressing the formation of metastable alumina[30-32]. All other oxides dissociate and become incorporated into the scale after the transient stage[33-39]. Similar results were also found by Golightly et al.[5, 40] who worked on the development of early stages of α-Al_2O_3 scales on FeCrAl alloys. They found that after the initial few minutes of oxidation, a stable α-Al_2O_3 developed beneath the aluminium, iron and chromium-rich transient oxide. It was also shown that this stage of stable α-Al_2O_3 growth is achieved more rapidly with increase in Cr content[5, 41, 42].

The alumina scale may have a different form at different temperatures; during the initial stages of oxidation all the different types of aluminas are formed, α- Al_2O_3, θ- Al_2O_3, γ- Al_2O_3 and δ-Al_2O_3. But as the oxidation progresses α- Al_2O_3 is the most stable phase above 1000°C and all other forms of alumina transform into α- Al_2O_3[43, 44].

The overall growth of the scale is influenced by both thermodynamics and reaction kinetics. The growth mechanism of Al_2O_3 scale has been a topic of study for many decades and has led to scattered results. Some of the earlier work done on FeCrAl suggests that Al_2O_3 scale predominantly grows by outward diffusion of aluminum to the free surface. However, some authors have reported scale grows by inward diffusion of oxygen and some authors have suggested that the growth mechanism was by both inward and outward diffusion of oxygen and aluminum respectively[45, 46]. Some of the work carried out on FeCrAl alloys found that the

alumina scale was wrinkled, wavy or convoluted with areas where contact has been lost between the scale and the alloy. The reason for this morphological development was as a result of deformation following the build-up of compressive stresses within the oxide as it grows. New oxides were found at oxide grain boundaries following the reaction between oxygen ions diffusing inwards and aluminium ions diffusing outwards, which led to lateral growth of the oxide scale. It was also suggested that, diffusing oxygen and aluminium species are unlikely to pass each other while moving along the same path. So it was proposed that oxygen ions move along the oxide grain boundary predominantly whereas aluminium ions move outward through the short circuit paths within the alumina grains[32]. Similar work done by K.Messaoudi et al.[47] showed that cationic and anionic diffusion are both important. According to these authors the cationic diffusion is more important than the anionic diffusion. Thus the growth of the α-Al_2O_3 scale occurs by the counter diffusion of oxygen and aluminum through the bulk and alloy grain boundaries. Some of the recent work carried out by Tolpygo and Clarke also illustrates the preferential diffusion of aluminum and oxygen along the grain boundaries in α-Al_2O_3 during scale growth[48] between 1100 -1200°C.

Work performed on these alloys also showed voids present at the metal-oxide interfaces. The formation of voids or interfacial cavities is the result of coalescence of vacancies arising from the outward diffusion of cations from the substrate to the scale. If inward diffusion of oxygen through the grain boundaries is predominant, void formation can be attributed to the fact that the rate of back diffusion to the alloy is faster than the rate of forward diffusion of oxidizable metal to the alloy scale surface[49-54].

2.4. Growth rate of alumina scales on FeCrAl alloys

A detailed knowledge of the rate law governing scale kinetics is absolutely essential for a reliable prediction of component life and materials application limits. When considering the

lifetime limits of FeCrAl alloys, the loss in a component's wall thickness due to oxidation is generally not life limiting. The reason being the scale thicknesses are in the μm range even after long periods of oxidation above 1000 °C. The lifetime limit is governed by the Al reservoir within the scale-forming alloy. Al is consumed during the scale growth and scale re-healing after spallation, which ultimately results in the exhaustion of the Al reservoir which leads to breakaway oxidation[55-57]. For a given alloy the breakaway depends on the volume/surface ratio of the component as well as the scale growth and spalling kinetics. The spalling kinetics is the crucial factor for the rate at which the Al reservoir is exhausted for thicker components. However for components which are about 100 μm thick or less, it is not usually the life-limiting factor and aluminum consumption is governed by the growth kinetics. It is this low Al reservoir which limits lifetime[25, 33, 34, 58-63].

The α-Al_2O_3 scales formed at or above 1000 °C generally exhibit a sub-parabolic and frequently near-cubic time dependent growth rate. Quadakkers et al. also showed that frequently used methods for determining the growth kinetics using weight change data by plotting $\Delta m/(t^{1/2})$ or $(\Delta m)^2/(t)$, gives an erroneous impression that scale growth kinetics are governed initially by transient-oxide and followed by a stable α-Al_2O_3 growth, which obeys parabolic time dependence[39]. In fact deviation from sub-parabolic and often near-cubic kinetics is frequently caused by scale cracking during thermal cycling.

2.5. Effect of Al content of the alloy

The influence of Al content is marked throughout the initial stages and final stages of the oxidation process and affects oxide nucleation, scale adhesion and growth rate.

The protective and adherent α-alumina scale formed on FeCrAl alloys grows with oxidation time, but after prolonged oxidation the aluminium content in the substrate is consumed by the continuously growing oxide scale. Once the level in the substrate falls below a critical value,

the alumina scale can no longer grow and chromium and iron oxide take over and start growing rapidly. Iron oxide grows more rapidly and does not have the same protective character as α-alumina scale and substrate consumption is significantly greater. This phenomenon is known as breakaway oxidation and corresponds to the end of lifetime of the alloy, marked by catastrophic failure of the substrate[64]. It has also been reported that formation of a chromia layer can effectively prolong the lifetime of the alloy once aluminium has been depleted. Hence the breakaway stage is no longer identical to the period of rapid weight change during oxidation[65].

The effect of aluminum content may be attributed to rapid formation of greater total number of Al oxide nuclei on the surface of the alloy thus reducing the inter-nuclear distances and hence a more rapid coverage of the surface. Some of the work done suggests that as Al content increased there was a reduction in the rate of oxidation[66]. This is due to rapid oxidation of base metal in the lower Al alloys, as it has been observed that, initially there is enhanced growth of base metal oxides at the metal surface. The amount of spallation decreased with increased Al content as spall particles became smaller in size and progressively finer [12, 56, 67-72].

2.6. Spalling of oxide scale

The oxidation of FeCrAl alloys involves nucleation followed by growth which ultimately forms the protective oxide scale on the surface. In some cases the oxide scale is smooth and adherent and does not spall, whereas in other cases the scale spalls at some stage of the oxidation process and is replaced with new intermediate scale formation at those spalled sites. The main reason for scale spallation is the stress generated during the isothermal oxidation. There are two principle modes of stress generation, the growth stresses and the thermal stresses

during oxidation of metal. Any of these modes of stress generation can be responsible for the scale spallation[12, 70, 72-75].

The growth stresses start accumulating in the oxide scale during its growth due to increase in volume as metal incorporates oxygen. As the thickness of the scale keeps increasing at a certain point the interface energy is much less than the stored elastic energy in the film and it releases the energy by spallation. Also the stress can be released either by cracking or buckling of the oxide scale and both these mechanisms would lead to scale spallation. The various factors which are responsible for the accumulation of growth stresses are discussed in the following paragraph.

An important factor is the difference in molar volumes of metal and the oxide scale formed on it, which can be denoted by a ratio described as the Pilling Bedworth Ratio (PBR).

$$PBR = \frac{V \text{ (per metal ion in oxide)}}{V \text{ (per metal atom in metal)}} \qquad \text{----------2 - 13}$$

where, V is the volume

The oxide is expected to be in compression if the PBR is greater than unity which is the case for most metal and FeCrAl alloys. The oxide is in tension if PBR is less than unity and alkali metals fall in to this category. If the PBR ratio is equal to 1 or close to 1, the oxide does not spall and the scale remains adherent to the substrate metal. This ratio is only useful when scale grows predominantly at the metal-oxide interface but is less important at the oxide-gas interface. This is because, when the oxide growth is controlled by the inward diffusion of anions, new oxide forms at the metal-oxide interface and this fresh oxide is constrained by the substrate metal and the existing oxide layer. This oxide growth is responsible for the growth

stress generated. The stress generated is due to the fact that the specific volumes of oxide are rarely the same as the metal consumed.

In the case of alumina, the formation of a mole of Al_2O_3 consumes two moles of Al based on the oxidation reaction (Equation 2-2). The Pilling Bedworth ratio is calculated as,

$$PBR = \frac{\text{Volume of a mole of } Al_2O_3}{\text{Volume of two moles of Al}} \qquad \text{----------2 - 14}$$

The volume (V) of one mole of oxide can be calculated as, $V = W/\rho$, where W is the mole weight of the oxide and ρ is the density of the oxide. PBR of oxidation of Al has been calculated as ≈ 1.29[76].

The other factors which are responsible for growth stresses are the epitaxial relationship between the metal and surface oxide, compositional changes between the metal/alloy and the oxide formed, and modes of diffusion.

Many applications of FeCrAl alloys at high temperature involve temperature fluctuation. The relative coefficient of expansion of the metal and oxide are therefore important in determining the additional stresses generated. The metals have higher coefficient of expansion than the oxide and on cooling introduce compressive stresses on the layer. The compressive stress generated are given by[2],

$$\sigma_{Oxide(compressive)} = \frac{E_0 \Delta T(\alpha_0 - \alpha_m)}{1 + 2(E_0 / E_m)(t_0 - t_m)} \qquad \text{----------2 - 15}$$

Where E_0 and E_m are the Young's moduli of oxide and metal/alloy, respectively

α_0 and α_m are the coefficients of thermal expansion of oxide and metal/alloy

t_o and t_m are the thicknesses of the oxide and metal/alloy

and ΔT is the temperature drop

The greater the disparity between expansion coefficients the greater the cyclic stresses generated and the less adherent the oxide becomes especially when PBR is > 1[24].

2.6.1. Spalling failure of α-Alumina scale

The influence of cooling rates and metal thickness on spalling failure of α-Al_2O_3 scale formed on FeCrAl alloys failure was studied by Tolpygo and Clark[48, 77, 78]. The α-Al_2O_3 scale was found to fail by spontaneous buckling and spalling at room temperature under constant residual stress. The authors suggested that for a given film thickness, the extent of spalling was independent of cooling rate, as might be expected if the residual stress alone motivated spalling. However it was found that for a given cooling rate, thinner metal plates exhibited more spalling, which was contrary to expectation as residual stress in the oxide is always greater on thicker metal plates. So, the extent of spalling cannot be related only to the residual stress in the film.

An explanation suggested in the literature is that slow cooling rates after isothermal oxidation, resulted in segregation of impurities at the oxide-metal interface[77]. If the interface was relatively clean during oxidation it remained free from impurities after fast cooling, whereas during slow cooling, there was a gradual decrease in impurity solubility in the alloy and hence impurities like sulfur, carbon, phosphorus were found to segregate at the interface which should weaken it. However the scale was found to be more adherent on slow cooling. This could be explained by considering residual compressive stresses in conjunction with impurity segregation in the oxide as follows: During slow cooling the interface is weakened but the stresses developed are too small to initiate buckling and spalling; during fast cooling, the stresses developed are high but the interface is strong as segregation to metal-oxide interface is prevented. However, a comparison of specimens of different thickness did not support the proposed hypothesis. As it was found that at any given cooling rate and at the same

segregation level, thinner specimens with lower oxide stresses exhibited more spallation[48, 79-86].

2.7. Effect of impurities and sulphur effect

All commercial alloys contain ppm levels of non-metallic impurities that segregate readily to the surfaces when alloys are oxidized at high temperatures. The segregant type and the extent of segregation at a given time and temperature depends upon the impurity concentration, the segregation free energy and the diffusion rate of the segregant. It has been known that sulphur can segregate to the growing metal-oxide interfaces thus weakening the interfacial bond and reducing scale adhesion. Hou et al.[6, 7, 87] tried answering such fundamental questions as, is it energetically favorable for a large sulphur ion to segregate to a metal-oxide interface. As discussed earlier, the scales formed on the FeCrAl are convoluted or wrinkled and the extent increases with time. It was found that the scale underside contained only Al and O, whereas S was found to segregate everywhere on the metal side of the interface[6]. It was found that sulphur built-up quickly at the interface and reached saturation level of about 22 – 26 atomic percent after just 10 minutes of oxidation. This rate was independent of cooling rate, oxidation time and interface morphology. Sulphur was found to co-segregate with chromium and nearly the same level of S was observed everywhere on the FeCrAl alloy as a result of co-segregation. It was concluded that the strong relationship between sulphur and chromium alters the segregation energy and dictates the interface sulphur content and is also independent of temperature or the type of interface morphology. The driving force for the segregation is the same as that to the free surface and independent of growth stresses. Carbon also segregated to interface during cooling owing to Cr enrichment at the interface. It has been found that adherence of alumina scale is greatly improved by the presence of small amount of RE. Many mechanisms have been proposed for this phenomenon but the most widely accepted one is known as the sulphur effect[7, 88].

In recent years the sulphur effect on the adhesion of oxide scales on metals has been a controversial topic. It is well established that sulfur in high-temperature alloys can deteriorate the oxidation resistance and enhance oxide spallation. The scales are more adherent on alloys with low-sulfur content, or after sulfur have been removed by repeated oxidation and grinding or desulfurization in H_2 at high temperatures, as has been been found by many authors[89, 90].

The oxidation resistance and oxide-scale adherence observed for high temperature alloys containing small alloying additions of Hf, Y, La, etc. could be partly explained by the fact that sulfur is tied-up effectively in the very stable sulfides of the rare-earth elements. The other major effect of sulphur was to enhance the interfacial void formation, creating a weaker interface by increasing its defect concentration. Sulphur-containing interfaces are weaker than sulphur-free interfaces. The interface formed on RE-containing alloys are much stronger, suggesting a positive effect of RE on scale adhesion. The sulphur effect on the adherence is due to the very high tendency for sulphur segregation to free metal surfaces which leads to a marked decrease in the metal surface energy. When void formation or scale detachment starts at some defect site on the interface, sulphur segregates immediately to the free metal surface formed thereby stabilizing the defect. Thus the presence of sulphur accelerates the growth to cavities and degrades the metal-oxide interface.

2.8. Structural data of alpha-alumina (α-Al_2O_3)

α-Al_2O_3 belongs to the space group $R\bar{3}c = D_3^6 d$ (International table for X-ray crystallography, Volume 1, 1972). The α-Al_2O_3 crystal structure is often described as having O^{2-} anions in an approximately hexagonal closed packed (HCP) arrangement with Al^{3+} cations occupying two-thirds of the octahedral interstices. The structure is composed of alternating O and Al planes[91]. This arrangement has been shown in Figure 2-3 and the empty site of the cation sub-lattice is used to define the corners of the unit cell which is shown schematically in Figure 2-4.

The α-Al_2O_3 is usually described in terms of hexagonal Miller-Bravais indices even though it is rhombohedral. This leads to a 30° rotation of the a-axes about the c-axis when compared to an hcp metal. Thus, the closed-packed direction in the anion sub-lattice lies along $<10\bar{1}0>$, whereas in hcp metals the closed-packed directions lie along the $<11\bar{2}0>$. The crystallographic specifications are given by the International table for X-ray crystallography, Volume 1, 1972 while the specific lattice parameters and atomic positions where determined by Newnham and DeHaan (1962).

Crystallographic specifications

I) The rhombohedral structural unit cell

Lattice	a=5.1284 A
Parameters	α=55.28 °
Cell volume	V=84.929 A^3
Formula units per cell	n=2

Atomic positions:

a) 4 Al3+ ions at 4c positions

w, w, w ; $\bar{w}$, $\bar{w}$, $\bar{w}$; 1/2 + w, 1/2 + w, 1/2 + w

and 1/2 - w, 1/2 - w, 1/2 – w

where w=0.3520

b) 6 O2- ions at 6e positions

u, 1/2 – u, 1/4 ; 1/2 –u, 1/4, u ; 1/4, u, 1/2 – u

$\bar{u}$, 1/2 + u, -1/4 ;1/2 + u, -1/4, $\bar{u}$ and -1/4, u, $\bar{1}$/2 + u

where u=0.556

II) The hexagonal structural unit cell

Lattice	a_0=4.7589 A
Parameters	c_0=12.991 °
Cell volume	V=254.792 A^3
Formula units per cell	n=6

Atomic positions:

a) 12 Al3+ ions at 12c positions

(0, 0, 0; 1/3, 2/3, 2/3; 2/3, 1/3, 1/3) +

0, 0, z; 0, 0, $\bar{z}$; 0, 0, 1/2 + z and 0, 0, 1/2 – z

where z=0.3520

c) 18 O2- ions at 18e positions

(0, 0, 0; 1/3, 2/3, 2/3; 2/3, 1/3, 1/3) +

x, 0, 1/4; 0, x, 1/4; x, x, -1/4; $\bar{x}$, 0, -1/4; 0, x, $\bar{-1}$/4 and x, $\bar{x}$, $\bar{¼}$

where x=0.306

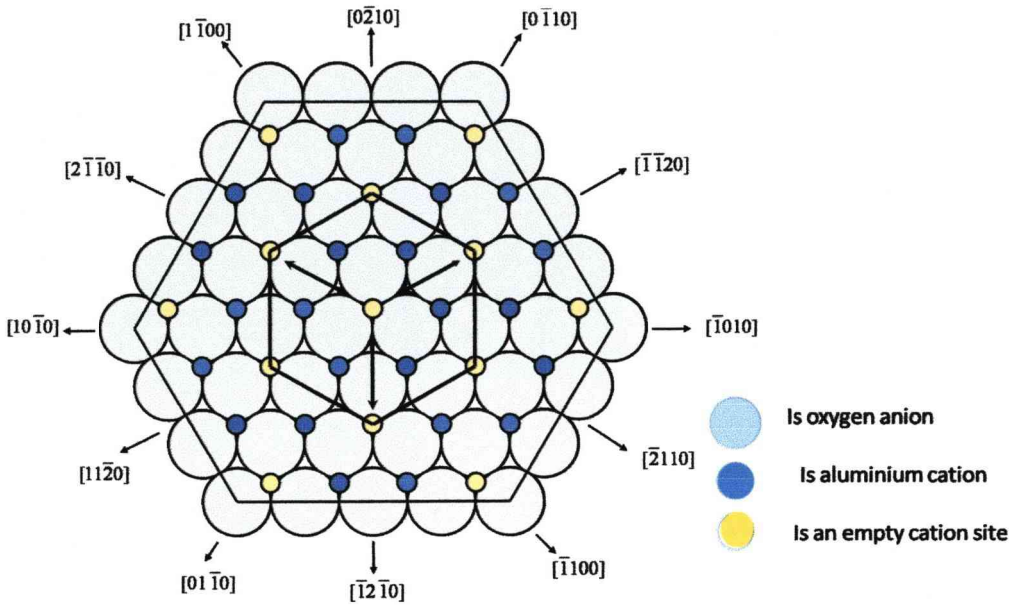

Figure 2- 3: The basal plane of sapphire, showing the HCP anion sublattice and the cation occupying two-third of the octahedral interstices (Kronberg 1957).

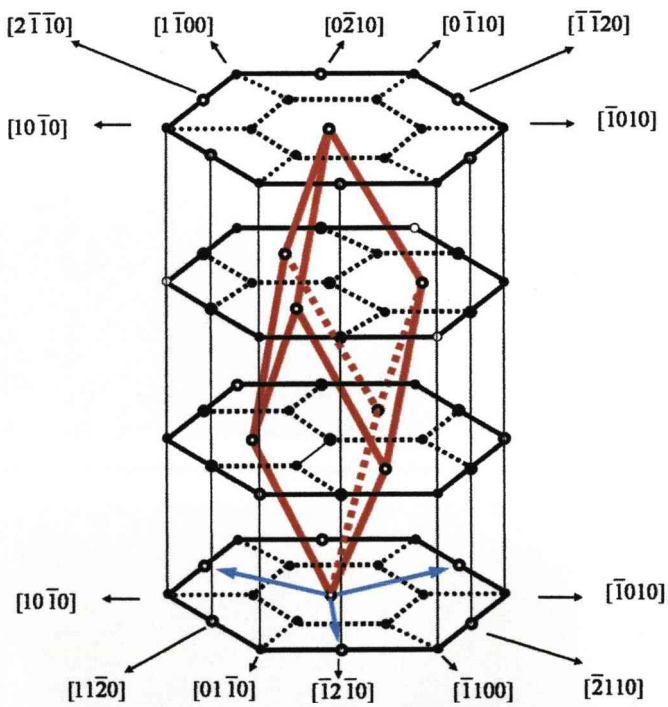

Figure 2- 4: The cation sublattice in sapphire. The vacant octahedral sites define the corners of a morphological unit cell (Kronberg 1957).

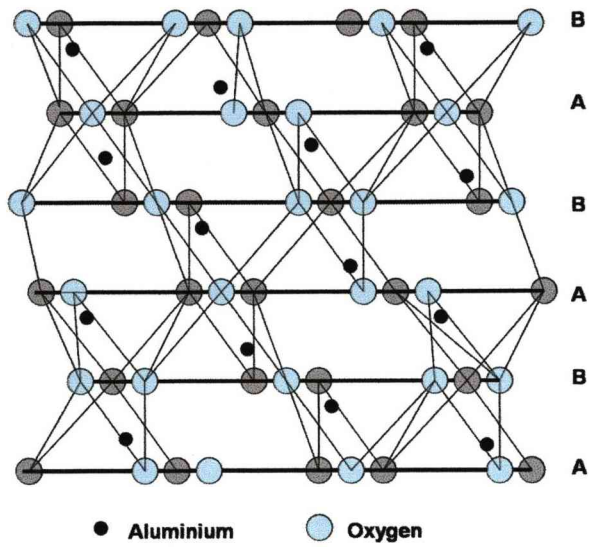

Figure 2- 5: Schematic showing the slice of the structure, one Al-polyhedron thick, showing the stacking sequence along [0001].

2.9. Grain-boundary segregation and grain-boundary diffusivity

Grain boundary segregation is a term which describes the localized concentration of solute species at the grain boundaries in solids. There are two main types of segregation; non-equilibrium and equilibrium. Solute pile-up at a moving interface or by solutes coupling to vacancies which are moving to grain boundary sources or sinks during quenching or under applied stress are a result of non-equilibrium segregation.

Equilibrium grain boundary segregation in metals and alloys is known to be severely detrimental to many important mechanical properties. It has been associated with the lattice disorder at the grain boundary and the sites which exist for solute atoms to segregate having a different energy from those in the lattice. In order to minimize the overall free energy of the system, in equilibrium segregation solute atoms partition unequally between the two sets of sites in accordance with the statistics of thermodynamics[88, 92-95].

2.9.1. The enthalpy of segregation

When a substitutional solute atom B is transferred from the matrix interior to the grain boundary in a matrix of A atoms, in the regular solution approximation, grain boundary segregation enthalpy (ΔH_b) is given by[88]

$$-\Delta H_b / N_0 = \tfrac{1}{2}\Delta Z_V(\varepsilon_{BB} - \varepsilon_{AA}) + (\Omega / N_0)(2Z_1 X_b + \Delta Z_V) \quad \text{----------2 - 16}$$

where ΔZ_v is the difference between the coordination number for atoms across an inter-atomic plane in the bulk (Z_v),and that across the grain boundary (Z_g). Z_1 is the coordination number in the atom layer which is assumed to be the same in the bulk as that of the grain boundary, R is the molar regular solution parameter, N_0 is Avogadro's number and ε_{AA} and ε_{BB} are the homogeneous interaction energies between nearest neighboring atoms A and B. The above calculation does not take account of the strain released as was discussed by McLean[96].

For solute atoms smaller than the matrix atoms no strain effect is expected, but for solute atom 10% greater than matrix atom, the strain term gives the dominant contribution to the enthalpy of surface segregation. At grain boundaries it is likely that this full strain term is again released[96]. Thus, using the relation for that of the molar sublimation enthalpy for species A, H_A^{sub} may be written as,

$$H_A^{sub} = -\tfrac{1}{2} Z\varepsilon_{AA} N_0 \quad \text{----------2 - 17}$$

$$\text{and } \Delta Z / Z_v = \gamma_b / 2\gamma_s \approx 1/6 \quad \text{----------2 - 18}$$

the above equations 2-16,2-17 and 2-18 can be combined to estimate the enthalpy of segregation where γ_b and γ_s are the surface energies.

2.9.2. Kinetics of segregation

Most models of the kinetics of segregation follow McLean's (1957) approach. Solute atoms are assumed to segregate to the boundary from two infinite half crystals of uniform solute content. Fick's laws are used to describe diffusion in the crystals.

The ratio of the solute in the grain boundary to that in the adjacent atom layer of the bulk is denoted as β. Assuming flux conservation at the boundary, the kinetics of the segregation are described by

$$\frac{X_b(t)-X_b(0)}{X_b(\infty)-X_b(0)}=1-\exp\left(\frac{4Dt}{\beta^2 f^2}\right)erfc\left(\frac{4Dt}{\beta^2 f^2}\right)^{1/2} \qquad \text{----------2 - 19}$$

where $X_b(t)$ is the grain boundary content at time t, D is the solute bulk diffusivity and is related to the atom sizes of the solute and matrix, b and a, respectively, by $f = a^3b^{-2}$. For short times the equation approximates to,

$$\frac{X_b(t)-X_b(0)}{X_b(\infty)-X_b(0)}=\frac{2}{\beta}\frac{b^2}{a^3}\left(\frac{4dt}{\pi}\right)^{1/2} \qquad \text{----------2 - 20}$$

The above equations are two extremes of a general problem. In general β is only constant for dilute systems with low segregation levels, as segregation proceeds β generally falls as a result of saturation.

2.10. Effect of Reactive Elements

Alumina-forming alloys are known to exhibit protective properties under high-temperature oxidizing environments. The presence of aluminum in the alloys allows the formation of a protective α-alumina scale. However, the oxide scale may spall under thermal cycling. Many investigations have shown that the addition of a reactive element such as yttrium, hafnium, or zirconium to the FeCrAl alloys improves their corrosion resistance at high temperature. In this

section the effect of these reactive elements are studied with respect to their effect on scale growth, adhesion and modification of oxidation mechanism. The effects of single reactive element as well as alloys co-doped with several reactive elements have been reviewed. The process by which the reactive element reduces scale spallation is known as the reactive element effect and is still poorly understood [5, 13, 27, 40, 44, 46, 63, 77, 79, 80, 82, 84-86, 89, 97-130]. There are various mechanisms by which the beneficial effect of reactive elements may be explained during the scale growth stage and the scale adhesion. One of the widely accepted mechanisms is promoting the nucleation of alumina and consequently reducing the aluminium content necessary to form a continuous alumina scale. The presence of a reactive element has been shown to change the growth mechanism of the scale from outward diffusion of Al ions and inward diffusion of O ions to predominantly inward diffusion of O ions through the scale[116]. The presence of reactive element has also been shown to enhance bond strength by binding impurities like sulphur and phosphorous and preventing their segregation to the metal-oxide interfaces, the effect is known as the sulphur effect[109].

The reactive element could be incorporated into the substrates as a pure element, as an oxide dispersoid or by various surface coating techniques. Figure 2-6 shows an schematic of different techniques by which reactive elements could be incorporated into the FeCrAl.

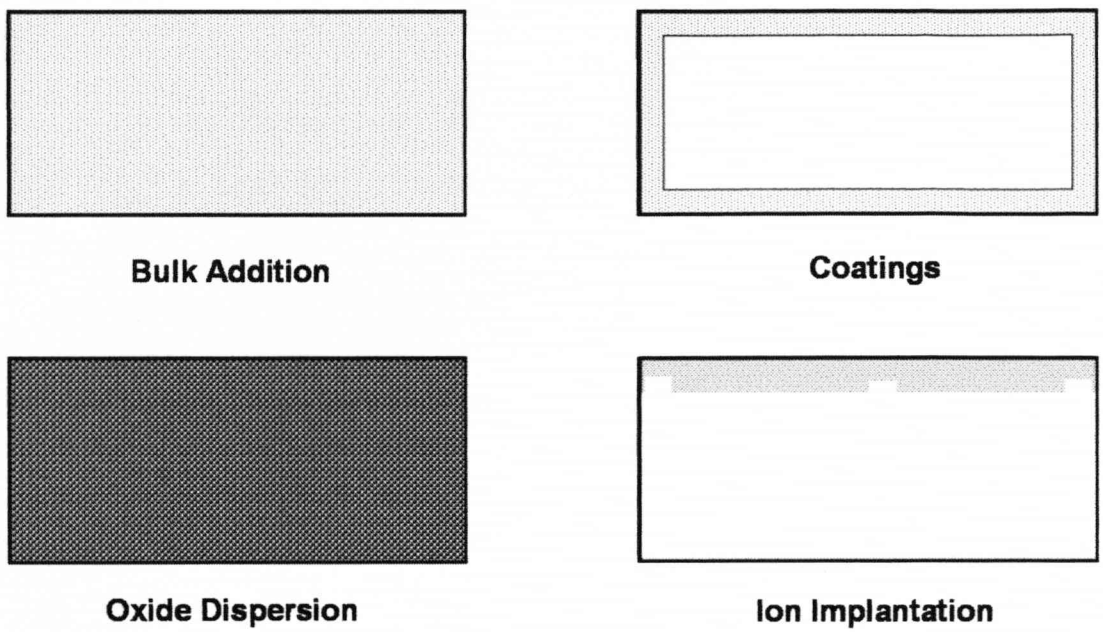

Figure 2- 6: Commonly used methods of adding reactive elements to the alloy substrate.

2.10.1. Effect of yttrium

In the last few decades a great deal of work has been done on studying the effect of yttrium (Y) on FeCrAl alloys. The reactive element yttrium has been added to improve the oxidation properties of the alloy. The research has indicated the effect of yttrium on the growth and structure of alpha-alumina scale, its effect on the chemistry and structure on the metal-oxide interface and the oxidation kinetics.

2.10.1.1. The effect of yttrium on the growth rate of scale

As discussed in the previous section, during the initial stages of oxidation, there is oxidation of all the constituent metals including aluminum. As the oxidation progresses only the stable alpha-alumina continues to form. The early growth and development of protective Al_2O_3 scales during oxidation at temperatures in the range of 900 to 1300 °C, is complicated by the

presence of transition alumina (γ -Al_2O_3, δ -Al_2O_3, and θ -Al_2O_3) which eventually transform into the stable α-alumina.

Previous authors studied growth rates using alloys doped Y and undoped alloy. It was found that, after an initial transient stage of about 8-10 hr, the oxidation kinetics of both doped and undoped specimens were controlled by diffusion[100, 101, 131]. It was shown, that a mainly parabolic growth rate law is followed after an initial transient stage and results in slower oxidation rates.

The oxide scale formed on undoped alloy was composed of transition alumina and α-Al_2O_3, whereas those formed on doped alloys were mainly α-Al_2O_3. It was found that there was no significant influence of Y on the oxidation rate of Y-doped alloy during the transient oxidation stage. However the parabolic part of the mass-gain curves showed a marked influence of yttrium on the growth rate of the oxide scale. The addition of the reactive element leads to a reduction of the parabolic rate constant by a factor of about 10. This mass gain analysis together with micro structural analysis suggested that the effect of the reactive element Y is to accelerate the phase transformation of transition alumina into α-Al_2O_3 and hence promotes the growth of a more protective oxide scale. This mechanism whereby reactive element influences the rate of transformation of metastable alumina into α-alumina at temperatures below 1000 °C is still a matter of discussion.

A further possible mechanism suggested by some authors involved the presence of more heterogeneous nucleation sites on the alloy surface and presence of yttrium causing early nucleation. This early nucleation leads to early formation of the stable alpha-alumina. Hence mostly alpha-alumina scale was observed on the surface of the doped alloys[13, 23, 45, 100, 102, 103, 108, 117, 132-135].

Some other authors, however, have reported that yttrium additions delay the phase transformation. Jedlinski has proposed a possible explanation of these various existing controversies[62, 136]. According to him the influence of the reactive element can be accounted

for in terms of parallel mechanisms, which lead respectively to an acceleration or a retardation of the phase transformation. The relative contribution of each of these mechanisms depends on the amount and form of the reactive element.

2.10.1.2. The effect of yttrium on the growth and structure of alpha-alumina

The yttrium (Y) addition protects the base FeCrAl alloys against oxidation at high temperatures by improving the adhesion of the α-Al2O3 scale produced. There were marked differences and similarities found when FeCrAl with and without yttrium additives were studied. It was found that the alloys with and without yttrium additive formed oxide scales which were roughly of the same thickness. The oxide surface on the undoped alloy revealed a coarse structure with small ridges on the oxide grain boundaries whereas the oxide surface of the Y-doped alloy showed a fine-grain oxide structure. There was no scale spallation observed on the Y-doped alloy, whereas the oxide on the undoped alloy spalled during cooling to room temperature. This spallation was limited to a few small areas, which were mainly located at metal grain boundaries.

The undoped alloy was found to exhibit large equiaxed α-Al_2O_3 grains which had a diameter of approximately 1 micron. In the undoped oxide scale, micro-voids were present at the metal-oxide interface, at intersections with oxide grain boundaries. These voids were spaced a few microns apart. Generally the oxide grains were found to be in good contact with the metal substrate. There were micro-voids detected within the outer half of the oxide scale.

On the other hand, an Y-containing alloy was found to have a columnar grain structure beneath a thin scale of equiaxed grains at the oxide-gas interface. The columnar grains were approximately 1± 2 micron in length and about 0.4± 0.6 micron in width. There were no micro-voids found in the scale and the metal–oxide interface was found to be intact.

The different growth mechanisms observed on Y-doped and undoped FeCrAl gave rise to the columnar or equiaxed oxide grain structure. It appears likely that the growth of columnar

grains is a result of formation of new oxide at the metal-oxide interface, indicating the scale grows predominantly by inward diffusion of oxygen. It could be concluded from the growth of such scale on Y-doped alloy that, Al diffusion was suppressed by Y ions segregating to oxide grain boundaries, while growth of equiaxed grains occurred mainly by oxide formation throughout the scale, which requires simultaneous inward and outward transport of oxygen and Al[45, 113, 114, 123, 128]

The Y diffusion seems to suppress void formation at the metal-oxide interface for Y-doped FeCrAl. As the scales on undoped alloys grew both by inward and outward diffusion, micro-voids were found near the upper half of the oxide scales.

The microstructure near the interface reveals a small number of particles which was found to be rich in yttrium, when analyzed using X-ray spectroscopy. The earlier work done to calculate the yttrium coverage shows a value of about 0.36-0.1 monolayer across most of the boundaries examined near the metal-oxide interface. Y-rich precipitates were also detected in small numbers at oxide grain boundaries using X-rays. Hence the presence of Y-rich precipitates in the scale at oxide grain boundaries was assumed not to have a significant influence on the diffusion properties.

2.10.1.3. Influence of yttrium on stress in the alumina scale

The addition of reactive elements such as yttrium to FeCrAl alloys significantly improves the adherence of thermally-grown oxide scales. One of the proposed beneficial mechanisms is based on the premise that yttrium helps to decrease the residual compressive stress in the oxide exerted by the substrate thus decreasing the driving force needed for spallation of the oxide scale[63, 116].

The microstructural variations have been studied most widely with yttrium as the most common reactive element additive. As mentioned in the above section, the scale formed on alloys containing yttrium tends to be flat and without any voids at the metal-oxide interface in

contrast to undoped alloys. The work carried out by Tolpygo and Clark et al has tried to look at different mechanisms generating reduction in stresses[48]. The results obtained showed that the compressive stress in the oxide scale formed on Fe-Cr-Al as a function of oxidation time at 1100°C was similar in the doped and undoped yttrium although the yttrium-containing material could sustain a larger compressive stress by about 0.7 GPa. It was also found that the stresses gradually increased with oxidation time.

Some of the recent work done to measure the effect of yttrium on boundary strength of the metal-oxide interface suggests that there is a marked improvement[82, 83, 86]. Although it was found that the Y-doped and undoped samples underwent similar microstructural changes, the interfacial strength of the Y-doped sample was reduced. The possible explanation suggested by the author was depletion of Y at the interface due to formation of yttrium-rich precipitates[97, 137].

2.10.2. Effect of Hafnium (Hf)

The effect of Hf on FeCrAl alloy without any other additive has been discussed previously by Pint et. al [138], who showed that Hf-doped FeCrAl lowered the parabolic rate constants at 1200 °C by a factor of 3. Work carried out on an alloy with an 0.05% hafnium addition showed a lower rate constant compared to alloys with an yttrium addition.

He found there were pegs present at the metal-scale interface and in the metal, which were filled with reactive element-rich oxides and showed the presence of internal oxidation. He also concluded that the amount of internal oxidation decreased as the reactive element content was reduced, which resulted in lower rate constants. He found that hafnium doping was the most effective in reducing the scale growth rate in FeCrAl. Even though the hafnium-doped alloy had the lowest growth rate it was found that it had the shortest useful lifetime, resulting from excessive spallation of the scale. No clear reason for the poor spallation performance of the

hafnium-doped FeCrAl has been given. Pint et al. suggested that as the alloy had higher sulfur content, it could be linked to scale spallation, but no direct correlation could be drawn.

2.10.3. Effect of Zirconium (Zr)

The grain boundary segregants may have either detrimental or beneficial effects on scale micro-structure and properties. Detrimental aspects of grain boundary segregation are segregation-induced inter-granular fracture embrittlement induced by impurity elements. Beneficial effects of dopant segregation on material properties have been demonstrated in FeCrAl alloys by improving the oxidation resistance. Cyclic oxidation tests were carried out to see the effect of zirconium on FeCrAl alloy, and it was found that they showed lower growth rate compared to alloys with other reactive element additives[139]. It was found that though the alloys with zirconium additive had a lower growth rate it spalled earlier compared to alloys having a higher growth rate.

As mentioned above, reactive element additions have also been responsible for increase in the creep resistance of the alloy by a factor of two to three times. Work carried out by Wang et al. [140, 141] showed the presence of zirconium at grain boundary sites in alpha alumina ceramics. It has been proposed that the ionic size mismatch between the solute and the matrix lattice is the dominant driving force for such solute grain boundary segregation. The Zr ions are larger than the Al ions, and they show strong tendency for segregating to alpha Al_2O_3 grain boundaries. This may be the reason for the poor spall resistance of the Zr-rich alloys.

Chapter 3

Electron Scattering Theory

3.1. Electron scattering theory

The scattering of fast electrons can be divided into elastic and inelastic components; the term elastic being taken to mean that the energy lost to the sample during the scattering is less than the experimental energy resolution.

In this section these two types of scattering will be discussed in detail. The theory of electron interaction within a solid is usually considered as scattering of an electron by a single isolated atom and then modified to accommodate the various states of agglomeration of atoms in amorphous and crystalline solids.

An electron travelling through a solid can be scattered in many ways when it interacts with an isolated atom as shown schematically in Figure 3-1.

Only forward scattered electrons are discussed in this chapter; Figure 3-2 defines the parameters of forward scattering. The electrons may be scattered through an angle θ (radians) into a solid angle Ω measured in steradians (sr). θ is assumed to be small and hence , $\sin\theta = \tan\theta = \theta$. The characteristics of scattering events are controlled by many factors such as the electron energy and the atomic number Z of the scattering atom and the closest approach of the electron.

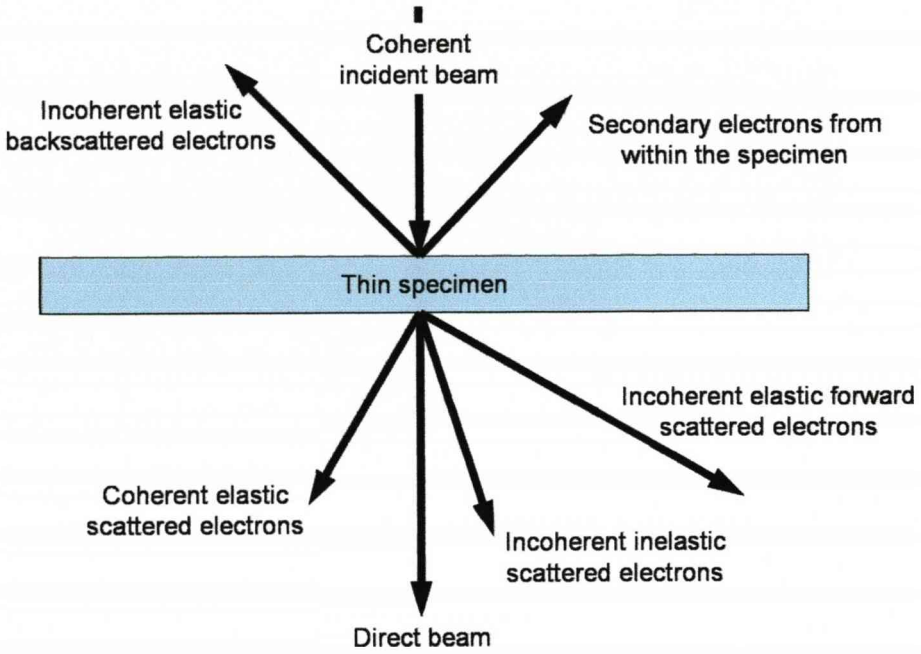

Figure 3- 1: Different kinds of electron scattering from a thin specimen[142]

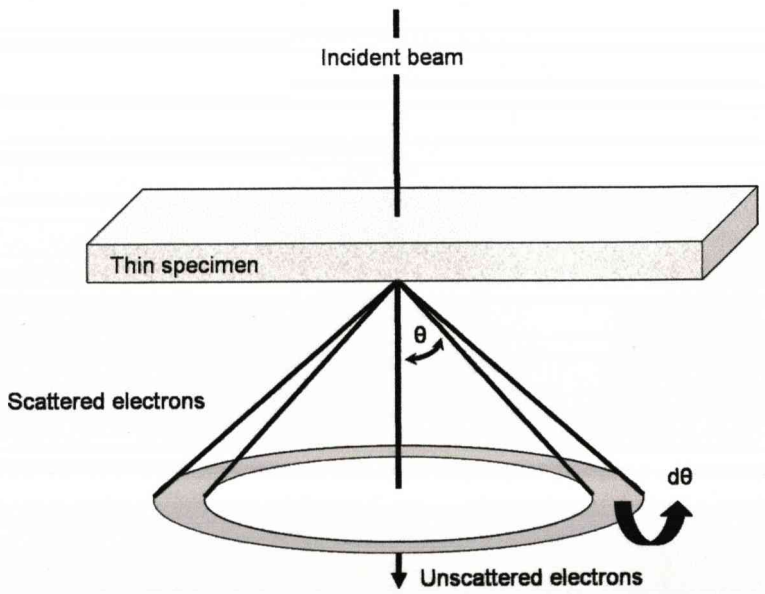

Figure 3- 2: Electron scattering by a single isolated atom. The electrons are scattered through an angle θ and the total solid angle of scattering is Ω. An incremental increase in scattering angle $d\theta$ gives an incremental increase in solid angle $d\Omega$ where $d\Omega=2\pi\theta d\theta$[142].

3.1.1. Elastic scattering

Interaction of an incident electron with the electrostatic field of an atomic nucleus is known as elastic scattering. A nucleus is some thousands of times more massive than an electron, so the energy transferred involved in elastic scattering is negligible. However, small fractions of electrons are scattered through large angles, the transfer can then amount to some tens of eV. Elastic scattering is not a subject of direct interest in electron energy loss spectroscopy, but it is of relevance because[143]

1) Some electrons undergo both elastic and inelastic interaction within the sample. The angular distribution of the inelastically scattered electrons is thus modified by convolution with elastically scattered electrons.
2) Elastic scattering may redistribute the electron flux (current density) within each unit cell in a crystalline material and thereby alter the probability of certain types of inelastic scattering.
3) Local atom number, i.e. chemical composition of a specimen, can be estimated by the intensity of elastic scattering as displayed by image contrast in Bright Field (BF), Dark Field (DF) and High Angular Dark Field (HADF).

3.1.2. Differential cross-section

Differential cross-section is an important basic quantity in scattering theory, which represents the probability of an incident electron being scattered (per unit solid angle Ω) by a given atom. For the elastic scattering, one can write the differential cross-section as,

$$\frac{d\sigma}{d\Omega} = |f|^2 \qquad \text{----------3 - 1}$$

where, f is the complex scattering amplitude or scattering factor, which is a function of the scattering angle θ or the scattering vector $\mathbf{q}$. f is proportional to the three dimensional Fourier

transform of the atomic potential V(r), within the first Born approximation (equivalent to assuming only single scattering within each atom).

$d\sigma/d\Omega$ can be expressed in terms of an elastic form factor $F(q)$,

$$\frac{d\sigma}{d\Omega} = \frac{4}{a_0^2 q^4}|F(q)|^2 \qquad \text{----------3 - 2}$$

$$\frac{d\sigma}{d\Omega} = \frac{4\gamma^2}{a_0^2 q^4}|Z - f_x(q)|^2 \qquad \text{----------3 - 3}$$

$a_0 = 4\pi\varepsilon_0 h^2 / m_0 e^2 = 0.529\times10^{-10} m$ is the Bohr radius

$\gamma = (1 - v^2/c^2)^{-1/2}$ is a relativistic factor dependent upon the electron velocity v and $q=2k_0 sin\theta/2$ is known as a scattering vector.

A more thorough discussion on the interference of electron scattering can be found in Egerton[143].

3.2. Inelastic scattering

Higher levels of energy sharing occur between particles of similar mass. Hence fast electrons are inelastically scattered through interaction with either outer- or inner-shell atomic electrons. These two processes predominate in different regions of the energy loss spectrum, the low loss arising from the interaction with outer-shell electrons and core-loss arising from the interaction with inner-shell electrons.

In this section, theories which predict the total cross section for inelastic scattering by atomic electrons are discussed briefly followed by application to low loss and core loss events.

3.2.1. Differential cross section

To have a comparison with elastic scattering, angular dependence of the total inelastic scattering (integrated over all energy loss) is expressed by the differential cross-section $d\sigma_i / d\Omega$.

Lenz in 1954, obtained a differential cross section by modifying Morse's theory of elastic scattering, and can be written in the form,

$$\frac{d\sigma_i}{d\Omega} = \frac{4\gamma^2 Z}{a_0^2 q^4}\left\{1 - \frac{1}{[1+(qr_0)^2]^2}\right\} \qquad \text{----------3 - 9}$$

r_0 is a screening radius and equal to $a_0 Z^{-1/3}$ for the Thomas-Fermi model.

The magnitude q of the scattering vector is given approximately by the expression

$$q^2 = k_0^2(\theta^2 + \bar{\theta}_E^2) \qquad \text{----------3 - 10}$$

where,

$k_0 = 2\pi / \lambda = \gamma m_0 v / \hbar$ is the magnitude of the incident electron wave vector

$\bar{\theta}_E = \bar{E} / (\gamma m_0 v^2)$ is a " characteristic angle" corresponding to the mean energy loss $\bar{E}$

The first term $(4\gamma^2 Z / a_0^2 q^4)$ is simply the Rutherford cross section for scattering by the atomic nucleus, the remaining term within the square brackets in Equation 3-9 is described as an inelastic form factor.

Equations (3-9) and (3-10) combined give an expression for the angular dependence,

$$\frac{d\sigma_i}{d\Omega} = \frac{4\gamma^2 Z}{a_0^2 k_0^4}\frac{1}{(\theta^2 + \bar{\theta}_E^2)^2}\left\{1 - \left[1 + \frac{\bar{\theta}_E^2}{\theta_0^2} + \frac{\theta^2}{\theta_0^2}\right]^{-2}\right\} \qquad \text{----------3 - 11}$$

where,

$\theta_0 = (k_0 r_0)^{-1}$ as in the elastic scattering model.

A more precise description of inelastic scattering by electron as given by Bethe follows.

3.3. Dielectric formulation

Bethe theory is useful in describing the inelastic scattering taking place inside a solid, particularly from inner atomic shells. However the wave functions are modified for outer shell scattering by added dimensions concerning chemical bonding. For the outer shell electrons a different approach where the interaction is explained in term of the dielectric response function $\varepsilon\ (q,\ \omega)$ is useful.

Ritchie derived an expression for the electron scattering power of an infinite medium. The transmitted electron represented as a point charge $-e\delta(\mathbf{r}-vt)$ which generates a spatially and, time dependent electrostatic potential $\phi(\mathbf{r},t)$ satisfying Poisson's equation,

$$\varepsilon_0\varepsilon(\mathbf{q},\omega)\nabla^2\phi(\mathbf{r},t)=e\delta(\mathbf{r},t) \qquad \text{----------3 - 12}$$

Using Fourier transform, the stopping power *(dE/dz)* which is equal to the force on the electron in the direction of motion is represented as,

$$\frac{dE}{dz}=\frac{2\hbar^2}{\pi a_0 m_0 v^2}\iint\frac{q_y\omega\,\mathrm{Im}[-1/\varepsilon(q,\omega)]}{q_y^2+(\omega/v)^2}dq_y d\omega \qquad \text{----------3 - 13}$$

The imaginary part of $[-1/\varepsilon\ (q,\ \omega]$ is known as the energy loss function and provides a complete description of an electron traveling through the medium. The stopping power can be related to the double differential cross section for inelastic scattering by,

$$\frac{dE}{dz}=\iint n_a E\frac{d^2\sigma}{d\Omega\ dE}d\Omega\ dE \qquad \text{----------3 - 14}$$

where,

n_a represents the number of atoms per unit volume of medium, by writing $dq_y = k_0\theta$ and $d\Omega = 2\pi\theta\ d\theta$, Equation (3-13) and (3-14) give,

$$\frac{d^2\sigma}{d\Omega\, dE} = \frac{\mathrm{Im}[-1/\varepsilon(q,E)]}{\pi^2 a_0 m_0 v^2 n_a}\left(\frac{1}{\theta^2+\theta_E^2}\right) \qquad \text{----------3 - 15}$$

$\theta_E = E/(\gamma m_0 v^2)$ contains the same Lorentzian angular dependence and the same v^{-2} factor as the corresponding Bethe equation, and comparing these two equations indicates that dielectric theory is equivalent to the Bethe theory if,

$$\frac{df}{dE}(q,E) = \frac{2E}{\pi E_a^2}\mathrm{Im}[-1/\varepsilon(q,E)] \qquad \text{----------3 - 16}$$

where,

$E_a^2 = \hbar^2 n_a e^2/(\varepsilon_0 m_0)$ is the plasmon energy corresponding to one free electron per atom.

EEL spectra are acquired over a small collection angle, and since $\varepsilon(q, E)$ varies little with q, it can be replaced with the optical relative permittivity of the specimen $\varepsilon(0, E)$, at an angular frequency, $\omega = E/h$. The EEL spectra can then be directly compared to the optical data, after applying Kramer's-Kronig transformation to obtain $Re[1/\varepsilon(0, E)]$, as explained in the experimental section.

3.4. Single scattering of electrons

The probability of an electron undergoing inelastic scattering in a thin specimen is low and the joint probability of more than one such event is negligible. Hence the energy loss spectrum corresponds to a single scattering distribution (SSD).

However there is a finite probability of a fast electron being inelastically scattered more than once in a thick specimen. This probability of n collisions through a sample of thickness t can be written following *Poisson's* distribution.

$$P_n = (1/n!)m^n \exp(-m) \qquad \text{----------3 – 17}$$

where m is the mean number of collisions within the specimen and can be written as t/λ where λ is the mean free path.

$$P_n = \frac{I_n}{I} = \left(\frac{1}{n!}\right)\left(\frac{t}{\lambda}\right)^n \exp\left(\frac{-t}{\lambda}\right) \qquad \text{----------3 - 18}$$

Assumptions have to be made such as; all scattering events have been recorded and the specimen is of uniform thickness. However spectrometer systems only accept electrons that have been scattered through an angle with a value less than β.

Multiple scattering occur in samples when the thickness of the sample is more than $t/\lambda = 10$, resulting in a broad peak at an energy loss of a few hundred eV, known as the *Landau* distribution. Before analysis of energy loss spectra it is important to remove plural scattering. Standard techniques to obtain the single scattered distribution (SSD) are explained in the experimental section.

3.5. X-ray and EDX Analysis

Throughout this research an EDX microanalysis system was used for collection and analysis of X-ray spectra. In this section there is brief discussion of the operation of EDX detectors and processing techniques. This section has been divided into three parts:

1] Theory of X-ray generation and measurement

2] Theory of qualitative and quantitative microanalysis

3] Practical steps involved in qualitative and quantitative analysis

3.5.1. X-ray generation and measurement

When a fast moving electron passes through a specimen it may be scattered elastically, inelastically or not at all. The energy lost by the transmitted electron depends upon the type of interactions it has undergone[144]. Inelastic scattering may be divided into three categories:

1] Brems-strahlung

2] Ionization of inner shells

3] Plasmon excitation

When a fast electron enters a sample it can interact directly with an electron in an atom, losing some of its energy or it may be attracted towards the nucleus which may lead to a change in its direction. When an electron gets close to the positive nucleus it will be attracted as electrons are negatively charged particles. This leads to a change in their direction involving acceleration while approaching the positive core and deceleration while moving away from it.

During the acceleration and deceleration the electron radiates its energy which is emitted as Brems-strahlung [breaking radiation]. We can see this type of radiation in our EDX spectrum as the continuum background known as white radiation. Figure 4-4 shows an schematic, showing Brems-strahlung radiation.

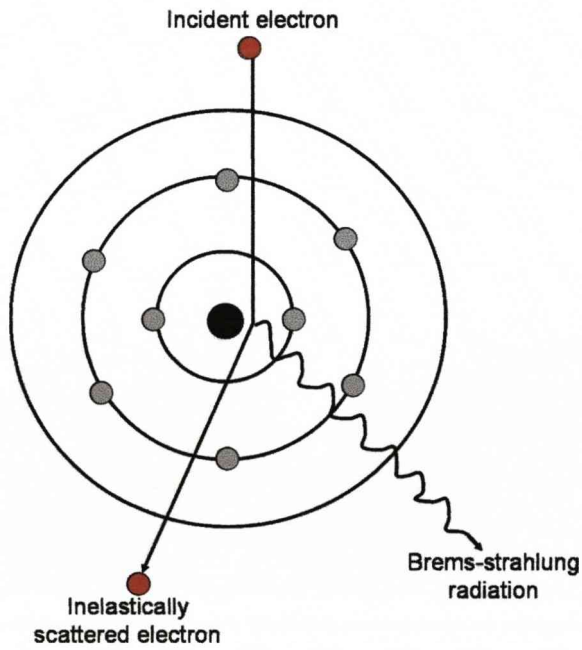

Figure 3- 3: Schematic representation of an electron interacting inelastically with the positive nucleus[28, 144].

3.5.1.1. Ionization of inner-shell electron

When a fast moving electron enters a specimen and interacts with an electron from the inner shell of an atom, it may lose some of its energy to the bound electron, thereby ejecting that electron from its shell and creating a hole in place of that electron. The gap or hole is filled by a further electron from an outer shell which releases an X-ray whose energy can be given by the difference in energy of the electron orbitals involved. Figure 4-5 shows a schematic of X-ray generation.

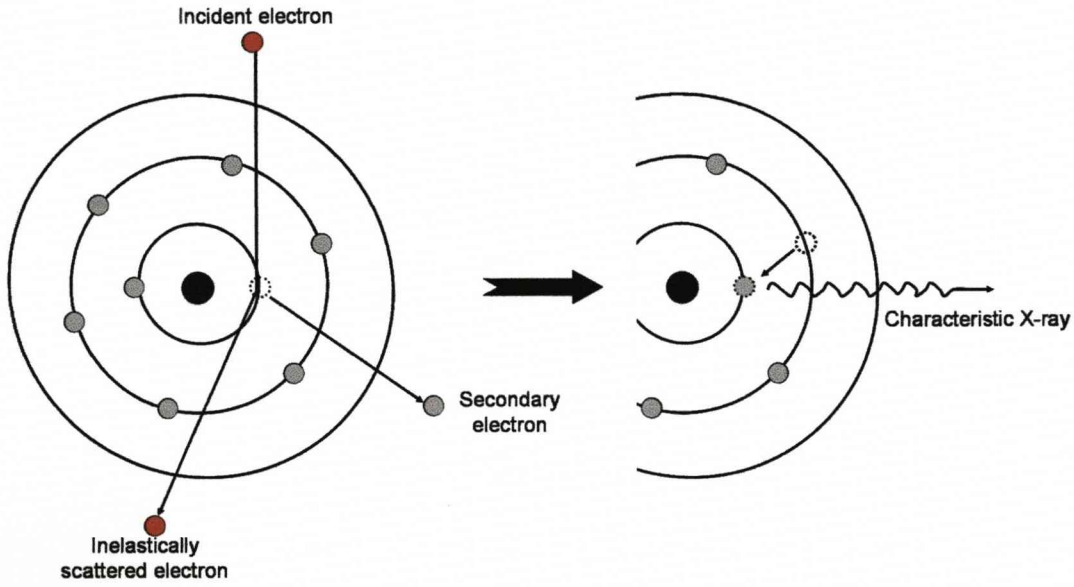

Figure 3- 4: Schematic of X-ray generation[144].

A nomenclature has been developed to indicate the source of X-rays depending upon the electron orbital involved. For example the Kα x-ray results from a K-shell electron being ejected and an L-shell electron moving into its position. A Kβ X –ray occurs when an electron jumps from an M-shell into the K shell. The Kβ X-rays will always have higher energy than Kα X-rays. Similarly Lα X-rays result from an electron from M-shell moving into L-shell to

fill a vacancy there. The presence of an Lβ X-ray means an electron from N-shell is allowed to fill a vacancy in the L-shell. Figure 4-6 below shows the schematic of nomenclature used to denote the X-ray.

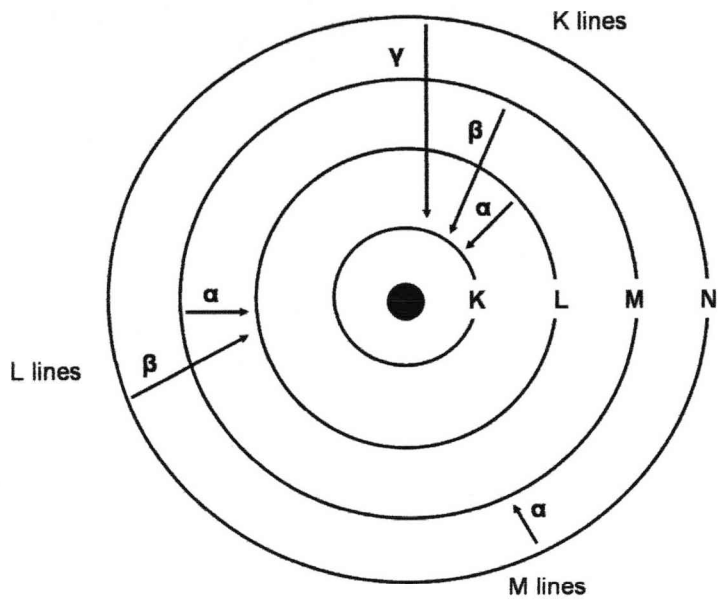

Figure 3- 5: Schematic of nomenclature developed to indicate the source of X-ray[144].

As the electron orbital structure is much more complex than shown in the diagram, there are actually many more L lines which can be present. M X-rays if present will always have energies lower than L or K series.

As all the electrons from a given shell do not posses exactly the same energy, there is specific variation within α and β radiation. For example Kα X-ray radiation comprises of Kα1 and Kα2 X-rays. These are very close together in energy and hence they are unresolved in most EDS systems and appear as a single Kα peak in the spectrum[144].

The X-rays produced are detected by an energy dispersive system (EDS). The EDS system consists of three main parts, namely the energy dispersive detector, the processing electronics, and a multi channel analyzer (MCA) display. A computer controls all three parts, First it controls whether the detector is on or off. Ideally we only want to process one incoming X-ray at a time, so the detector is switched of when an X-ray signal is detected. The effective time for which the detector is switched off is called dead time. The detector is protected by a collimator that ensures the X-rays generated from surrounding parts of the STEM or TEM column cannot reach the detector. The X-ray detector is normally separated from the specimen by a window which is transparent to X-rays above 0.3 KeV while it also separates the column/detector vacuums.

The detector is a reverse-biased p-i-n diode which consists of lithium doped silicon [Si (Li)] coated in front with a thin layer of gold. The X-rays produce charge pulses in the silicon. The charge is proportional to the absorbed energy of the X-ray.

When an X-ray interacts with a semiconductor the primary method of energy deposition is the transfer of electron from a valance band to the conduction band creating an electron-hole pair. A high energy electron loses energy in silicon (Si) in a similar way as described, generating electron/hole pairs until it has been totally absorbed or it escapes.

The energy required for a transfer of an electron from the valance band to the conduction band in silicon is approximately 3.8 eV at liquid nitrogen operating temperature. Since X-rays of interest have energy > 0.5 keV. Thousands of electron hole pairs can be generated by a single X-ray. The charge is amplified and measured in a pulse height analyzer (PHA) and posted on to a digital multichannel analyzer. Because the quantity of charge is a small fraction of the charged pulse, the PHA gives a good statistical measurement of each pulse and a spectrum with typically 150 eV resolution is attainable resulting in a very useful spectrum.

Secondly the computer controls the processing electronics to balance pulse integration time against count rate. It is also an integral part of the MCA.

Finally the computer software governs both the calibration of the spectrum readout on the MCA screen and adds alpha-numeric's which record the condition under which the spectrum was acquired.

Chapter 4

Experimental procedure

4.1. Cyclic Oxidation of FeCrAlRE (M11) and Kanthal A1

The oxidation behaviour of two different alloys has been examined. A Model alloy with controlled reactive element additives and a commercial alloy, Kanthal A1, were used in this study of the oxidation growth rate and their composition is listed in Table 4-1. Rectangular test pieces of size 17 x 12 x 1.5mm were polished to 1200 grit finish, removing the top oxide layer and any damaged layers from as received samples. The samples were then degreased by ultrasonic cleaning in analar-isopropanol. The initial weight of the samples was recorded using a micro balance. The weight of the crucible, silica rod and sample is given as total weight (W_T). The weight of the crucible and silica rod is given as (W_C) and hence the weight of the sample was calculated by subtracting W_T from W_C and represented as W_S.

	Elements (Wt%), Balance = Fe								
Alloy	Cr	Al	Si	Mn	Zr	C	Y	Hf	Ti
Kanthal A1	22.2	5.66	0.26	0.13	0.083	0.022	-	-	0.016
M11	19.55	4.85	-	-	0.032	0.0131	0.033	0.030	-

Table 4- 1: Elemental composition of Kanthal A1 and M11.

Figure 4-1 shows a schematic diagram of the horizontal furnace used for cyclic oxidation of the samples. Short-dwell-time cyclic oxidation tests were performed in the laboratory atmosphere at 1250°C; the hot-dwell time was 1 hour followed by 15 minutes cold-dwell time. Cooling was performed in air. The weight gain behavior of the alloys was monitored by removing and weighing the samples every 7 or 14 cycles in a microbalance with an experimental error of ± 0.2mg. Figure 4-2 shows schematic of the technique used to measure the weight of the samples.

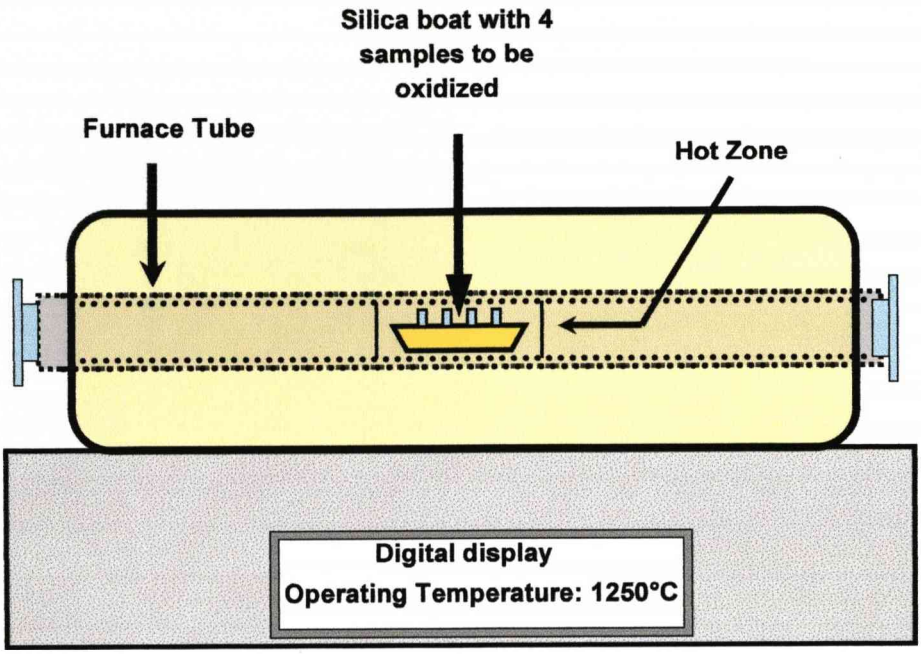

Figure 4- 1: Schematic of horizontal furnace used in the cyclic oxidation of FeCrAlRE (M11) and Kanthal A1.

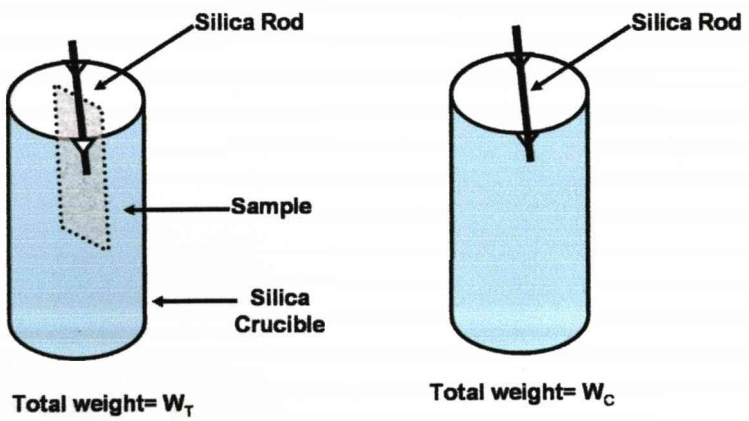

Figure 4- 2: Schematic of the method used to measure the weight of the samples.

4.2. Sample preparation for the TEM, STEM and SuperSTEM

The model alloy used throughout the experiment was designated M9 and supplied by Jean Le Coze, Ecoles des Mines, France

	Elements (Wt%), Balance = Fe								
Alloy	Cr	Al	Si	Mn	Zr	C	Y	Hf	Ti
M9	19.53	4.85	-	-	-	0.0115	0.033	0.031	-

Table 4- 2: Composition of Model alloy M9.

Samples were supplied as rectangular pieces of size 17 x 12 x 1.5 mm. The samples were surface ground on 1200 grit, to remove the surface oxide layer. The ground samples were then polished using 6 and 1 micron cloth to achieve a one micron finish and then degreased by ultrasonic cleaning in isopropanol. After finishing the ultrasonic cleaning, the samples were oxidized for 100 hours at 1250 degree centigrade in a horizontal furnace. The oxidation was carried out under laboratory air. The oxidized samples were taken out from the furnace and left to cool down under ambient conditions. After cooling, the oxide layer from one of the sides was removed by grinding and polishing on the 1200 grit so that the metal surface was exposed. The other side of the sample was covered with wax to prevent the oxide from falling off the substrate by holding them together. The exposed metal surface was etched away using ferritic stainless steel etch. Ferritic stainless steel etch is an etchant which has a composition of 43 % HCl, 14 % HNO_3 and the balance is distilled water. Once the metal was etched away, the oxide with wax on one side floated to the surface and could easily be picked up using a pair of tweezers. The wax was then dissolved in acetone and the remaining oxide, which floated on the top of bath, was picked up and rinsed in distilled water and ethanol two or three times and then picked up on a copper TEM grid. The oxide was glued to the grid using a small amount of

epoxy to hold it in place. The oxide with copper grid was thinned using a precision ion polishing system (PIPS) with 5 kV argon (Ar) ions at an angle of 5 degrees. The sample was thinned until electron transparent. The whole process of sample preparation is shown schematically in Figure 4-3 given below. The oxide scales where then examined using a JEOL FX 2000 TEM operated at 200 kV, a VG 601 U X Scanning Transmission Electron Microscope (STEM) which operated at 100 kV and an aberration corrected SuperSTEM.

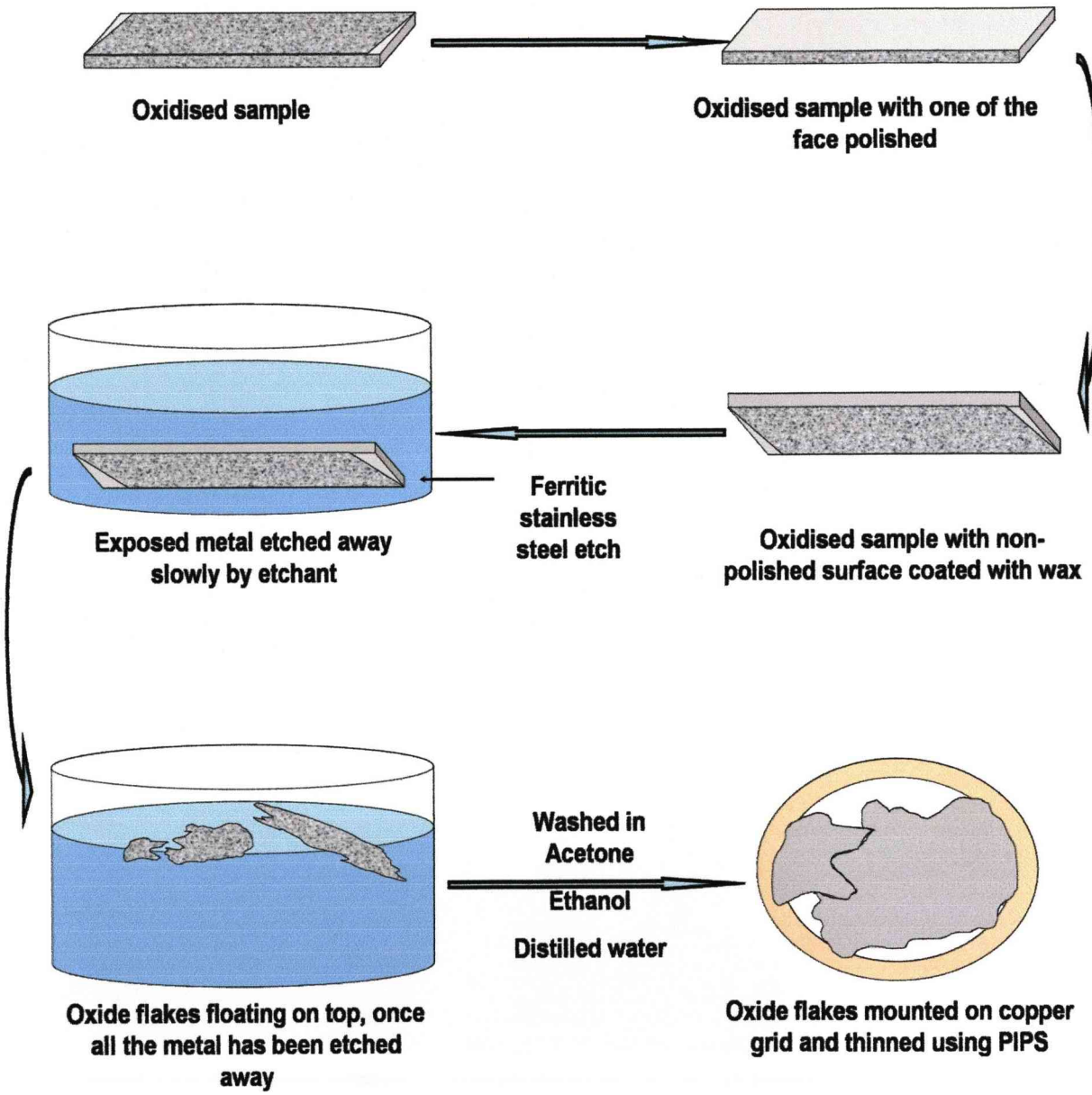

Figure 4- 3: Schematic of sample preparation steps.

4.3. Transmission Electron Microscope (TEM)

A JEOL 2000FX Transmission Electron Microscope operating at 200 kV was used throughout the experiment to conduct the initial study of the samples prepared by ion milling. In the operation mode the first two condenser lenses C1 and C2 were adjusted so as to illuminate the specimen with a parallel beam of electrons typically at 20 K – 45 K magnifications. Before starting the analysis, the microscope was aligned following the standard steps laid down by manufacturer. The TEM was fitted with an EDX detector for element analysis which could be carried out on regions of interest. It was possible to record a transmission micrograph using the camera located below the phosphor viewing screen.

4.3.1. Electron diffraction

Electron diffraction patterns were recorded from the oxide grains found in the region of interest. The recorded patterns were indexed to examine the orientation relationship between the adjacent grains.

4.3.2. TEM and EDX

Initial EDX chemical analysis was carried on the particles using a small spot size of approximately 200 Angstroms at high magnification of about 200 to 300 K.

4.4. Scanning Transmission Electron Microscope (STEM)

The STEM Microscope used for the experimental work was a VG HB601 UX which used a 100 kV convergent beam with approximately 1 nA current and 8-10 Angstrom diameter spot at the specimen.

In this microscope the electron source was a cold field emission gun (FEG), resulting in low energy spread in the electron probe, ≤ 0.5 eV per channel.

The microscope was also fitted with an EDX detector and EELS spectrometer. The grain boundary analysis was done using the EDX detector. Line scans across grain boundaries were collected and quantified using the Cliff-Lorimer equation, which is explained in detail in the following section. Elemental maps where recorded from grain boundaries and regions having particles rich in reactive elements. For statistical quantitative analysis, X-ray spectra were collected from rectangular regions having dimensions 10 x 10 nm.

4.5. Qualitative and quantitative microanalysis

The most important step in qualitative analysis is to acquire a spectrum over the desired X-ray energy range. However as the STEM has a much higher accelerating voltage compared to the SEM, it is possible to generate and detect higher energy X-rays. An X-ray spectrum should be collected for several hundred seconds to ascertain that all the characteristic peaks are present in the range of 0-40 keV. Once this is ascertained the energy range may be reduced if the elements to be studied are clearly distinguished in this energy range, thereby improving the resolution of the MCA display by lowering the number of eV per channel. For good qualitative analysis the X-ray spectrum collected should be displayed with no more than 10 eV per channel resolution on the MCA and a display range of 0-20 keV.

Dead time should be noted while acquiring the original spectrum to make sure that the combination of probe current and specimen thickness do not overload the detector electronics. Dead time should be kept below 50% and an output count rate of several thousand per second maintained.

Once a good low noise spectrum has been recorded over a suitable energy range, a well defined sequence of steps needs to be followed to identify each peak in the spectrum and disregard those peaks which are statistically insignificant or are due to Si escape or peak combination. The microanalysis system can be used to run an automatic identification to assign different peaks in the spectrum assuming the PHA is well calibrated which is usually done before recording the spectrum. This may well be adequate for identification, if the spectrum is simple, containing few well separated peaks. However if the X-ray spectrum contains multiple peaks and there is an overlap of peaks, then use of this technique might lead to misidentification of some peaks. Under these circumstances a well established manual sequence has been developed for analysis of spectra. The analysis is started with identification of the most intense peak and working down its family and in the next step the second most

intense peak is analyzed, excluding the previous family of peaks. These steps are repeated until all peaks are identified bearing in mind the peak combinations.

4.5.1. Quantitative analysis

The essential steps required for quantification of X-ray spectra were proposed by Castaing in 1951and still form the basis of quantification. According to Castaing the intensity of the X-rays is proportional to the concentration of the element in the specimen generating X-rays[145, 146].

The procedure that Castaing proposed forms the basis of the most of the quantification routines used today. Castaing assumed that the concentration C_i of an element i in the specimen generates a certain intensity of characteristics X-rays. In practice it was difficult to measure this generated intensity, so Castaing suggested that a known standard composition $C_{(i)}$ be chosen for that element i and then the intensity ratio $I_i/I_{(i)}$ be measured, where I_i is the measured intensity emerging from the specimen and $I_{(i)}$ is the measured intensity emerging from the standard. A reasonable approximation was proposed by Castaing,

$$C_i / C_j = K.I_i / I_j \qquad \text{----------4 - 1}$$

where K is a sensitivity factor that takes into the account the difference between the generated and measured X-ray intensities from both the standard and the specimen and comes from three factors:

- Z The atomic number
- A The absorption of X-rays within the specimen
- F The fluorescence of X-rays within the specimen

The correction procedure is referred as ZAF correction

4.5.2. Line Scan

The digital line scan software instructs the microscope to scan a line anywhere on an image and collect an element profile. The profiles recorded are displayed as an excel worksheet, which may be further quantified using the Cliff-Lorimer method. The line scan can be collected along a line starting anywhere and moving in any direction, but during most of the current analysis, care was taken to draw the line perpendicular to grain boundaries to be profiled.

Figure 4-4 shows an schematic of a Line Scan process which takes in the EDAX software and the region from which the signal is collected for a definite time fed by the user.

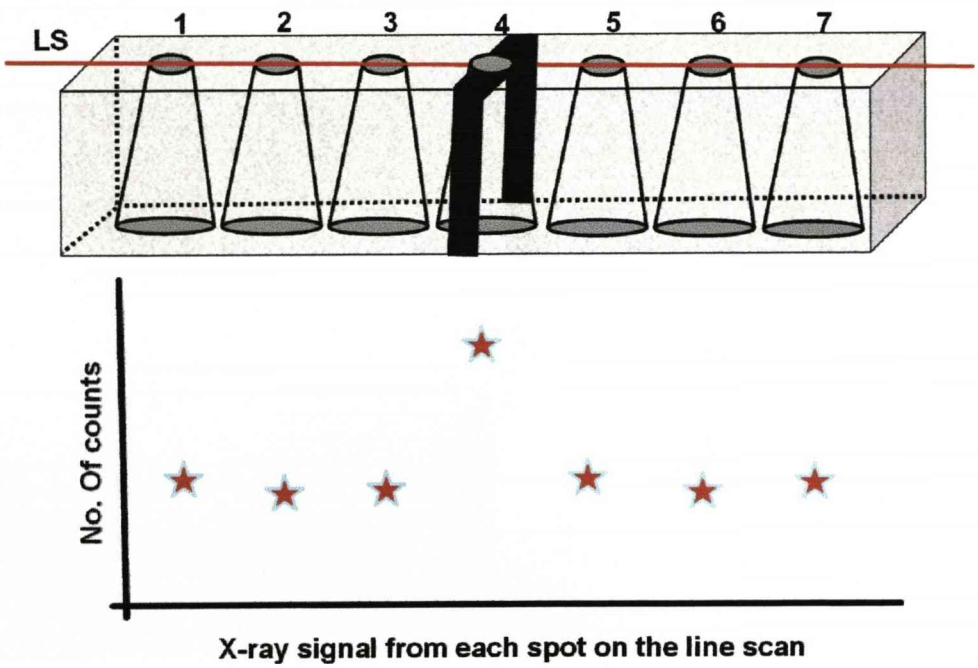

Figure 4- 4: Schematic of an Line Scan process.

Figure 4-5 below shows a BF image and the line scan position across a grain boundary. The line profile is for hafnium (Hf) distribution at grains separated by a vertical grain boundary.

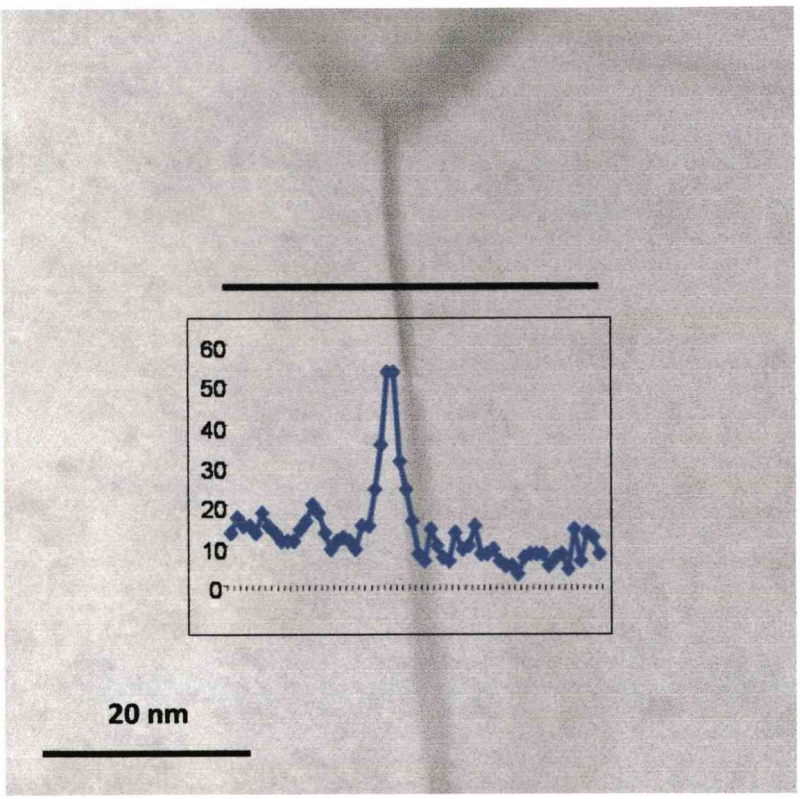

Figure 4- 5: BF image of alumina grains separated by a grain boundary and Hf line scan through the grain boundary.

4.5.3. Cliff-Lorimer method

The most common method used to quantify a line scan is the ratio or Cliff-Lorimer method. The weight percent of each element C_A and C_B can be related to the measured intensities by the Cliff-Lorimer equation. This method is based on comparing the intensity ratio of one of the elements with intensities of the other elements in the sample[146, 147].

One of the assumptions made in this, is that the specimen is thin enough so that we can ignore any absorption or fluorescence. This assumption is known as the thin-foil criterion.

The basic equation for binary alloy can be written as:

$$\frac{C_A}{C_B} = K_{AB} \bullet \frac{I_A}{I_B} \qquad \text{----------4 - 2}$$

The term K_{AB} is known as the Cliff-Lorimer factor, and as the effect of absorption and fluorescence is ignored, K_{AB} is only related to the atomic number correction factor Z. So the only quantity to be determined is K_{AB} the relative efficiency value for all the element couples present in the sample. To obtain the absolute value for C_A and C_B a second equation is required and is assumed that A and B constitute 100% of the specimen.

$$C_A + C_B = 100\% \qquad \text{----------4 - 3}$$

The above equation can be extended to higher order systems, as for the case of three elements, the equation can be written as,

$$\frac{C_B}{C_C} = K_{BC} \bullet \frac{I_B}{I_C} \qquad \text{----------4 - 4}$$

and $C_A + C_B + C_C = 100\%$ ----------4 - 5

K factors for different pairs can be related by,

$$K_{AB} = \frac{K_{AC}}{K_{BC}} \qquad \text{----------4 - 6}$$

There are a number of ways in which this quantity can be determined. We can use the default values EDAX has inserted in its proprietary program. These values were measured some time ago by an EDAX user at 200 kV accelerating voltage. As these values were recorded on 200 kV machine and the STEM operates at 100 kV, these values used may lead to some error in the quantified data.

Secondly we could calculate the K_{AB} from first principles. The basic equation for intensity generated in the specimen can be calculated as:

$$I_A = const \bullet \frac{\omega_A \bullet P_{IJ} \bullet Q_A}{A_A} \bullet C_A \bullet t \qquad \text{----------4 - 7}$$

where, ω is the fluorescence yield

P_{IJ} is the fraction of the total K, L or M line that is measured

Q is the ionization cross-section

A is the atomic weight

and, t is the specimen thickness

Since we do not know the exact value of the specimen thickness, we take the ratio:

$$\frac{I_A}{I_B} = \frac{const \bullet \frac{\omega_A \bullet P_{IJ} \bullet Q_A}{A_A} \bullet C_A \bullet t}{const \bullet \frac{\omega_B \bullet P_{IJ} \bullet Q_B}{A_B} \bullet C_B \bullet t} \qquad \text{----------4 - 8}$$

The above equation can be re written without thickness term as:

$$\frac{C_A}{C_B} = \frac{\omega_B \bullet P_{IJB} \bullet Q_B \bullet A_A}{\omega_A \bullet P_{IJA} \bullet Q_A . A_B} \bullet \frac{I_A}{I_B} \qquad \text{----------4 - 9}$$

As we measure the intensity in a detector surrounded by several layers of polymer, aluminum, metal contact layer and silicon dead layer, the efficiency is reduced and is dependent on X-ray energy. The dependence could be shown as:

$$I_{detector} = \varepsilon \bullet I_{generated} \qquad \text{----------4 - 10}$$

And hence the final equation could be written as:

$$\frac{C_A}{C_B} = \frac{\omega_B \bullet P_{IJB} \bullet Q_B \bullet A_A}{\omega_A \bullet P_{IJA} \bullet Q_A . A_B} \bullet \frac{\varepsilon_B I_A}{\varepsilon_A I_B} \qquad \text{----------4 - 11}$$

4.6. Standardless analysis

EDAX software uses a unique procedure called SEC method to do standardless analysis. In this method the intensities of reference materials are calculated from first principles [147].

The composition can be calculated from the measured intensities of X-rays using:

$$W\% = Z \bullet A \bullet F \bullet \frac{I^{Meas}}{I^{Std}} \qquad \text{----------4 - 12}$$

where Z, A and F are the matrix correction parameters describing the Atomic number effect (Stopping power and backscattered effect), the absorption effect and the fluorescence effect. I^{Meas} and I^{Std} are the measured and standard X-rays intensities of the element involved when $I^{Std} = I_{100\%}$.

Since for standardless analysis no standard intensities are available. EDAX calculates the standard intensity using the following equation:

$$I^{Sts}_{Calculated} = n\frac{\Omega}{4\pi}\varepsilon_d \omega_j p_{jl} f(x)\frac{N_0}{A} R \int_{E_0}^{E_j} \frac{Q_j(E)}{dE/d(\rho s)} dE \qquad \text{----------4 - 13}$$

where n is the number of electrons entering the sample

since n is unknown and is usually set to unity. The calculated intensity might be of different order of magnitude as the measured intensity. Normalising the weight percent to 100% solves this problem.

This function has been shown to work very accurately for analysis using K-lines.

The disadvantage of this technique is that detector efficiency cannot be predicted with sufficient accuracy for X-ray lines below 1keV. Hence EDAX has introduced SEC factor (standardless element coefficient factor)

The first equation becomes:

$$W\% = Z \bullet A \bullet F \bullet \frac{I^{Meas}}{SEC \bullet I^{Std}} \qquad \text{----------4 - 14}$$

Software calculates SEC factor. When an element is chosen an SEC factor of 1 is allotted. The SEC factors for other elements are calculated and scaled relative to it.

4.7. Elemental Map

The EDAX software package allows us to collect multiple X-ray maps combined with simultaneous intake of an electron image from the same area. The BF detector is used to record the BF electron image. The maps can be collected by selecting suitable dwell time which would give the desired signal to noise ratio. The maps can be stored in digital form.

4.8. SuperSTEM

The base microscope used in the construction of the SuperSTEM is a VG HB 501 FEG STEM. The SuperSTEM microscope at the Daresbury Laboratory offers considerable potential for detailed study of the segregation to oxide grain boundaries at the atomic level. This microscope has a spherical aberration corrector fitted to the objective lens, allowing the formation of a sub-Angstrom probe for simultaneous ultra-high resolution high angle annular dark field (HAADF) imaging and atomic-column electron energy loss spectroscopy (EELS).

The C_S corrector basically consists of Quadrupole and Octupole lenses which are executed by computer controlled currents. The SuperSTEM operates at 100 kV and therefore requires a thinner sample than the 2000 FX. The current density at the specimen is about 0.1 nA in a 1.0 A° beam which is equivalent to~1X 10^6 A/cm^2.

HAADF lattice imaging was carried out to see high Z segregants at the grain boundary as the intensity in HAADF image can be directly related to Z. EEL spectra recorded have very small

spectral features to identify the elements present at grain boundaries; both techniques are explained briefly in the next section. Figure 4-6 shows an schematic of SuperSTEM.

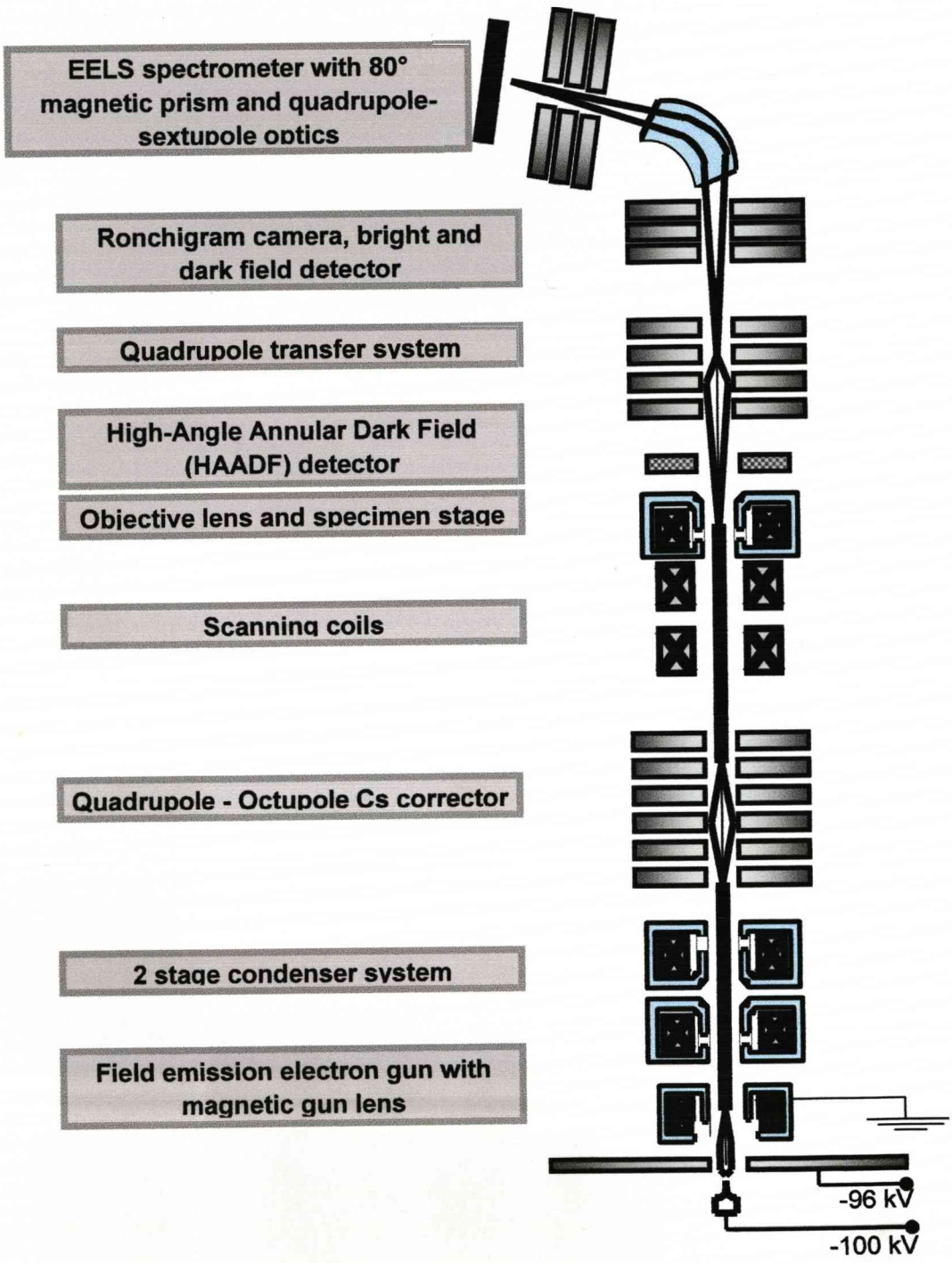

Figure 4- 6: Schematic of SuperSTEM showing the lenses, correctors and detectors in the microscope.

4.9. Lattice imaging and Scanning Transmission Electron Microscope

Atomic resolution high angle annular dark field (HAADF) Scanning Transmission Electron Microscopy (STEM) is a relatively recent technique which has been used to characterize the structures of grain boundaries and precipitates as well as perfect crystals. The image characteristics in STEM and conventional TEM are frequently related by the reciprocity principle. The Bright Field (BF) image from STEM using an on axis detector is similar to BF TEM image, of the same aperture angle according to the reciprocity rule. However the intensity in HAADF when a large solid angle, off-axis detector is used is directly proportional to the atomic number of the elements present. As can be seen in Figure 4-7 the HAADF image shows bright spots at grain boundaries and these could be due to the presence of heavier elements such as Y, Hf etc. at the grain boundaries.

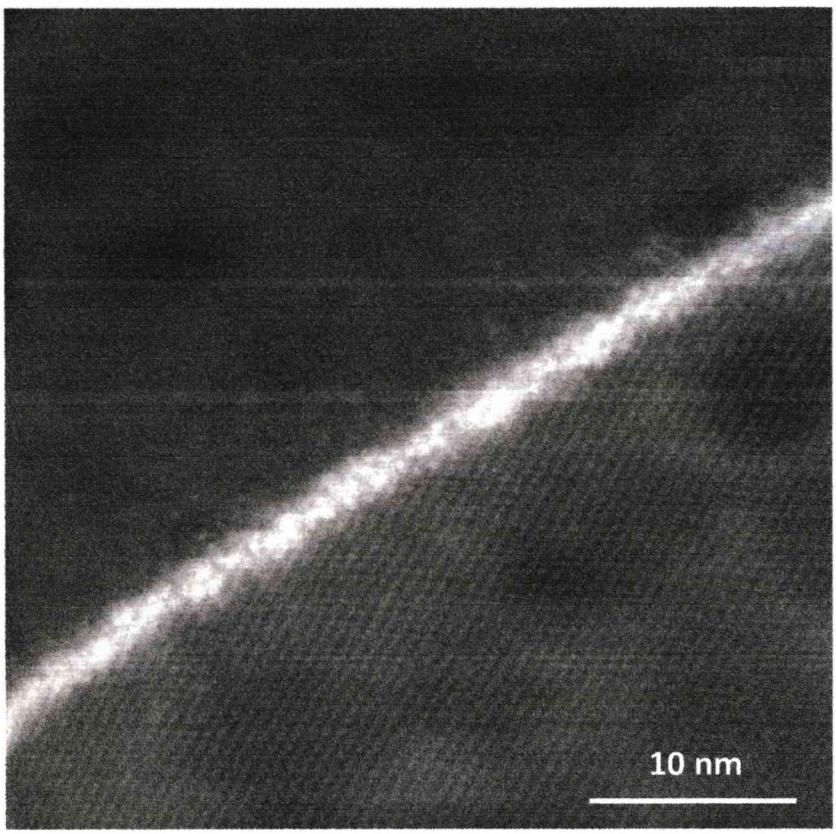

Figure 4- 7: HAADF image showing a grain boundary with bright spots which could be due to heavier elements present at those sites.

4.10. Electron energy loss spectroscopy

During this project, grain boundary analysis at higher spatial resolution was attempted with SuperSTEM using electron energy loss spectroscopy. In an electron energy loss (EEL) spectrometer the primary process of X-ray excitation which results from a fast moving electron beam losing a characteristic amount of energy is monitored. The beam of transmitted electrons is directed into a high resolution electron spectrometer which disperses the electrons according to their kinetic energy and the spectrum is obtained by detecting the dispersed spectrum on a multi channel analyzer. The EEL spectrometer used had a magnetic prism with 80 degree bending angle. The detector was interfaced with the post specimen detector chamber of the

SuperSTEM. The detector was a scintillator charge coupled device (CCD) detector which was 25-30 times more sensitive than the typical detectors.

4.10.1. The magnetic prism

The schematic diagram below (Figure 4-8) shows the Gatan spectrometer which is installed beneath the camera system and above the HAADF detector in SuperSTEM.

From the schematic we can see that the electrons are selected by a variable entrance aperture. They travel along a drift tube and are deflected through 80° by the magnetic field of the dispersion prism. Electrons with greater energy loss, i.e. lower kinetic energy, are deflected further than those suffering lower energy losses. Figure 4-8 shows a schematic of the magnetic prism, the electrons suffering higher energy loss are shown by the gray full line and the transmitted electron suffering zero energy loss are shown by a black full line. A spectrum is thus formed in the dispersion plane which is detected as a distribution of electron counts or intensity (I) vs. energy loss (E).

In a magnetic prism spectrometer the electrons travelling with a speed V in the Z-direction are directed between the poles of the electromagnet which has a magnetic field (B) in the Y-direction, perpendicular to the incident electron. The transmitted electrons travel in a circular orbit in the magnetic prism, whose radius of curvature is given by

$$R = (\gamma m_0 / eB)v \qquad \text{----------4 - 15}$$

where, $\gamma = 1/(1 - v^2/c^2)^{1/2}$ is the relativistic mass factor and m_0 is the rest mass of the electron.

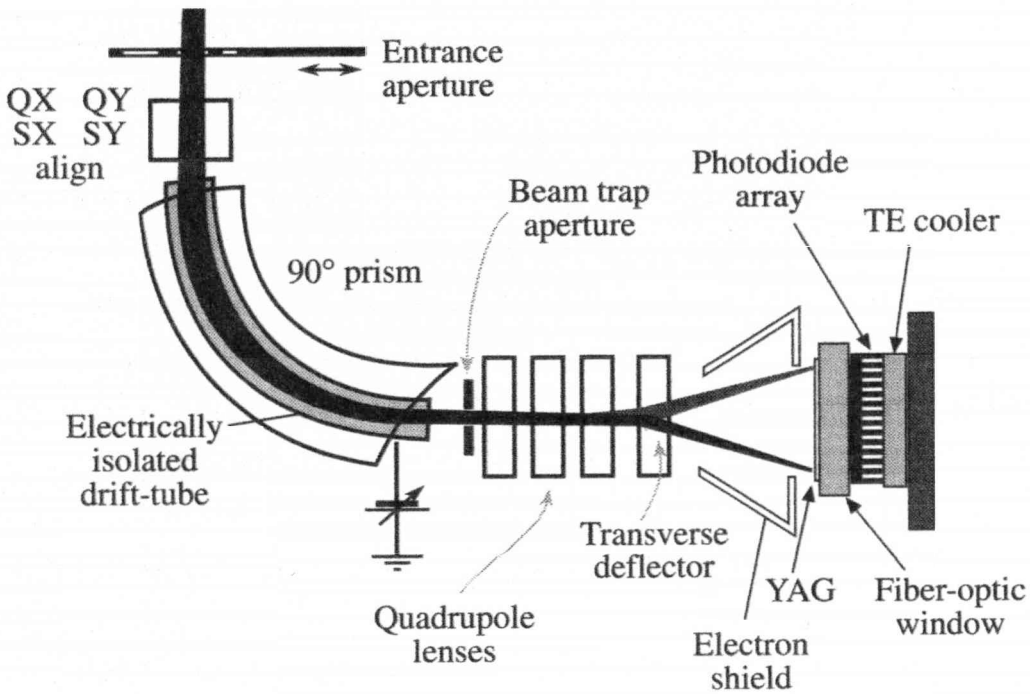

Figure 4- 8: Schematic of an spectrometer used in STEM[148]

4.10.2. The collection angle (β)

The collection semi angle of the spectrometer β is the most important parameter in determining the resolution of EELS. The collection angle used in SuperSTEM is 19 radians and is given by[148]

$$\beta = d/2h \qquad \text{----------4 - 16}$$

Where, d is diameter of the spectrometer entrance aperture and h the distance from the specimen to the aperture as shown by the schematic in Figure 4-9.

However the calculation of collection angle for SuperSTEM is not straight forward as it has post specimen lenses. Hence the value of β in STEM diffraction mode is determined by the

effective diameter of the spectrometer entrance aperture (d_{eff}), projected into the plane of diffraction pattern.

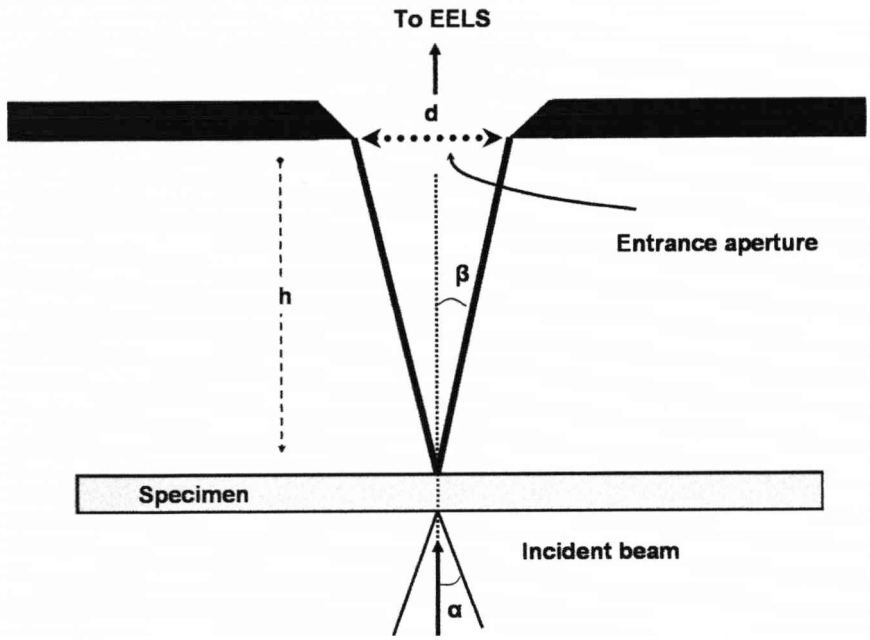

Figure 4- 9: Schematic diagram showing the collection angle calculation in STEM assuming no lenses between specimen and spectrometer.

4.11. Energy Loss Spectrum

Energy loss spectroscopy implies that we are mainly interested in inelastically scattered electrons but the spectrum also contains electrons which are elastically scattered and those which are not scattered. Figure 4-10 shows a typical electron spectrum; it can be divided into three main regions, which will be described in the sections to follow

1) Zero Loss Peak

2) The Low Loss Region

3) The High Loss Region

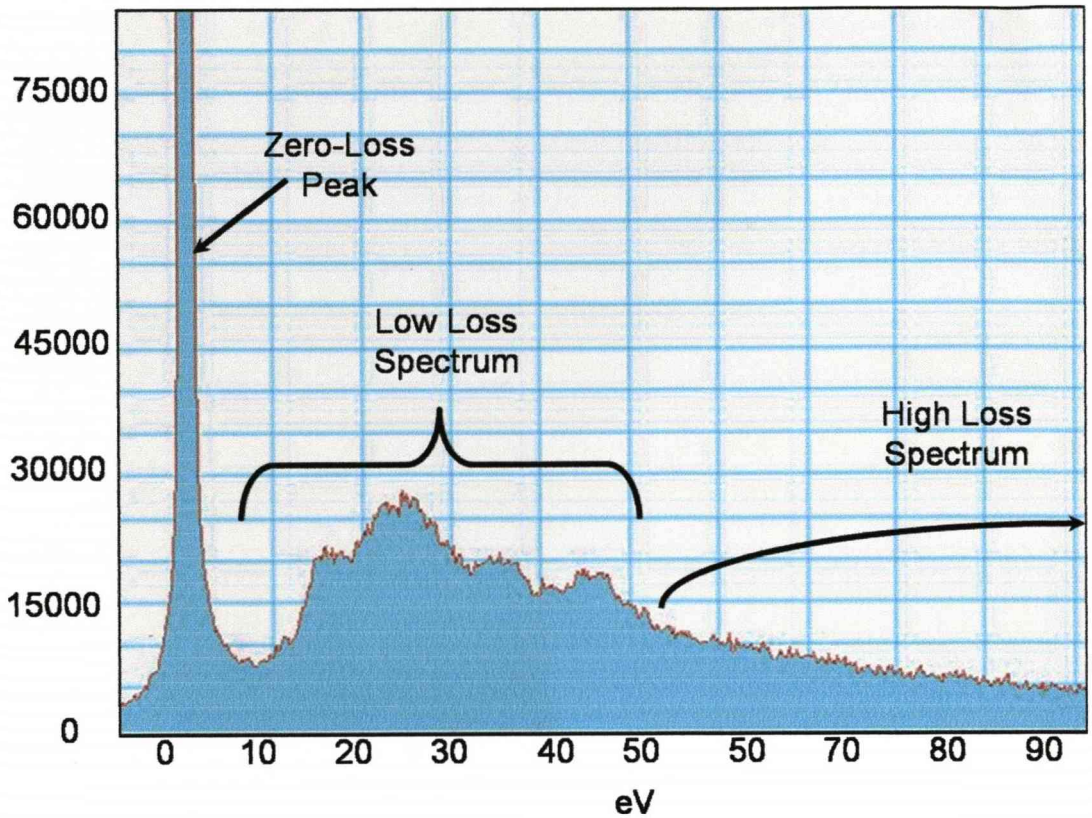

Figure 4- 10: An EELS spectrum recorded at 100 keV in SuperSTEM. The spectrum shows different energy loss regions.

4.11.1. Zero Loss Peak

The zero loss peak mainly consists of the electrons that have retained their energy and these electrons are forward scattered in a relatively narrow cone within a few milli radians of the optic axis and would mainly be found in the 000 spot in the diffraction pattern. The zero loss peak also contains electrons which have lost small quantities of energy which cannot be resolved by the spectrometer, together with unscattered electrons.

The zero loss peak is so intense that sometimes it causes saturation of the spectrometer detectors and hence sometimes it is useful to collect a spectrum without including a zero loss peak. It can be seen that in the above spectrum, to the right there is a series of small peaks which is where we start to get useful information.

4.11.2. The Low Loss Spectrum

The low loss spectrum or low loss region describes the electron energy loss up to 0 – 50 eV. These low loss electrons have excited plasmon oscillations or have generated inter or intra band transitions.

4.11.2.1. Plasmons

Plasmons can be thought of as longitudinal wave like oscillations of weakly bound electrons. The valence electrons in a solid can be thought of as a set of coupled oscillators which interact with each other and oscillate when excited by the transmitted electron pulse from the passing electrons. The oscillations are rapidly damped and have a very short life time of 10^{-15} s. The plasmon loss is the second most intense feature of EEL spectra after the Zero loss peak.

The energy E_P lost by the electron when exciting a plasmon of frequency ω is given by[143]:

$$E_P = \frac{h}{2\pi}\omega_P = \frac{h}{2\pi}\left(\frac{ne^2}{\varepsilon_0 m}\right)^{1/2} \qquad \text{----------4 - 17}$$

where, h is Plank's constant

e and m are the electron charge and mass of the electron

ε_0 is the permittivity of free space

n is free electron density

The value of plasmon loss energy E_P is found to be in the range of 0-25 eV.

4.11.2.2. Inter- and Intra-Band Transitions

An electron in the beam may transfer sufficient energy so that a core electron can change its orbital state; this would result in energy losses up to 25eV, but multiple losses can also occur. Interaction with the molecular orbital such as a π orbital would produce characteristic peaks in the low loss region of the spectrum. The intensity of these characteristics peaks could be used to identify the elements present in the specimen.

4.11.3. The High Loss Spectrum

The high loss spectrum consists of electrons which have lost energy greater than 50 eV. These are the electrons which have undergone inelastic scattering with the inner or core shells of an atom. The relaxation of these events produces the X-rays detected by EDX.

4.11.3.1. Inner Shell Ionization

When an incident electron transfers sufficient energy to an electron in the K, L, M or N shells, so that this electron moves to higher orbital away from the attractive force of the nucleus, the atom is said to be ionized. As stated in a previous section, the decay of an ionized atom back to ground state results in an X-ray. So EELS and EDX are analogous techniques as they are different aspects of the same phenomenon. However, EDX collects a low intensity signal which, particularly in STEM, sits on a very low background, thus giving clearly interpretable spectra. EELS, on the other hand, collect a very high proportion of the loss events, but they sit on a high background. Interpretation therefore requires lot of computation.

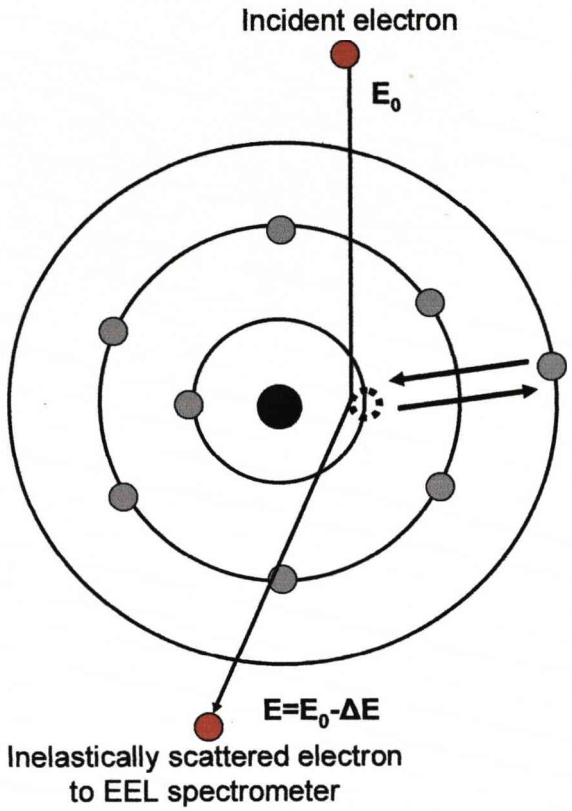

Figure 4- 11: Schematic showing process of inelastic scattering.

The above Figure 4-11 shows a schematic of inelastic scattering. The nomenclature used for an EELS edge is similar to that of X-rays. As we had K, L, M and N peaks in the EDX spectrum, so we have ionization edges from K, L, M, N etc. shell electrons. The greater energy resolution of the EELS spectrometer makes it easier to detect edges arising from different energy states in the shell.

4.12. Quantitative Microanalysis

The EELS data were processed to emphasize the edges by removing plural scattering background as follows:

4.12.1. Background Subtraction

The background intensity arises from plural scattering events which are usually associated with outer shell interactions. The background appears in the spectrum as a rapidly changing continuum which decreases from a maximum just after the plasmon peak at 15-20 eV to a minimum of 0 eV which is indistinguishable from the instrument noise typically at a few hundred eV. Figure 4-12 is a part of an EEL spectra, showing a background fitted to it and background subtracted signal appearing after ≈ 27 eV.

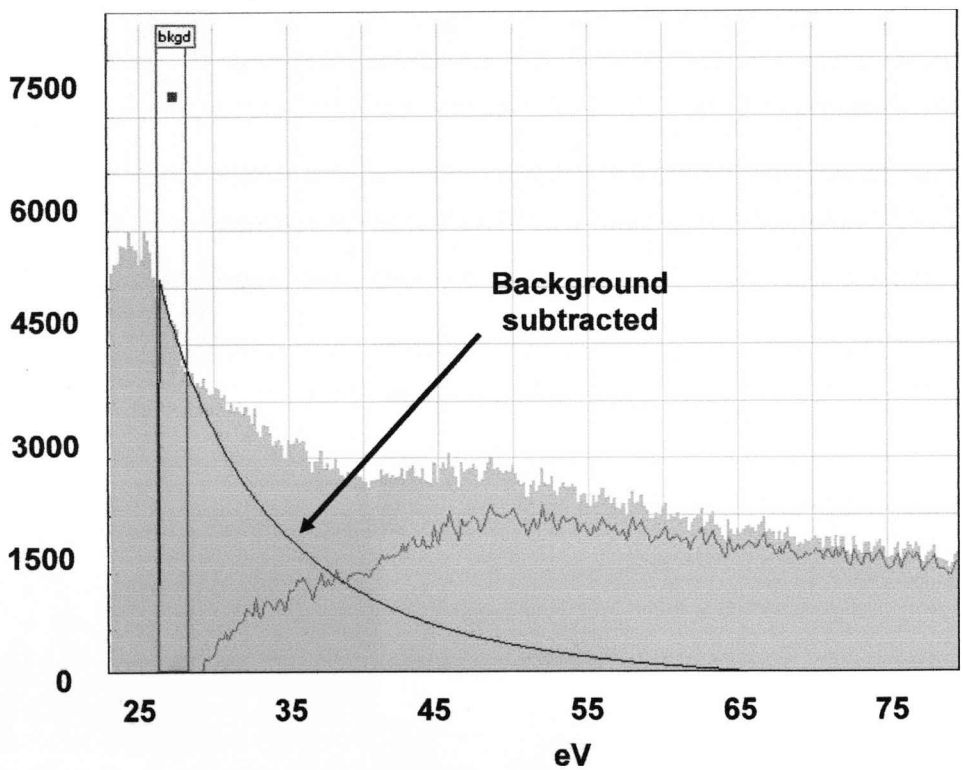

Figure 4- 12: An EEL spectrum showing background subtracted. As can be seen the background decreases from a maximum to a minimum.

4.12.2. Removal of Plural Scattering from the Low Loss Region

Plural scattering adds to the intensity of an ionization edge which is mainly due to the combined result of inner and outer shell losses. The aim of deconvolution is to extract the

single scattering distribution SSD. There are two ways of obtaining SSD from an EEL spectrum. The two methods are The Fourier-Log method and the Fourier-Ratio method. Both these methods are incorporated in Gatan EELS software. The Fourier-Log method is explained briefly in following section.

4.12.2.1. The Fourier-Log Method

This method removes the effect of plural scattering from the whole of the spectrum. This technique describes the spectrum in terms of the sum of individual scattering components, i.e. the sum of zero-loss (elastic component), single scattering, double scattering, etc. First each of these terms is convoluted with the instrument response function i.e. its energy resolution function of the spectrometer. For PEELS the instrument response function is defined as a point spread function.

The Fourier transform of whole spectrum is given by the equation:

$$F = F(0)\exp(\frac{F(1)}{I_0}) \qquad \text{----------4 - 18}$$

Where, F (0) is the transform of the elastic contributions

F (1) is the transform of the single scattering

and I (0) is the zero loss intensity

Hence to get the single scattering transform the logarithm of both sides is taken. Extracting the single scattering spectrum involves an inverse transformation of F (1) which results in too much noise in the spectrum. The noise can be removed by subtracting the background in the usual way.

Figure 4-13 shows an EEL spectra recorded from an RE-rich particle showing multiple peaks and Figure 4-14 is the corresponding deconvoluted spectra using Fourier-Log method. The intensity of the deconvoluted spectra has decreased by a factor of 10.

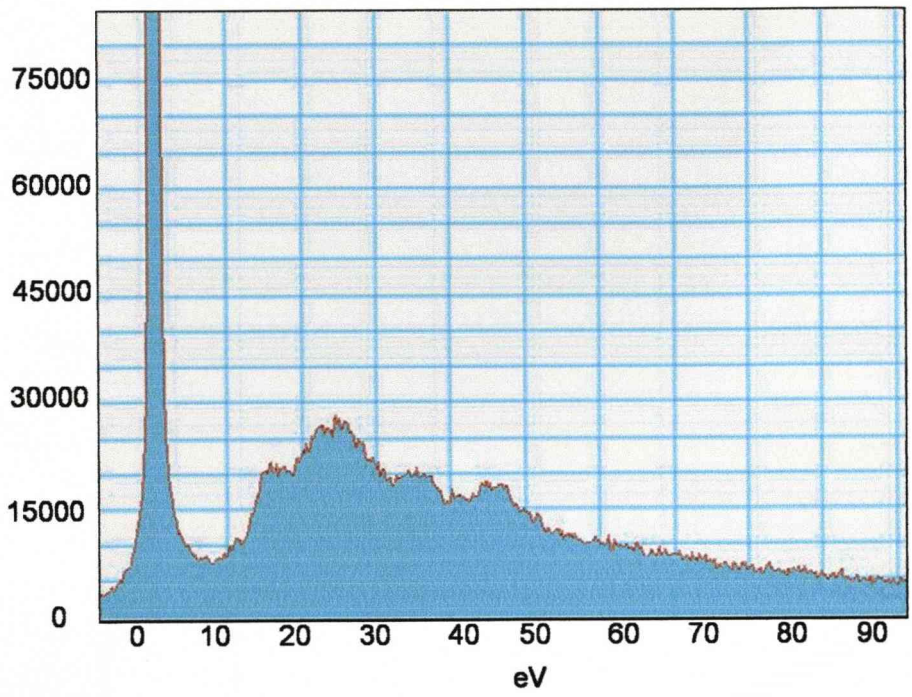

Figure 4- 13: As recorded EELS spectrum from a RE-rich particle showing zero loss and multiple plasmon peaks.

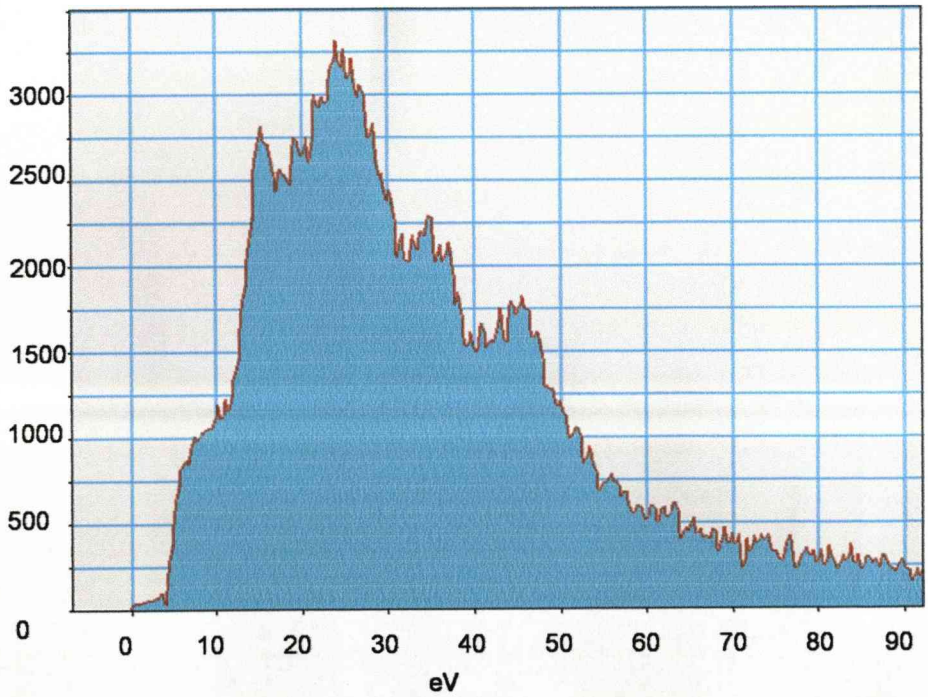

Figure 4- 14: Deconvoluted EELS spectrum from a RE-rich particle, as can be seen no zero loss present and plasmon intensity increased.

4.12.3. Kramers-Kronig Analysis

Kramers-Kronig Analysis was carried on the recorded EEL spectra which gives the energy dependence of the real and imaginary parts. This energy dependence can be calculated from the single scattered distribution data of the energy loss spectrum.

Single scattering distribution is related to the complex permittivity or dielectric constant ε of the specimen by[143]

$$J^1(E) \approx S(E) = \frac{2I_0 t}{\pi a_0 m_0 v^2} \mathrm{Im}[-1/\varepsilon(E)] \int_0^{\beta} \frac{\theta d\theta}{\theta^2 + \theta_E^2} \quad \text{----------4 - 19}$$

$$= \frac{I_0 t}{\pi a_0 m_0 v^2} \mathrm{Im}[-1/\varepsilon(E)] Ln[1 + (\beta/\theta_E)^2] \text{----------4 - 20}$$

Where, I_0 is the zero-loss intensity, t the specimen thickness, v the incident electron velocity, β is collection semi angle, and $\theta_E = E/(\gamma m_0 v^2)$ the characteristic scattering angle for energy loss.

The function Re[1/ε(E)] can be derived from Im[-1/ε(E)] by Kramers-Kronig transformation.

$$\mathrm{Re}[\frac{1}{\varepsilon(E)}] = 1 - \frac{2}{\pi} P \int \mathrm{Im}[\frac{-1}{\varepsilon(E')}] \frac{E' dE'}{E'^2 - E^2} \quad \text{----------4 - 21}$$

Where, P denotes the Cauchy principal part of the integral.

The Johnson method is used by Gatan software to carry out the Kramers-Kronig transformation. This is accomplished by taking the sine transform of $\mathrm{Im}[-1/\varepsilon(E)]$ followed by an inverse cosine transform. This technique is quite fast as it uses a Fast-Fourier algorithm.

Several parameters are required by Gatan software before the calculation can be completed. The incident beam energy E_0, 100 KeV; the convergence semi angle α, 24 mrad (which is defined by the objective aperture); the collection semi angle β, 19 mrad (which is defined by the collector aperture) and the refractive index for visible light n, 1.6.

After computing the dielectric function is obtained from[143],

$$\varepsilon(E) = \varepsilon_1(E) + i\varepsilon_2(E) = \frac{\mathrm{Re}[1/\varepsilon(E)] + i\,\mathrm{Im}[-1/\varepsilon(E)]}{\{\mathrm{Re}[1/\varepsilon(E)]\}^2 + \{\mathrm{Im}[-1/\varepsilon(E)]\}^2} \quad \text{----------4 - 22}$$

Separate functions $\varepsilon_1(E)$ and $\varepsilon_2(E)$ can be obtained by equating the real and imaginary parts of the above equation.

4.12.3.1. Epsilon 1 (ε_1)

ε_1 is the real part of the dielectric function and represents the dispersive element of the transition. The real part is derived from the equation,

$$\varepsilon_1(E) = \frac{1}{\pi} P \int_{-\infty}^{\infty} \frac{\varepsilon_2(E')}{E' - E} dE \quad \text{----------4 - 23}$$

4.12.3.2. Epsilon 2 (ε_2)

E_2 is the imaginary part of the dielectric function and represents the absorption energy by optical transmission. The imaginary part is derived from the equation,

$$\varepsilon_2(E) = \frac{1}{\pi} P \int_{-\infty}^{\infty} \frac{\varepsilon_1(E')}{E' - E} dE \quad \text{----------4 - 24}$$

4.12.3.3. Effective number of electrons

The output from Gatan digital micrograph also contains an effective number of electrons, n_{eff} which can be calculated from imaginary part of the dielectric function. The output is in units of electrons per nm^3.

$$n_{eff}(\varepsilon_2) = \frac{2\varepsilon_0 m_0}{\pi h^2 e^2} \int_0^{\infty} E' \varepsilon_2(E') dE' \quad \text{----------4 - 25}$$

Where, ε_0 is permittivity of free space, m_0 is rest mass of electron, h is plank's constant and e is electronic charge.

4.12.3.4. Absolute sample thickness

An iterative computation of thickness can be calculate from Kramers-Kronig sum rule, which is given by

$$t = \frac{4a_0 F E_0}{I_0(1-n^{-2})} \int_0^{\infty} \frac{S(E)dE}{E \ln(1+\beta^2/\theta_E^2)} \qquad \text{----------4 - 26}$$

where, a_0 is Bhors radius, F is relativistic factor, E_0 is the beam energy, I_0 the zero loss intensity, n the refractive index for visible light , $S(E)$ the single scattered distribution, β the effective collection angle and θ_E the characteristic scattering angle.

4.12.3.5. Optical absorption coefficient

The optical absorption coefficient can also be calculated from the dielectric function.

$$\mu(E) = \frac{E}{hc}[2(\varepsilon_1^2 + \varepsilon_2^2)^{\frac{1}{2}} - 2\varepsilon_1]^{\frac{1}{2}} \qquad \text{----------4 - 27}$$

where c is the speed of light in vacuum.

4.13. Multislice simulation

The procedure for the STEM image simulation is based on the multislice algorithm, which requires a relatively large super cell of about 40 by 40 angstrom. Since this is required to sample the real and reciprocal spaces with sufficient accuracy, it cannot be reduced even when simulating the STEM image for a sample with a smaller unit cell. For simulation of alumina the unit cell was repeated 10 by 10 times.

The steps involved in multislice simulation are described below, a detailed description can be found in the book by E.J.Kirkland[149].

Dividing the specimen into thin slices, each slice must be thin enough to be a weak phase object and is in a plane perpendicular to the optic axis of the electron microscope and is

typically one atomic layer of the specimen. The optic axis of the electron microscope is in positive z direction. All the atoms within $z + \Delta z$ are compressed into a single slice at z.

The projected atomic potential and transmission function are calculated for each of the slices.

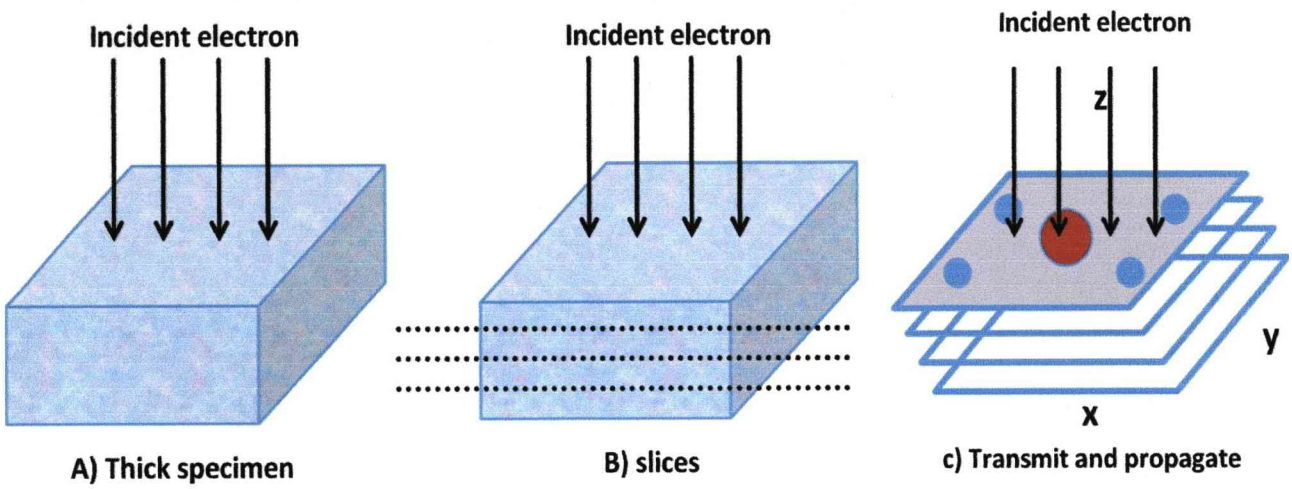

Figure 4- 15: Schematic representation of multislice procedure.

At each probe position, a probe wave function is calculated.

The probe wave function is recursively transmitted and propagated through each slice until the wave function has traversed all the way through the specimen.

A Fourier transform of the transmitted wave function is then taken to get the wave function in the far field diffraction plane.

Integrating the intensity of the wave function in the diffraction plane for those signals falling on the detector gives the signal for one pixel in the image. This is repeated for all the pixels.

Chapter 5

Results: STEM and EDX

5.1. Cyclic oxidation tests

The effects of reactive element additions to FeCrAl alloys were investigated by cyclic oxidation testing. The tests were carried out in a horizontal furnace, which involved manual removal of the sample from the furnace, leaving the sample in laboratory atmosphere for the cold dwell duration and then returning to the furnace afterwards for continuation of cyclic oxidation. Figure 5-1 shows a comparison of mass gain data curves for two of the alloys. The alloy Kanthal A1 (with only Zr as RE additive, but also containing small amounts of Si and Ti) showed a lower mass gain rate compared to the Model alloy M11 (with Y, Hf and Zr as RE additives). The mass-gain data were recorded after each 7 cycles initially until 150 cycles, and after each 14 cycles thereafter. The plot of cyclic data for Kanthal A1 shows a dip in the oxidation curve first after 60 cycles and then regularly after every few cycles, which is loss in mass of the oxide and may be due to spallation. Oxidation may take place at these exposed regions followed by spallation and then re-oxidation. Optical images were recorded after the test. The optical image for Kanthal A1 alloy showed large regions of spallation, whereas the Model alloy showed cracks but did not spall as much as the Kanthal A1 (Figure 5-2). SEM micrographs in Figure 5-3 show the spalled region, the spallation occurred within the scale and not at the interface, as oxide can be seen under the spalled regions shown by ovals. The model alloy M11 sample showed cracks but did not spall as much as the sample of Kanthal A1. The reproducibility of the mass gain results is illustrated by comparison with data recorded on the same commercial alloy in the DECHEMA Institute, where the tests were performed under similar conditions, as shown in Figure 5-4. The plots compare well initially for about 200 cycles after which there is slight variation, which could be due to minor differences in laboratory conditions since the data was from different laboratories situated in different countries.

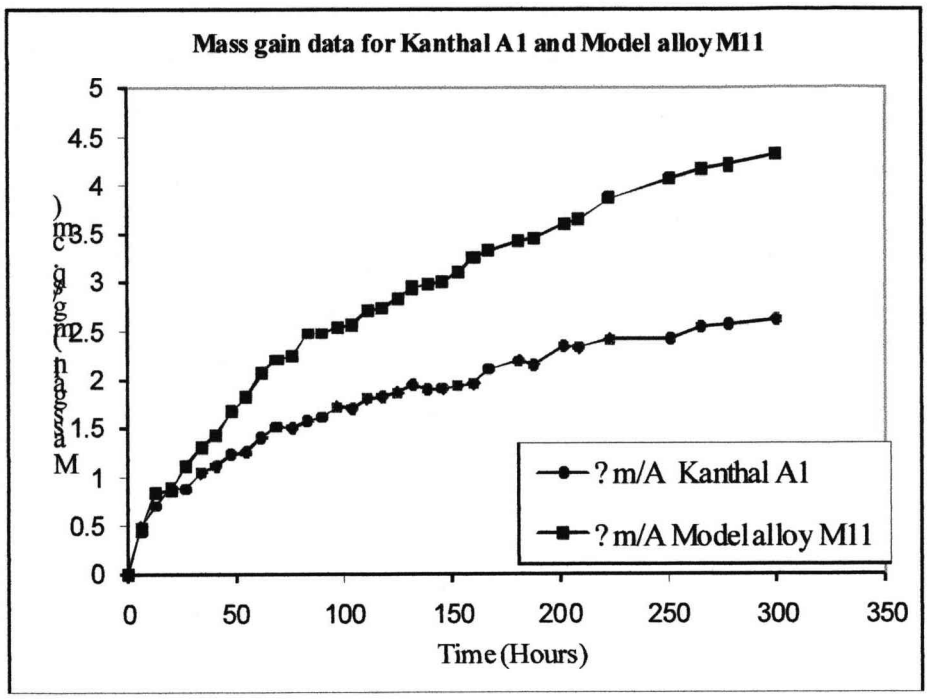

Figure 5- 1: Mass-gain data for the commercial alloy Kanthal A1 and the Model alloy M11.

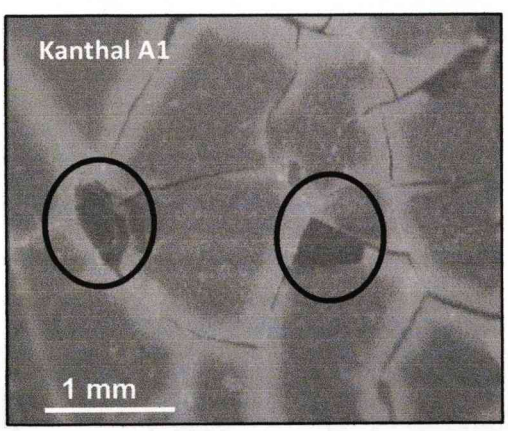

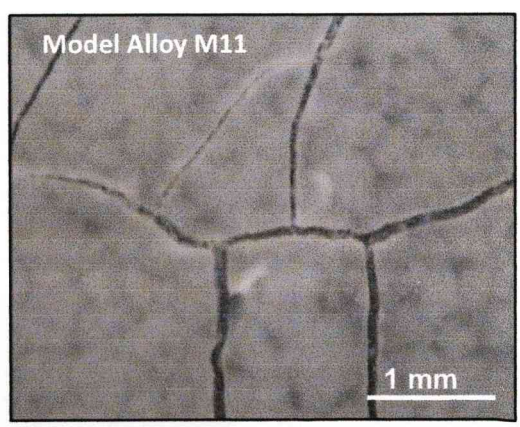

Figure 5- 2: Optical images of the oxide scales from both the alloys. Kanthal A1 shows spallation, shown by ovals on the alloy, whereas model alloy M11 shows cracks but not much spallation.

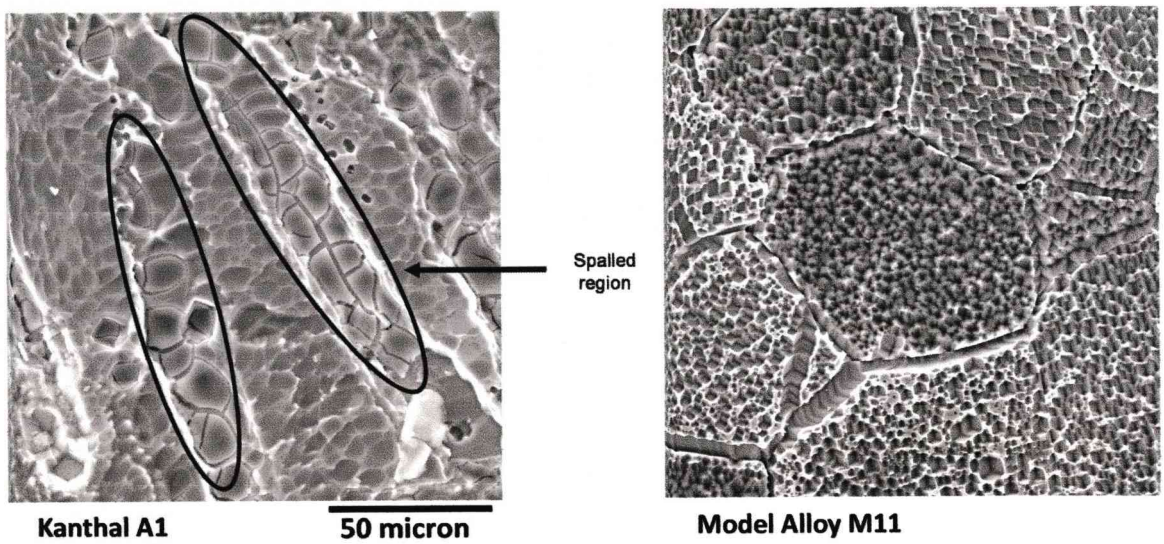

Figure 5- 3: SEM images showing the spalled region in Kanthal A1 alloys, whereas no spallation observed on M11 alloy.

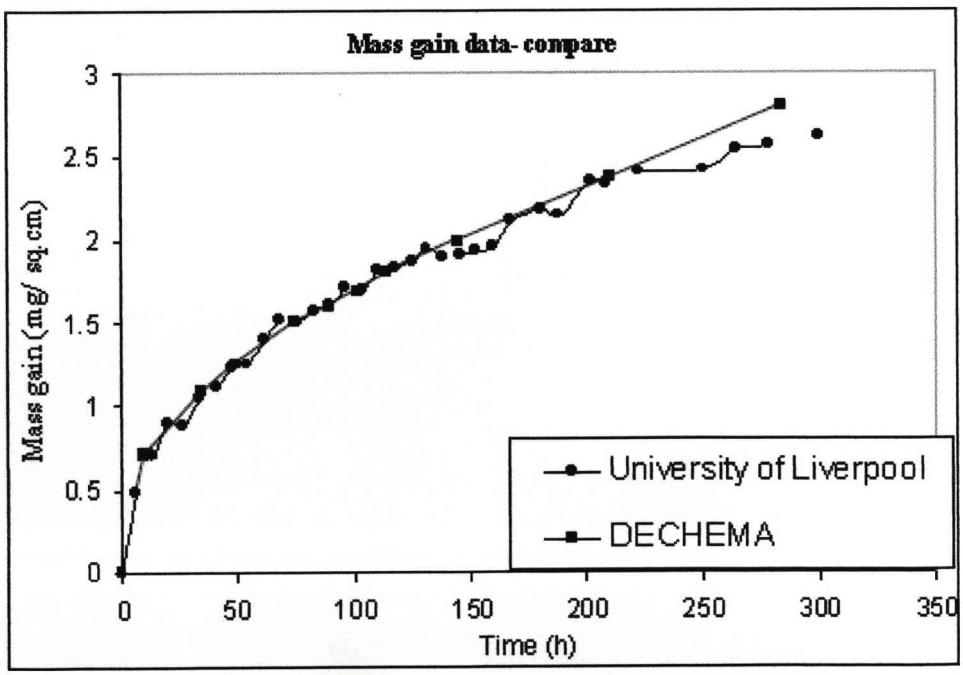

Figure 5- 4: Mass-gain data comparison for commercial alloy Kanthal A1 from two different institutions.

5.2. Transmission Electron Microscopy

Figure 5-5 shows a scanned image of a plan view alumina scale formed on Model alloy M9 at 1250°C after 50 hours of oxidation, from a JEOL 2000 FX machine and several corresponding selected area diffraction (SAD) patterns. Micrograph A is the electronically inverted image of the scanned micrograph B which is a BF image. The image has been inverted to enhance the contrast at the grain boundaries. The SAD pattern was indexed by measuring the distance and angles between the spots manually.

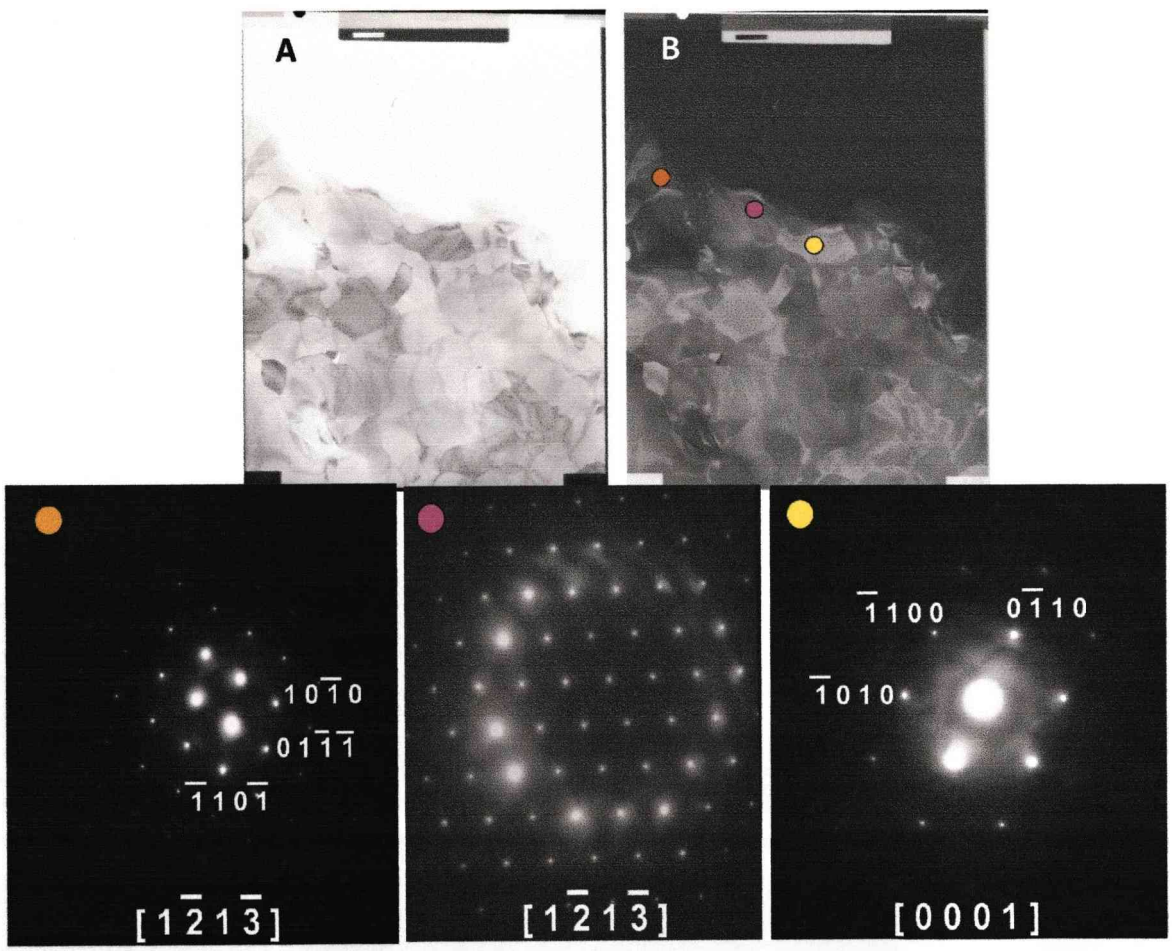

Figure 5- 5: TEM micrographs and corresponding diffraction patterns from the marked spots.

A plan view sample of the oxide scales was examined using TEM. Figure 5-6 shows a bright-field image of the oxide scale and a particle formed in alloy M9 after 50 h oxidation at 1250°C.

The EDX analysis of the particle revealed that it was a hafnium-rich oxide, which had formed in the outer region of the scale. EDX analysis from the bulk only showed Al and O peaks and did not show any detectable Hf or Y peaks. The RE rich particles have formed in the bulk and not at the GB's or had formed at the GB's but had not been pinned there. At 1250°C particles were formed far earlier compared to those at 1200°C.

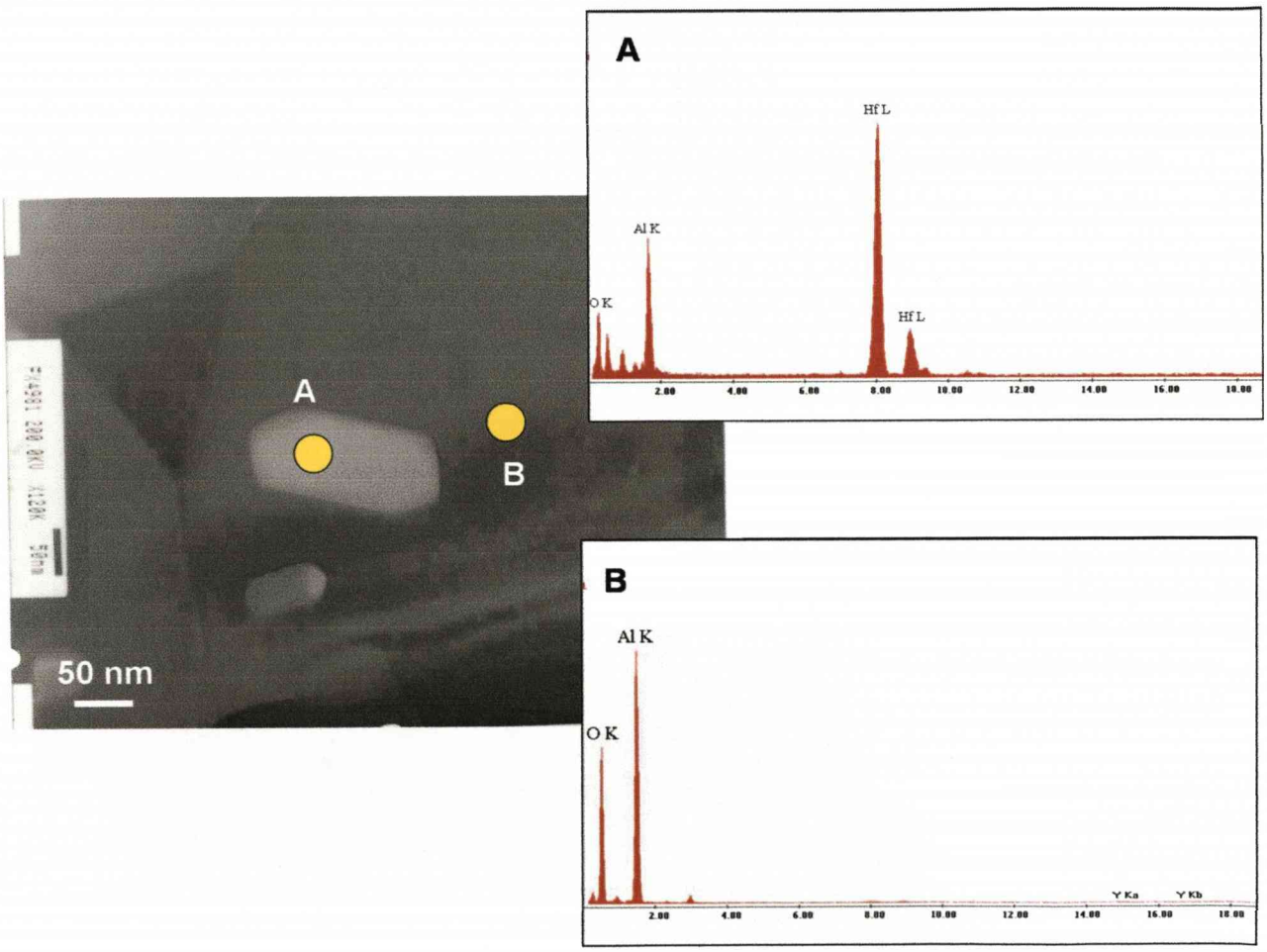

Figure 5- 6: A TEM micrograph with a particle and EDX spectrums from the particle and the bulk of the grain.

5.3. Scanning Transmission Electron Microscope and EDX

The plan view sample of the oxide scale taken from model alloy M9 in the region just below the equiaxed grains was examined using STEM. Figure 5-7 shows a Bright Field (BF) and

Angular Dark Field (ADF) image. The BF image shows grains of varying sizes lying in the size range of 0.5 to 1 μm and two particles of about 0.2 μm in width, having dark contrast. As can be seen from the DF image, these particles have a bright contrast, indicating them to be made of heavier elements as contrast in DF is proportional to atomic number. The DF image shows a few voids, which appear as a dark region in the image and could have formed during the process of thinning the sample in the ion mill, as the Ar ion thinning may have removed the particles or other material present at those positions.

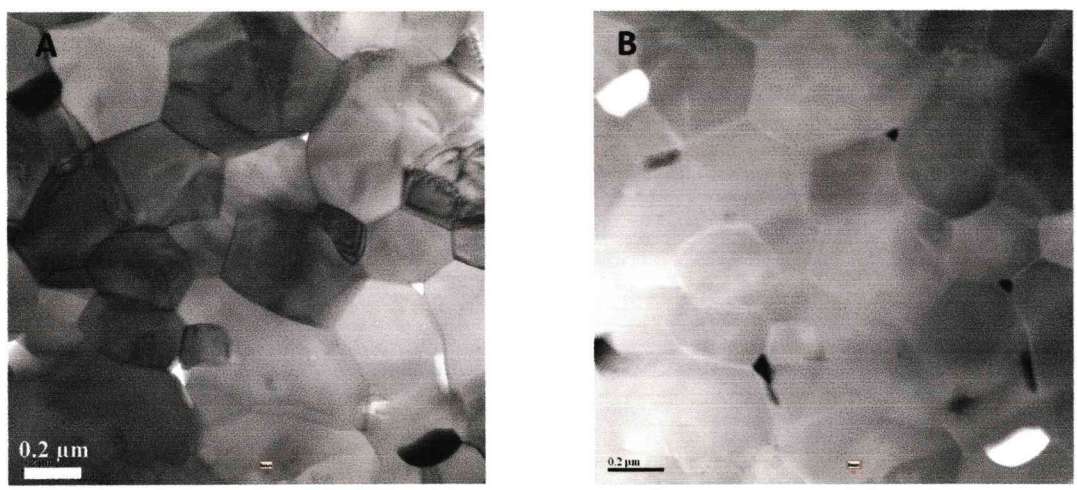

Figure 5- 7: A) BF and B) ADF image showing alumina grains and particles formed at 1200°C after 50 hours of oxidation.

The next sub-section looks at segregation of reactive elements (RE) to GB and tries to look at the composition of the particles present in the oxide with the help of EDX elemental mapping. The second sub-section looks in more detail as to whether it is possible to detect RE at the GB, using a Line Scan (LS) across a GB. The third sub-section tries to quantify the RE present across the grain boundaries and in and around the particles.

5.4. Elemental Mapping to see RE at boundaries

Figure 5-8 shows a Bright Field (BF) image and corresponding elemental maps of a triple point in the scale. The scale is a plan view sample prepared from alloy M9 at 1200°C after 100 hours of oxidation. The elemental mapping has illustrated the enhanced concentration of Hf and Y, which may have been caused by their migration to the GB. The GB's are nearly parallel to the incident electron beam as the dark contrast at the boundaries is limited to a smaller width, which is about 1 – 2 nm. The concentration profiles for Hf and Y show enhanced concentration at these boundaries. The Y concentration profile is not as clear as Hf and Y seems to be presented in the bulk too. There could be an effect due to the thickness of the sample and hence the data needs to be carefully processed. There is no change in the concentration profile of Al, O and Cu. Cu was looked for as the sample was mounted on a Cu grid and thinned using PIPS. Hence some Cu may have been carried over onto the sample during thinning.

The experiment was also repeated for GB's which were inclined by a large degree. Figure 5-9 shows a Bright Field image at a triple point were three inclined boundaries meet and the corresponding elemental maps. The GB spread is over a few nm as can be estimated from the BF image by measuring the dark contrast at the GB's. The elemental maps are in agreement with the previous triple point analyzed in Figure 5-8, showing enhanced Hf and Y concentration at the GB's. Y can be seen segregating more clearly, at the GB's compared with the previous triple point analyzed. The elemental profile for Al, O and Cu show no variation at all the GB's.

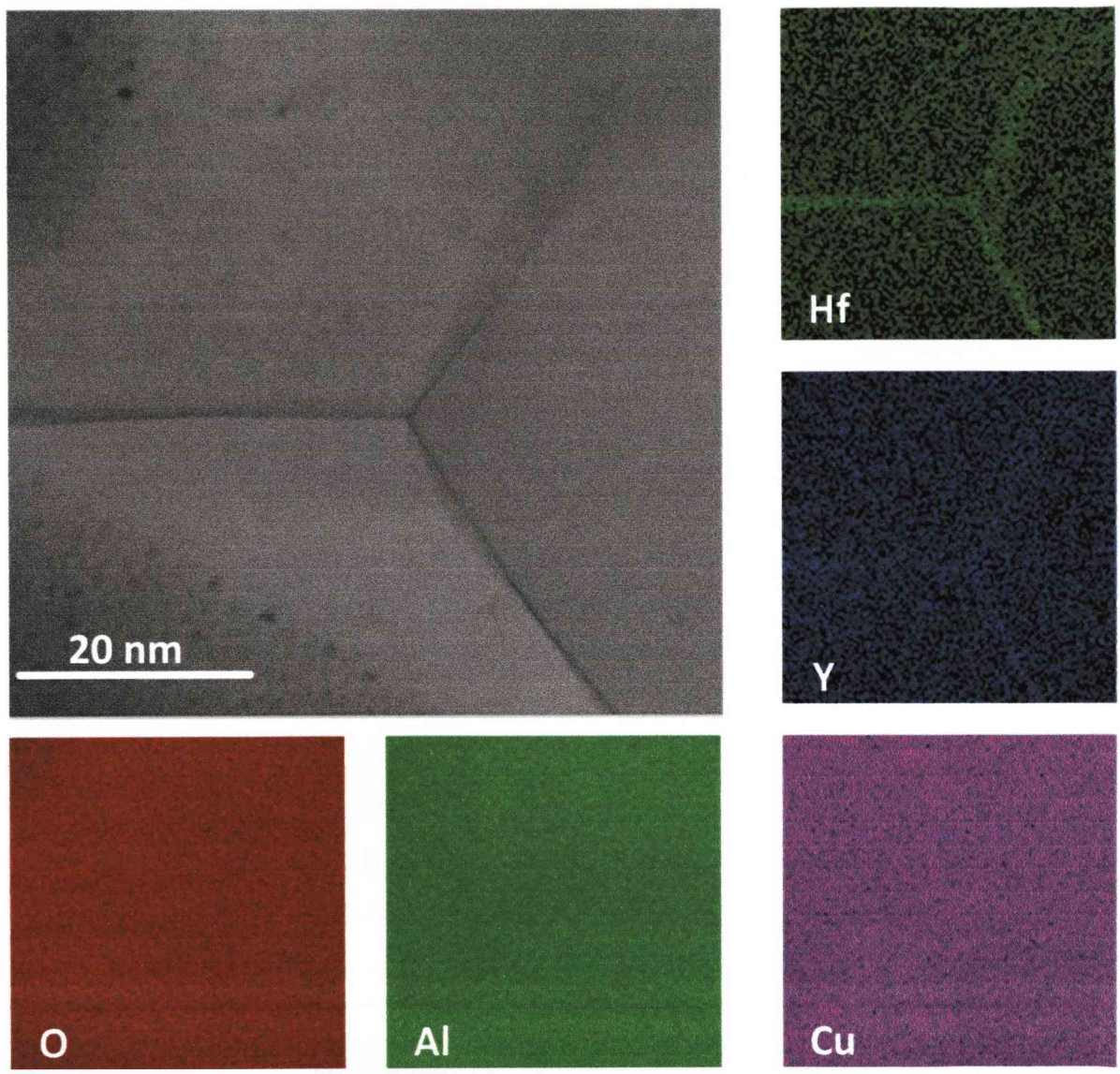

Figure 5- 8: BF image showing GB of an alpha-alumina grain and corresponding Hf and Y elemental maps formed at 1200°C after 100 hours of oxidation.

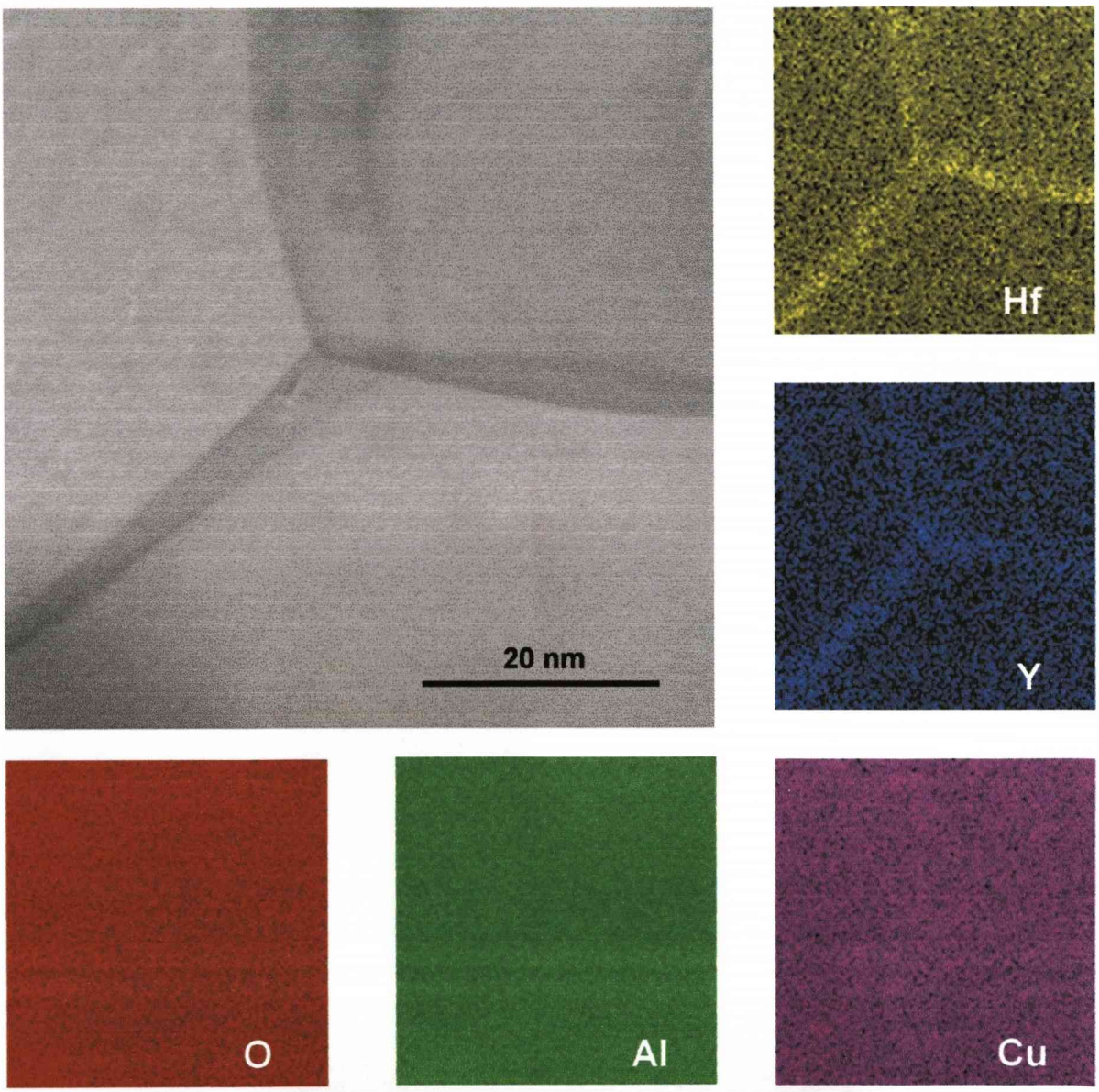

Figure 5- 9: A triple point junction from the GB's which are inclined by an large angle formed at 1200°C after 100 hours of oxidation.

Figure 5-10 shows a Bright Field (BF) image of a particle at the GB's and the corresponding elemental maps. It can be deduced that the oxide particle is rich in Hf and Y. From the O elemental maps the particle appears to be deficient in the O content compared to the rest of the grain. There is no hint of Hf segregating to the GB's connected to the particle and the same could be said about the Y.

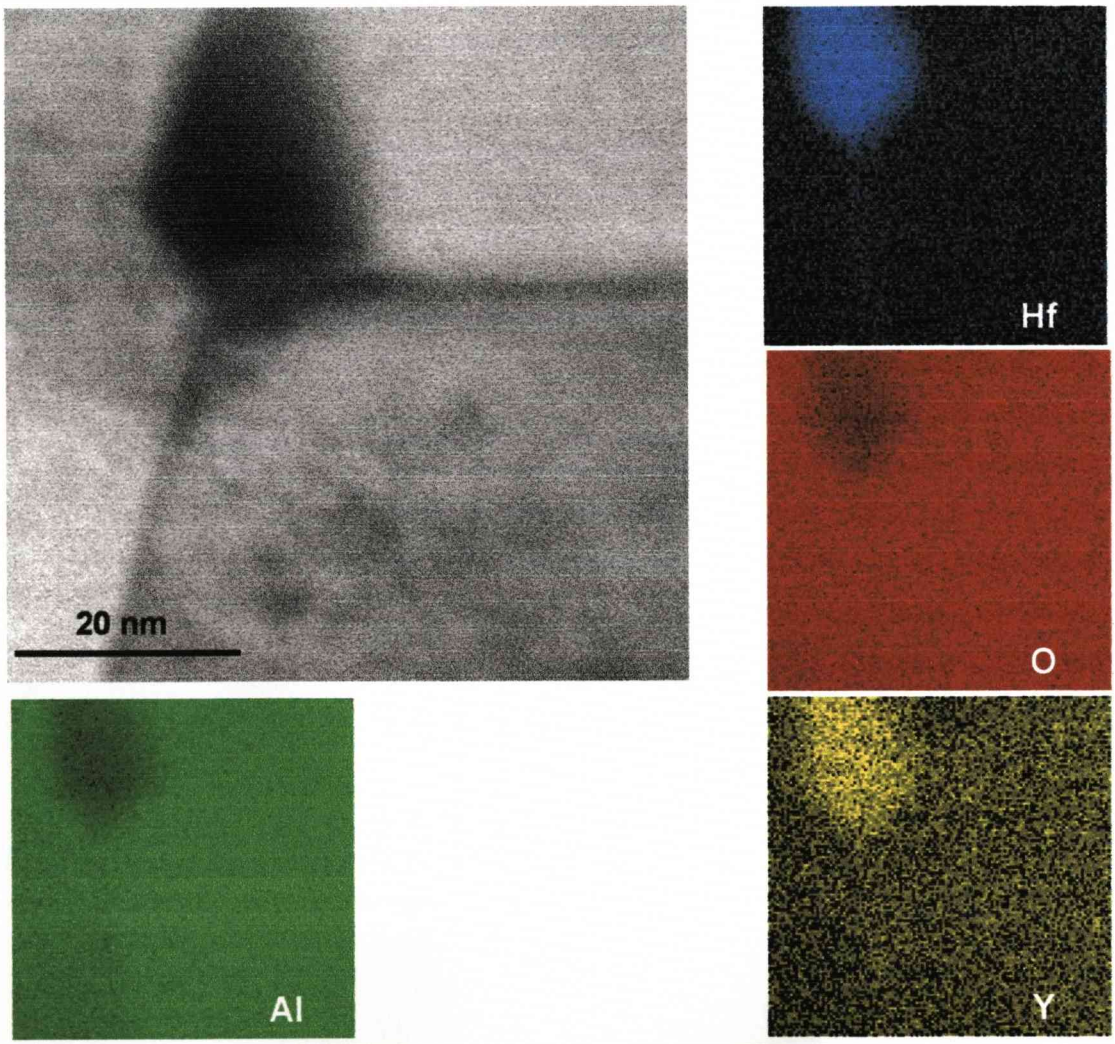

Figure 5- 10: BF image from a particle and corresponding elemental maps for Hf, Y, Al and O respectively formed at 1200°C after 100 hours of oxidation.

Figure 5-11 shows a Bright Field image of a cluster of heavier particles. There are some thickness fringes present in the particles appearing as alternate bands of bright and dark contrast. Elemental profiles seem to suggest that the particles are mainly rich in Hf. The Y signal was not present or was below the detection level, indicating absence of Y in these particles. There are no GB's clearly visible and there is no clear indication of whether the particle lies within an alumina grain or is present at a GB junction. There is a possibility of a grain boundary being highly inclined and thus giving no contrast in the BF image. If it is assumed that the particles are connected through GB's, it could be said that there is no segregation to these GB's. The elemental profile for Al and O indicate the particle to be deficient in these, whereas elemental profile for Cu suggest, particle being rich in Cu. It is not clear why Cu signal is enhanced, even though there is no Cu present in the alloy. Cu is only present in the grid used and if Cu was sputtered onto the sample it should be uniform throughout, which is not shown by the concentration profile. This can also be an error due to the fact that Hf and Cu peaks are overlapping each other in the spectrum. Figure 5-12 shows a bright field image of a particle and corresponding elemental analysis shows the particle to be rich in Hf and Y. The concentration profiles for Al and O show the particle to be deficient in it, but once again the Cu concentration is enhanced. There is no detectable segregation of RE's to the GB's as can be seen from the elemental maps. A number of particles were analyzed and few were rich in both Hf and Y. It is still not clear whether the particles are Hf-Y-O complexes or whether they are separate oxides of Hf and Y coexisting. There is a possibility of having both as there is slight solubility between Hf and Y oxides. No grain boundary segregation of Hf and Y appeared to be present or it was below the detection limit.

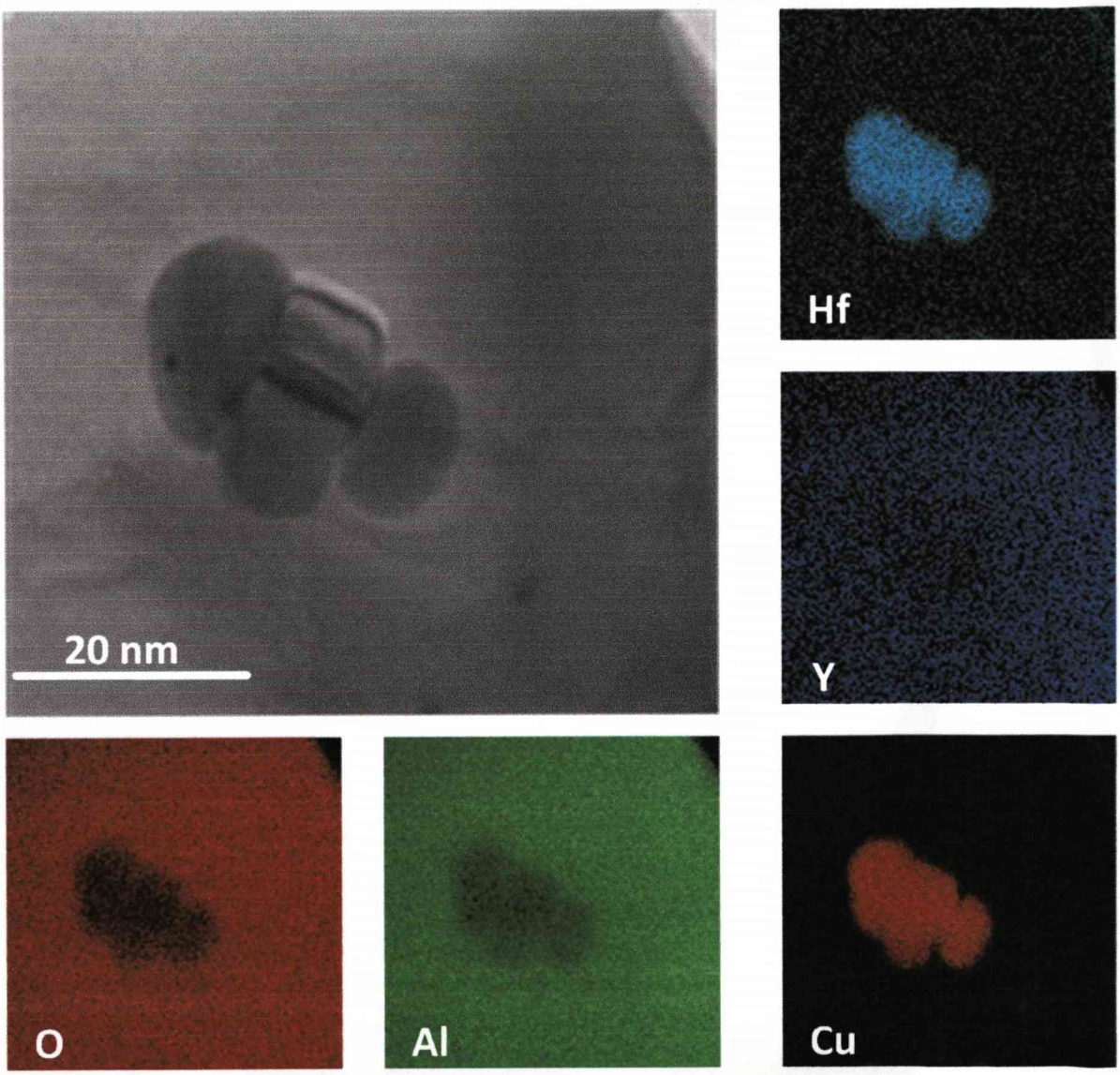

Figure 5- 11: BF image of a particle rich in Hf as can be seen from the elemental maps formed at 1200°C after 100 hours of oxidation.

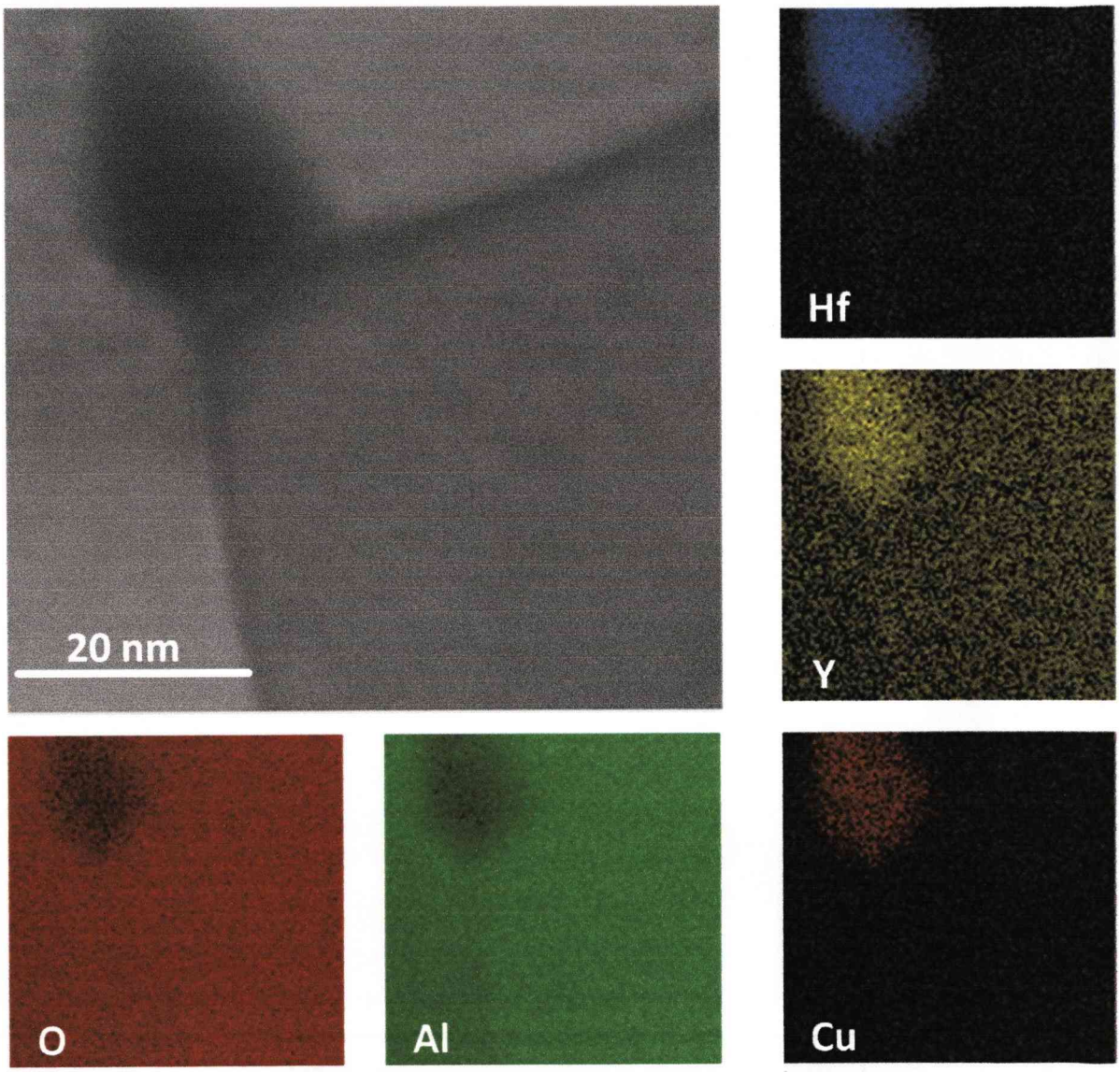

Figure 5- 12: BF image of a particle at a triple point rich in hafnium and yttrium formed at 1200°C after 100 hours of oxidation.

5.5. Line Scan Analysis for Detection of RE

In the following section, Line Scan analysis is carried out across the GB with respect to RE rich particles. As has been seen from the elemental maps there is segregation of RE to some GB with RE-rich oxide particles formed in the scale. Hence it was important to look at the different parameters which affected the segregation and formation of the particles. First, the quantification technique used to quantify a line scan data set is discussed, followed by two sub-sections looking in detail at the segregation behavior of the RE's in the form of RE-rich particles.

Line Scans collect data at a series of points along a line defined by the user and are plotted as a graph. The type of Line Scan to be performed can be selected from either a standard line scan or a quant line scan. In a standard Line Scan, a spectrum is collected at each point and number of counts within the region of interest will be recorded in the Line Scan. In a quant Line Scan, the data will be collected as in a standard Line Scan but a background subtraction and peak deconvolution is performed at every point. The Line Scan data collected can be quantified using the Cliff-Lorimer method, as explained in the literature review, and the steps involved are explained in the following paragraph.

5.5.1. Quantification using Cliff-Lorimer method

Steps involved in quantification of line scan data are as follows:

1) A Line Scan data set is collected across a line defined by the user.
2) The main equation is written as,

$$\frac{C_A}{C_B} = K_{AB} \bullet \frac{I_A}{I_B}$$

Hence K_{AB} factor for all the elements present in the sample were determined using one of the three different routes present.

a) Using the default values present in the EDAX software, which were recorded a long time ago by a user at 200 kV accelerating voltage.

b) Secondly, let the software calculate the K_{AB} factors from the first principle.

c) Calculating the K_{AB} factor using a set of standards, using the functions built in the software. This was the method used for calculating the K_{AB} in the quantification of line scan. Figure 5-13 show the screen shot of the dialog box from the EDAX software, showing the cross section model "Zaluzec" used.

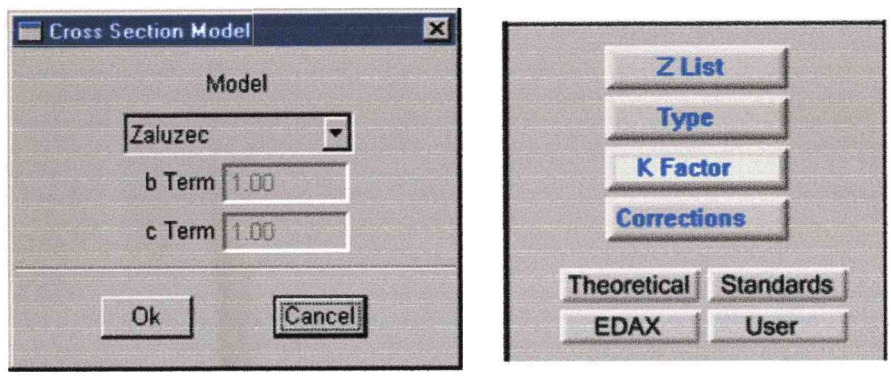

Figure 5- 13: Screenshot of the dialog box from the EDAX software, indicating the model used.

In the current sample, the elements present were Al, O, Fe, Cr, Hf and Y. The values K_{AlAl}, K_{AlO}, K_{AlFe}, K_{AlCr}, K_{AlHf} and K_{AlY} were calculated using the software and the values were scaled to Al. The total intensity was calculated using the formula,

$$I_{Total} = (K_{AlAl} I_{Al}) + (K_{AlO} I_{O}) + (K_{AlFe} I_{Fe}) + (K_{AlCr} I_{Cr}) + (K_{AlHf} I_{Hf}) + (K_{AlY} I_{Y})$$

where, I_{Total} is the total intensity and I_X is the intensity from the element X.

The concentration of the elements present were calculated as a percentage of the total using the formula,

$$C_{Hf} = ((K_{AlHf} I_{Hf}) / I_{total}) * 100$$

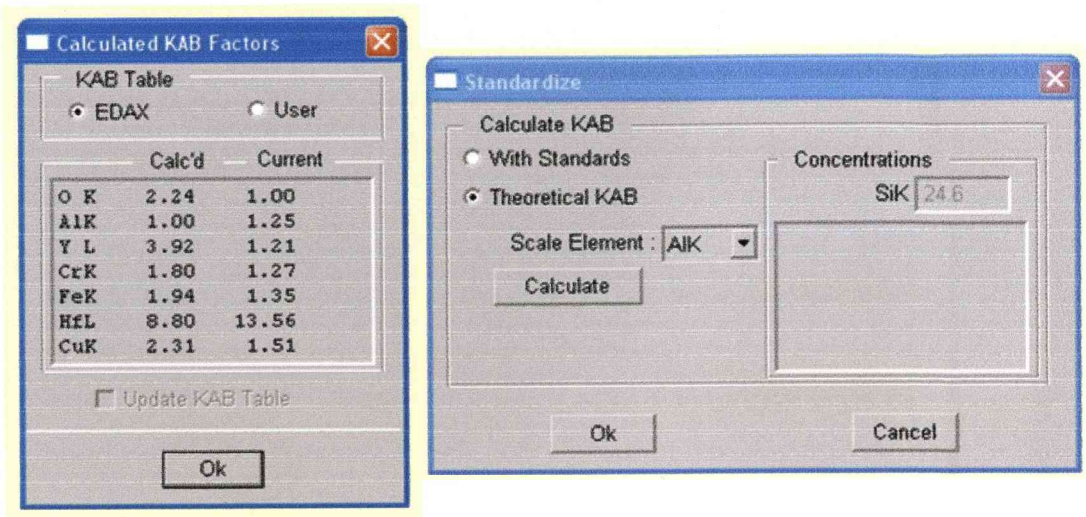

Figure 5- 14: Screen shot showing the calculated K factors for each element present and standardized to Al K.

The above screenshot Figure 5-14 shows the K values calculated for each element and scaled to Al. A concentration profile was obtained across the line, from the concentration values calculated at each point. Concentration values were averaged over the width of the boundary measured.

5.5.2. Line Scan for Hafnium (Hf) Detection

This section represents in detail the segregation behaviour of hafnium (Hf) over different boundaries with respect to RE particles, i.e. GB's which are connected to smaller RE-rich particles (typically < 20 nm in size), GB's which are connected to larger RE-rich particles (typically > 30 nm in sizes) and GB's which are far away from these RE-rich particles or GB's which are not directly connected to RE-rich particle.

Figure 5-15 shows an ADF image of the area near to the hole on the scale with several grains and grain boundaries, across which line scan was carried out to detect the segregation of

reactive elements. A pie chart is plotted in order to see the percentage of boundaries which showed Hf and Y to that of boundaries without any segregation. It can be seen from the pie chart, the percentage of boundaries which did not showed Hf are far fewer compared to those of the boundaries which did not show Y and could be due to the lower detectability.

Figure 5-16 and 5-17 shows a plot of Hf and Y distribution across about 80 boundaries from the ADF image shown in Figure 5-15 calculated using Cliff-Lorimer method as shown in previous section. There is a slight correlation at few boundaries, were Y content increases as Hf content increases and vice versa; whereas some boundaries show inverse correlation between Hf and Y content and hence a new method was needed to give more insight into the statistics. The spectrum analysis discussed in the next section yields better statistics.

When the GB's were analyzed with respect to position and size of particle, a pattern seems to emerge. It was found that there was a distinct difference in the amount of segregant present at different boundaries, with respect to size and position of the RE-rich particles.

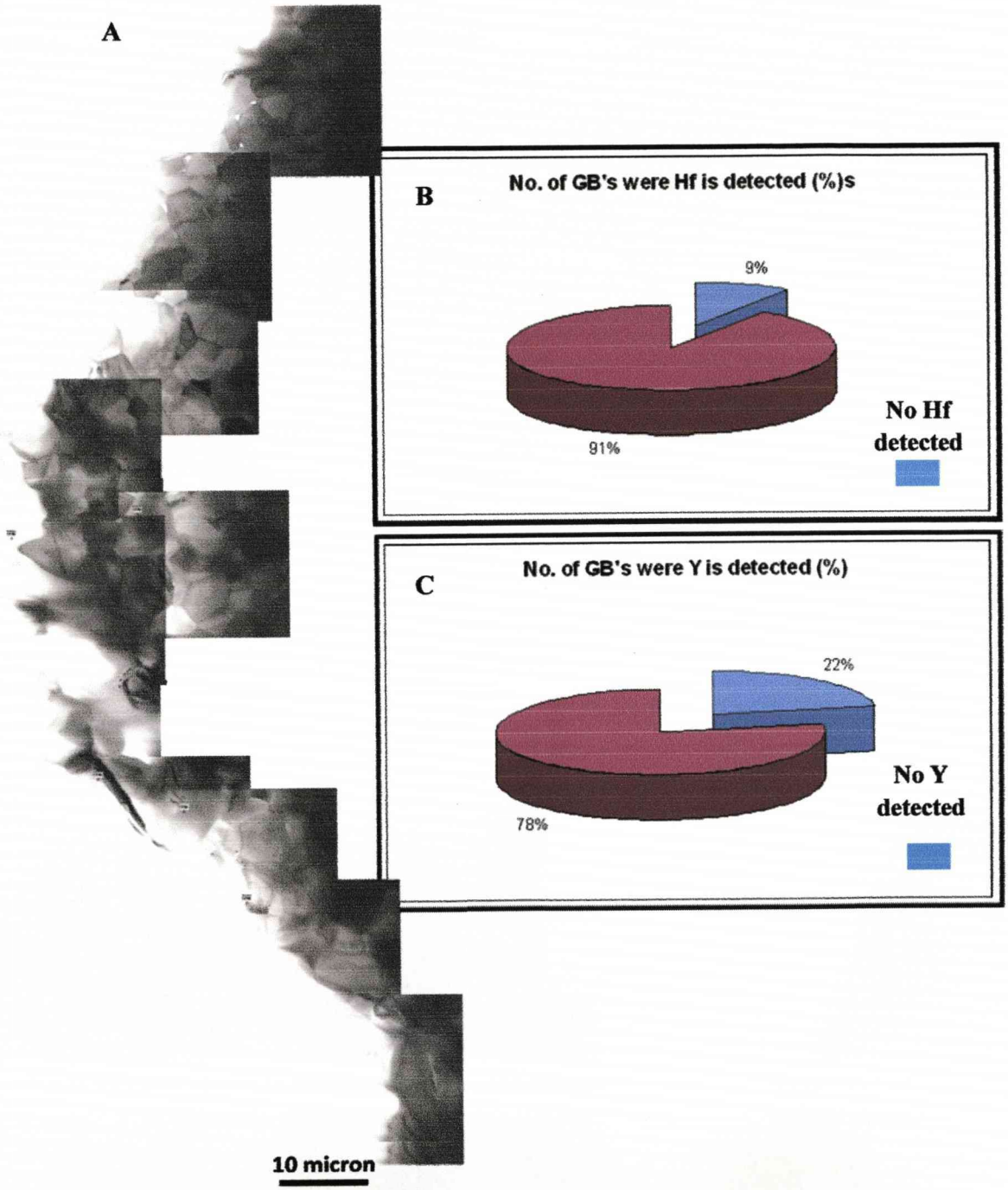

Figure 5- 15: A) BF montage of the alumina grains showing large number of grain boundaries around which the hafnium and yttrium line scan quantification was carried out. B) Hf distribution and C) Yttrium distribution across the GB's.

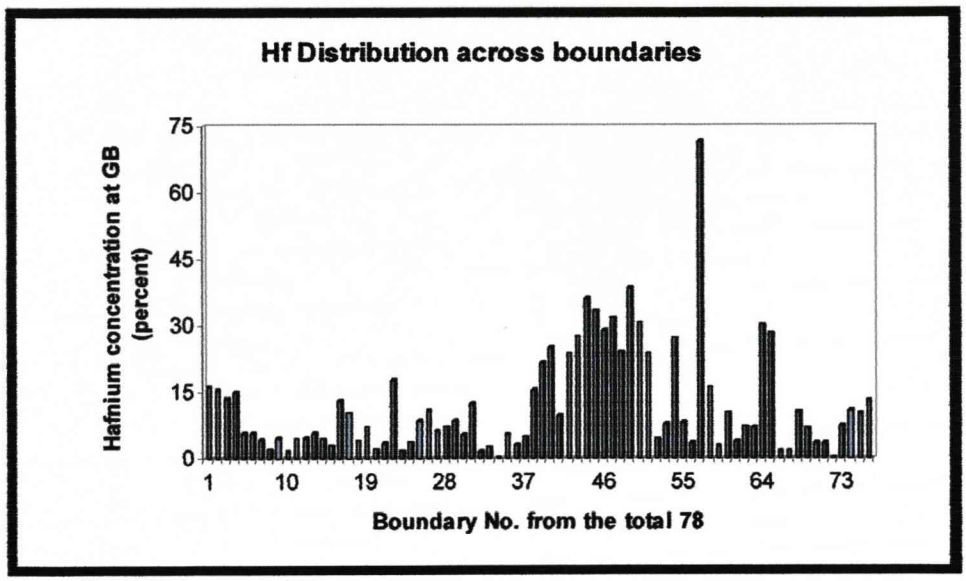

Figure 5- 16: Graph showing Hf wt. percent distribution over 80 boundaries analyzed.

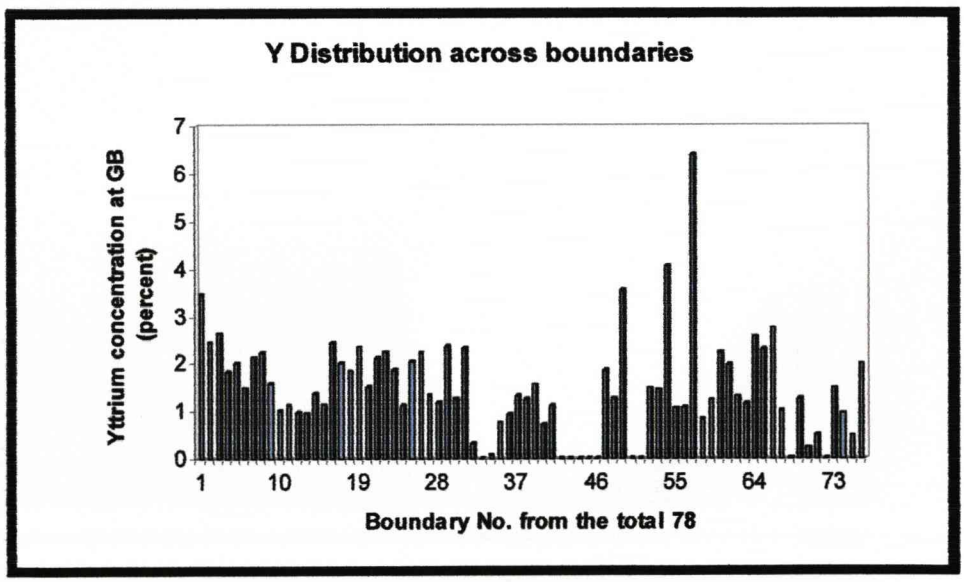

Figure 5- 17: Graph showing Y wt. percent distribution over 80 boundaries analyzed.

5.5.2.1. Line Scan across a boundary connected to a small particle

Figure 5-18 is a BF image of a scale with a small particle and Figure 5-19 shows the corresponding line scan over a boundary which is directly connected to this small RE-rich particle.

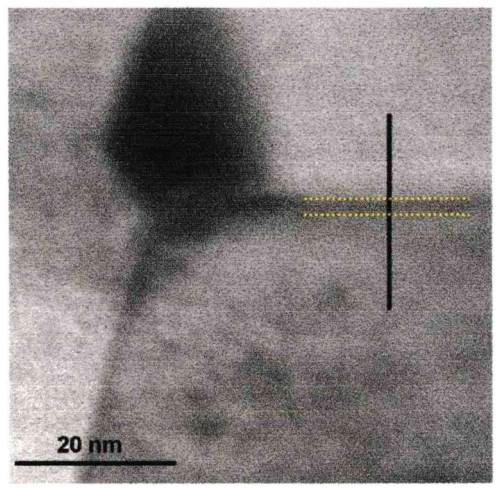

Figure 5- 18: BF image of GB's connected by a small particle

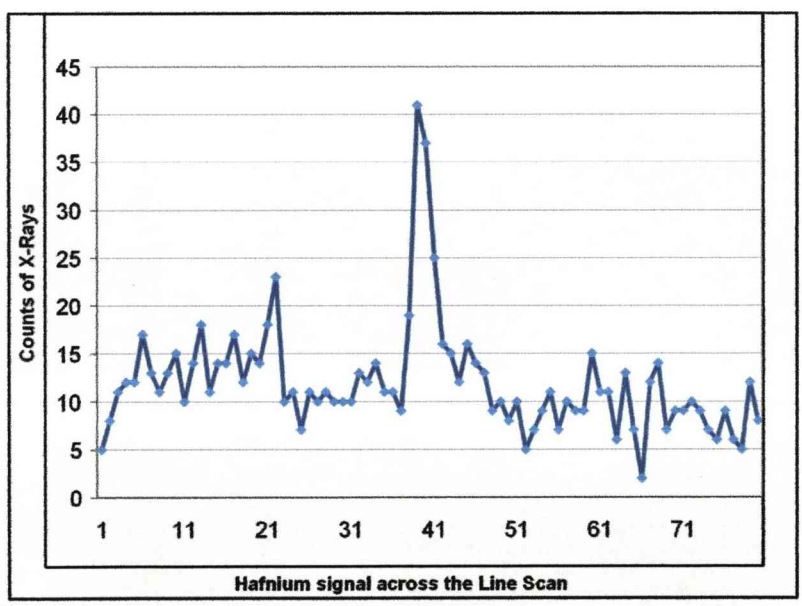

Figure 5- 19: Line scan across the boundary connected by small particle

The particle appears dark in the BF image recorded and the width of the particle is about 20 nm. It can be seen from the Line Scan that the hafnium (Hf) segregates to the GB, observed as a peak in the plot. The width of the boundary is approximately 2-3 nm, calculated using the scale function built into the EDAX programme. The data sets for each element were collected at every 0.5 nm (approximately). The width of the peak corresponds to 2.5 – 3.5 nm, which compares with that of the width in BF image. Few smaller peaks can be observed on both sides of the major peaks. These could be excluded from the Hf signal, as they do not fit into criteria of differentiating a peak from noise. The criteria used was,

$P - B \geq 3(2B)^{1/2}$

where, P is peak height and B is the height of background noise

A number of grain boundaries were analysed which were connected to a small RE rich particles. These Line Scan data were quantified by the Cliff-Lorimer technique. It was found that different grain boundaries had different hafnium weight percent.

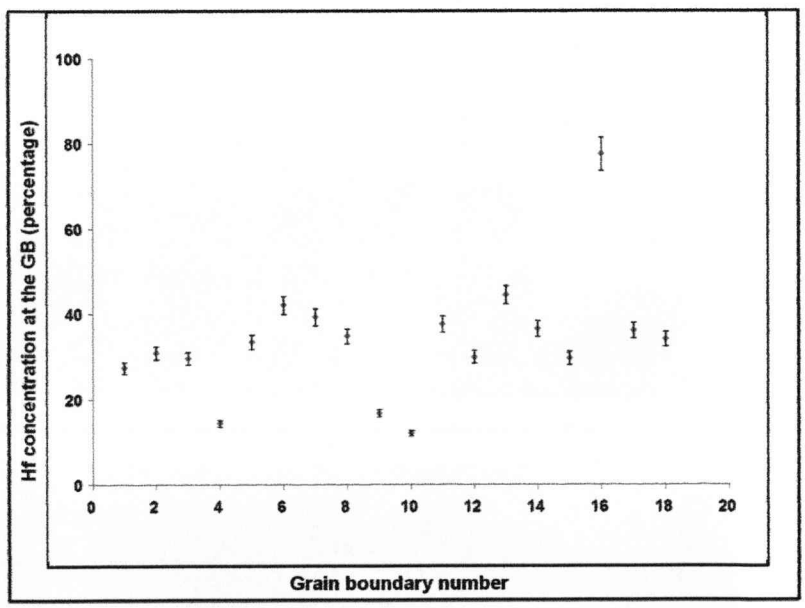

Figure 5- 20: Hf concentration over different GB's analyzed over several GB's.

Figure 5-20 shows the distribution of Hf across all the GB analyzed and which were connected to small RE particle. As found the hafnium concentration was spread over a large range of about 20-50%, and an odd boundary which showed 70 percent Hf concentration. There could be an error associated with these values, as the data were collected over a number of days under similar conditions.

5.5.2.2. Line Scan across a boundary connected by a large particle

Figure 5-21 is a BF image of a scale with a large particle and Figure 5-22 shows a Line Scan over a boundary which is directly connected to the large RE-rich particle shown in the top left hand corner of the BF image. The Line Scan for the hafnium (Hf) does not show any peak for hafnium segregation.

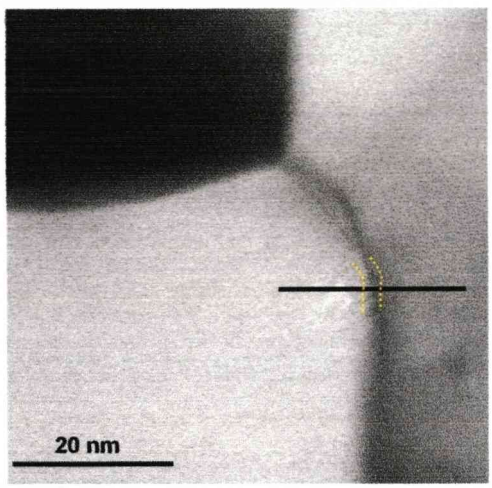

Figure 5- 21: BF image of GB's connected by large particle

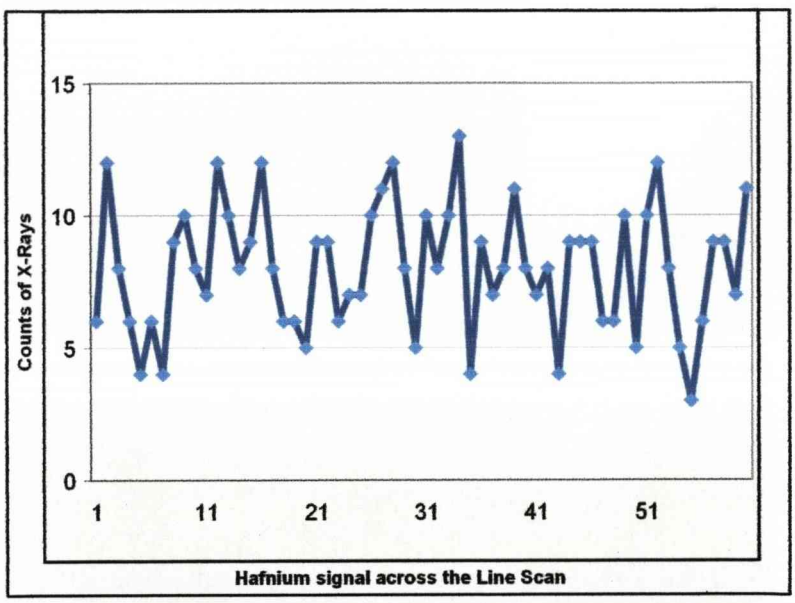

Figure 5- 22: Line scan across a boundary connected by large particle

Again a number of similar grain boundaries were analysed, which were connected by a large RE rich particles. These line scan data was again quantified using Cliff-Lorimer technique. It was found that most of the grain boundaries showed very little hafnium weight percent. The Figure 5-23 shows quantified data for several GB's connected by large RE particles. It was found that hafnium concentration was low compared to GB's connected with small RE particles and sometimes no hafnium was found. A few of these GB's had higher amounts of segregation of Hf of about 8 percent.

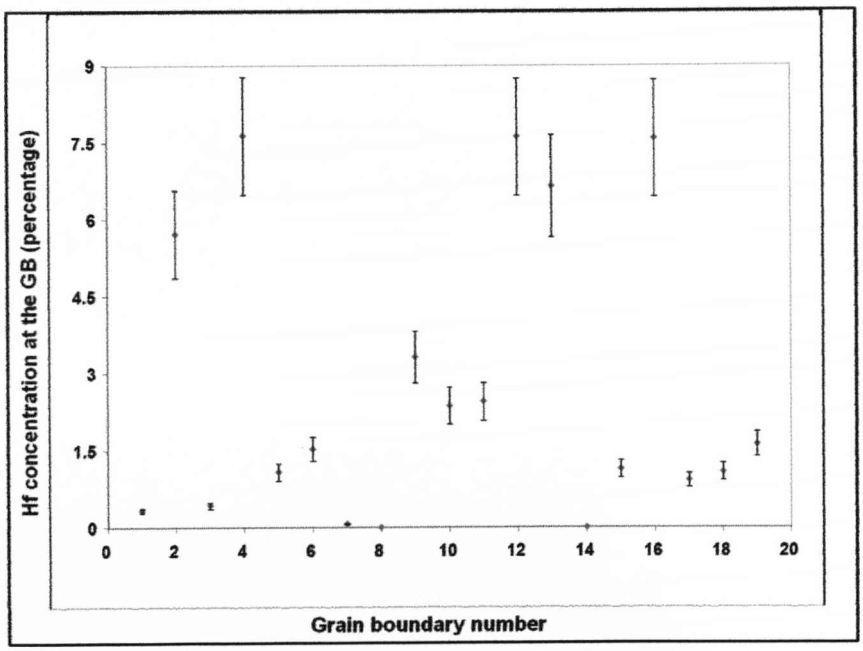

Figure 5- 23: Hf concentration over several GB's connected via a large RE rich particle.

5.5.2.3. Line Scan across a boundary away from particles

Figure 5-24 shows a BF image of a scale with no nearby RE-rich particle and Figure 5-25 is a Line Scan over the marked boundary. The Line Scan for the hafnium (Hf) shows that there is some segregation to the GB.

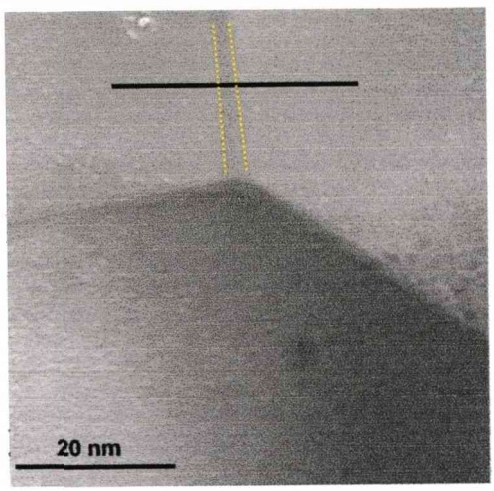

Figure 5- 24: BF image of triple point in alpha alumina scale far away from particles

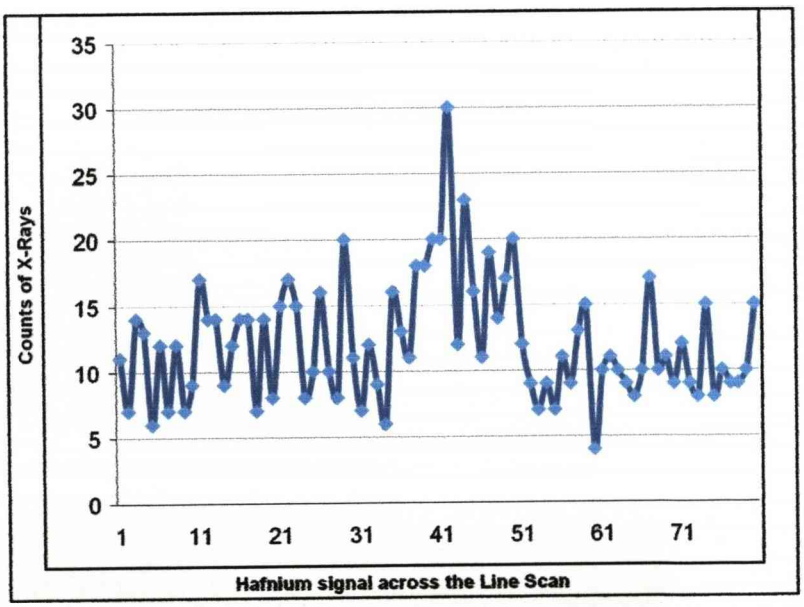

Figure 5- 25: Line scan across a boundary which is far away from particles

Further grain boundaries of these types were analysed, and line scan data were quantified using the Cliff-Lorimer technique. It was found that all the grain boundaries which were not directly

connected to RE-rich particles had an Hf concentration between 10 – 20 percent as shown in the Figure 5-26.

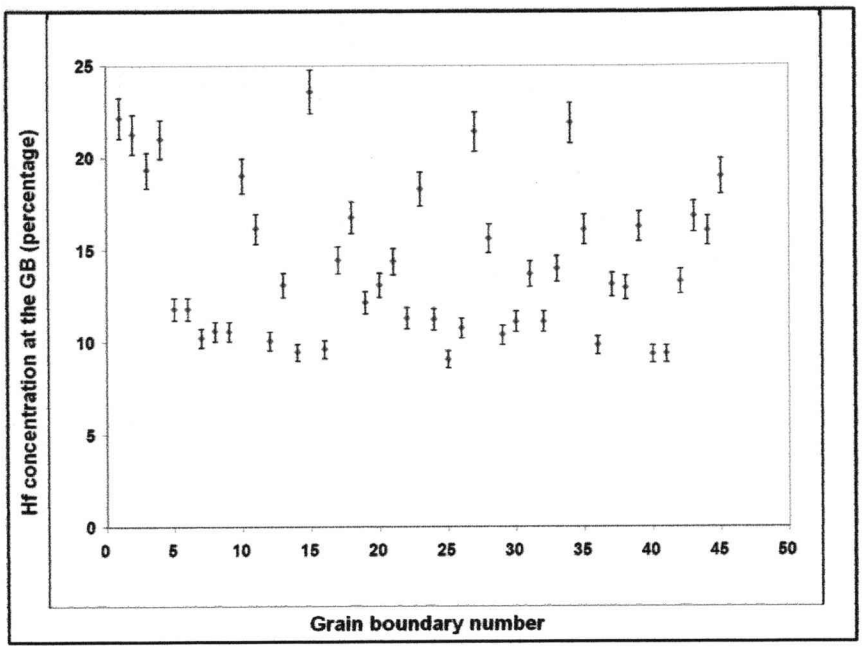

Figure 5- 26: Hf concentration over several GB's away from RE rich particles.

5.5.3. Line Scan for yttrium (Y) Detection

This section looks in detail at the segregation behaviour of yttrium (Y) over different boundaries. Similar analysis was carried out across the GB's which are connected by small RE-rich particles (typically < 20 nm in size), GB's which are connected by large RE-rich particles (typically > 30 nm in size) and GB's which are far away from these RE-rich particles or GB's which have no RE-rich particle. The data collected for Y were compared with those for Hf to see if there was a relation between two species segregating at these GB's. The Line Scan data for all the elements were collected simultaneously over a number of days to have a quantitative measure of the trend followed.

5.5.3.1. Line Scan across a boundary connected by a small particle

Figure 5-27 shows a BF image of a scale with a small particle and Figure 5-28 shows the corresponding line scan.

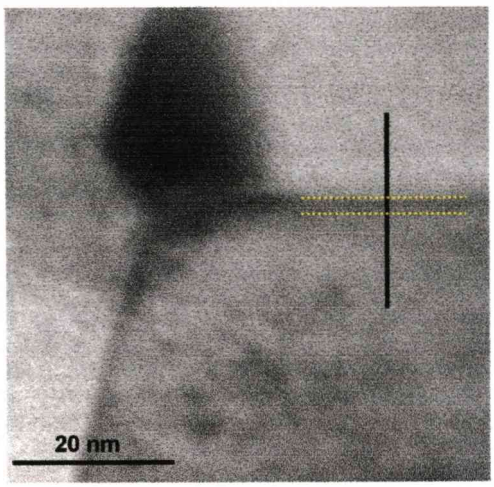

Figure 5- 27: BF image showing a small RE rich particle and a line scan.

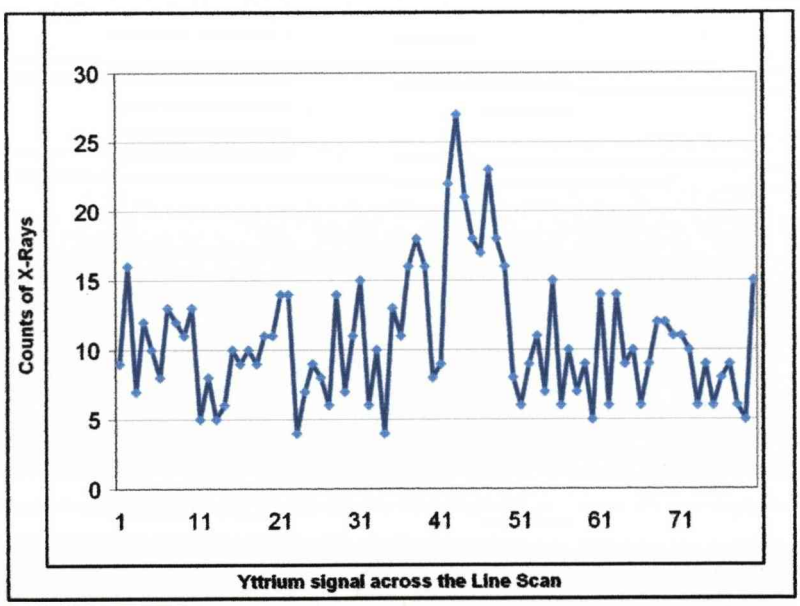

Figure 5- 28: Corresponding line scan for yttrium across a GB connected by small particle

The line scan data is similar to that obtained for hafnium and from the peak observed in line scan data it can be said that the yttrium (Y) segregates to the GB.

The Figure 5-29 shows concentration distribution of Y over several GB's connected by small RE particle. The yttrium weight percent lay within a range 0.5 – 2.5%.

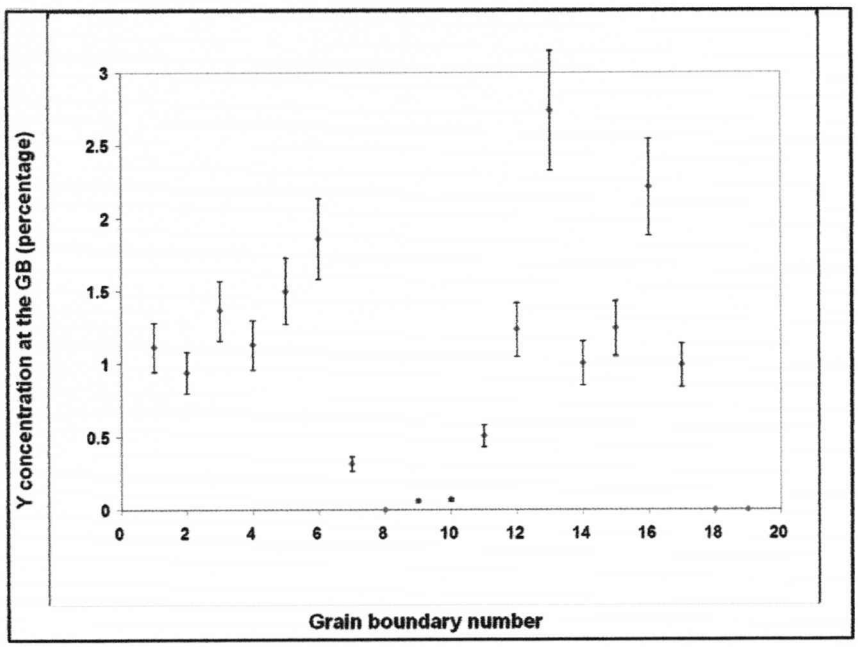

Figure 5- 29: Yttrium distribution across GB's connected by small particles

5.5.3.2. Line Scan across a boundary connected by large particle

Figure 5-30 a BF image of a scale with a large particle and Figure 5-31 shows the Line Scan over a boundary which is directly connected by a large RE-rich particle. The Line Scan for the yttrium (Y) has no strong peak, similar to the data obtained for hafnium Figure 5-22.

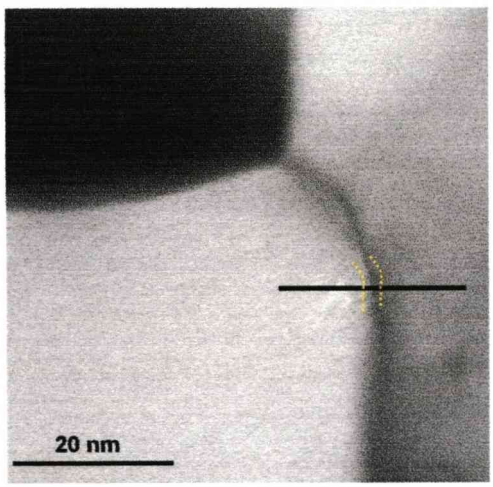

Figure 5- 30: BF image across a GB connected by a large particle

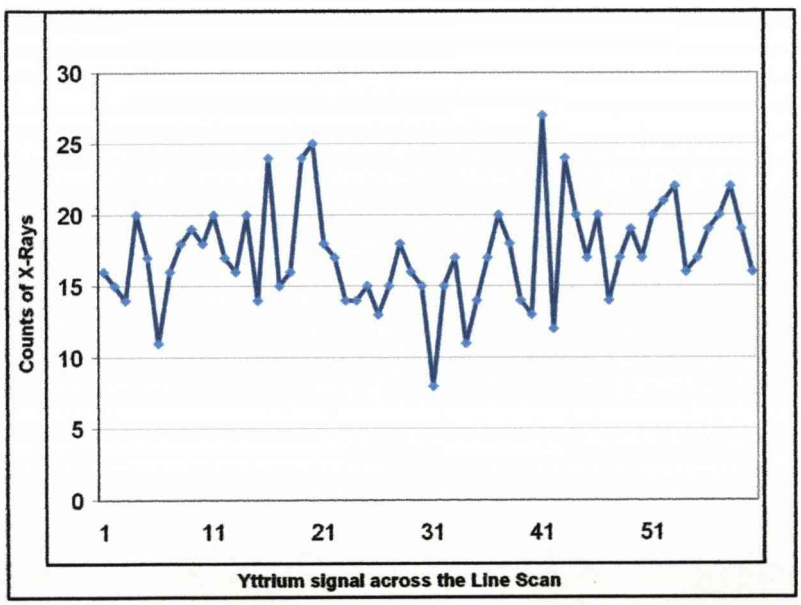

Figure 5- 31: Line scan across the GB connected by large particle.

The Figure 5-32 shows quantified data for GB's connected by a large RE particle. Once again it was found that yttrium weight percent segregation was low compared to GB's connected with small RE particles and sometimes no yttrium was found to segregate.

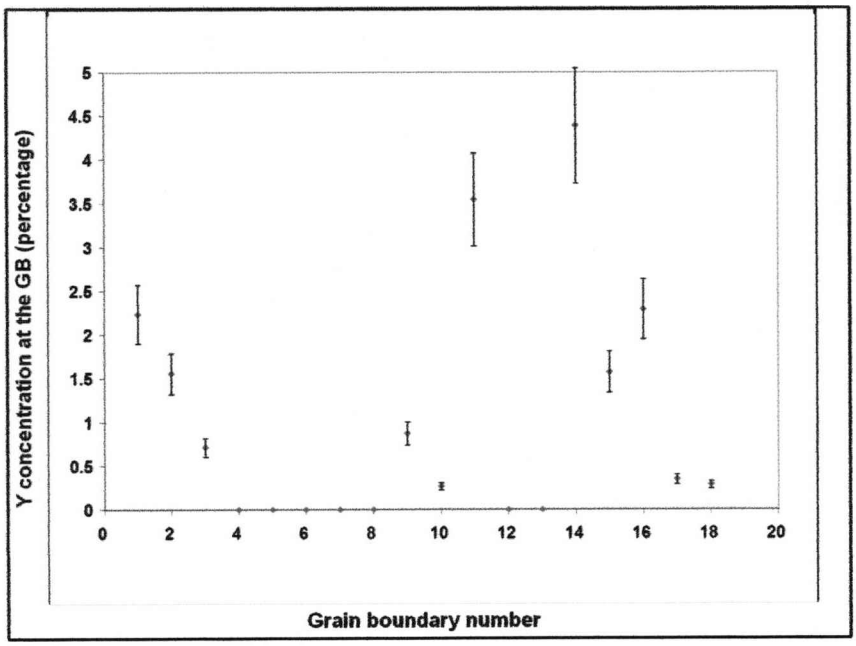

Figure 5- 32: Y distribution across the GB's connected via a large RE rich particle.

5.5.3.3. Line Scan across a boundary away from particles

Figure 5-33 shows a BF image of a scale at a triple point with no RE particle in the vicinity and a Line Scan over a GB as shown in Figure 5-34.

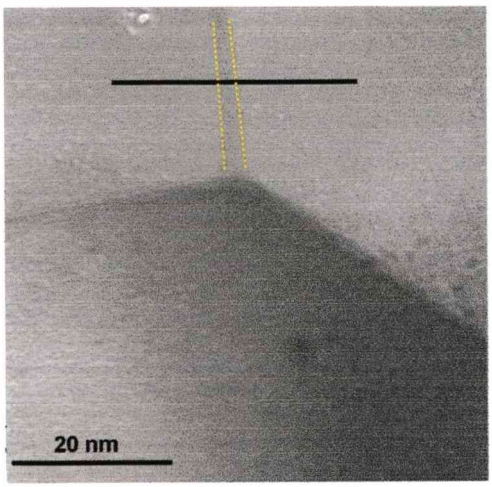

Figure 5- 33: BF image of a GB which is not connected by any particles.

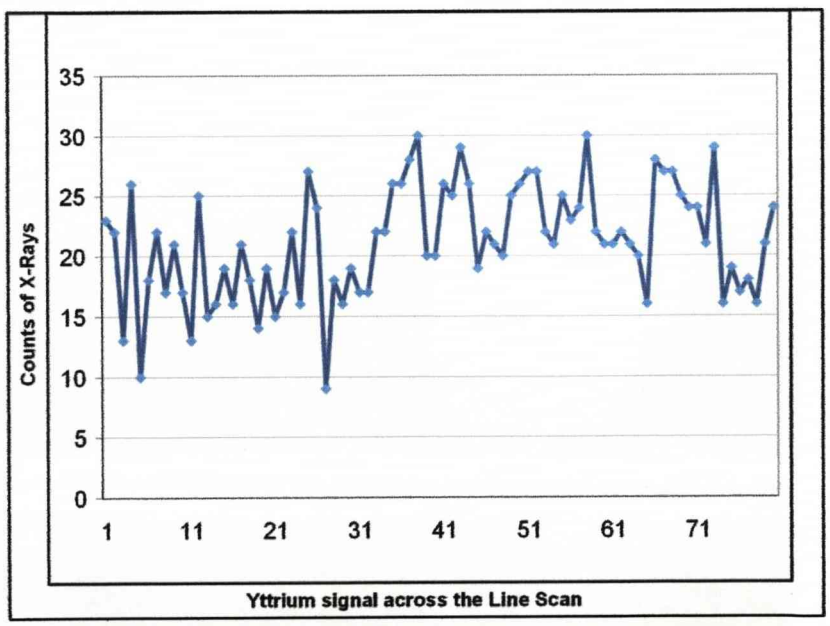

Figure 5- 34: Y concentration across a GB which is not connected to any particle.

The Figure 5-35 shows a plot of quantified data for GB's which are not connected directly by RE-rich particle. It is found that yttrium weight percent segregation value lies in and around 2±0.8 weight percent.

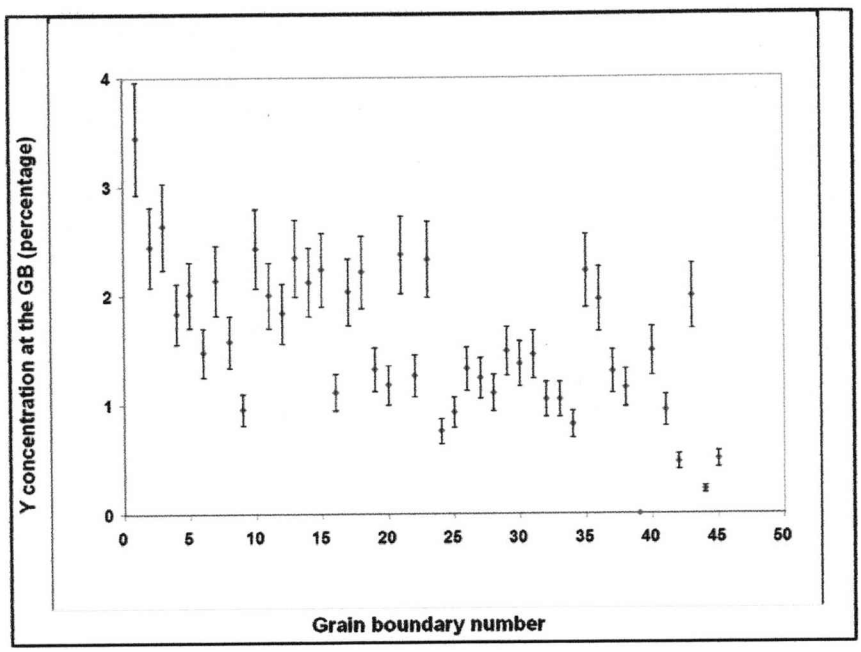

Figure 5- 35: Y distribution across all the GB's analyzed, which were not connected to any particle.

5.6. Quantification using spectrum analysis

In the following section instead of quantifying line scan data using Cliff-Lorimer method, a spectrum was collected from a fixed area/volume over the different boundaries and quantified. This section also looks in detail at the segregation behaviour of hafnium (Hf) and yttrium (Y) over different boundaries with respect to RE's particles, i.e. GB's which are connected by smaller RE-rich particles (typically < 20 nm in size), GB's which are connected to larger RE rich particles (typically > 30 nm in size) and GB's which are far away from these RE-rich particles or GB's which are not directly connected to RE-rich particles.

5.6.1. Quantification for hafnium (Hf) and yttrium(Y)

In this section the spectrum from different regions on the GB's are collected and quantified. The Figure 5-36 to 5-39 show the BF image of different regions on the scale and GB's with and without RE rich particles and corresponding EDX spectrum collected from the area of 100 nm^2 indicated by the white box. It can be seen from the EDX spectrum that the RE signal differs for boundaries connected to a small particle to that connected to large particles.

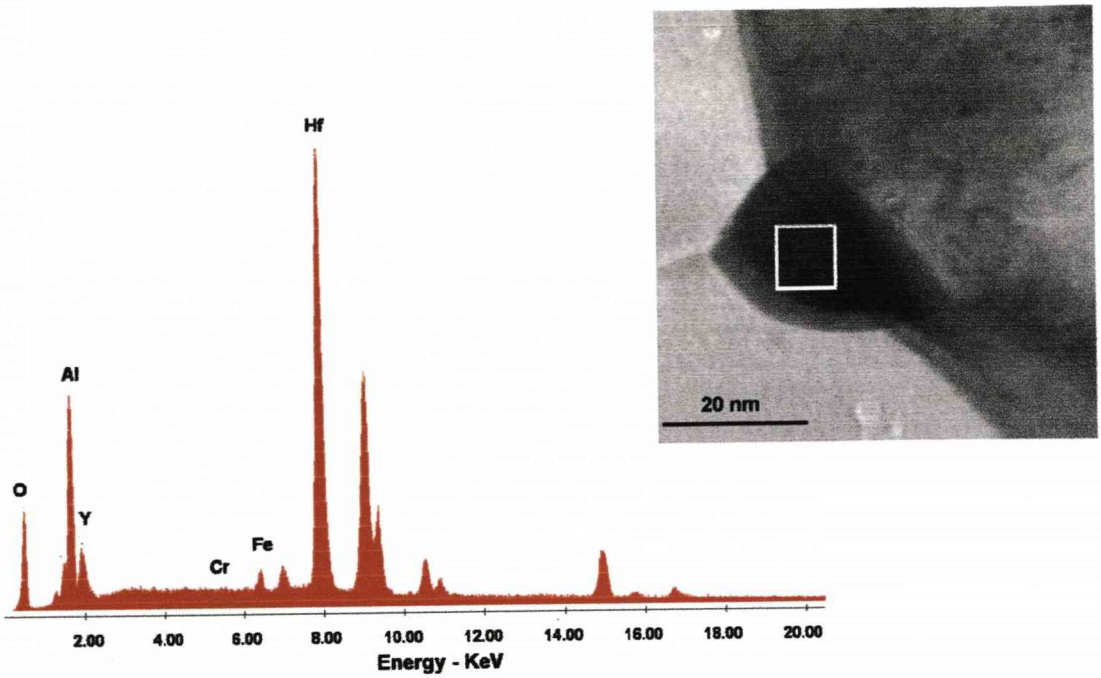

Figure 5- 36: EDX spectrum from the particle, marked on the BF image.

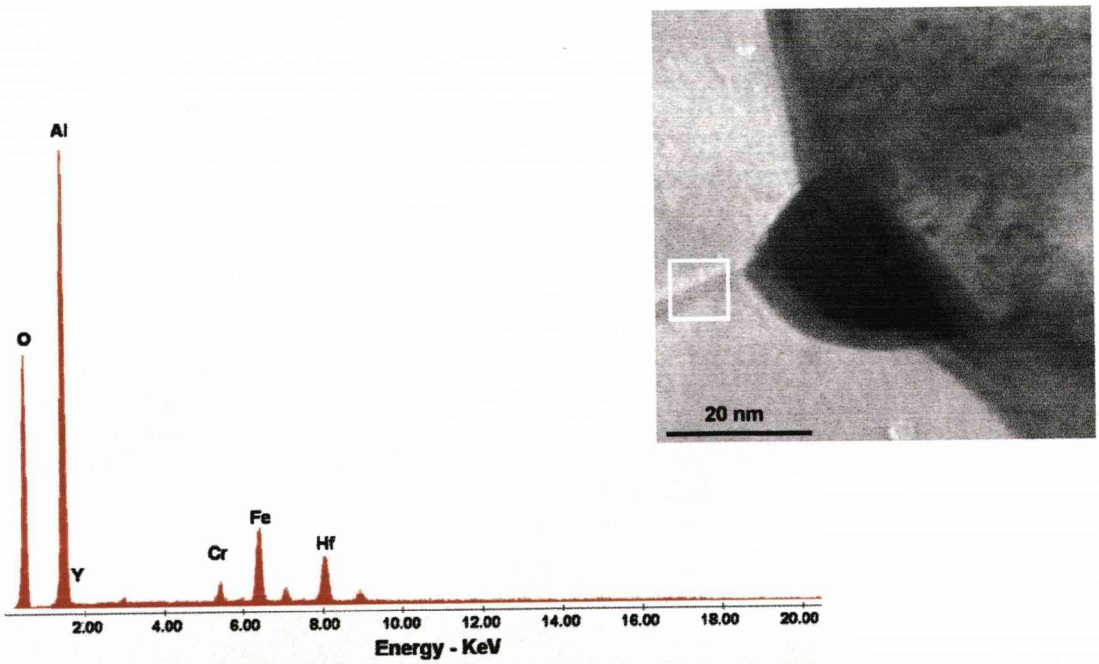

Figure 5- 37: EDX spectrum from the GB connected by small particle.

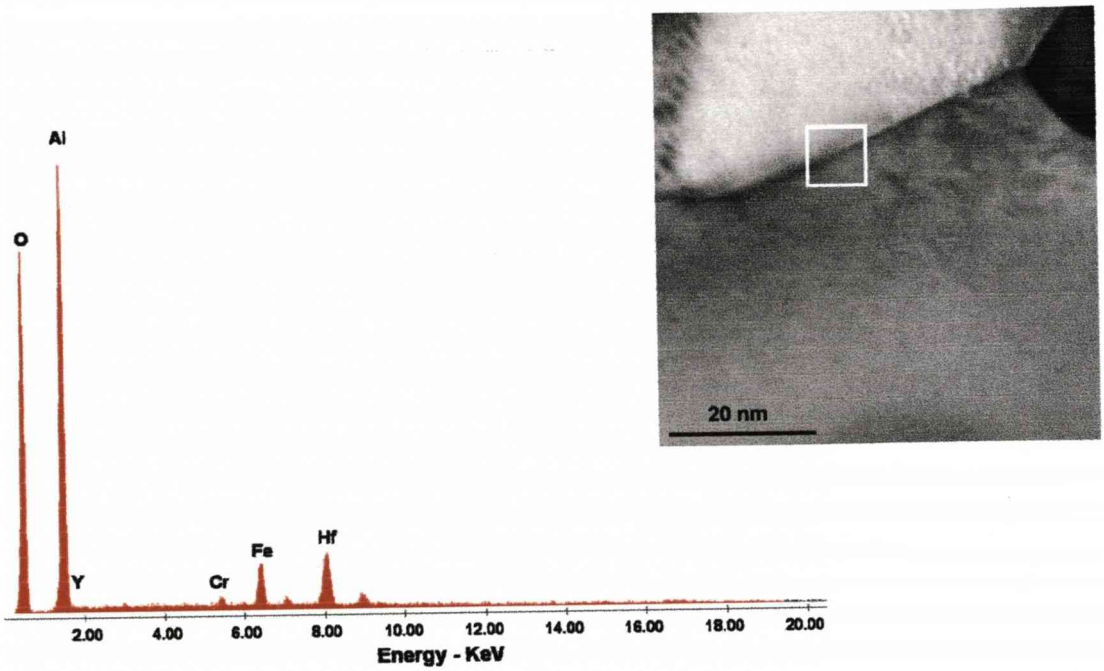

Figure 5- 38: EDX spectrum from the GB far away from particles.

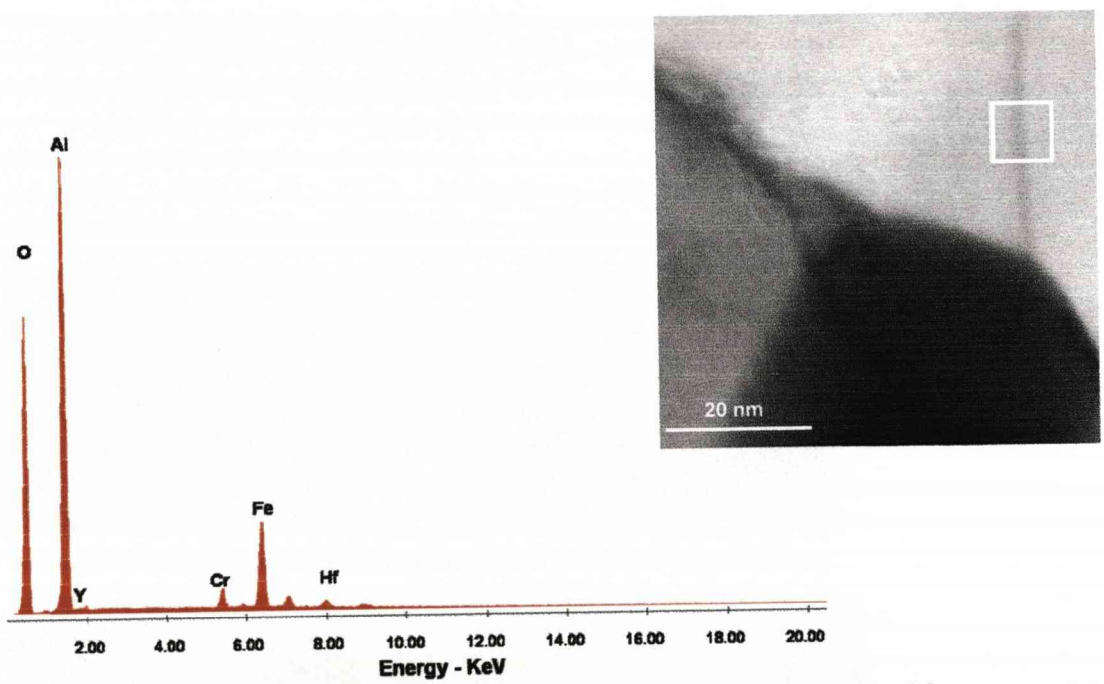

Figure 5- 39: EDX spectrum from the GB connected by a large particle.

Quantification was carried out using the Exceptional Standardless Quantification programme built in to the EDAX genesis system which has been explained in the experimental section, Quantification shows that the Hf and Y content of the boundaries connected to large particles is lower than that of the boundaries connected to particles less than 20 nm diameter.

Table 5-1 shows the quantified data from the EDX spectra and it reinforces the same trend of different boundary types seen in the line scans.

Description	Hf Wt. %	Y Wt. %
Bulk of the particle	88±2	6±1
GB connected to a small particle	12±2	3±0.8
GB not connected to a particle	7±1	1±0.5
GB connected to a large particle	1.5±1	0.3±0.2

Table 5- 3: Quantified data showing Hf and Y variation across different GB's.

Figure 5-40 shows BF image with the marked regions from were the spectrum was collected for duration of 100 seconds and quantified. The quantified data was plotted for Hf and Y and is shown in the Figure 5-41, it is seen that Hf and Y content remain same everywhere on the GB, except for the first region were Hf and Y content seem to be higher than the rest of the region on the boundary. The reason for this is not clear and could be due to instrumental instability. The GB width is about 2 nm and is parallel to the beam throughout the regions analyzed.

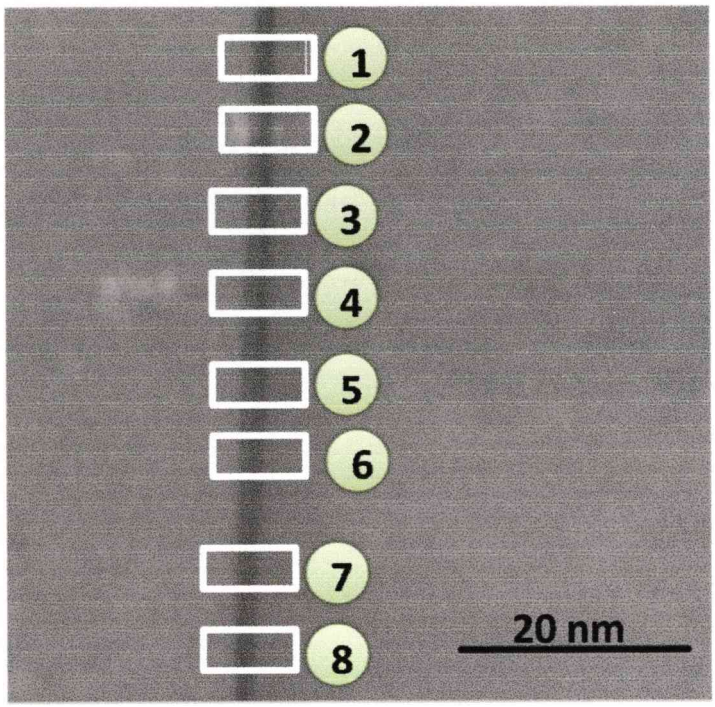

Figure 5- 40: BF image of a GB and marked regions from which the spectrum was collected.

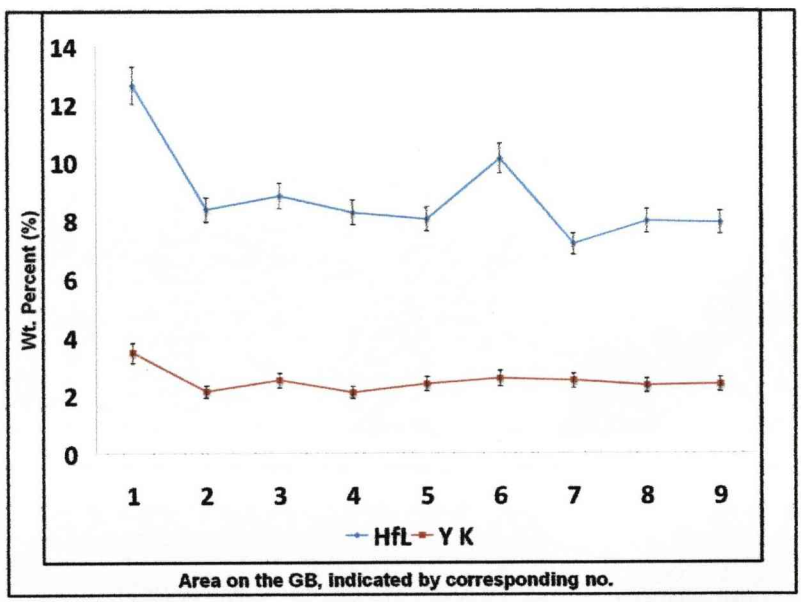

Figure 5- 41: Quantified Hf and Y data from the marked regions on the GB.

Figure 5-42 shows a BF image from an alpha alumina scale containing two particles of different sizes. The yellow spots on the image represent the positions from where the EDX spectra were collected (each spectrum collected from 100 nm^2) and plotted, whereas the white spots represents the region in the bulk from which spectrum was collected to see if Hf and Y could be detected. No Hf and Y were detected in the bulk.

Figure 5-43 below shows the plot of quantified data for Hf wt. percent using the Exceptional Standardless Quantification method based on Cliff-Lorimer method. It can be seen from the chart that the Hf content of the GB varies from place to place across the sample and is much higher or lower than average on GB's near particles. The quantified values are in agreement with the line scan data obtained thus confirming the difference in GB composition adjacent to a particle. The same is true for Y, as can be seen from Figure 5-44. It shows the plot of quantified data for Y wt. percent using the Exceptional Standardless Quantification method based on Cliff-Lorimer method. It can be seen that the Y content of the GB varies from place-to-place across the sample and is much higher or lower than average on GB's near particles. The quantified values are in agreement with the line scan data obtained thus confirming difference in GB composition adjacent to particles. These experiments were repeated on another area of the sample and results obtained were in agreement with the current one.

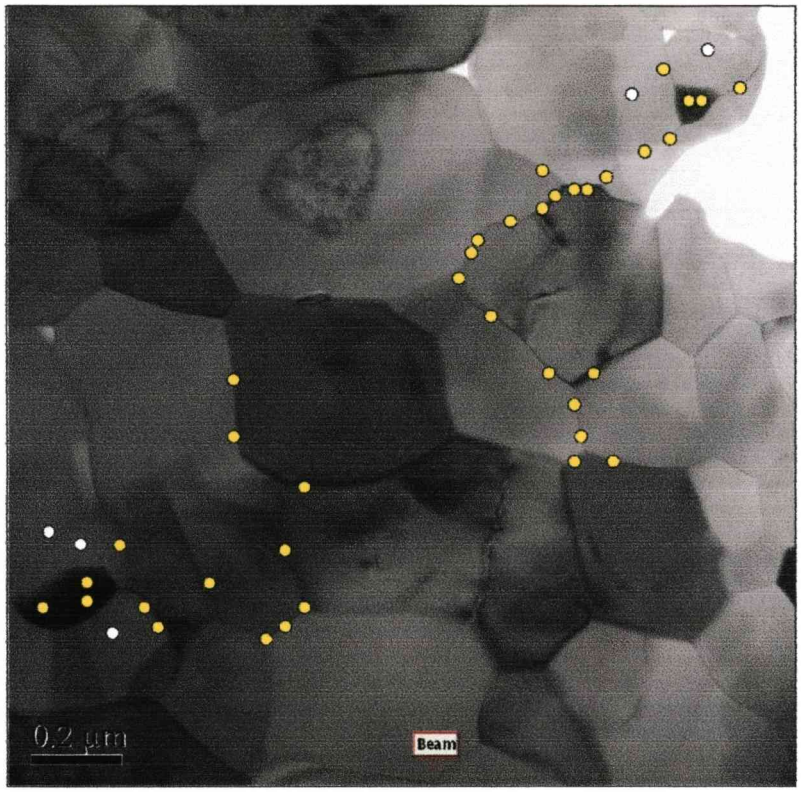

Figure 5- 42: BF image of an alpha-alumina scale containing small and large particles

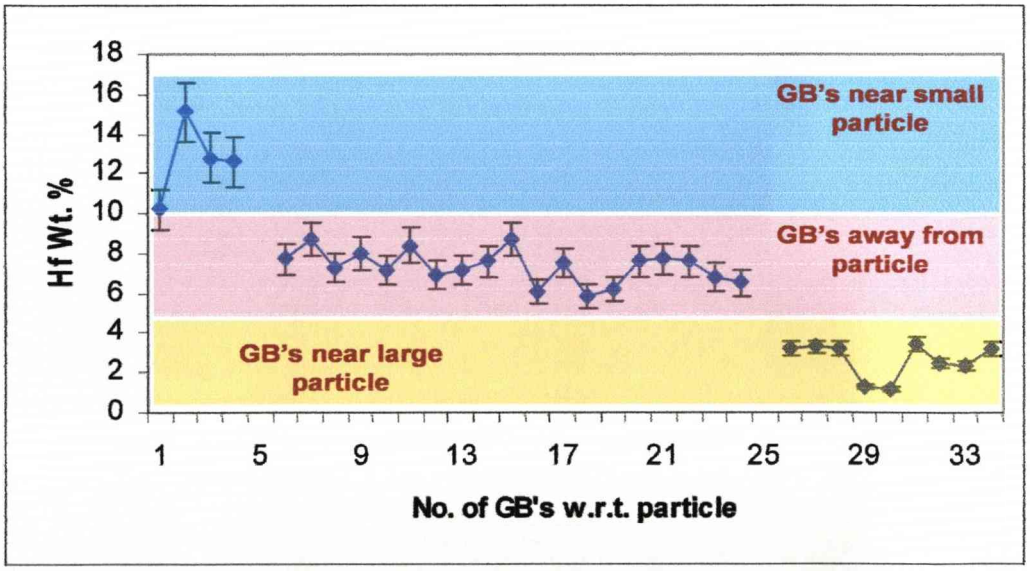

Figure 5- 43: Plot of Hf weight percent segregating to the boundary regions.

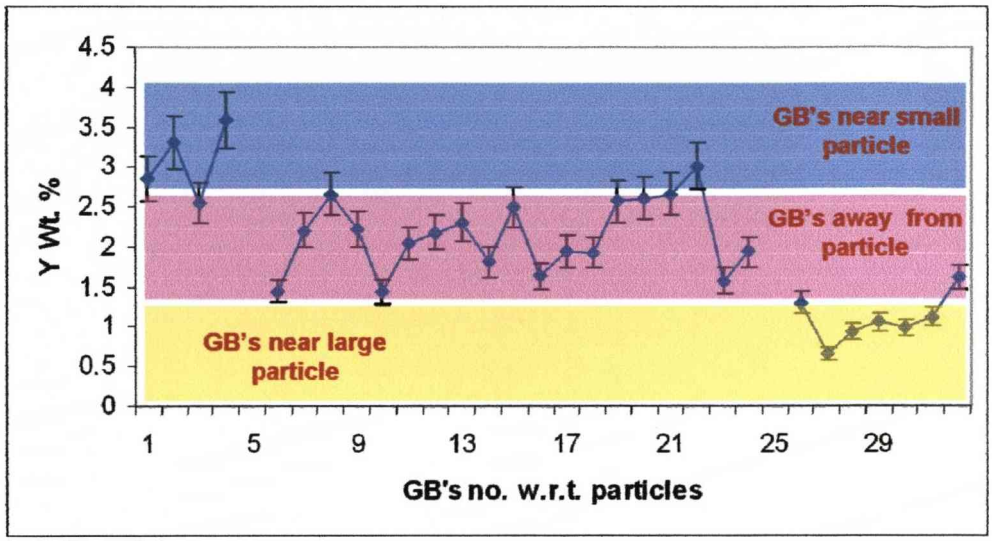

Figure 5- 44: Plot of Y weight percent segregating to the boundary regions.

5.7. Anomalies during the line scan

During the Line Scan analysis, it was sometimes found that there were some anomalies. Sometimes the width of peak did not correspond to the one measured from the BF image. Sometimes dual peaks were observed, possibly indicating surface segregation to the top and bottom of the scales. Some of these are presented in the following section.

Figure 5-45 shows line profiles across a grain boundary for Hf and Y and the corresponding BF image in the top corner. The BF image shows the GB to be oriented almost parallel to the beam. But as can be seen, dual peaks were observed for Hf whereas no significant signal for Y was observed.

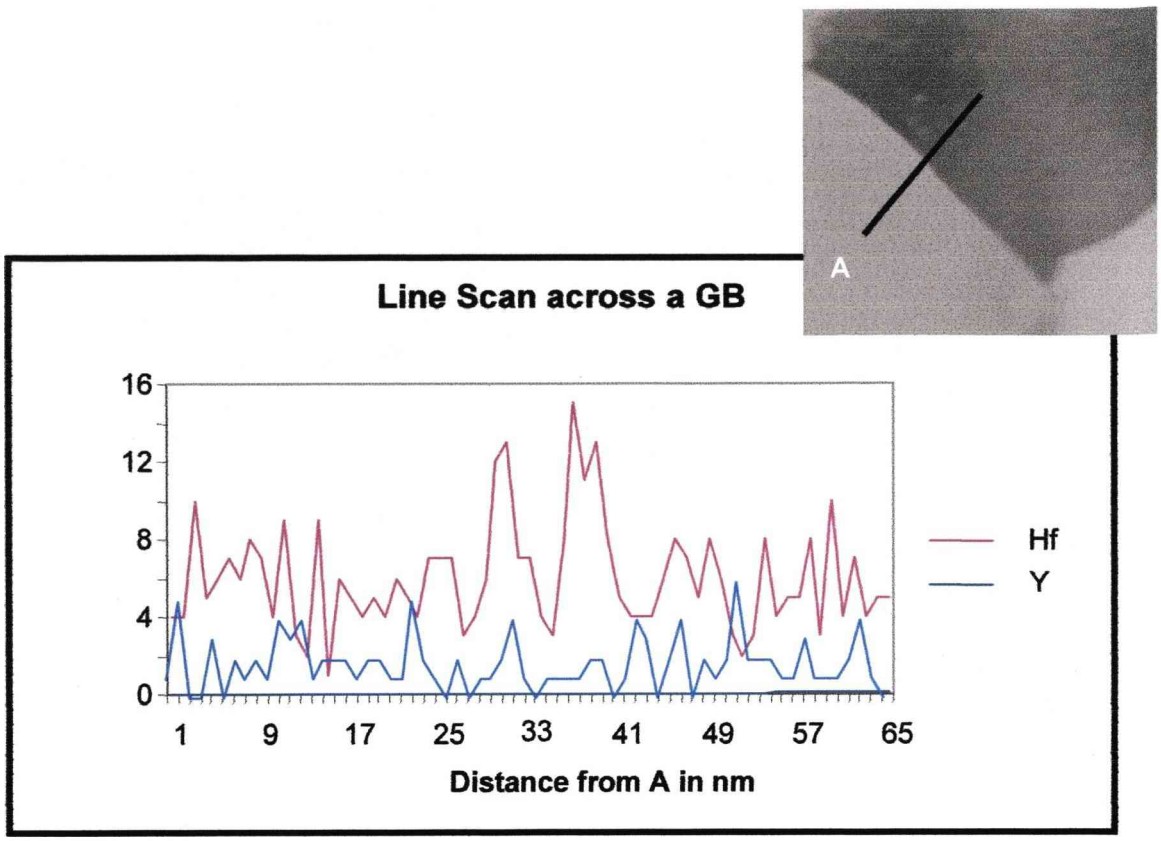

Figure 5- 45: Line Scan data showing dual Hf peak.

One of the possible suggestions could be that GB is highly inclined and there is top and bottom segregation taking place. The GB inclination could not be confirmed from the BF image due to lack of contrast. It is still not clear why no Y was detected and this needs to be analyzed carefully.

Figure 5-46 shows a line profile, in which the Hf signal shows an extended peak and a small Y peak. The GB is oriented parallel at the point were the Line Scan was carried but from the Line Scan plot it seems to be spread over few tens of nm. Again no Y was detected or very low Y was detected.

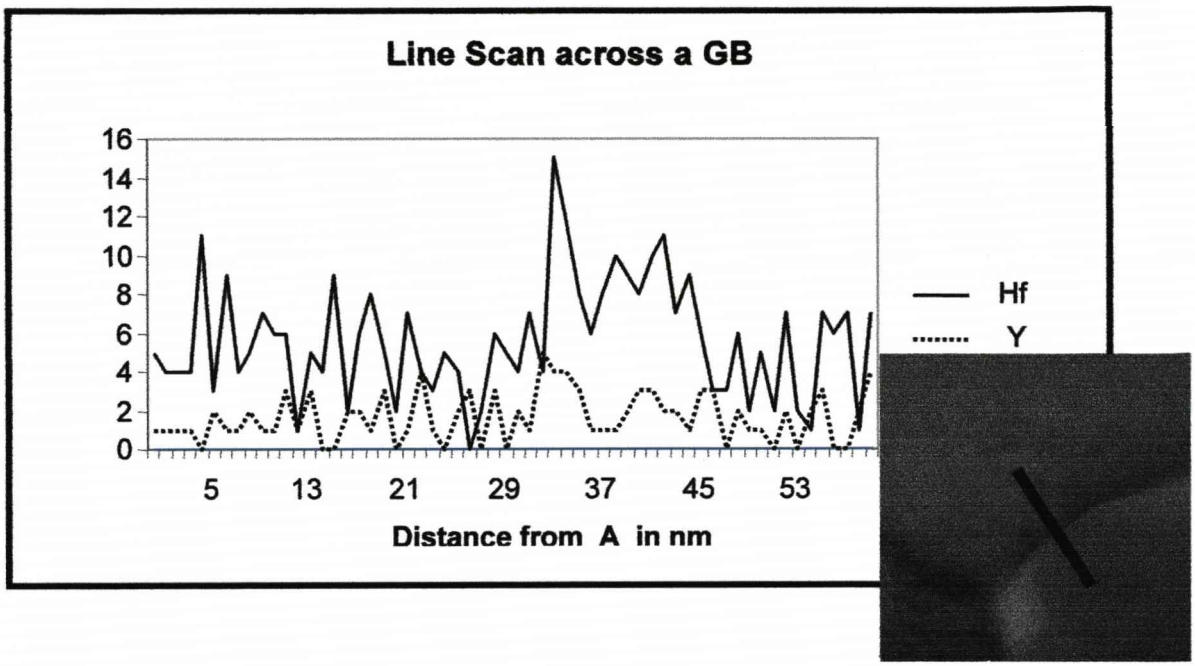

Figure 5- 46: Line Scan data showing a broadened peak for Hf.

Chapter 6

Results: SuperSTEM and EELS

6.1. Segregation studies using SuperSTEM

This section is divided into three parts. In section 1 the structure of the scale to be studied in this thesis is explored. This is followed by the section where useful elemental loss edges are identified in the low and high loss region, and are used to map the segregation of reactive elements at the grain boundaries. The last section probes the effect of specimen thickness and contamination.

6.2. Orientation of the scale

The samples analysed herein have been prepared by the conventional method of mechanical grinding and low angle ion beam thinning which minimises modification of the oxide scale and grain boundaries. The Table 6-1 shows the composition of the model alloy used for investigation.

	Elements (Wt%), Balance = Fe								
Alloy	Cr	Al	Si	Mn	Zr	C	Y	Hf	Ti
M9	19.53	4.85	-	-	-	0.0115	0.033	0.031	-

Table 6- 1

The orientation of the GB with respect to the electron beam greatly affects the EEL spectrum. Figure 6-1 shows a HAADF image of a grain with all its GB's inclined. The width of the GB is about 50 nm and if a Line Scan was to be carried out it might lead to scattered result. Most of the times the GB's were inclined to the incident electron beam and a real search was required to find boundaries which were sufficiently parallel to the incident electron beam. This is important in the present case as there is less degree of tilt on SuperSTEM (±10°).

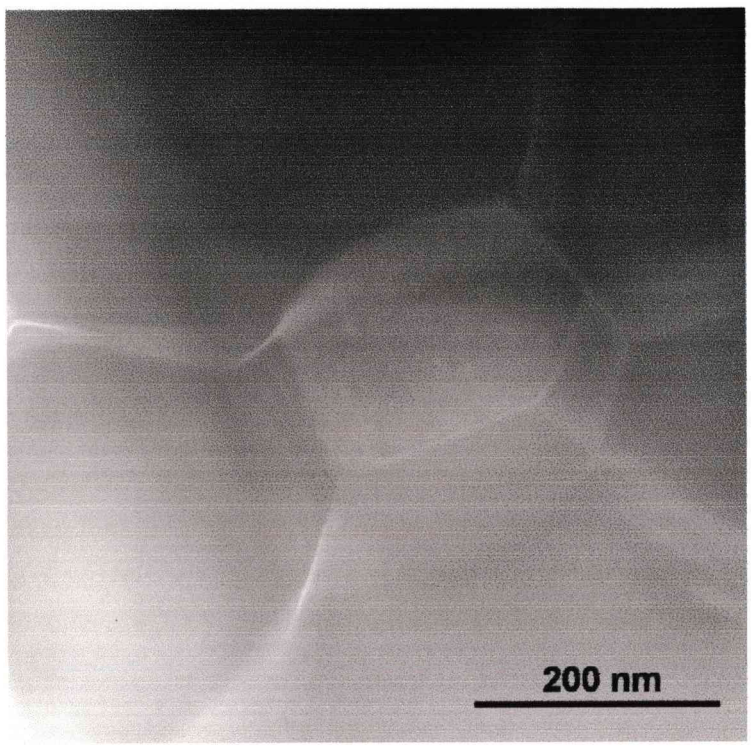

Figure 6- 1: HAADF image of alpha-alumina scale.

It could be seen the image becoming darker on the top right hand corner, this could be due to the fact that the sample is getting contaminated. The above HAADF image is an integrated image of the several images taken one after another and then added all together. The horizontal streaks or lines observed in the above HAADF image are due to scan settings. Figure 6-2 shows a HAADF image of an oriented grain on the [0 1 -1 1] zone axis. One of the GB could be said to be oriented parallel to the beam whereas one of the boundaries is inclined by an angle as could be seen through the intensity distribution in the HAADF image. Figure 6-3 shows an intensity profile across the boxed region in the image. The intensity profile has dual peaks which are at the top and bottom of the boundary. These intensities at the top and bottom of the boundary could be due segregation of heavier elements at those position or these might be due to strain present at the boundaries.

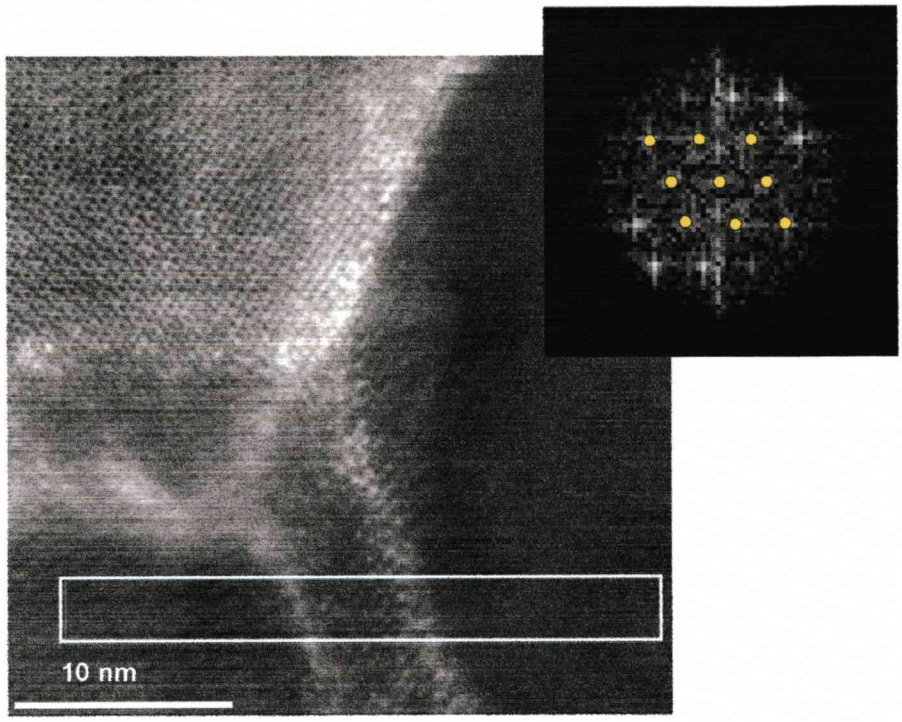

Figure 6- 2: HAADF image of a oriented grain at a triple point. High intensities could be due to strain at GB and/or heavier atoms may be present at those sites.

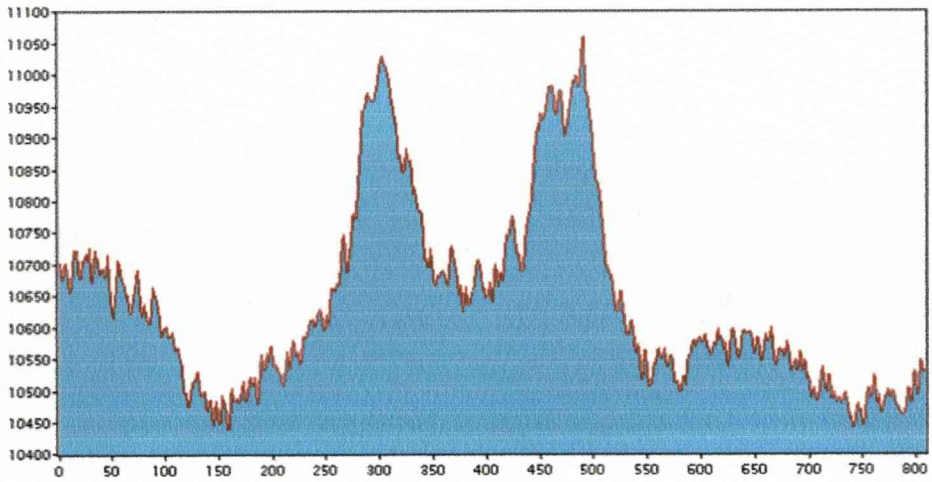

Figure 6- 3: Electron intensity profile across the boxed region, which has been integrated over given width. The dual peaks represent the higher intensities observed at edges of GB.

Particles were present in the scale. These particles were mostly found in the upper region of the scale near equiaxed grains. Figure 6-4 shows an HAADF image of oxide scale with these particles. The particles appeared bright indicating that they are likely to contain heavier atoms.

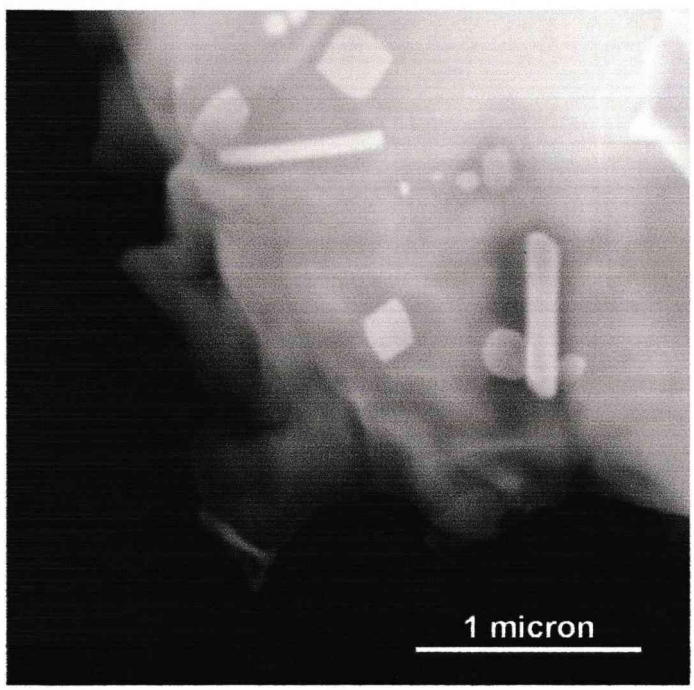

Figure 6- 4: HAADF image at low magnification showing more dense particles of different shapes and sizes present in upper region of the scale. The high intensity is due to heavier atoms present in the particles.

6.3. Identification of edges in low loss and high loss region

The following section deals with the identification of RE edges in the low loss region and high loss region using the techniques previously described in the experimental procedure section. For low loss analysis the spectrum along with zero loss peak was collected and analyzed and for higher loss the spectrum was collected from 1500 eV onwards.

6.3.1. Identification of edges in low loss region

The compositional results from the EELS spectrum will be discussed in this section. The main emphasis has been on the low loss region of the spectrum collected from GB in the alumina scale. The low loss spectra did not show any specific edges as the edges for Hf and Y lie below the first plasmon peaks and hence to extract the edges, the spectra were processed. Different techniques have been applied to the data acquired from a large area of the scale containing a GB. In one method the spectrum from one pixel is deconvoluted for the beam spread and searched for edges at characteristic energy losses. In the other method, summed spectra from regions of the GB and the bulk are compared to see the differences, and edges coming up in the spectrum after some post processing of the spectrum image analyzed. Figure 6-5 shows an HAADF image of the two alumina grains separated by a GB. The spectrum map was collected from the marked region in the HAADF image and its intensity profile is shown in the Figure 6-6. A rainbow scale was used where pink/blue represents a low energy/intensity and red/yellow represents a higher loss energy/intensity usually associated with high Z. Light colouration in this HAADF image corresponds to a high level of hafnium and /or yttrium. The original HAADF image showed a lot of scan lines which were removed electronically. The script used for removing the scan lines from the image is shown in Appendix 1. The width of the GB can be calculated approximately from the bright intensity spread recorded on the HAADF image, which is about 3 - 4 nm.

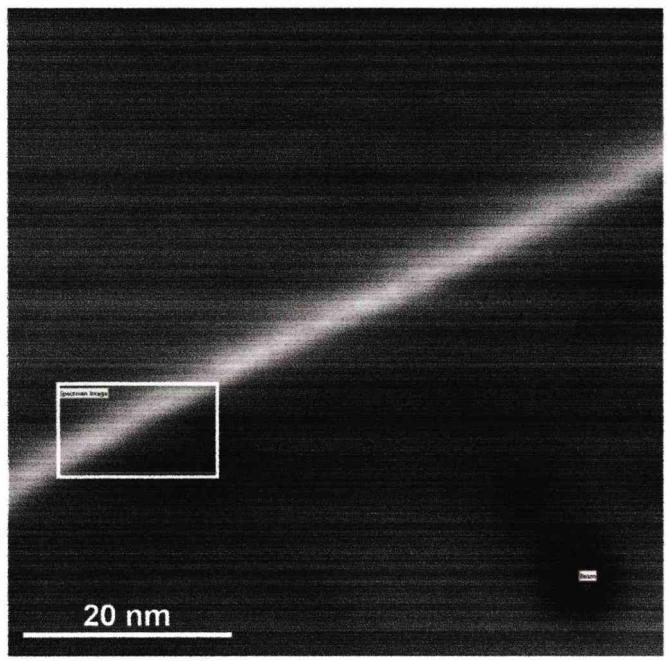

Figure 6- 5: HAADF image showing a grain boundary. The width of the boundary is ~3-4 nm.

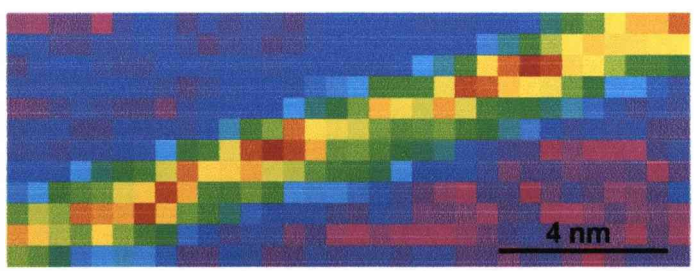

Figure 6- 6: EELS spectral image collected from the marked region in the above HAADF image. The above spectrum shows change in energy intensity when energy range window is 22.4 – 32.2 eV

It can be seen from the spectral image that the intensity distribution across the GB seems to vary from point to point. There are few regions on the GB which show higher intensity compared to the rest of the GB. The spectrum from one of the pixels on the GB was analyzed but did not show any easily identifiable edges. The other possibility could be change in thickness of the sample over the region analyzed, but still there is no pattern followed by the intensity change and hence this could be excluded. However the thickness of the specimen affects the EELS spectrum. Plural scattering occurs if the specimen thickness approaches or

exceeds the mean free path (MPF*) of the inelastic scattering process. As stated in the experimental section, plural scattering can drastically alter the observed shape of inner shell ionization edges and has to be removed before the near edge structure could be predicted. Depending upon the scattering event, for a 100 keV instrument, the MPF can be of the order 50 – 150 nm. Hence it is necessary to remove the plural scattering event from the EELS spectrum by deconvolution. The spectrum is deconvoluted using Fourier-Log deconvolution technique explained in the experimental section. Figure 6-7 shows an EELS spectrum image after deconvolution. A temperature scale is used where blue/black represent a high energy and yellow/white represent low energy. It can be seen that there is high energy loss at the GB of the mapped region.

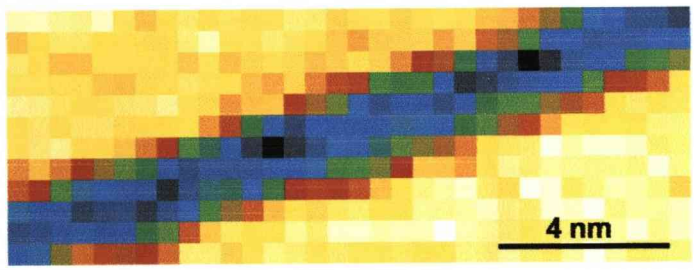

Figure 6- 7: EELS spectral image after deconvolution. The above spectral image shows change in energy intensity through the sample from 22.4 – 33.2 eV.

To see whether there was thickness variation at the GB; absolute thickness is plotted in Figure 6-8 using the function built into Digital Micrograph. It can be seen the thickness spectrum map does not show a large variation in thickness and was fairly uniform and within the range 80 – 100 nm. Again a temperature scale is used where blue/black represent a low thickness and green/yellow represent high thickness.

*Mean free path is described as the distance traveled by an electron between two scattering events of a particular class.

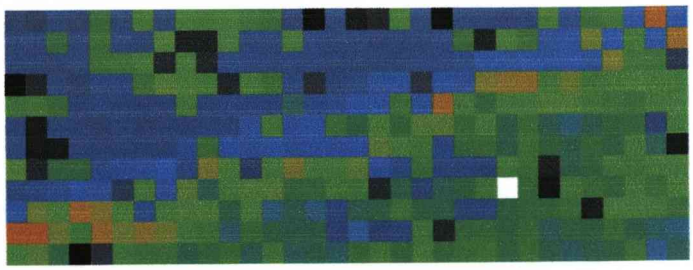

Figure 6- 8: The above spectral image shows change in thickness which is in the range of 80 – 100 nm.

As can be seen from the above spectral image, there is only a small variation in thickness from one grain to another. In the above spectrum image a white pixel can be seen which must be considered a dead pixel as the program failed for that pixel. Figure 6-9 shows a spectrum from one pixel on the GB. When the background is carefully subtracted there is a slight hint of a hafnium edge present at 31 eV. The background removal must be performed in such a way that the best possible fit to the background is obtained for every spectrum in a spectral image. The background could be seen to continuously decrease to zero and the signal is plotted in green. The edge appears at 31 eV. No clear Y edge was found, except a small peak at 26 eV and could still be under the plasmon peak.

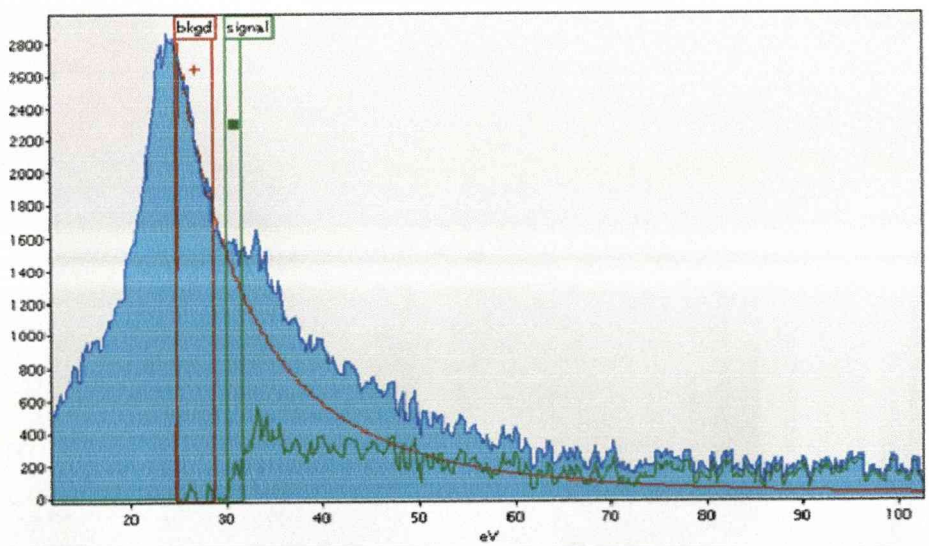

Figure 6- 9: The low loss spectrum from the GB with background subtracted.

Figure 6-10 and Figure 6-11 show the spectrum image built from yttrium and hafnium edges respectively. The Y map was plotted by selecting the signal at 26 eV for each pixel and similarly for Hf at 31 eV. A temperature scale is used where blue/black represent a high energy and yellow/red represent low energy. As can be seen from the built spectrum there is not much information available regarding the distribution of these elements and hence there was a need for further processing.

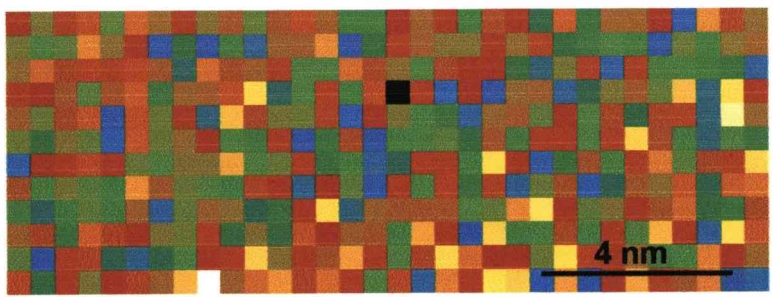

Figure 6- 10: EELS spectral image formed from Hf edge present at 31 eV. The energy window is 29 – 31.8 eV.

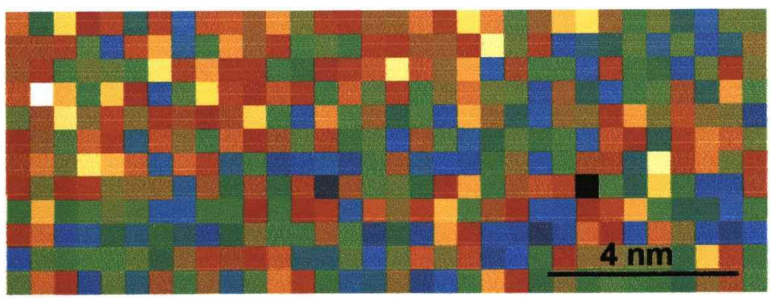

Figure 6- 11: EELS spectral image formed from Y edge present at 26 eV. The energy window is 23.6 –26.8 eV

The raw spectra obtained were further processed in stages. Firstly, once plural scattering was removed from the data, second and higher order plasmon scattering effects were deleted from the processed spectrum by Kramers-Kronig analysis. As explained in the experimental section Kramers-Kronig analysis yields Epsilon 1 and 2 with a few other quantities. Figure 6-12 shows an Epsilon 2 spectral image, which was used for further analysis. Figure 6-13 shows the resultant spectrum obtained when the processed spectrum from the grain boundary region was

subtracted from that of the bulk grain and indicates the Y and Hf contributions at 26eV and 31eV respectively. It can be seen there is increase in intensity at 26 eV and when a background was fitted, there is increase in intensity at 31 eV.

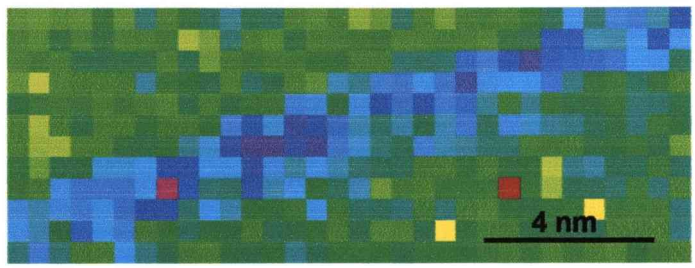

Figure 6- 12: Epsilon 2 EELS spectral image after Kramers-Kronig routine.

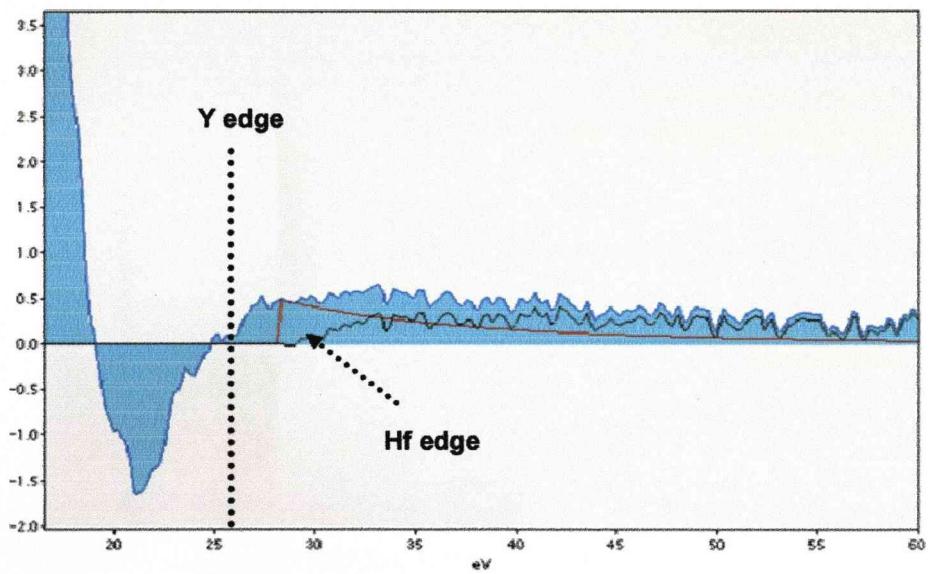

Figure 6- 13: Spectrum showing yttrium and hafnium edges when the spectrum from the GB was subtracted from one taken from the bulk.

In contrast, when a spectrum collected from the centre of an oxide grain was subtracted from that taken from another oxide grain, the resultant spectrum did not show any RE edges as can be seen in Figure 6-14. The same was found when the resultant spectrum collected from the GB was subtracted from another region on the GB as can be seen in Figure 6-15. The variation found is noise.

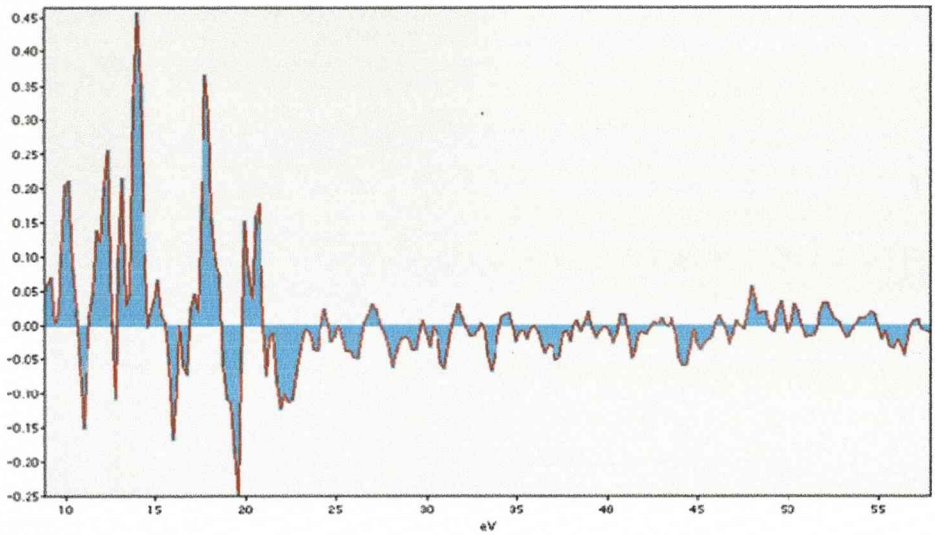

Figure 6- 14: Spectrum does not show any significant edges when one spectrum from the bulk grain was subtracted from another.

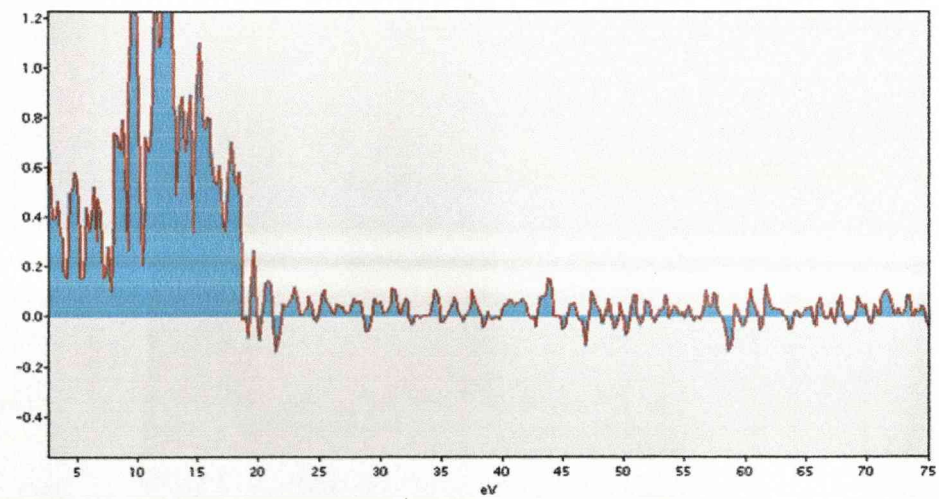

Figure 6- 15: Spectrum does not show any significant edges when one spectrum from the GB was subtracted from another.

We therefore conclude that this is a meaningful technique to reveal Y and Hf at a near vertical GB. The technique was repeated over several boundaries to verify the exactness of the technique.

Figure 6-16 shows a HAADF image of a particle, found among the outer regions of the oxide grains. The bright intensity is from the particle and at the edge of particle intensity drops gradually, indicating an inclined boundary. Figure 6-17 is the corresponding spectral image collected from the marked region. In this case a rainbow scale was used where pink/blue represent a low energy/intensity and red/yellow represent a higher energy/intensity and corresponds to a high level of hafnium. Even from the spectrum it can be confirmed that the grain boundary is spread over a large width indicated by green color in the map and the width at the boundary is about 3-4 nm. Adjacent to the particle are two grains separated by a boundary which does not show a high contrast. The particle itself is represented by red color in the colored map.

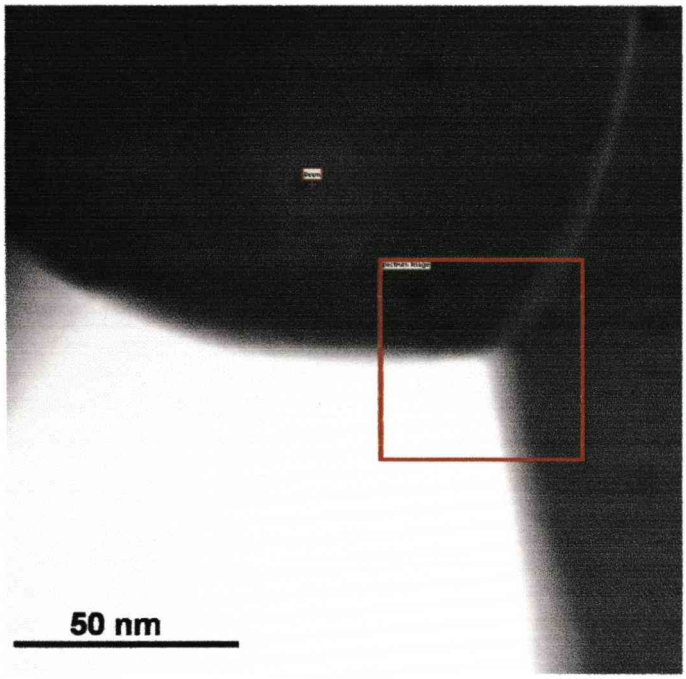

Figure 6- 16: HAADF image showing a heavier particle. The particle appears bright because it contains heavier atoms.

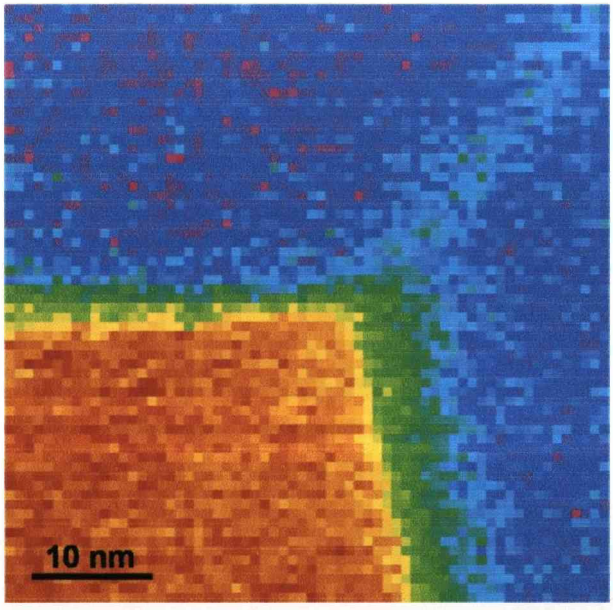

Figure 6- 17: EELS spectral image from the region marked on the above HAADF image.

Figure 6-18 is a spectrum collected from one point on the particle. Spectra from pure HfO_2 and Y_2O_3 are overlaid on top of it. The spectrums from HfO_2 are represented in blue and that of Y_2O_3 in grey and are taken from the EELS atlas. It can be said that the addition of both spectra would result in a spectrum similar to the experimental result and thus confirms the presence of hafnium and yttrium. In most of the cases mixtures of Y- and Hf- rich particles were found, they could be thought as discrete overlapping particles rather than mixed oxide particles. Figure 6-19 shows the same spectrum deconvoluted in order to compare the edges with standard EEL spectra for hafnia and yttria. It appears to be richer in hafnium than yttrium since a higher percentage of the signal from the hafnia contributes to the base spectra.

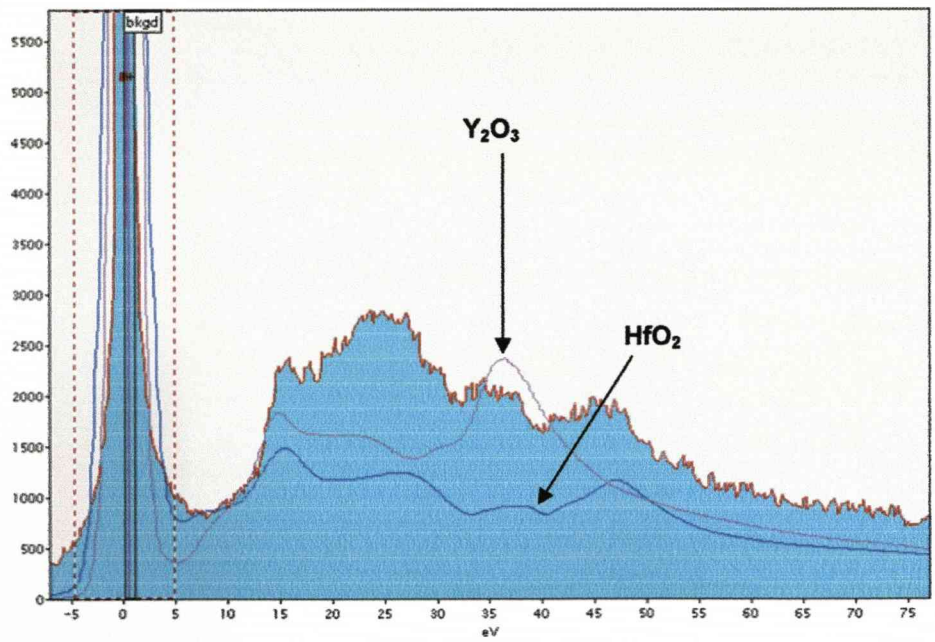

Figure 6- 18: Spectrum from a pixel in the bright region. After comparing with EELS spectrum for hafnium and yttrium there seems to be a very good match.

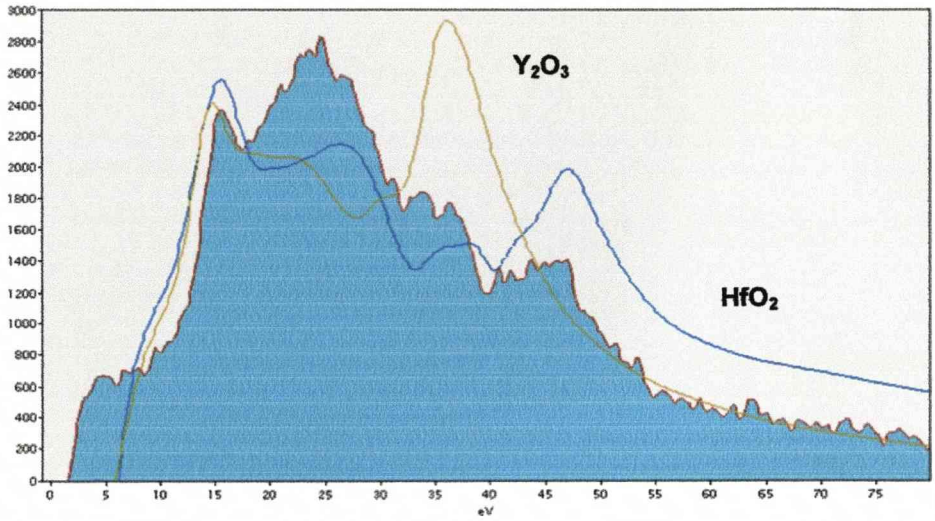

Figure 6- 19: Spectrum after deconvolution showing it is an hafnium-rich particle.

6.3.2. Identification of edges in a high loss region

In this section once again the compositional results from the EELS spectrum will be discussed but the main emphasis this time will be on the high loss region of the spectrum. Figure 6-20 shows an HAADF image of an alumina scale and a GB. The spectrum was collected from the marked region in the HAADF image and was compared with a spectrum collected from bulk. Figure 6-21 shows both the spectrum from GB and bulk overlapped but with background subtracted. The same energy window was used for subtracting the background from both spectra. The spectrum in red is from the GB and the spectrum in blue is from the bulk. As can be seen from the spectra there is a marked difference between them and edges of hafnium (Hf $M_{4,5}$), yttrium (Y $L_{2,3}$) and silicon (Si K) are observed at 1660, 2100 and 1850 eV respectively. Figure 6-22 shows spectrum from the GB in sky blue, spectrum from the bulk in green and resultant signal once the background is subtracted from the spectrum recorded from GB. A hafnium edge can be observed at 1660 eV in the spectrum shown in red from the GB, after a background fit to the spectrum. Similarly when a background is shifted to higher end, the yttrium edge could be picked up as shown in Figure 6-23.

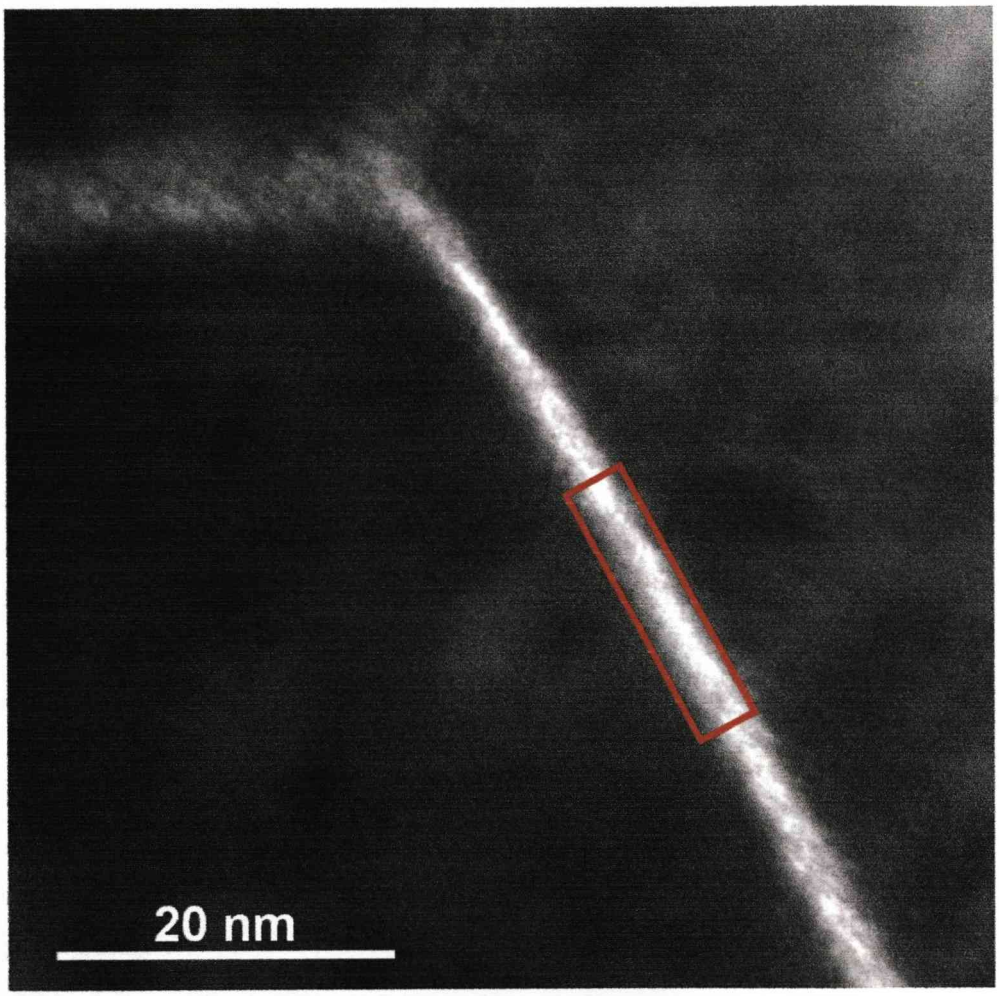

Figure 6- 20: HAADF image from alpha-alumina scale.

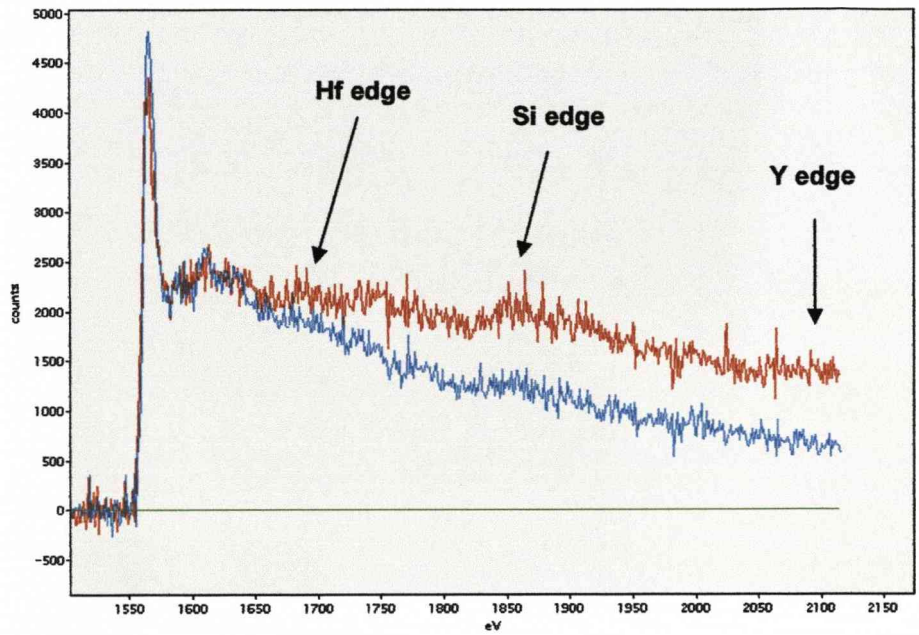

Figure 6- 21: Overlapped spectrum from the marked region on GB (red) and bulk (blue).

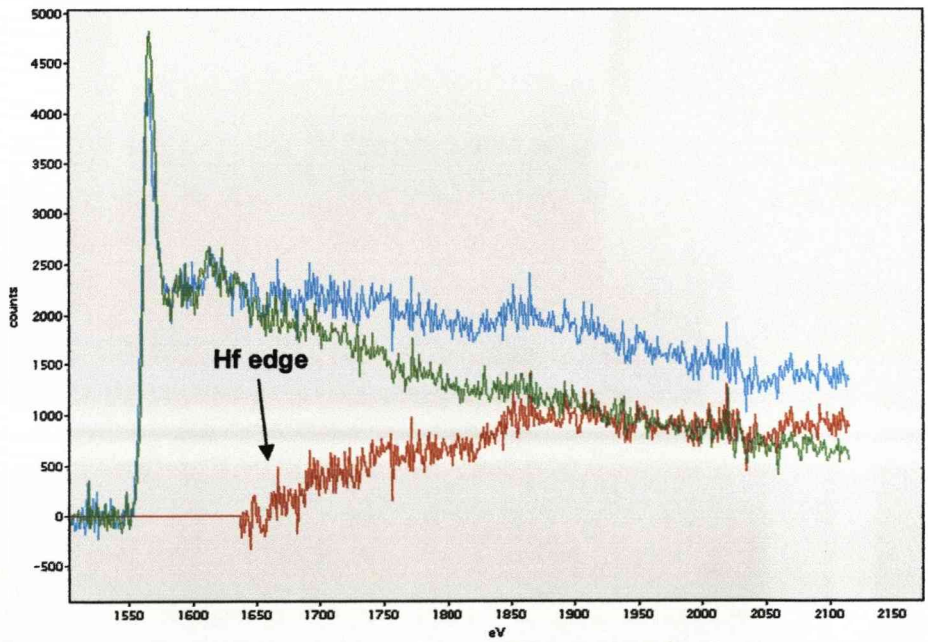

Figure 6- 22: Spectrum showing a hafnium (Hf $M_{4,5}$) edge after background removal.

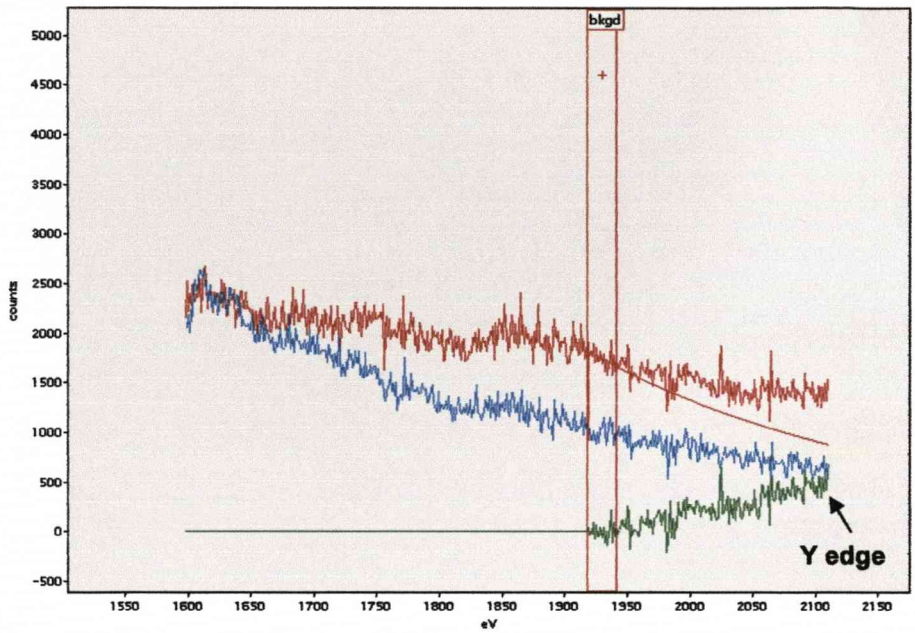

Figure 6- 23: Spectrum showing an yttrium (Y $L_{2,3}$) edge after background removal.

Figure 6-24 shows an HAADF image and a spectrum map collected from the marked region. The spectrum image intensity profile is shown in Figure 6-25. A rainbow scale was used where pink/blue represent a low energy/intensity and red/yellow represent a higher energy/intensity. Light colouration in this HAADF image corresponds to a high level of hafnium and /or yttrium. Figure 6-26 shows an hafnium spectrum image map when hafnium edge is used to form the spectrum image. As can be seen from the hafnium spectrum image intensity map, there is not a uniform distribution of hafnium along the GB. It seems to be that the Hf segregates in groups. The alumina grains appear different in colour because of slight change in the intensity, which could be due to different orientation of the grains.

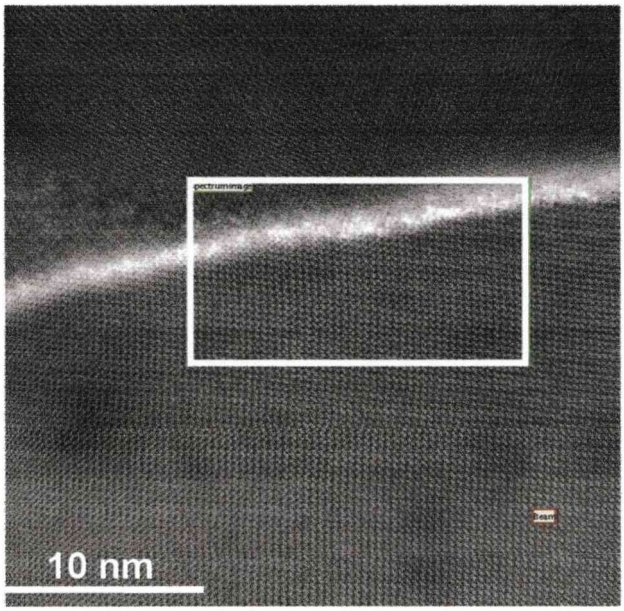

Figure 6- 24: HAADF image showing a lattice image and a GB.

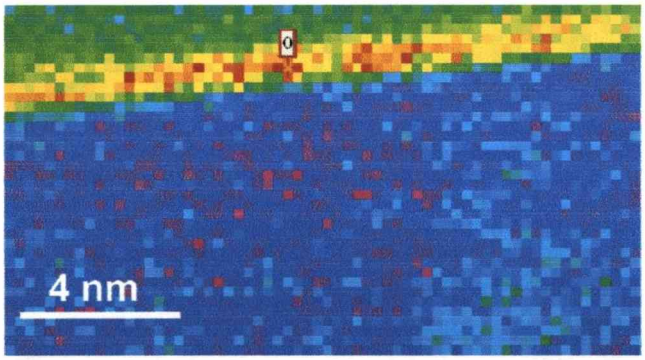

Figure 6- 25: EELS spectral image from the marked region.

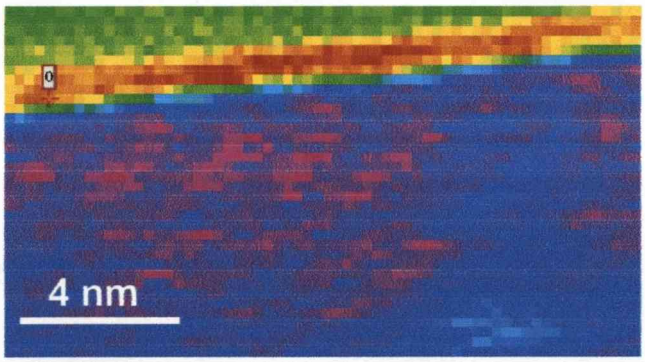

Figure 6- 26: EELS spectral image formed using hafnium (Hf $M_{4,5}$) edge.

Figure 6-27 shows a HAADF image and spectrum collected from the GB and bulk to see whether there is difference in near edge structure of oxygen. As can be seen from the HAADF image the intensity is not uniform over the whole of the GB. One of the reasons for this could be contamination with C and other could be due to beam damage associated with the sample. Contamination could be seen as the black blobs on the HAADF image and beam damage seems to modify the GB, these two effects are discussed later. Figure 6-28 shows the overlapped spectra from the GB and bulk. The oxygen (O K) edge is similar in both spectra. The EEL spectrum was collected from the single spots marked on the GB and bulk. The spectrum from GB is in green and the spectrum from bulk in red. A small pre-peak is observed in the spectrum from the GB which is from Ti.

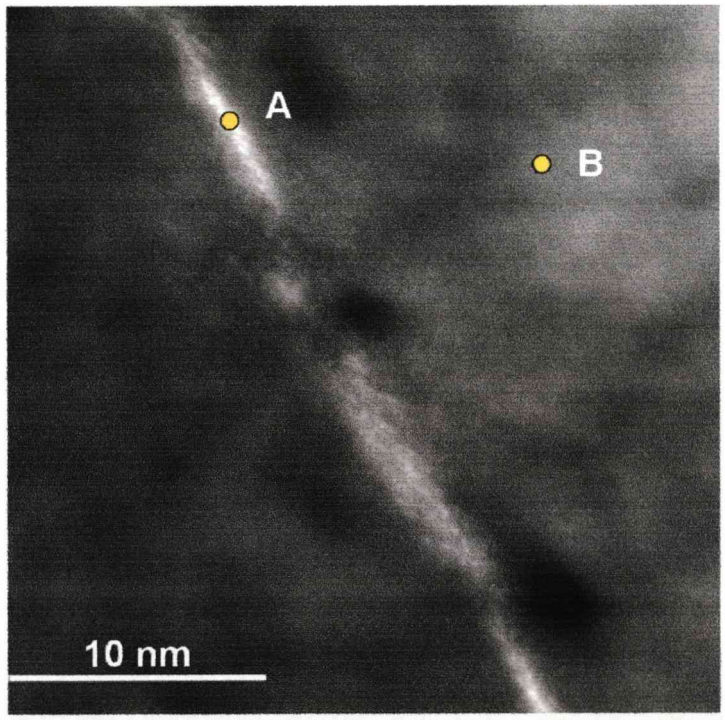

Figure 6- 27: HAADF image of alpha-alumina scale.

Cr $L_{2,3}$ edge is observed at 575 eV in the bulk whereas not at the GB. Fe $L_{2,3}$ edge is found at 700 eV in the bulk as well as the GB.

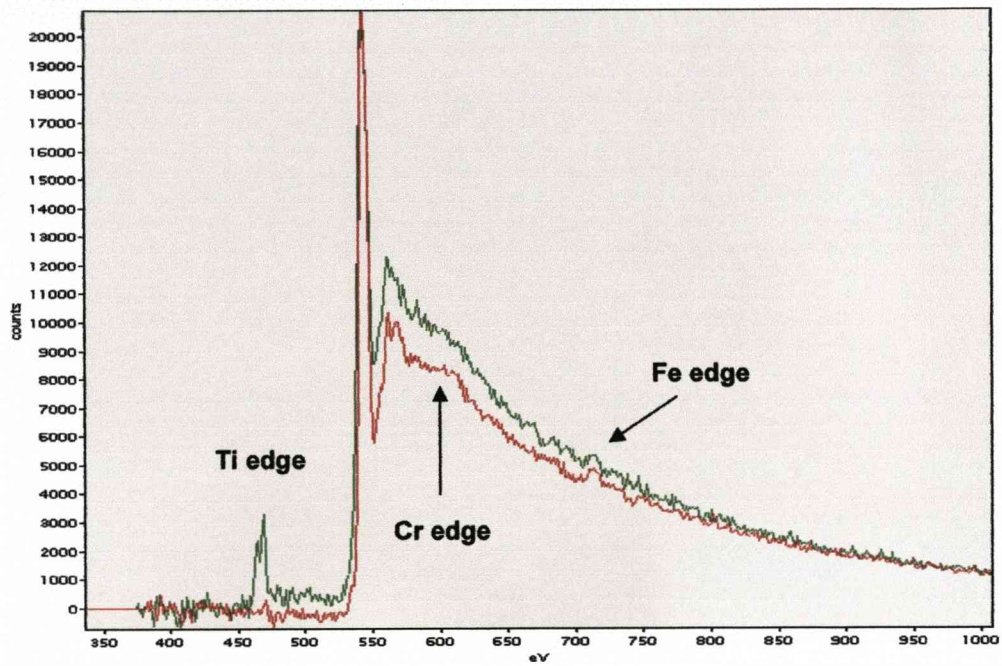

Figure 6- 28: Overlapped spectrum collected from a point A (green) on GB and B(red) from bulk.

6.3.3. Lattice imaging

The HAADF images shown in Figure 6-29 are lattice images of alumina grains separated by grain boundaries. Both the grains are oriented to the same zone axis, except one grain is twisted with respect to the other. As can be seen, there are bright individual spots in some areas on these grain boundaries. The bright spots could be due to heavier elements or ions present on these sites, scattering strongly into the detector, although some of the contrast changes could also be due to strain and thickness effects. Figure 6-30 shows a blown-up view of the GB with the bright individual spots distributed all over it, close to the boundary.

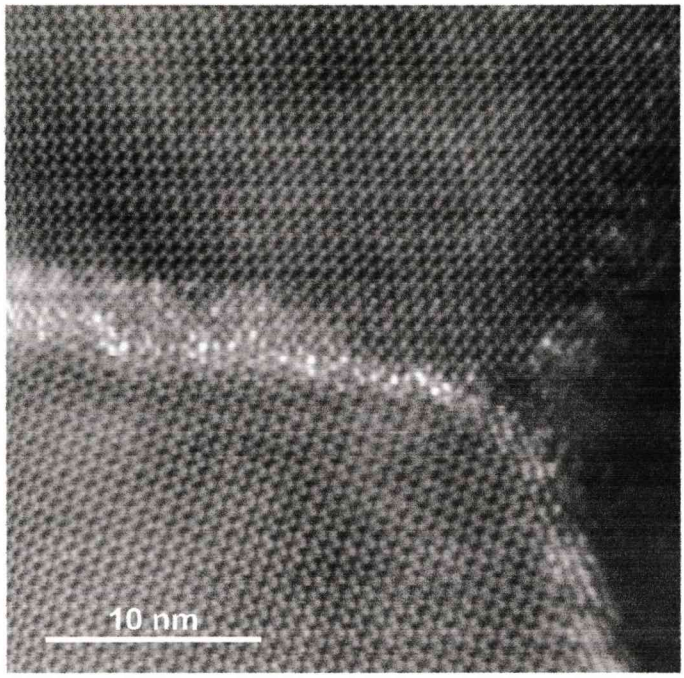

Figure 6- 29: Lattice image showing a triple point in the oxide scale and bright spots distributed across it.

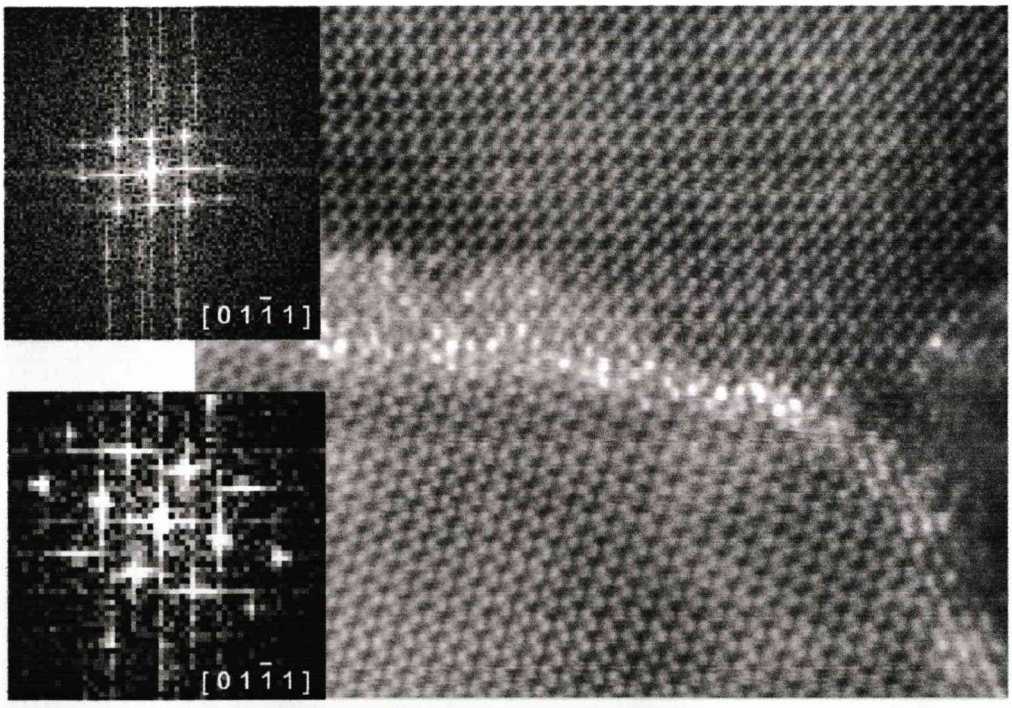

Figure 6- 30: Blown up image of the above HAADF image and corresponding Fourier transform, which was used for indexing.

Figure 6-31 shows an HAADF image of an oriented alumina grain and bright spots distributed across the GB. The bright spots are spread over a few nanometres, but this could again be due to the fact that grain boundaries are inclined to the beam. Unfortunately the optimum contrast conditions used to view the bright spots also coincides with the conditions, which maximize the intensity changes due to minor instabilities in the electron gun. Hence the horizontal lines in the micrographs

Figure 6-32 shows a blown-up view of the bulk of the alumina grain. Blue spots have been laid on the blown-up image to show the hexagonal pattern and the grain is oriented to the [0 1 -1 1] zone axis.

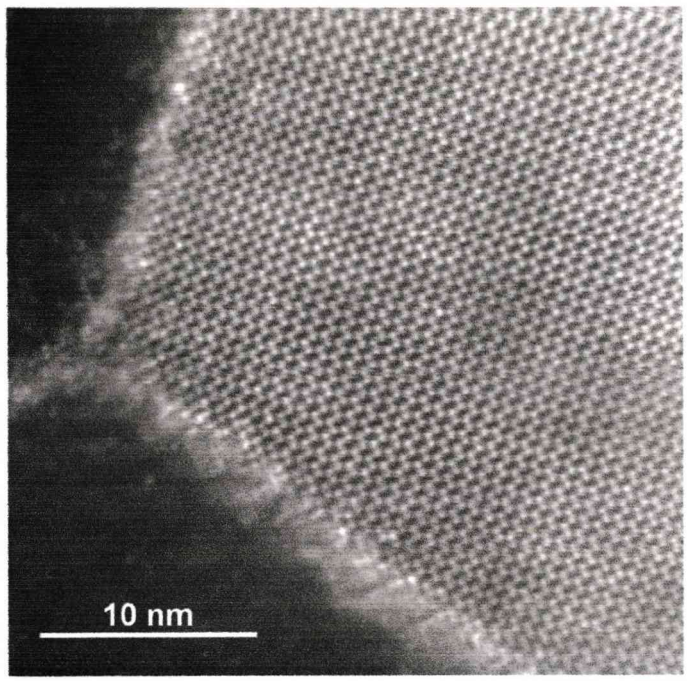

Figure 6- 31: Lattice image showing a triple point in the oxide scale and bright spots distributed across it.

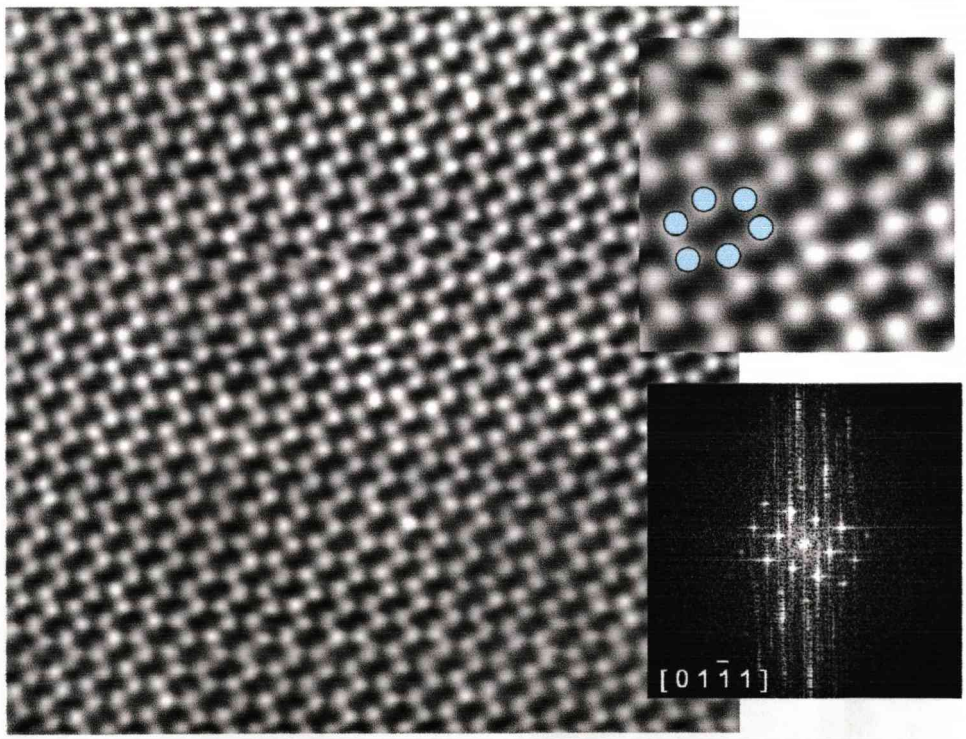

Figure 6- 32: Blown up image from the bulk of the grain and a Fourier transform.

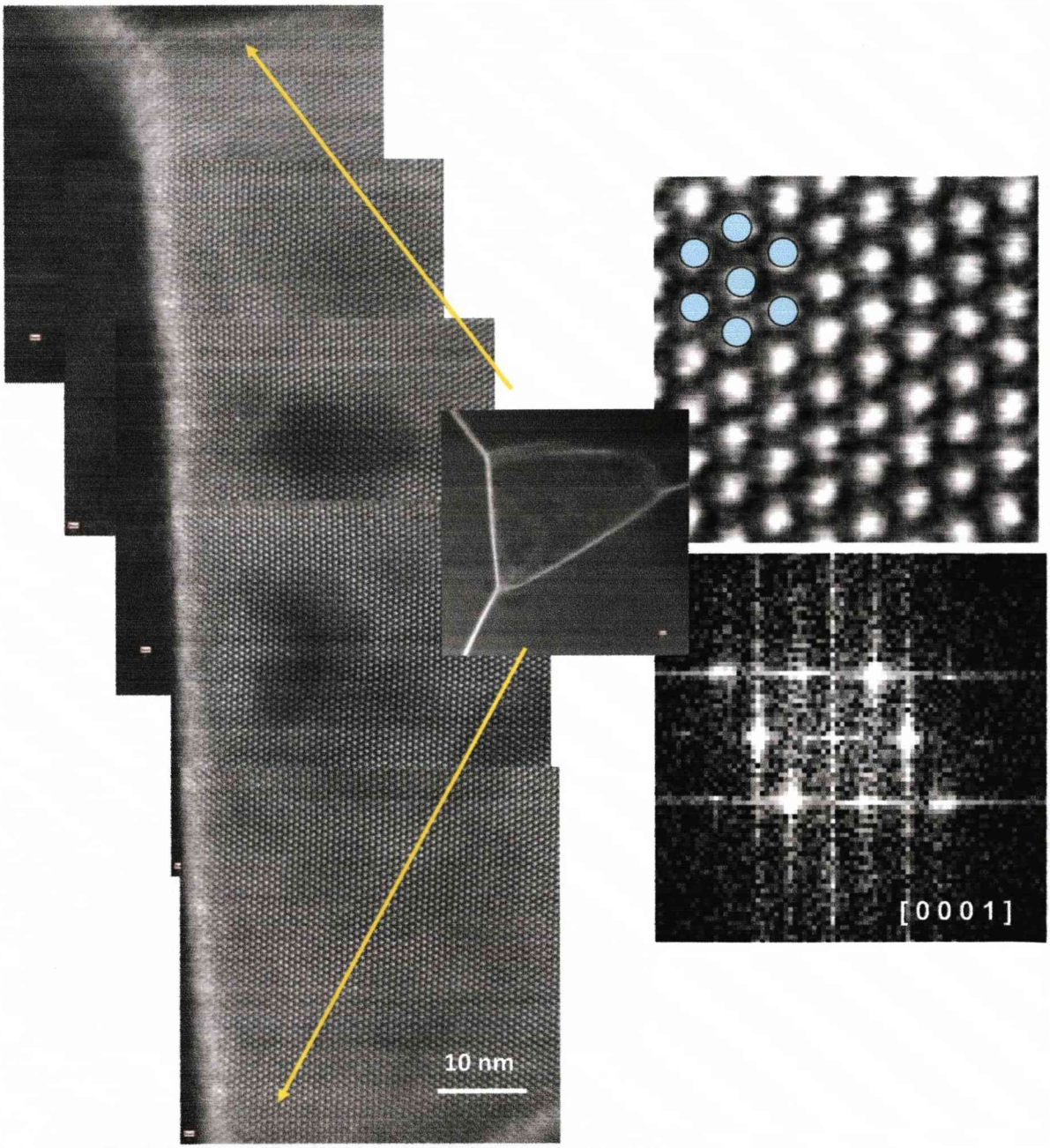

Figure 6- 33: Montage of lattice image showing the GB with bright spots distributed all over it. Blown-up of the bulk showing spots forming a regular hexagonal pattern and a Fourier transform.

Figure 6-33 shows montage of lattice images covering the whole boundary and the distribution of bright spots over it. The blown-up image shows regular hexagon showing it to be oriented on the C-axis. The alumina grain is oriented on the [0 0 0 1] zone axis.

It was not possible to collect the spectrum from one of these bright spots, because of the damage caused by the electron beam. Hence instead of collecting from a single bright spot, the electron beam was moved manually over different bright spots and spectra collected. Another way to reduce damage was by collecting a spectrum from each bright spot for a short exposure time and summing over the entire spectra collected. Hence a composite spectrum was collected by moving the beam manually over the region. The spectral image was analyzed and again hafnium (Hf $M_{4,5}$) and yttrium (Y $L_{2,3}$) edges could possibly be identified.

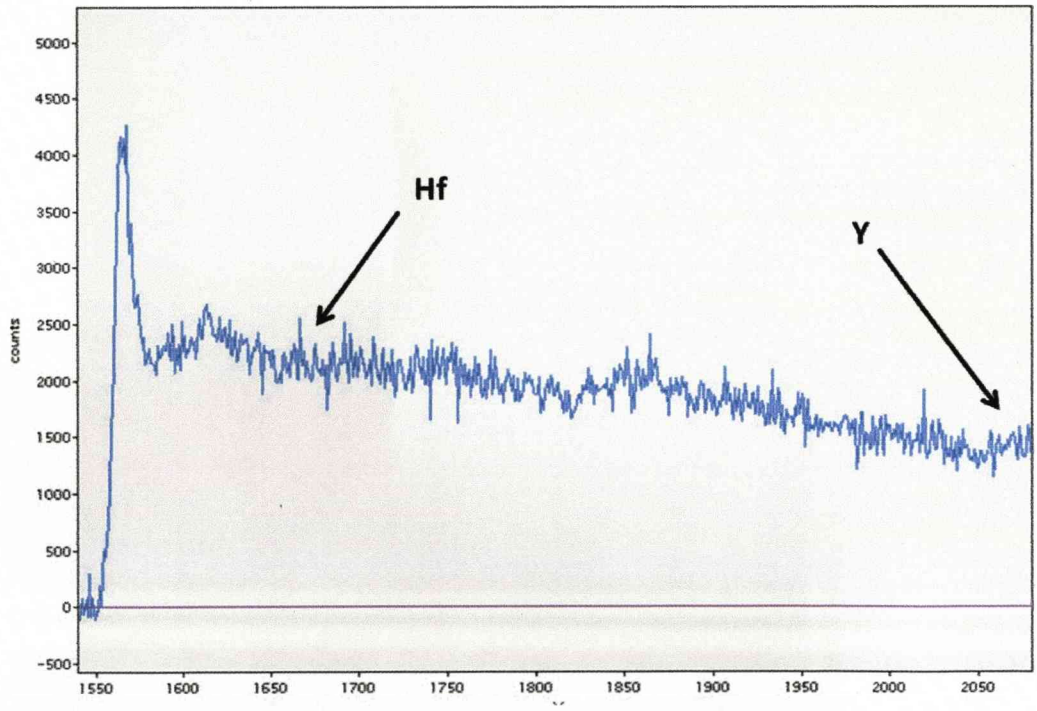

Figure 6- 34: The spectrum showing Hf and Y edges coming-up on the spectrum.

6.4. Factors affecting the energy loss spectrum

In this part factors which affect the energy loss spectrum are looked at, namely the effect of specimen thickness and contamination of the specimen. The low loss region of the EEL spectrum contains a great deal of information. Contamination can, however, alter the observed spectrum, especially if carbon is present, as it has several broad peaks in the low loss region around 30 eV. Hence it is important to monitor if carbon is present and whether the sample is getting contaminated as there is often a build-up of carbon during acquisition.

6.4.1. Thickness effects on the energy loss spectrum

The thickness of the specimen that the electron beam has to pass through affects the EEL spectrum. If the specimen is thick, plural scattering will take place. The plural scattering is often removed from the EEL spectra by a Fourier-Log deconvolution and it is therefore not a problem as long as there is still a significant contribution from single scattered electrons and the spectra has a high signal-to-noise ratio. Figure 6-35 shows an HAADF image and its absolute thickness has been calculated to be 80 ±10 nm using the EEL spectrum. Figure 6-36 shows the same region after about 10 -15 scans. It can be seen there is not much difference in the positions and intensities of the bright spots.

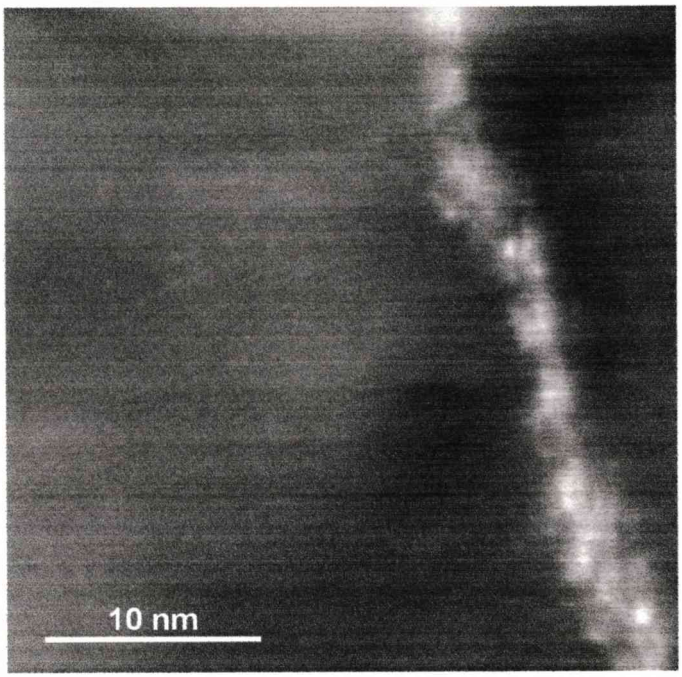

Figure 6- 35: HAADF image from an region of scale which is 80 – 100 nm thick.

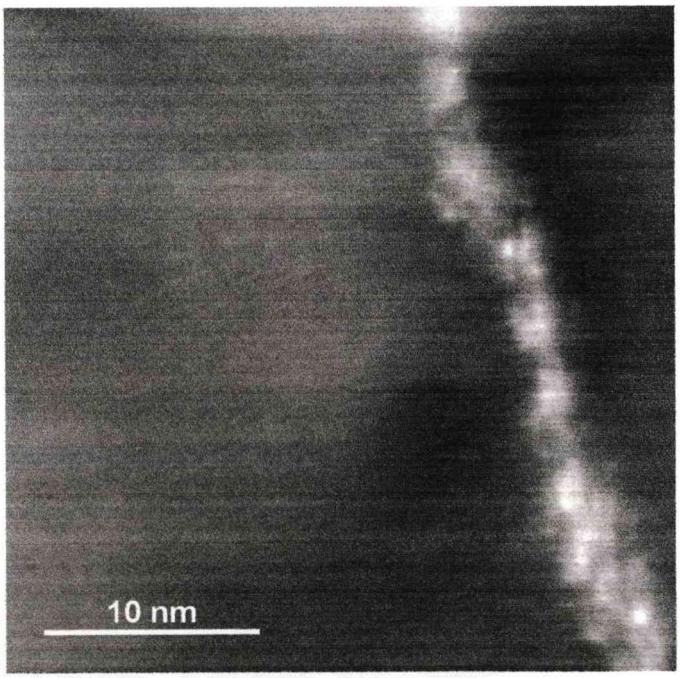

Figure 6- 36: HAADF image from the same region after 10 - 15 scans.

However, if the specimen is too thin it can cause other problems such as the introduction of surface plasmons into low energy EEL spectra. As was seen when the specimen thickness falls below ~30 nm there is also GB modification. Figure 6-37 and Figure 6-38 show an HAADF image from the same region, one image from the first scan and a second one recorded several scans later. It can be clearly seen from the second HAADF image that there is a redistribution of the bright spots around the GB.

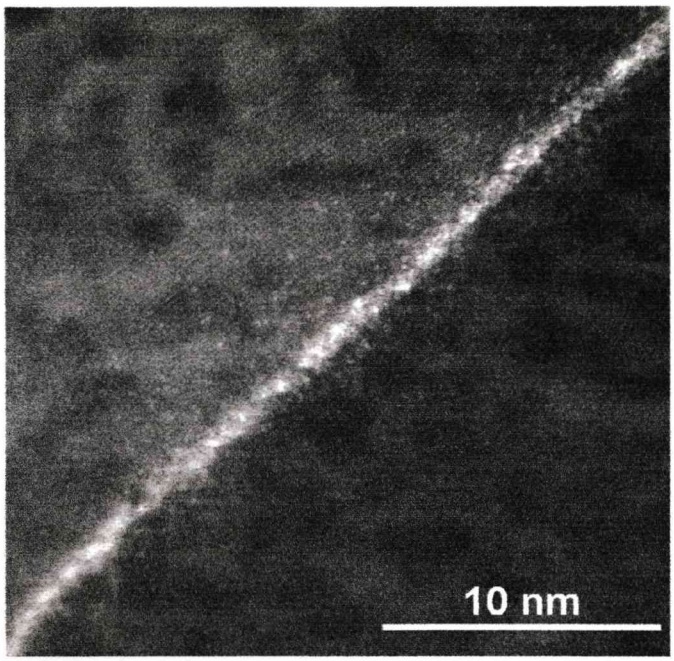

Figure 6- 37: HAADF image from a very thick region near the hole in a TEM specimen.

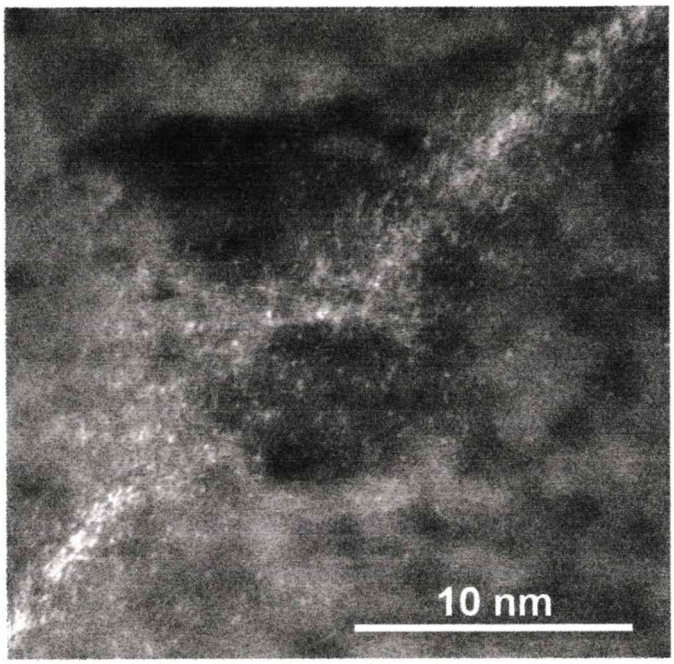

Figure 6- 38: HAADF image from the same thin region showing redistribution across the GB.

6.4.2. Contamination during energy loss acquisition

Carbon contamination is predominant in the electron microscope; even in the high vacuum of the SuperSTEM carbon migration to the beam forms deposits. This is due to the intensity of the focused beam at the specimen.

Figure 6-39 shows an HAADF image of an alumina scale contaminated wherever the beam was located on the sample.

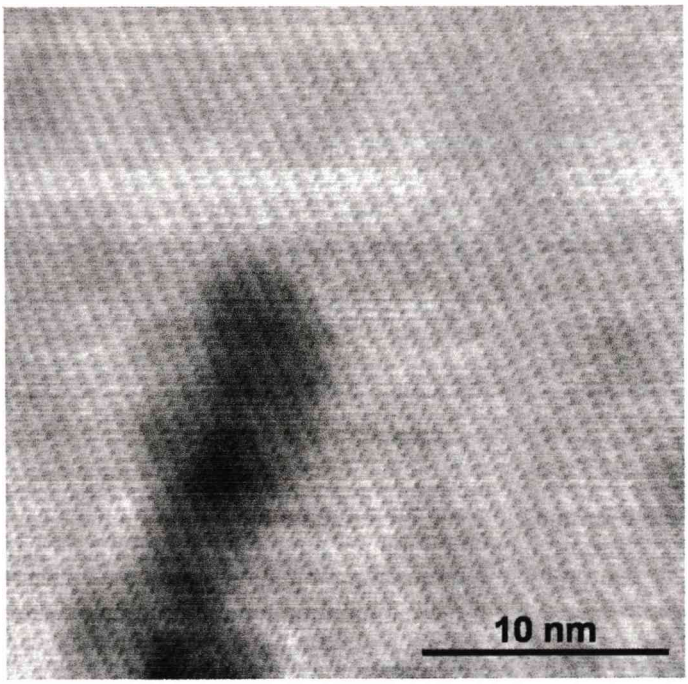

Figure 6- 39: HAADF image from a sample, the dark area was contaminated with carbon by stationary beam.

Chapter 7

Discussion

7.1. Discussion

The discussion chapter consists of three sections. Section one mainly deals with the cyclic oxidation test and the contribution of reactive elements to oxidation mechanisms. The segregation of reactive elements to the oxide-grain boundaries is discussed in section two along with the formation of reactive element-rich oxide particles near the scale-gas interface. Finally, section three discusses the segregation of reactive elements as observed in an aberration corrected scanning transmission electron microscope.

7.2. Cyclic oxidation tests

The high temperature oxidation behavior of commercial FeCrAl and model alloys has been studied quite extensively[5, 40, 63, 118, 127, 131, 150-152]. The cyclic oxidation data obtained for the model alloy M11 and commercial alloy Kanthal A1, as shown in Figure 5-1 show that the alloy M11 (FeCrAl+Y+Hf+Zr) has a higher mass-gain rate compared to the commercial alloy which only has zirconium as a RE additive. The dips in the mass-gain curve show regions were spallation takes place. This confirms similar findings obtained previously[13]. Metallographic observation of the scale revealed in Figure 5-2, showed much more spallation from Kanthal A1 compared to that of the Model alloy M11. The spallation in the Kanthal A1 sample seems to be taking place within the oxide scale as could be seen from the SEM micrographs. Oxide scale is observed below the spalled region, which may have formed after spallation or may be due to spalling within the oxide. Different spallation mechanisms can be argued; firstly the spallation may take place at the metal-oxide interface and subsequent oxidation takes place at the surface, and needs to be analyzed further. Secondly, one of the mechanisms could be the formation of zirconia particles near the equiaxed zone, below the gas-oxide interface and spallation taking place at those sites due to built-in stresses[153]. It has been observed that the addition of zirconium prevents the negative effects of carbon apparently by tying up the carbon impurity into more stable carbides. Zr is rapidly incorporated into alumina scale thereby modifying its

microstructure by reducing the oxide grain size as well as by the formation of zirconia precipitates and nano-porosity[12, 13, 153]. Rapid incorporation of Zr into the alumina scale leads to an early exhaustion of the Zr reservoir and thus a loss of Zr effect or RE effect on scale microstructure after long exposures. Some authors found that the alumina scale possesses an increased density of oxygen paths which resulted in an increased oxidation rate initially due to the presence of in-scale porosity[153].Any of these could have affected the spallation mode and need to be studied further in order to understand the spallation mechanism associated with these alloys. Pint et. al found that alloys with only Zr as an additive resulted in formation of oxide intrusions or oxide pegs, which created a convoluted metal-scale interface[45, 154]. This may also enhance the driving force for the spallation of oxide scale at the metal-oxide interface and thus support the second argument of scale spallation. There were large numbers of cracks found on the Model alloy (M11), as shear stresses created by thick scales are sufficient to cause cracking through the oxide scale and the scale may spall by further propagation of cracks along the smooth interface. This scale did not show any signs of spallation and would suggest that the metal-oxide surface was a flat adherent surface.

7.3. Scanning Transmission Electron Microscope and EDX

The combination of high resolution STEM and EDX were used to show the presence of RE at the GB and the boundaries associated with the particles.The segregation of reactive elements along oxide grain boundaries in co-doped alloys has been reported before in the literature[13, 98, 109, 124, 155]. It has been speculated that RE ions segregate to defect sites along the grain boundaries.

It is known through the literature that the alumina scale grows by either or both inward diffusion of oxygen through the oxide and reacting at metal-oxide interface or by aluminum diffusing out through the oxide and reacting at the free oxide-gas interface, when no reactive elements additives are present in the alloy. But when reactive elements are present, the second

mechanism, i.e. the oxidation mechanism, is modified and oxide scale grows predominantly by inward diffusion of oxygen through the scale. Pint et. al suggested a model to explain the effects associated with the addition of the reactive elements that was based on the segregation of reactive element ions to the scale grain boundaries and metal-oxide interfaces[63, 116, 117]. Interfaces have been shown to be used by reactive element ions as a pathway for diffusion from the substrate to the gas interface of the oxide scale. An oxygen potential gradient across the scale is the driving force for this type of outward diffusion. This type of segregation of reactive element ions to the grain boundaries can be explained by the dynamical theory of segregation. The fundamental postulate of this theory is that certain large oxygen active elements present in the alloy diffuse toward the scale-gas interface as a result of the oxygen potential gradient in the metal-scale-gas system [49, 99, 156-158]. Figure 7-1 shows the schematic diagram of the diffusion path of RE ions across the oxide scale along the grain boundaries. The RE's from the bulk diffuse through GB to the interface and then into the oxide scale through the GB's. RE-rich particles are usually found near oxide-gas interface.

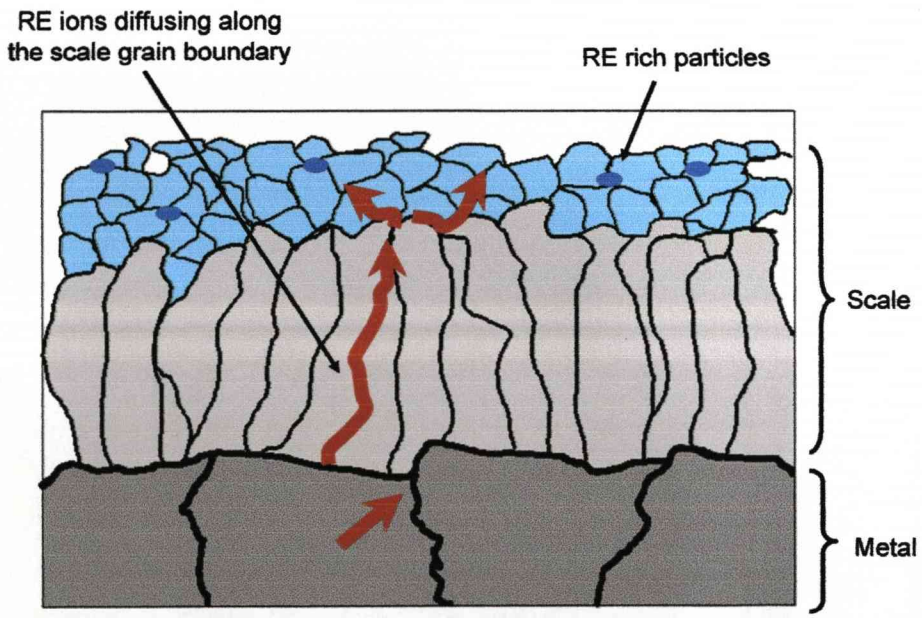

Figure 7- 1: Schematic of the observed outward diffusion of RE ions along scale grain boundary during high temperature oxidation

To analyze different aspects of RE segregation, plan view TEM samples were prepared and depending upon the region to be analyzed, i.e. outer most regions of equiaxed grains or somewhere in the columnar region, samples were thinned accordingly using PIPS. The thinned samples were analyzed in STEM using EDX for elemental analysis.To analyze a large area, usually elemental mapping was carried out, which showed the presence of particles which were made up of Y and Hf, as was observed in Figure 5-10, 5-11 and 5-12. The particles were usually present in the region near to gas-oxide interface and they were found to increase in number with the passage of time or temperature. When X-ray maps were collected from grains and grain boundaries present in the equiaxed regions, they showed reactive elements segregated to the grain boundaries (Figure 5-8 and Figure 5-9). There were particles present at the grain boundaries which were rich in reactive element/elements. Sometimes the signals showed that the particles were rich in hafnium and or yttrium and a few particles were only rich in hafnium. When the particles were rich in both Hf and Y, it is still not clear whether the particles were mixed oxides of yttrium and hafnium or separate oxides of yttrium and hafnium. Hence it could be argued that when both Y and Hf signal were present, the particles were lying one below the other, i.e. yttrium oxide on top of the hafnium oxide or vice versa. But this could be contradicted by the fact that both the Y and Hf maps showed the same particle shape and size and hence could be a complex of Y-Hf-O. It was found that the O signal dropped in the region of the particle compared with the surroundings, normally indicating a lower O content. Figure 7-2 shows the concentration of different elements present in five different regions in five different particles that were selected at random, the spectrum analysis was carried out on a fixed volume each time, assuming the thickness of the sample did not change. It was found that the particles contained 60 – 65 atomic percent of Hf, 12 – 15 atomic percent Y, about 12 - 16 atomic percent of O, which is considerably less than the 55 – 65 atomic percent O found in the bulk and at the GB's; the particles also showing very little Al (about 1-3 atomic percent).

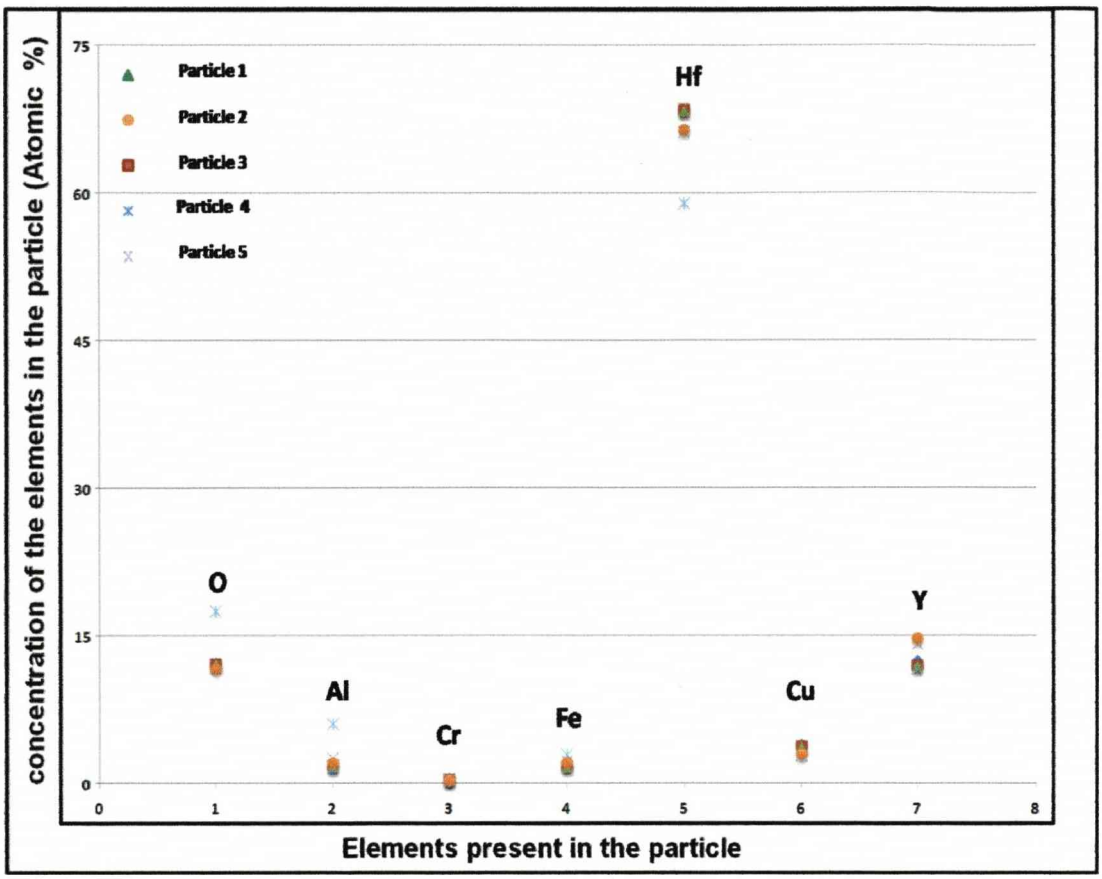

Figure 7- 2: Concentration of different elements present in the particle.

An approximate empirical molecular formula was calculated using the data above, and was (5 Hf, Y) O_2. Calculating mole fractions using the this atomic percent leads to an approximate value of 80-85 mole percent HfO_2 and 15-20 mole percent Y_2O_3 with Al_2O_3. The results from the X-ray analysis of the particles in Figures 5-10, 5-11 and 5-12, shows that most of the time the particles were rich in Hf and Y with very little Al, which enforces the possibility that the particles are a mixed phase oxide of Hf and Y . EEL spectrum obtained from the particle also supports the possibility of a mixed phase oxide.

In order to understand the stability of the particles and the phases present, the equilibrium ternary phase diagram for HfO_2, Y_2O_3 and Al_2O_3 at 1100 °C must be considered (Figure 7-3)

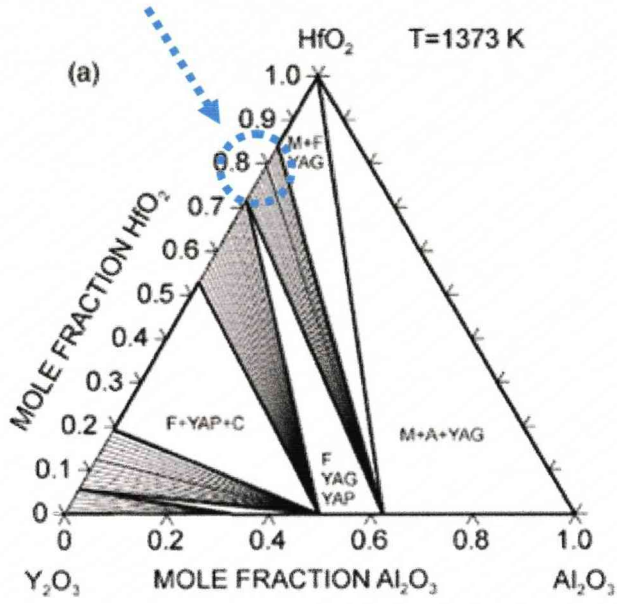

Figure 7- 3: Isothermal section for HfO_2-Y_2O_3- Al_2O_3 system at 1100 °C[161].

As we know (Figure 7-2) that there was hardly any Al in the particle, the composition must lie in the region marked by the blue dotted circle on the ternary phase diagram.

In order to understand the different phases present and relate these to the ternary diagram it is worthwhile considering the HfO_2 and Y_2O_3 binary phase diagram, keeping in mind that whatever exists in these particles has to form in the presence of alumina.

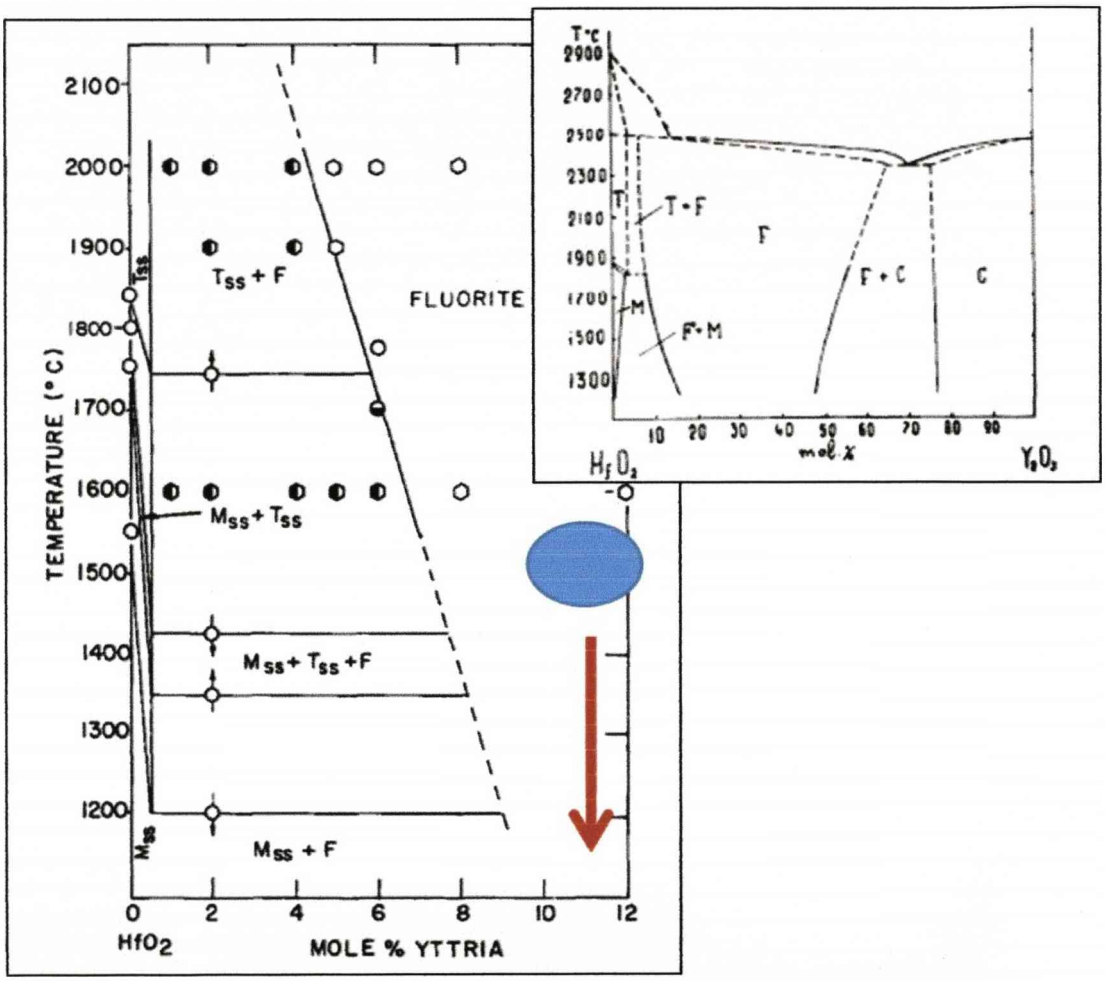

Figure 7- 4: Hafnia-rich region of tentative Y_2O_3-HfO_2 phase diagram[126].

The blue oval, in Figure 7-4, represents the region on phase diagram were the composition of the Hf – Y RE rich particle is most likely to lie. The binary diagram shows that the most likely structure is fluorite, but the ternary diagram shows that this should be in equilibrium with YAG not alumina. This may be due to the presence of a thin layer of YAG around the particle that was not detected, and that the YAG layer is in contact with the alumina, or that the phases present are metastable rather than stable. This metastable form may be present if it is easier to nucleate or if the surrounding oxide makes it easier to grow.

Hafnium and yttrium were also found to segregate to the oxide grain boundaries. The thicknesses of the grain boundaries on which the Hf and Y have segregated seem to be a few nanometers in width. Most of the time the width of the GB's were comparable with peak widths in the Line Scan, as observed in Figure 5-18 to 5-35 hence indicating that the segregation was limited to the GB's and not to the bulk in the vicinity of the boundary. However it is not possible to determine accurately the width of these boundaries as they might be slightly inclined or curved. Line Scan data were collected from a number of boundaries and analyzed by EDX. It was found that the concentration of reactive ions varied from boundary-to-boundary and there was not a good correlation between the Hf and Y segregating to different boundaries. The Line Scan data were quantified for Hf and Y weight percent over the GB and plotted against each other as shown in the Figure 7-5. There was a limited correlation on a few boundaries but mostly showed no correlation between Y and Hf concentration.

Some of the scatter in the above figure could be due to experimental errors associated with the state of the microscope, as the data was recorded over a period of time and not in a single sitting. The shaded area represents the region were most of the points lie.

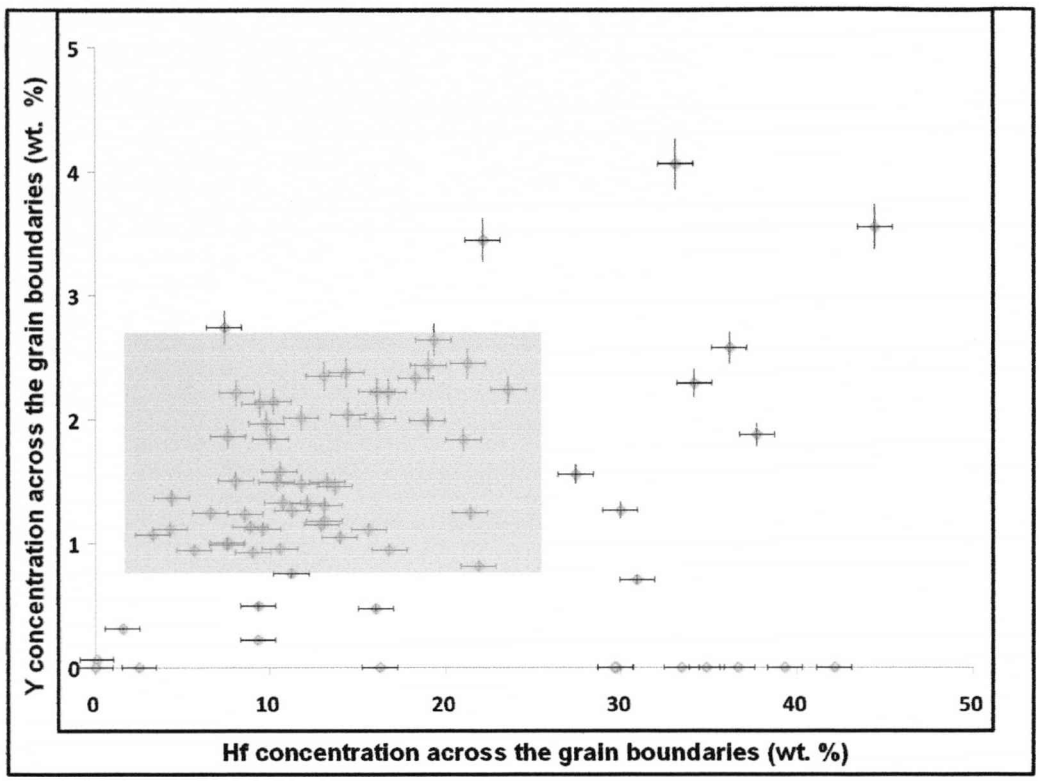

Figure 7- 5: Graph showing the distribution of yttrium vs. hafnium, and as can be seen not a strong correlation exits.

When the Line Scan data were compared with segregant particle size, a correlation was observed; i.e. as the particle size grows the reactive element concentration at the boundaries directly connected by these particles showed a lower amount of segregant. The problems associated with quantification of these line scan data was, firstly, deciding the actual peak width and its relationship to boundary width signal coming from the boundaries. Secondly there was not an accurate technique for subtracting the background or instrumental noise from the line scan.

Hence a new method was sought and analysis repeated across different grain boundaries connected via large/small particles or away from particles. Instead of collecting a line scan, spectra were collected from a fixed cross-sectional area at the boundaries for duration of 200 seconds. Assuming that the thickness was quite uniform over the whole of the oxide scale, the analysis led to a better statistical result. The results obtained were on similar lines to the ones obtained through Line Scan analysis. The GB's connected to large particles did not show presence of Hf or Y or was below detectable levels, whereas the GB's connected to smaller particles showed different levels of Hf and Y.

7.4. The Segregation Model

The results from the X-ray Line Scans and spectrum analyses, of particles in the region of equiaxed grains near the gas-oxide interface, show that the GB's connected to large particles have very low levels of Y and Hf present, whereas GB's connected to smaller particles have higher but varying amounts of Y and Hf. The transient oxides are formed initially, but with longer oxidation times the columnar grains grow and during this time the RE's appear to build up at the GB's. At some point nucleation occurs from the saturated or supersaturated boundaries, leading to the formation of the observed particles just below or within the equiaxed grains. What is not observed are RE oxides at the gas oxide interface, which is somewhat surprising, as this would seem the easiest place for nucleation. This may be an effect of oxygen partial pressure on precipitate nucleation, that the particle nucleate during the formation of the transient stage or that some regions within the transient scale form special interfaces that lower the energy barrier for nucleation .

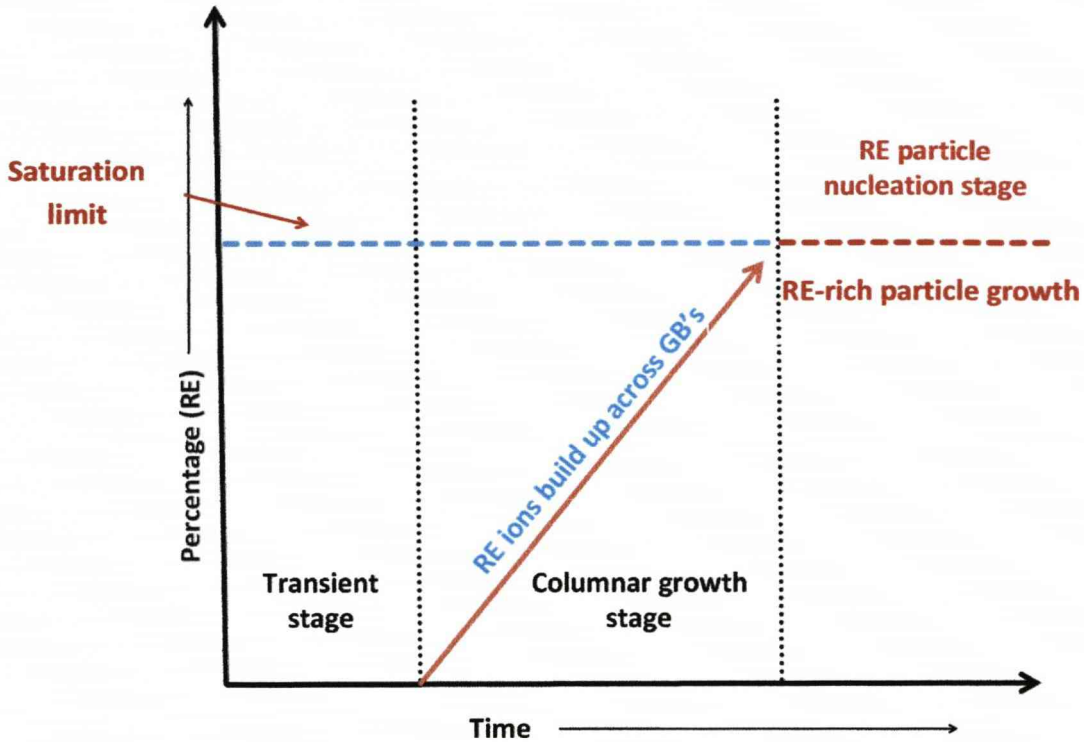

Figure 7- 6: Schematic of RE ions starts build-up after transient stage and continues till a saturation limit is reached at the grain boundaries.

The behaviour observed can be explained by a number of possible different mechanisms. The first mechanism, by Pint et al is based on the supersaturation of the GB's with RE with time, leading to the nucleation of RE-rich particles and then to their growth by absorbing RE by GB diffusion. Figure 7-6[49-51, 53, 54, 117, 162-166] shows a schematic of this process with the development of the transient stage followed by the buildup of RE within the oxide before nucleation occurs and the RE rich particles grow. However, the only way supersaturation normally occurs is when the temperature drops possibly during cooling of the sample. If it is assumed that the oxide scale is saturated during oxidation it will become supersaturated on cooling and the RE-rich particles nucleate. This would however create particles with no RE in the surrounding GB's, which is not what was observed as different amounts of RE were observed in the boundaries near small and large particles.

Pint et. al., concluded that RE ions become incorporated into RE-rich particles because this is a lower energy state than as a boundary segregant but they do not explain why they diffuse out through the oxide as this is also true near the metal/oxide interface. This mechanism fails to explain why the reactive elements do not form oxides at the metal/oxide interface. They form more (thermodynamically) stable oxides than aluminium and in a similar way that chromia forms at the metal/oxide interface under the iron oxide, in Fe-20Cr, the reactive elements should be able to form at the metal/oxide interface. Thus, thermodynamically the reactive elements are 'supersaturated' even at the metal oxide interface, as they are above the concentration that should produce precipitates. However, they do not form precipitates and instead they diffuse through the scale before reacting, and this is probably because the critical free energy for nucleation of the reactive element oxide phase at the metal/oxide interface (or in the alloy) is too high. However, they can nucleate in the outer part of the scale possibly as an effect of the transient oxidation process.

Another mechanism for the growth of the precipitates in the outer scale is based on the development of activity gradients along the oxide grain boundaries between large and small particles. The RE-rich particles formed in the growing oxide scale during the transient oxide growth stage, will tend to be larger than those formed later on and as such will be more stable. The common tangent construction shows that the stability of a precipitate affects the composition of the grain boundaries and bulk that surrounds it and this lead to the formation of activity gradients that drive diffusion. This is the process of Ostwald or precipitate ripening.
Figure 7-7 shows a free energy versus composition diagram and shows that the free energy of the particles affects the local composition of the surrounding material, which in turn drives diffusion that controls whether particles grows or shrink. Thus, any small Hf/Y oxide particles that form in the matrix or lower scale would tend to disappear as the more stable particles grow by Ostwald ripening and this mechanism would lead to higher concentrations of RE in the

boundaries near small particles and low concentration near large particles as was observed experimentally.

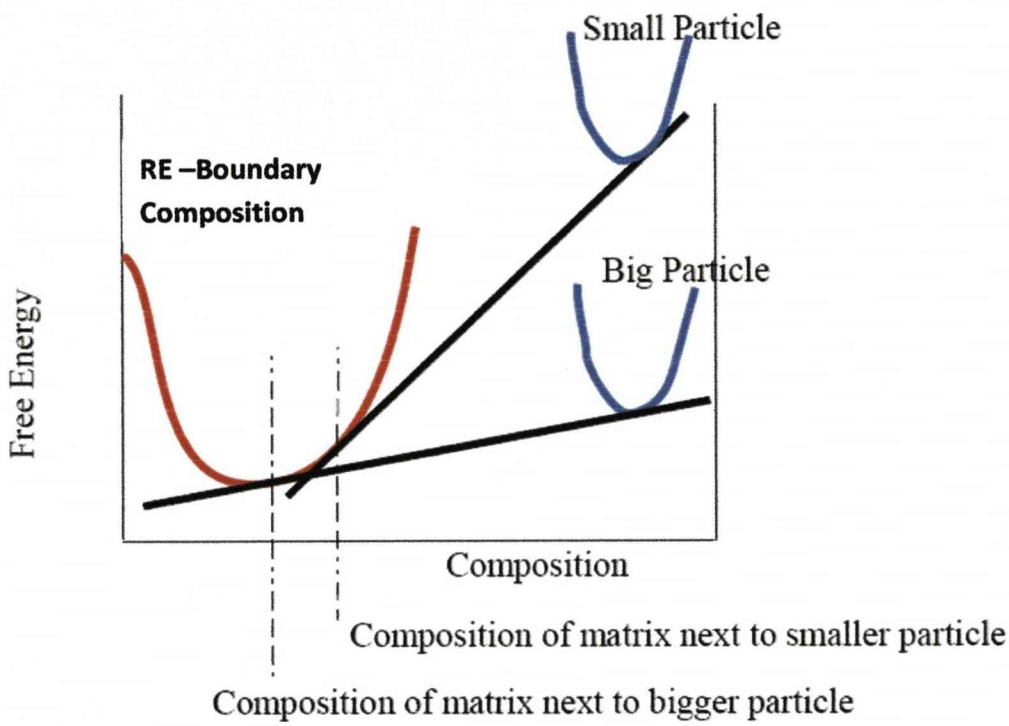

Figure 7- 7: Ostwald ripening mechanism: Schematic of free energy versus composition curve.

The above arguments and discussion allow a thermodynamically feasible model to be proposed (Figure 7-8) to explain the formation of the RE-rich particles and their growth. Figure 7-8 shows an ADF image of the oxide and as the GB's are not clearly visible, they are overlaid by white lines. As the oxidation progresses with time, there is build-up of RE from the bulk to the metal-oxide interface and then to the oxide grain boundaries (the RE in the transient stage being incorporated into growing oxide scale). This build-up continues with time until precipitates nucleate somewhere in the scale. (Figure 7-8C, were the GB saturation is shown in yellow and RE-rich particles in blue color). Whether a RE-rich particle grows or shrinks depends on its relative size with some particles initially growing before shrinking as the

particle size distribution changes. If a particle is growing it will show a low RE concentration in the surrounding GB's, while those that are shrinking will be surrounded by boundaries rich in reactive elements. Figure 7-8D show the particle of different size with different concentration of RE. This is what was observed around larger particles, whereas other particles which have different RE content in the GB connected to them are shrinking to produce an excess of RE at GB's.

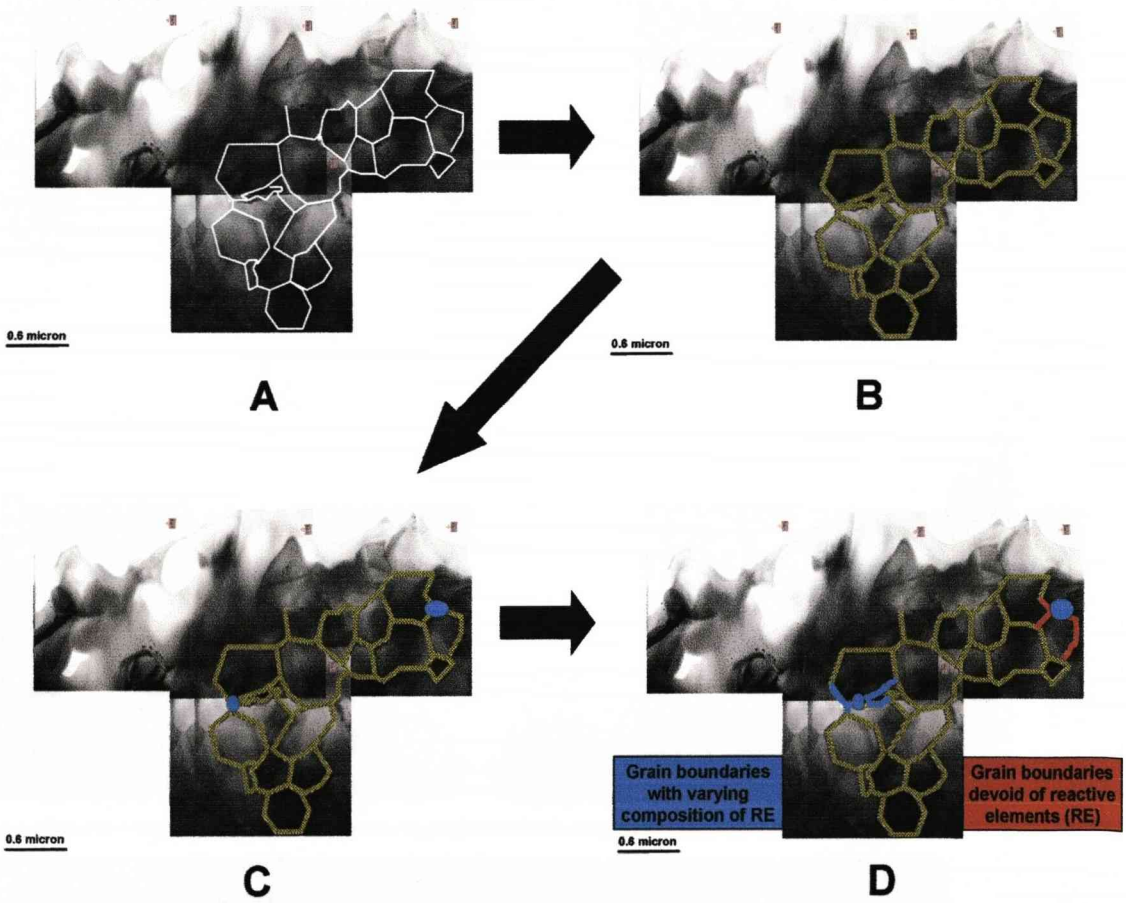

Figure 7- 8: Proposed model for formation and ripening of reactive element - rich particles near the equiaxed region. A) ADF image with grain boundaries outlined, B) RE ions diffuse outward and continue diffusing outward till saturation of the grain boundaries, C) RE-rich particles incorporated during columnar growth and saturated GB's, and D) RE-rich particles grow and/ shrink, and is controlled by common tangent construction mechanism and ripening mechanism described as Ostwald ripening.

7.5. Calculating number of RE ions at the GB

The spectrum collected from a fixed cross-section on the scale was quantified using the EDAX genesis program which yields the weight percent of each element present in the volume analyzed. As weight percent of each element present in the volume is known, a few assumptions evaluate an estimate of the number of RE ions present at different GB's.

Assumptions:

1) The volume over which whole spectrum was collected is the same, i.e. thickness of the sample is constant throughout the analysis. In this analysis it was assumed that the volume is 10 x 10 x 30 nm
2) There are no defects present in the volume analyzed, viz. no point defects, interstitial defects or dislocations.
3) Excluding the edge effect, i.e. even at the edges of the cube, the complete ions of the elements are considered.
4) No beam broadening within the specimen depth.
5) RE ions are distributed uniformly within the grain boundaries.

Figure 7-9 shows a schematic of the volume used for analysis. Assuming the above, the total number of ions of Al and O present in the total volume can be calculated. If substitutional segregation takes place, the number of RE ions present in the GB could be calculated approximately as shown in Appendix 2.Table 7-1 shows the numbers of ions of reactive element present at different type of boundaries.

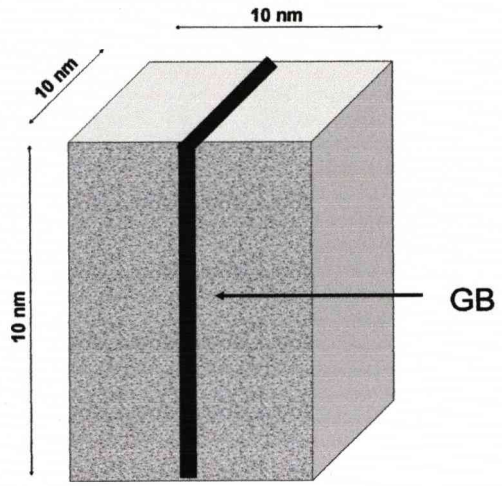

Figure 7- 9: Schematic of the volume analyzed for calculation.

Description	Approximate no. of Hf ions/unit volume of alumina GB (nm^3)	Approximate no. Y ions/unit volume of alumina GB (nm^3)
Bulk of the particle	20.25	4
GB connected to a small particle	7.2	1.9
GB not connected to a particle	3.52	0.65
GB connected to a large particle	0.8	0.048

Table 7- 1: Approximately calculated number of ions at different GB's (Error ±10%).

7.6. Anomalies during the line scan

During the acquisition of spectral profiles across grain boundaries, sometimes dual peaks and sometimes broad peaks of RE were observed. These anomalies are explained with the help of the schematics below. Figure 7-10 shows a schematic for dual peak observation, where the grain boundary is tilted by a large angle. If RE ions are present at the top and bottom surface of the scale, dual peaks would be observed as observed in Figure 5-45 and Figure 6-2. It is not clear why the RE segregates to the top and bottom of the GB. The other possibility could be that the RE segregates to the top and bottom surface of the grain where the boundary emerges, as this would require lower energy and would be energetically favorable and most likely in the current situation. There may be one or two different mechanism responsible for this, firstly during ion milling, the Ar ions hitting the sample may cause localized heating of the region which is about 150 – 200 °C. This process would not impart enough energy for much segregation to take place and could be ruled out. Secondly, when Ar ions hit the sample they may knock out an ion from the lattice creating a point defect and segregation of RE may take place and finally during the analysis under an intense electron beam in an electron microscope there is a possibility of electron induced segregation.

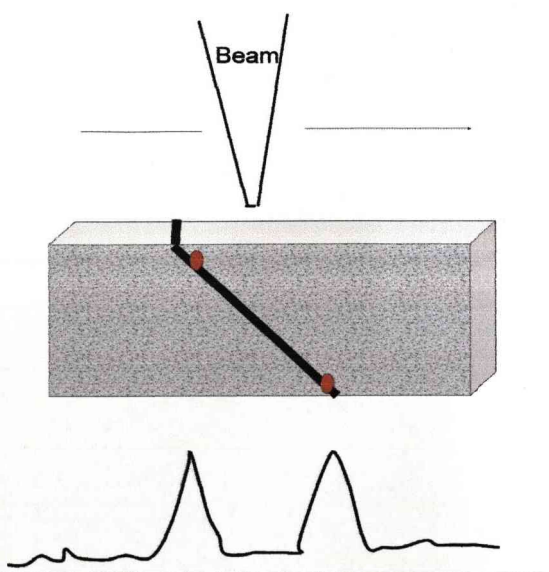

Figure 7- 10 Schematic explaining the reason for dual peak in a line scan.

Again if a grain boundary is inclined by a few degrees and RE segregates are present all over the boundary as observed in Figure 5-46, it is possible to end with an extended peak as shown in the schematic, Figure 7-11. During such conditions when the peaks are broadened it was difficult to analyze the actual width of the GB and may have contributed some percentage towards the error associated with the Line Scan data quantified. Most of the time the boundary analyzed was oriented almost parallel to the incident beam thus reducing the errors.

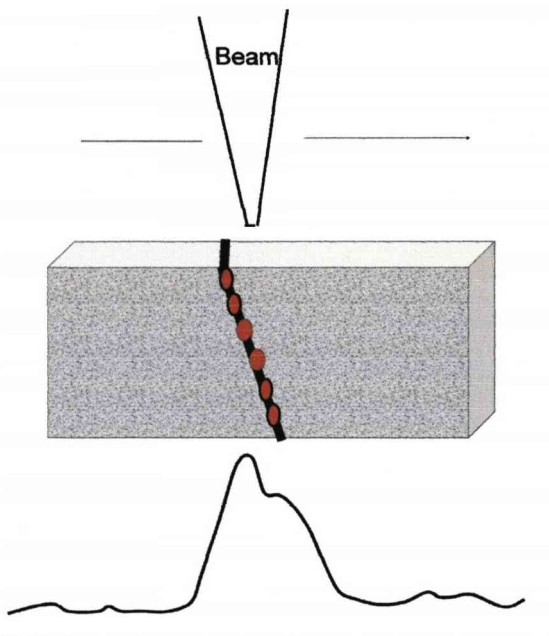

Figure 7- 11: Schematic explaining the occurrence of an extended peak.

7.7. SuperSTEM and EELS

In recent years, high-angle annular dark field (HAADF) imaging in scanning transmission electron microscopy (STEM) has become a widely recognized technique that provides atomic resolution structure images that are generally more directly interpretable than conventional high-resolution transmission electron microscope images. The intensities in the HAADF image are directly proportional to the average atomic number (Z). Transverse interference effects

between neighboring atomic columns are minimized when electron probes of a fixed size that are smaller than the distances between the atomic columns are used and for large HAADF detector inner angles.

EEL spectroscopy was carried out across the grain boundaries to see the segregation of RE's and co-related with the HAADF image recorded at that point. Almost every grain boundary showed a bright intensity as was seen in Figure 6-1 to 6-5, but these changes in intensity can arise from strain effects. The understanding of HAADF image intensities in terms of occupancy of the atomic columns is still a subject of continuing research. Some authors have suggested the influence of probe channeling on HAADF image contrast. The tendency of the probe to focus along the atomic columns is expected to be different for columns occupied by different species, also known as channeling. These effects may cause the image to become a function of sample thickness, it was therefore necessary to repeat the experiments.

7.7.1. Low loss and High loss edges

Low loss spectra with the zero loss peak included were recorded at the GB's. The edges present in the low loss region could not be interpreted simply as the edges for Hf and Y lie under the first Plasmon peaks and hence it was necessary to process the spectra using the sophisticated techniques discussed in the experimental section.

The HAADF image (Figure 6-2) showed the bright intensities at the top and bottom of the scale indicating segregation of RE ions at these levels, which again support the dual peaks observed in the EDX spectra in Figure 7-10. The spectra were deconvoluted to remove the plural scattering, but even after this it was quite difficult to say whether Hf or Y was present or not. Therefore Kramer's-Kronig processing was carried out in order to see the RE edges. Kramer's-Kronig analyses yield the real and imaginary part of the dielectric function and were used to show the presence of RE elements. When the difference between the imaginary part of the dielectric constant from the RE-rich region and the bulk was studied, specific edges could

be seen at the specific energy. As the spectra were subject to much mathematical processing, errors propagate and increase; hence the experiments were repeated several times to check the repeatability. The results were consistent with those obtained by X-ray analysis.

High energy loss spectra were also collected to see whether it was easier to observe the RE edges present at high energies. This was confirmed when Hf ($M_{4,5}$) and Y ($L_{2,3}$) edges were observed at 1560 and 2060 eV respectively. Usually these edges were accompanied by a Si K edge at 1670 eV. Si could have become incorporated during the oxidation of the alloys in the furnace.

O edges from the GB's were compared to that of the bulk to see whether there was any difference in the near edge structure. No statistically significant difference was found. Hence it is assumed that the O was in the same state at the GB and in the bulk.

7.7.2. Lattice imaging and EELS

Alpha-alumina grains were oriented to one of the poles and lattice images recorded. These images showed random bright spots distributed across the GB's. The intensity in the bulk was quite uniform, whereas over the GB's there were sites which showed brighter intensities. As the intensity in HAADF image is directly proportional to the atomic number, these intensity spots are probably from the heavier atoms. To verify this, EELS spectra were collected from these spots and examined for edges.

It was not possible to collect the spectra from single spot due to the effect of beam damage and hence spectra were collected manually moving the beam over different bright spots. The EELS spectra collected from these bright spots showed they were from Hf and Y, these were again repeated to compare the results and they were consistent with each other. Hf ($M_{4,5}$) and Y ($L_{2,3}$) edges were observed at 1560 and 2080 eV respectively in the spectra obtained from most bright regions.

7.7.2.1. Intensity in the HAADF lattice image

To estimate the intensities arising from a few atoms and whether it was possible to detect a single RE atom present at the GB representation, Multislice simulations were carried out. These were carried out for an alumina grain oriented on a C-axis and then by substituting one of the Al sites with the RE atom in order to see whether it was possible to detect any change in intensity. Figure 7-12 shows the HAADF and BF simulated images of a hexagonal closed pack structure with Al ions and O ions substituted at similar sites as in the alpha alumina grain. For the first multislice calculation only two slices were used, one with Al ions and another with O ions in an HCP arrangement. The stacking sequence used in calculation was 10 (ab), where a is the Al ion slice and b was the O ion slice.

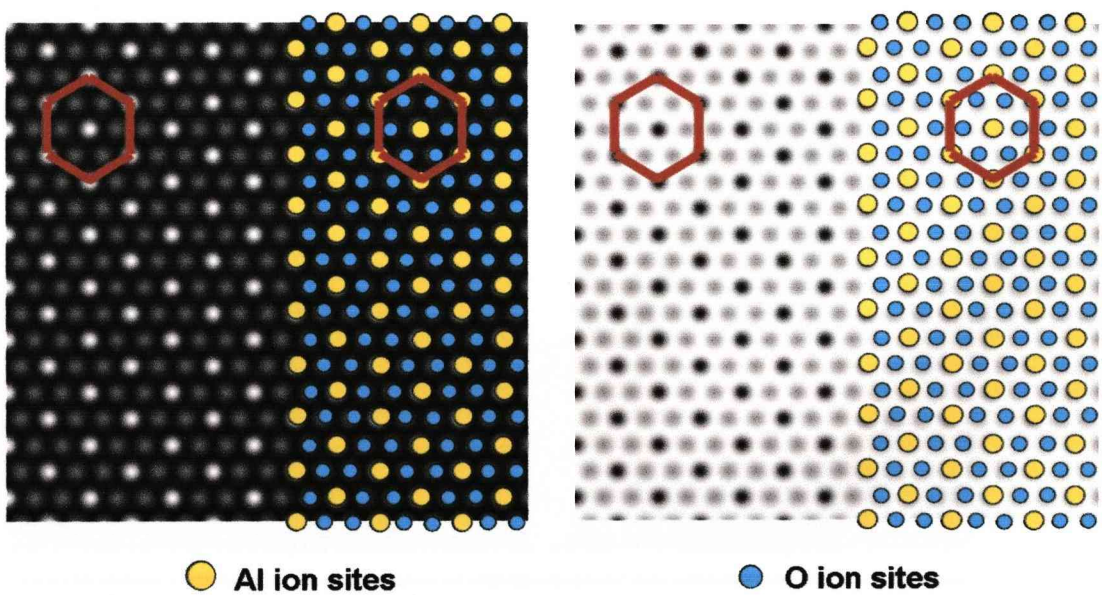

Figure 7- 12 Multislice simulated HAADF and BF images without a RE.

Figure 7-13 is the simulated HAADF and BF image of the same HCP structure when one of the centre Al ions was substituted by an Hf ion under similar conditions to the previous one.

As can be seen from the HAADF image only Hf sites were visible, whereas there is hardly any intensity from the Al and O sites.

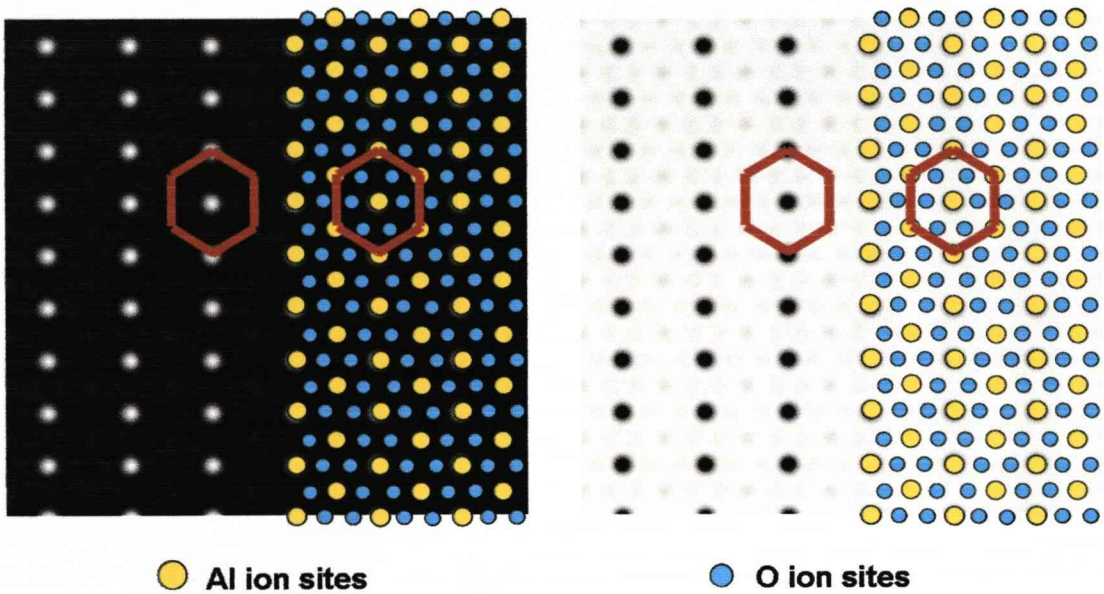

Figure 7- 13: HAADF and BF simulated image with a RE.

In the next approach a much larger cell was used for calculation (4 x 4). As can be seen from the Figure 7-14, there was a clear difference in the HAADF and BF images generated after simulation for the same thickness.

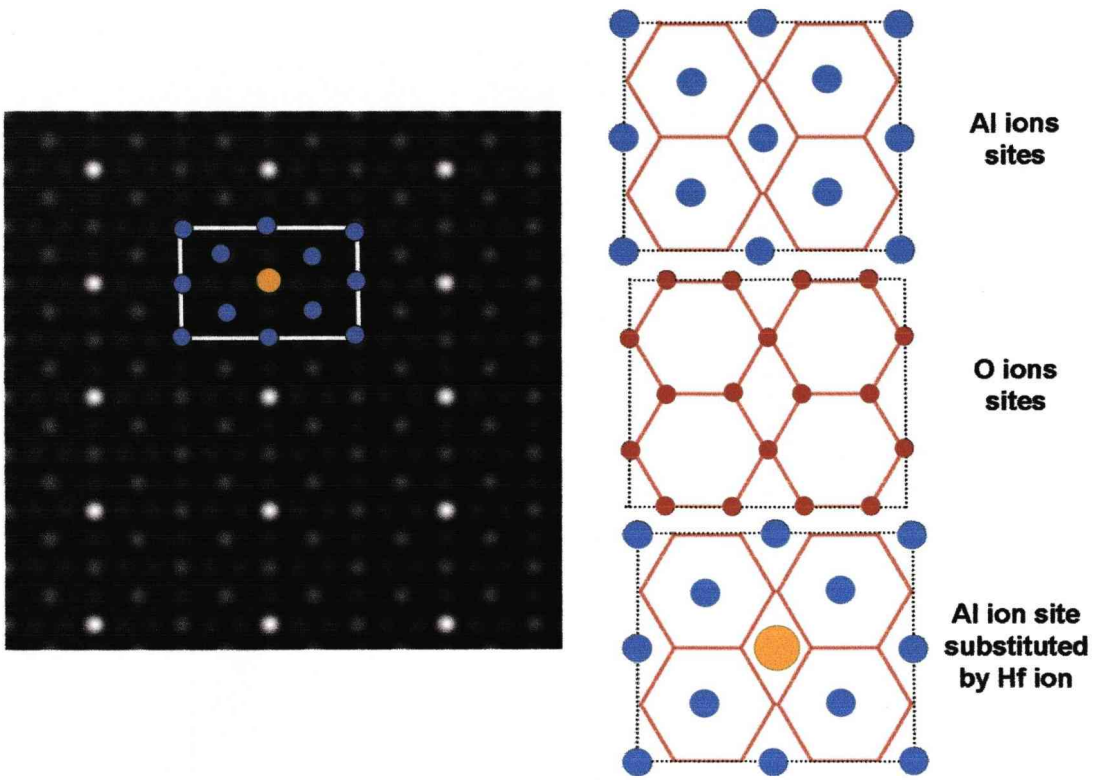

Figure 7- 14: Multislice simulated HAADF image with a RE. RE ion substituted at an Al site.

Figure 7-15 shows the HAADF image from multislice calculation of the alpha-alumina grains with Hf ions at different depth in the sample. As can be seen from the calculations intensity of Hf sites keeps increasing as it moves deeper in the sample and was maximum at the exit surface and intensities at O sites keep decreasing and Figure 7-16 shows the corresponding BF image .

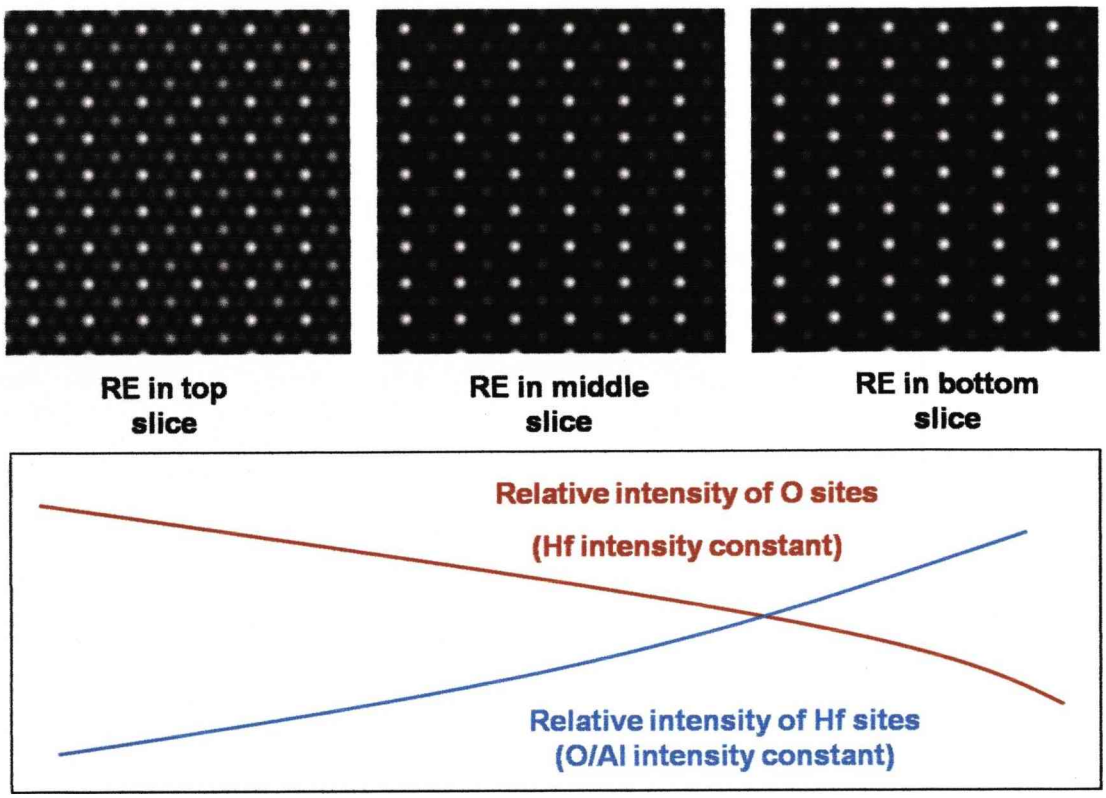

Figure 7- 15: Multislice simulations showing the effect of Hf position in the alumina lattice and the graph showing intensity variation with Hf sites in the lattice.

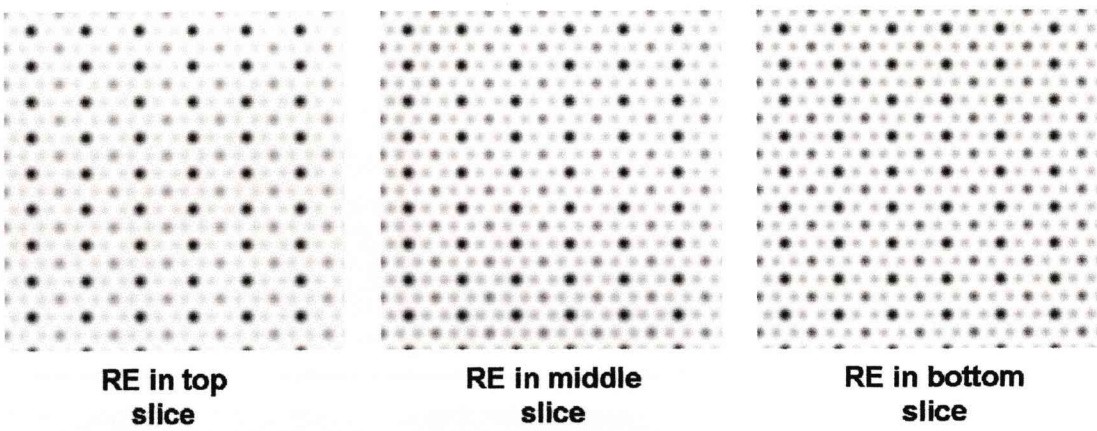

Figure 7- 16: Multislice calculation showing BF image and intensity variation for Hf ion with respect to its position in lattice.

Figure 7-17 shows the HAADF image from multislice simulation of alumina cell with a top and bottom slice containing Hf ion. The difference in intensities coming from Hf ion in top and bottom slice is quite clear and again it can be seen the intensity coming from Hf ion near exit surface is considerably higher.

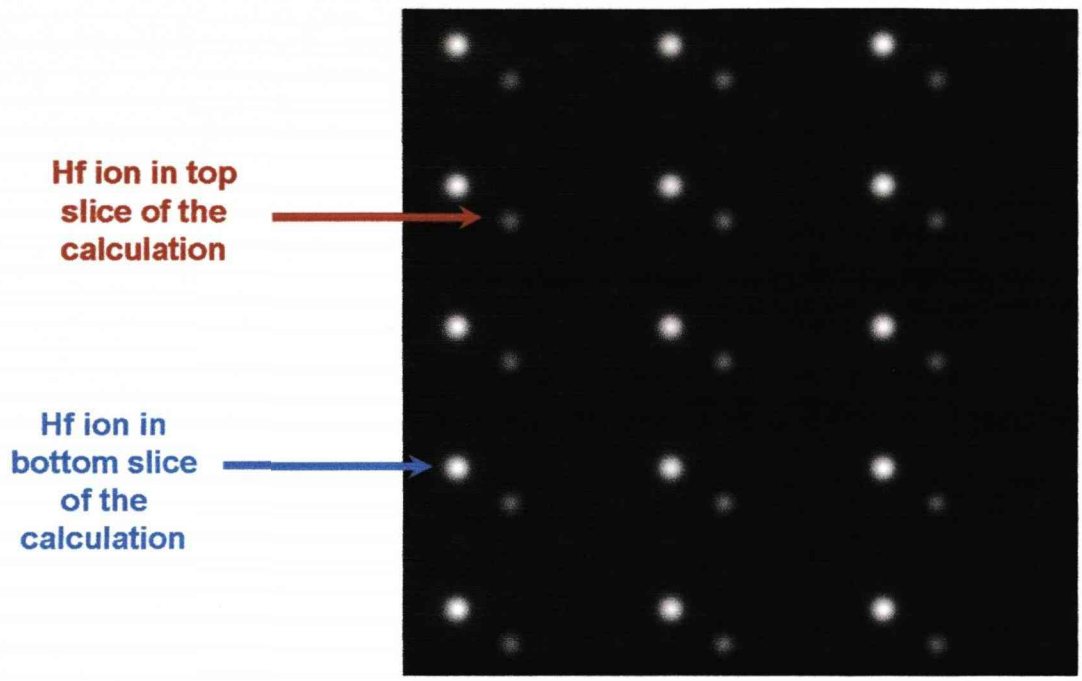

Figure 7- 17: HAADF image multislice simulation with Hf ion in the top and bottom slice of the calculation.

The multislice calculations were then repeated for an alpha-alumina structure oriented on a C-axis ([0 0 0 1]). The number of slices used and positions of different ions on the slice is shown in Appendix 3.

Figure 7-18 shows an HAADF and BF image from multislice calculation of alpha-alumina grain without any RE additive and Figure 7-19 shows an HAA DF and BF image with an RE. The results obtained were similar to those obtained for the simple HCP structure with RE. Only Hf sites show an increase in bright contrast. However the positions of Hf and Al ions could be seen in the BF image.

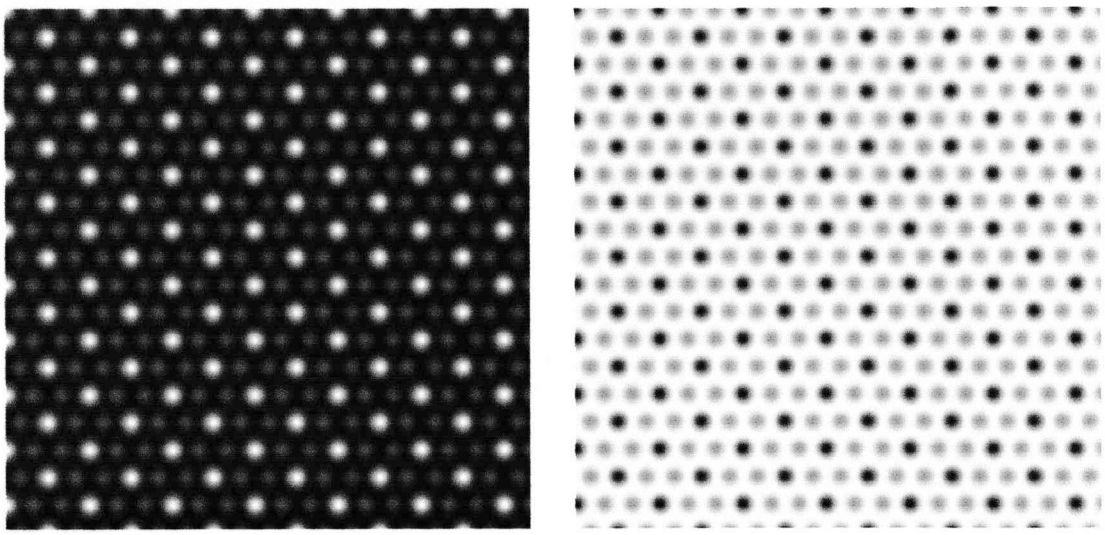

Figure 7- 18: HAADF and BF simulated image without any RE.

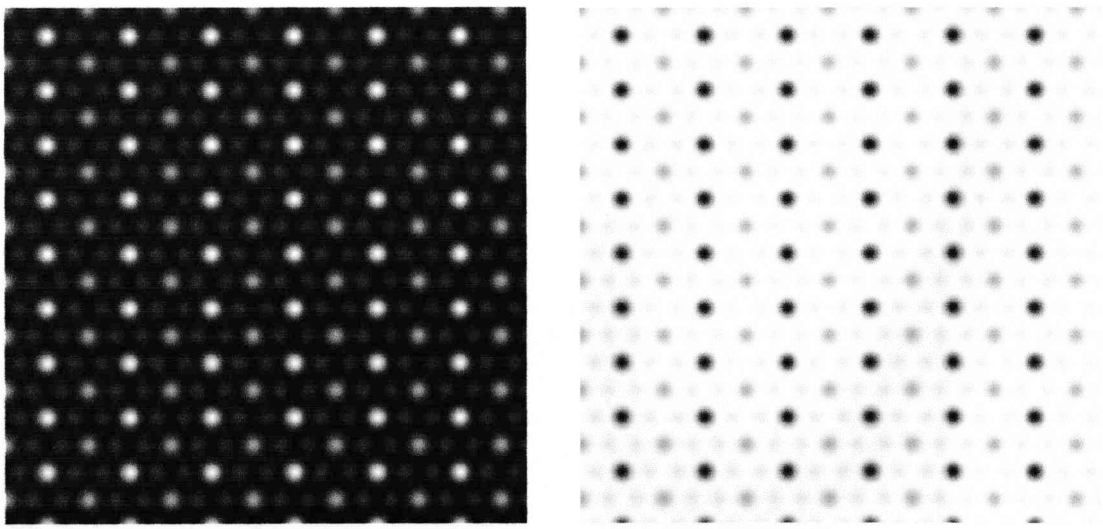

Figure 7- 19: HAADF and BF image with a RE.

Hence the above simulations showed that a single atom of RE should be detected in an alumina lattice.

The effect of beam damage plus ion mill damage was studied on the alumina scale and it was found to be large on the thin regions of the sample. The electron beam was found to displace

the RE ions from the grain boundary to the bulk of the sample. It was difficult to say, whether they moved into the bulk of the sample or were segregated to the vacuum surface of the scale. It would be easier for the RE ions to move over to the free surface rather than moving through the bulk, which would require higher energy. This would also complement the dual peak observed in Line scans which showed segregation to the top and bottom of the scale. The beam damage was only observed in the regions which were thinner than 60 nm and usually near the hole in a TEM sample. The electron beam did not seem to have the same effect on the regions away from hole, and regions which were 80 – 100 nm thick.

Chapter 8

Conclusion and suggestion for future work

8. Conclusions and suggestions for future work

This first study of oxide scales formed on important technological alloys has demonstrated the potential of the SuperSTEM to achieve higher spatial resolution and accuracy, and indicates that further development of this instrument is essential if we are to understand the detailed segregation mechanisms involved.

8.1. Cyclic oxidation of alloys

- During high temperature oxidation at 1250°C the high purity model alloy M11 with Y, Hf and Zr as additives showed a higher growth rate compared to commercial alloy Kanthal A1 with only Zr.
- The model alloy (M11) showed better adhesion and did not spall, whereas the Kanthal A1 alloy started to spall after about 90 cycles.

8.2. TEM and EDX analysis

- EDX analysis in the TEM showed the presence of yttrium and hafnium at the oxide grain boundaries and individual hafnium-rich crystallites precipitated in the outer region of the scale.
- Electron diffraction pattern indicated that the columnar alumina grains were oriented near the C-axis with a small degree of rotation indicating a fibre texture.

8.3. STEM and EDX analysis

- EDX results from STEM verified the results obtained by TEM at much higher spatial resolution (i.e. segregation of yttrium and hafnium ions at grain boundaries) and also the presence of hafnium-rich particles.
- Hf and Y start segregating after the transient stage and continue to segregate till saturation. The average values of Hf and Y found at GB's away from RE-rich particles were 7± wt. % and 1± 0.5wt. % respectively.
- The GB's which were connected to the small particles (average diameter less than 20 nm in size) showed a large variation in the region of 12±3 wt. % Hf and 3±0.8 wt. % Y.
- The GB's which were connected to the large particles (average diameter greater than 20 nm in size) showed an average of 1.5±1 wt. % Hf and 0.3±0.2 wt. % Y. There were few boundaries which did not show any Hf or Y.
- There were RE-rich particles found near the equiaxed region. These particles were found to be rich in Hf, average composition being 88±2 wt. % Hf and 6±1 wt. % Y and empirical formula being (8Hf, 4Y) $11O_2$.
- The growth mechanism proposed for the growth of these RE-rich particles is by absorbing Hf and Y from GB's. These particles grow till there is no Hf and Y present at the GB.

8.4. SuperSTEM and EELS

- Lattice image collected from the alpha-alumina grains showed the presence of bright regions and individual bright spots. Bright regions observed were along the grain boundaries and indicate the presence of individual columns of ions containing heavier reactive ions.

- EEL spectrum collected from these bright regions showed the presence of Hf and Y along the grain boundaries. Low loss edges were observed after processing of the spectra using Kramer's-Kronig criteria. Edges at high loss were observed by fitting a background curve to the recorded spectrum.
- Multislice simulation carried out on alumina grains showed that a single atom of Hf could be detected. Intensity from the heavier reactive ions present at the exit surface were higher than those observed if reactive ion was present on top or somewhere within the sample.
- Beam damage effects were observed on thinner regions in and around the central hole in the sample but this was less obvious in regions away from hole.

8.5. Suggestion for future work

Much work is still needed to be done in order to understand the RE effect. The first study of oxide scales formed on important technological alloys showed the potential of the SuperSTEM to achieve higher spatial resolution and accuracy, and indicates that further development of this instrument is essential if we are to understand the detailed segregation mechanism involved.

High angle annular dark field (HAADF) imaging of the alpha-Al_2O_3 grains has provided some of the answers to the question of grain boundary segregation. But there are still a few questions which remain unanswered and would seem worthwhile trying to answer. For example:

1) If another RE is present along with Hf and Y, how would that affect the segregation to GB.
2) Since the alloy had a similar amount of Hf and Y present, it would prove useful studying the alloys with varying compositions of Hf and Y.
3) The technique could be further utilized to study the concentration profiles over different GB and across different GB's connected via RE-rich particles.

4) Cross-section samples could be looked at to see the depth profile of these RE's and how they vary and affect the growth rate of the scale.
5) The SuperSTEM 2 could be used to perform tilting experiments as it will have a larger tilt angle of ± 35°. This would provide a better understanding of the RE distribution over a grain boundary and would help in understanding the anomalies observed in current research.
6) The oxide-rich particles formed could be studied in detail to understand the compositions and growth over varying periods of time, with different amounts of RE and varying numbers of RE additives.
7) The metal-oxide interface could be studied in order to understand the transport mechanisms of RE's from the bulk to the interface and then to the oxide grain boundaries.
8) The effect of impurities at the atomic level could be studied in order to find the segregation sites for impurities at the metal-oxide interface.

Reference

1. Birks, N., G.H. Meier, and F.S. Pettit, ***Introduction to the high temperature oxidation of metals***. 2nd ed. 2006. Cambridge University Press. ISBN:13 978-0-521-48042-0 Hardback. 75 - 78.
2. Birks, N., G.H. Meier, and F.S. Pettit, ***Introduction to the high temperature oxidation of metals***. 2nd ed. 2006. Cambridge University Press. ISBN-13 978-0-521-48042-0 Hardback. 134-139.
3. Birks, N., G.H. Meier, and F.S. Pettit, ***Introduction to the high temperature oxidation of metals***. 2nd ed. 2006. Cambridge University Press. ISBN-13 978-0-521-48042-0 Hardback. 101 - 102.
4. Klöwer, J., A. Kolb-Telieps, H. Bode, M. Brede, J. Lange, R. Brück, and L. Wieres. ***Development of high-temperature corrosion resistant FeCrAl alloys for automotive catalytic converters***. *Congress for Innovative Materials, Processes, and Applications.* 1998. Munich.
5. F.A.Golightly, F.H.Stott, and G.C.Wood., ***The early stages of development of α-Al_2O_3 scales on Fe-Cr-Al and Fe-Cr-Al-Y alloys at high temperature***. Oxidation of Metals, 1980. **14**: p. 217-234.
6. Hou, P.Y. ***Impurity segregation to scale/alloy interfaces and its effect on interfacial properties***. *5th International Symposium on High Temperature Corrosion and Protection of Materials, May 22-26 2000.* 2001. Les Embiez: Trans Tech Publications Ltd.
7. Hou, P.Y., ***Segregation Phenomena at Growing Alumina/Alloy Interfaces***. Journal of Corrosion Science, 2003. **6**: p. 1-29.
8. Al-Badairy, H., D.J. Prior, and G.J. Tatlock, ***FEG-SEM examination of alumina scales formed on FeCrAl alloys.*** Materials at High Temperatures, 2005. **22**(3-4): p. 453-460.
9. Al-Badairy, H. and G.J. Tatlock, ***The Application of a Wedge-Shaped Sample Technique for the Study of Breakaway Oxidation in Fe-20Cr-5Al Base Alloys.*** Oxidation of Metals, 2000. **53**(1-2): p. 157-170.
10. Al-Badairy, H. and G.J. Tatlock, ***Influence of the moisture content of the atmosphere on alumina scale formation and growth during high temperature oxidation of PM2000.*** Materials at High Temperatures, 2000. **17**(1): p. 133-137.
11. Strehl, G., D. Naumenko, H. Al-Badairy, L.M. Rodriguez Lobo, G. Borchardt, G.J. Tatlock, and W.J. Quadakkers, ***Effect of aluminium depletion on the oxidation behaviour of FeCrAl foils.*** Materials at High Temperatures, 2000. **17**(1): p. 87-92.
12. Tatlock, G.J. and H. Al-Badairy. ***Scale spallation in alumina-forming FeCrAl alloys***. *John Stringer Symposium on High Temperature Corrosion, John Stringer Symposium*

on High Temperature Corrosion, 2001, p 132-137 Indianapolis, IN, United States: ASM International, 9639 Kinsman Road, OH 44073-0002, United States.

13. Al-Badairy, H., D. Naumenko, J. Le Coze, G.J. Tatlock, and W.J. Quadakkers, ***Significance of minor alloying additions and impurities on alumina scale growth and adherence in FeCrAl alloys.*** Materials at High Temperatures, 2003. **20**(3): p. 405-412.
14. Bennett, M.J., R. Newton, J.R. Nicholls, H. Al-Badairy, and G.J. Tatlock. ***The oxidation behaviour of the commercial FeCrAlRE alloys aluchrom YHf and Kanthal AF foils in air at 800°-950°C.*** *Materials Science Forum*, v 461-464, n I, *High Temperature Corrosion and Protection of Materials 6*, 2004, p 463-472. Les Embiez, France: Trans Tech Publications Ltd, Zurich-Ueticon, CH-8707, Switzerland.
15. Tatlock, G.J., H. Al-Badairy, M.J. Bennett, R. Newton, J.R. Nicholls, and A. Galerie, ***Air oxidation of commercial FeCrAlRE alloy foils between 800 and 950°C.*** Materials Science and Technology, 2005. **21**(8): p. 893-900.
16. Kochubey, V., H. Al-Badairy, G. Tatlock, J. Le-Coze, D. Naumenko, and W.J. Quadakkers, ***Effects of minor additions and impurities on oxidation behaviour of FeCrAl alloys. Development of novel surface coatings compositions.*** Materials and Corrosion, 2005. **56**(12): p. 848-853.
17. Prior, D.J., H. Al-Badairy, G.G.E. Seward, C.J. Veltkamp, and G.J. Tatlock, ***Microstructural development of a alumina scales developed on FeCrAl alloys.*** Materials Science and Technology, 2006. **22**(11): p. 1316-1324.
18. A.S.Khanna, ***Introduction to High Temperature Oxidation and Corrosion***. 2003: ASM International 325. Replika Press Pvt Ltd. ISBN:0-87170-762-4
19. Muangjunburee, P., ***Degradation of joints in ODS ferritic stainless steels***, in *Materials Science and Engineering*. 2005, University of Liverpool: Liverpool.
20. Al-Badairy, H., ***The mechanical and chemical failure of alumina scales formed on Fe-Cr-Al alloys***, *Material Science and Engineering*. 1999, University of Liverpool: Liverpool. p. 27 - 28.
21. Zhang, Z.G., F. Gesmundo, P.Y. Hou, and Y. Niu, ***Criteria for the formation of protective Al_2O_3 scales on Fe-Al and Fe-Cr-Al alloys.*** Corrosion Science, 2006. **48**(3): p. 741-765.
22. Zhang, Z.G. and Y. Niu. ***Effect of chromium on the oxidation of a Fe-10 Al alloy at 1000°C.*** *PRICM 5: The Fifth Pacific Rim International Conference on Advanced Materials and Processing, Nov 2-5 2004*. 2005. Beijing, China: Trans Tech Publications Ltd, Zurich-Ueticon, CH-8707, Switzerland.
23. Al-Badairy, H. and G.J. Tatlock, ***The oxidation of thin foils of FeCrAl(RE) alloys in moist air.*** Materials at High Temperatures, 2001. **18**(2): p. 101-106.

24. Birks, N. and G.H. Meier, ***Introduction to High temperature Oxidation of Metals***. 2006. Cambridge University Press. ISBN:13 978-0-521-48042-0 Hardback. 105 - 118.

25. Berthome, G., E. N'Dah, Y. Wouters, and A. Galerie, ***Temperature dependence of metastable alumina formation during thermal oxidation of FeCrAl foils.*** Materials and Corrosion, 2005. **56**(6): p. 389-392.

26. Cambridge, U.o., ***Ellingham Diagrams***, DoITPoMS, Department of Materials Science and Metallurgy, University of Cambridge.
Website: http://www.doitpoms.ac.uk/tlplib/ellingham_diagrams/ellingham.php

27. Pint, B.A., P.F. Tortorelli, and I.G. Wright, ***Effect of Cycle Frequency on High-Temperature Oxidation Behavior of Alumina-Forming Alloys.*** Oxidation of Metals, 2002. **V58**(1): p. 73-101.

28. Zhang, Z.G., F. Gesmundo, P.Y. Hou, and Y. Niu, ***Criteria for the formation of protective Al_2O_3 scales on Fe-Al and Fe-Cr-Al alloys.*** Corrosion Science, 2006. **48**(3): p. 741-765.

29. Wood, G.C., ***Oxidation of Fe-Al and FeCrAl alloy.*** Oxidation of Metals, 1970. **V2**(1): p. 11-57.

30. Klöwer, J., ***Factors affecting the oxidation behaviour of thin Fe-Cr-Al foils Part I: Effect of foil dimensions.*** Materials and Corrosion, 1998. **49**(10): p. 758-763.

31. Klöwer, J., ***Factors affecting the oxidation behaviour of thin Fe-Cr-Al foils. Part II: The effect of alloying elements: Overdoping.*** Materials and Corrosion, 2000. **51**(5): p. 373-385.

32. Prescott, R.a.G., M.J, ***The formation of aluminum oxide scales on high-temperature alloys.*** Oxidation of Metals, 1992. **38**(3/4): p. 233-254.

33. Stott, F.H., ***Oxidation of alumina-forming alloys.*** Proceedings of the 1996 4th International Symposium on High Temperature Corrosion and Protection of Materials. Part 1 (of 2), May 20-24 1996. Materials Science Forum, 1997. **251-254**(pt 1): p. 19-32.

34. Jedlinski, J., ***Oxidation behaviour of FeCrAl `alumina forming' alloys at high temperatures.*** Proceedings of the 1996 13th International Symposium on the Reactivity of Solids, ISRS. Part 2 (of 2), Sep 8-12 1996. Solid State Ionics, 1997. **101-103**(pt 2): p. 1033-1040.

35. Andrieu, E., A. Germidis, and R. Molins, ***High temperature oxidation of thin FeCrAl strips.*** Proceedings of the 1996 4th International Symposium on High Temperature Corrosion and Protection of Materials. Part 1 (of 2), May 20-24 1996. Materials Science Forum, 1997. **251-254**(pt 1): p. 357-364.

36. Stott, F.H. ***Formation of protective Al_2O_3 scales during high-temperature oxidation***. *Proceedings of the 1996 125th TMS Annual Meeting, Feb 4-8 1996*. 1996. Anaheim, CA, USA: Minerals, Metals & Materials Soc (TMS), Warrendale, PA, USA.

37. Wu, Y., ***Kinetics of oxide formation on FeCrAl thin films***. Second Int. Conference on Thin Film Physics and Applications, Apr 15 1994
Proceedings of SPIE - The International Society for Optical Engineering, 1994. **2364**: p. 499-504.

38. Stott, F.H., ***Developments in understanding the mechanisms of growth of protective scales on high-temperature alloys***. Materials Characterization, 1992. **28**(3): p. 311-325.

39. Quadakkers, W.J., A. Elschner, W. Speier, and H. Nickel, ***Composition and growth mechanisms of alumina scales on FeCrAl-based alloys determined by SNMS***. Applied Surface Science (1985), 1991. **52**(4): p. 271-287.

40. F.A.Golightly, F.H.S.a.G.C.W., ***The influence of yittrium additions on the oxide-scale adhesion to an iron-chromium-aluminium alloy***. Oxidation of Metals, 1976. **10**: p. 163-187.

41. Grabke, H.J., ***Surface and interface segregation in the oxidation of metals***. Surface and interface analysis, 2000. **30**: p. 112-119.

42. Hou, P.Y., A.P. Paulikas, and B.W. Veal. ***Growth strains and stress relaxation in alumina scales during high temperature oxidation***. *Proceedings of the 6th International Symposium on High Temperature Corrosion and Protection of Materials, May 16-21 2004*. 2004. Les Embiez, France: Trans Tech Publications Ltd, Zurich-Ueticon, CH-8707, Switzerland.

43. Blachere, J.R., E. Schumann, G.H. Meier, and F.S. Pettit, ***Textures of alumina scales on FeCrAl alloys***. Scripta Materialia, 2003. **49**(9): p. 909-912.

44. El Kadiri, H., R. Molins, Y. Bienvenu, and M.F. Horstemeyer, ***Abnormal high growth rates of metastable aluminas on FeCrAl alloys***. Oxidation of Metals, 2005. **64**(1-2): p. 63-97.

45. Pint, B.A., ***Optimization of reactive-element additions to improve oxidation performance of alumina-forming alloys***. Journal of the American Ceramic Society, 2003. **86**(4): p. 686-695.

46. Pivin, J.C., D. Delaunay, C. Roques-Carmes, A.M. Huntz, and P. Lacombe, ***Oxidation mechanism of Fe---Ni---20---25Cr---5Al alloys-influence of small amounts of yttrium on oxidation kinetics and oxide adherence***. Corrosion Science, 1980. **20**(3): p. 351-373.

47. Messaoudi. K, Huntz. A. M., and L. B, ***Diffusion and growth mechanism of Al2O3 scales on ferritic Fe-Cr-Al alloys.*** Materials Science and Engineering A 1998. **247**(1-2): p. 248 - 262.

48. Tolpygo, V.K. and H. Viefhaus, ***Segregation at the Al_2O_3-FeCrAl interface during high-temperature oxidation.*** Oxidation of Metals, 1999. **52**(1): p. 1-29.

49. Pint, B.A., ***Experimental observations in support of the dynamic-segregation theory to explain the reactive-element effect.*** Oxidation of Metals, 1996. **45**(1-2): p. 1-16.

50. Pint, B.A., ***On the formation of interfacial and internal voids in α- Al_2O_3 scales.*** Oxidation of Metals, 1997. **48**(3-4): p. 303-328.

51. Pint, B.A., ***Study of the reactive element effect in ODS iron-base alumina formers.*** Materials Science Forum, 1997. **251-254**(pt 1): p. 397-404.

52. Pint, B.A., ***Oxidation behavior of oxide-dispersed β-NiAl: I. Short-term performance at 1200 °C.*** Oxidation of Metals, 1998. **49**(5-6): p. 531-559.

53. Pint, B.A. ***Progress in understanding the reactive element effect since the Whittle and Stringer literature review.*** 2001. Indianapolis, IN, United States: ASM International, 9639 Kinsman Road, OH 44073-0002, United States.

54. Pint, B.A. and K.B. Alexander, ***Grain boundary segregation of cation dopants in α-Al_2O_3 scales.*** Journal of the Electrochemical Society, 1998. **145**(6): p. 1819-1829.

55. Wright, I.G., R. Peraldi, and B.A. Pint. ***Influence of aluminum depletion effects on the calculation of the oxidation lifetimes of FeCrAl alloys***. *Proceedings of the 6th International Symposium on High Temperature Corrosion and Protection of Materials, May 16-21 2004*. 2004. Les Embiez, France: Trans Tech Publications Ltd, Zurich-Ueticon, CH-8707, Switzerland.

56. Pint, B.A., L.R. Walker, and I.G. Wright, ***Characterization of the breakaway al content in alumina-forming alloys.*** Materials at High Temperatures, 2004. **21**(3): p. 175-185.

57. Stott, F.H. and N. Hiramatsu, ***Breakdown of protective scales during the oxidation of thin foils of Fe-20Cr-5Al alloys at high temperatures.*** 4th International Conference on the Microscopy of Oxidation, Sep 20-Sep 22 1999. Materials at High Temperatures, 2000. **17**(1): p. 93-99.

58. Bachorczyk, R. and R. Fordham, ***Long-term, cyclic oxidation behaviour of alumina- and chromia- forming alloys.*** Diffusion and Defect Data. Pt A Defect and Diffusion Forum, 2005. **237-240**(PART 2): p. 1107-1114.

59. Badini, C. and F. Laurella, ***Oxidation of FeCrAl alloy: Influence of temperature and atmosphere on scale growth rate and mechanism.*** Surface and Coatings Technology, 2001. **135**(2-3): p. 291-298.

60. Bongartz, K., W.J. Quadakkers, J.-P. Pfeifer, and J.S. Becker, ***Mathematical modelling of oxide growth mechanisms measured by O tracer experiments.*** Surface Science, 1993. **292**(1-2): p. 196-208.

61. Graham, M.J. and R.J. Hussey, ***Characterization and growth of oxide films.*** Corrosion Science, 2002. **44**(2): p. 319-330.

62. Jedlinski, J., G. Borchardt, B. Rajchel, and M. Nocun. ***The effect of aluminium ion implantation on the oxidation behaviour of Fe-xCr-yAl alloys***. *Proceedings of the 6th International Symposium on High Temperature Corrosion and Protection of Materials, May 16-21 2004*. 2004. Les Embiez, France: Trans Tech Publications Ltd, Zurich-Ueticon, CH-8707, Switzerland.

63. Pint, B.A., ***On the formation of interfacial and internal voids in Al_2O_3 scales.*** Oxidation of Metals, 1997. **V48**(3): p. 303-328.

64. Lesage, B., L. Marechal, A.M. Huntz, and R. Molins, ***Oxidation behaviour of ODS FeCrAl alloys : Aluminium Depletion and Lifetime.*** Oxidation of Metals, 2003. **60**(1/2): p. 1-28.

65. Strehl, G., D. Naumenko, H. Al-Badairy, L.M. Rodriguez Lobo, G. Borchardt, G.J. Tatlock, and W.J. Quadakkers, ***Effect of aluminium depletion on the oxidation behaviour of FeCrAl foils.*** 4th International Conference on the Microscopy of Oxidation, Sep 20-Sep 22 1999. Materials at High Temperatures, 2000. **17**(1): p. 87-92.

66. S.E.Sadique, M.M.A., M.M.Haque, S.Basri, M.M.H.M.Ahmad and S.M.Sapuan, ***Influence of aluminium additions on the rate of oxidation of iron chromium alloys.*** The journal of corrosion science and engineering, 2000. **1**(18): p. 18-26.

67. Al-Badairy, H., G.J. Tatlock, and M.J. Bennett, ***Comparison of breakaway oxidation in wedge-shaped and parallel sided coupons of FeCrAl alloys.*** Materials at High Temperatures, 2000. **17**(1): p. 101-107.

68. Lesage, B., L. Marechal, A.-M. Huntz, and R. Molins. ***Aluminium depletion in FeCrAl alloys during oxidation***. *Proceedings of the Fifth International Conference on Diffusion in Materials (DIMAT 2000), Jul 17-21 2000*. 2001. Paris, France: Trans Tech Publications Ltd.

69. Molins, R. and A.M. Huntz. ***Recent improvements in the understanding of alumina film formation and durability***. *Materials Science Forum*, v 461-464, n I, *High Temperature Corrosion and Protection of Materials 6*, 2004, p 29-36. Les Embiez, France: Trans Tech Publications Ltd, Zurich-Ueticon, CH-8707, Switzerland.

70. Nicholls, J.R., M.J. Bennett, and R. Newton, ***A life prediction model for the chemical failure of FeCrAlRE alloys: Preliminary assessment of model extension to lower temperatures.*** Materials at High Temperatures, 2003. **20**(3): p. 429-438.

71. Quadakkers, W.J. and K. Bongartz, ***Prediction of breakaway oxidation for alumina forming ODS alloys using Oxidation Diagrams.*** Werkstoffe und Korrosion, 1994. **45**(4): p. 232-241.

72. Wilber, J.P., M.J. Bennett, and J.R. Nicholls, ***Life-time extension of alumina forming FeCrAl-RE alloys: influence of alloy thickness.*** Materials at High Temperatures, 2000. **17**(1): p. 125-132.

73. Nicholls, J.R., R. Newton, and M.J. Bennett. ***Modelling the onsets of breakaway oxidation for alumina forming FeCrAl-RE alloys under cyclic oxidation conditions.*** 2001. Indianapolis, IN, United States: ASM International, 9639 Kinsman Road, OH 44073-0002, United States.

74. Wright, I.G., B.A. Pint, C.S. Simpson, and P.F. Tortorelli, ***High-temperature oxidation life characteristics of ODS-Fe_3Al.*** Materials Science Forum, 1997. **251-254**(pt 1): p. 195-202.

75. Wright, I.G., B.A. Pint, and P.F. Tortorelli, ***High-temperature oxidation behavior of ODS-Fe_3Al.*** Oxidation of Metals, 2001. **55**(3-4): p. 333-357.

76. Rieck, T., S. Majumdar, and K. Natesan, ***Spallation Studies on Alumina-Forming Model Alloys***, *Fossil Energy Program*. 2000, Argonne National Laboratory. Website: http://www.doe.gov/bridge

77. Tolpygo, V.K. and D.R. Clarke, ***Spalling failure of α-alumina films grown by oxidation: I. Dependence on cooling rate and metal thickness.*** Materials Science and Engineering A: Structural Materials: Properties, Microstructure and Processing, 2000. **278**(1-2): p. 142-150.

78. Tolpygo, V.K. and D.R. Clarke, ***Spalling failure of α-alumina films grown by oxidation. II. Decohesion nucleation and growth.*** Materials Science and Engineering A: Structural Materials: Properties, Microstructure and Processing, 2000. **278**(1-2): p. 151-161.

79. R.J.Christensen, V.K.T.a.D.R.C., ***The influence of the reactiv eelement Yttrium on the stress in alumina scales formed by oxidation.*** Acta Materiala, 1997. **54**(4): p. 1761 - 1766.

80. Tolpygo, V.K. and D.R. Clarke, ***Alumina scale failure resulting from stress relaxation.*** Surface and Coatings Technology, 1999. **120-121**: p. 1-7.

81. Tolpygo, V.K. and D.R. Clarke, ***Tensile cracking during thermal cycling of alumina films formed by high-temperature oxidation.*** Acta Materialia, 1999. **47**(13): p. 3589-3605.

82. Tolpygo, V.K. and D.R. Clarke, ***Wrinkling of α-alumina films grown by oxidation - II. Oxide separation and failure.*** Acta Materialia, 1998. **46**(14): p. 5167-5174.

83. Tolpygo, V.K., J.R. Dryden, and D.R. Clarke, ***Determination of the growth stress and strain in α- Al_2O_3 scales during the oxidation of Fe-22Cr-4.8Al-0.3Y alloy.*** Acta Materialia, 1998. **46**(3): p. 927-937.

84. Tolpygo, V.K. and D.R. Clarke, ***Competition between stress generation and relaxation during oxidation of an Fe-Cr-Al-Y alloy.*** Oxidation of Metals, 1998. **49**(1-2): p. 187-212.

85. Tolpygo, V.K. and D.R. Clarke, ***Wrinkling of α-alumina films grown by thermal oxidation - I. Quantitative studies on single crystals of Fe-Cr-Al alloy.*** Acta Materialia, 1998. **46**(14): p. 5153-5166.

86. Christensen, R.J., V.K. Tolpygo, and D.R. Clarke, ***Influence of the reactive element yttrium on the stress in alumina scales formed by oxidation.*** Acta Materialia, 1997. **45**(4): p. 1761-1766.

87. Hou, P.Y. and G.D. Ackerman, ***Chemical state of segregants at Al2O3/alloy interfaces studied using μ-XPS.*** Applied Surface Science, 2001. **178**(1-4): p. 156-164.

88. Hondros, E.D. and M.P. Seah, ***Segregation to interfaces.*** International Metals Reviews, 1977. **22**: p. 262-301.

89. Stasik, M.C., F.S. Pettit, G.H. Meier, A. Ashary, and J.L. Smialek, ***Effects of reactive element additions and sulfur removal on the oxidation behavior of FeCrAl alloys.*** Scripta Metallurgica et Materialia, 1994. **31**(12): p. 1645-1650.

90. Sarioglu, S., J.R. Blachere, F.S. Pettit, G.H. Meier, J.L. Smialek, and C. Mennicke, ***Effects of reactive element additions, sulfur removal, and specimen thickness on the oxidation behaviour of alumina-forming Ni- and Fe-base alloys.*** Proceedings of the 1996 4th International Symposium on High Temperature Corrosion and Protection of Materials. Part 1 (of 2), May 20-24 1996
Materials Science Forum, 1997. **251-254**(pt 1): p. 405-412.

91. Lee, W.E. and K.P.D. Lagerlof, ***Structural and electron diffraction data for sapphire (alpha-alumina).*** Journal of electron microscopy technique 1985. **2**: p. 247-258.

92. Lea, C. and M.P. Seah, ***Surface segregation as a guide to grain boundary segregation.*** Scripta Metallurgica, 1975. **9**(6): p. 583-586.

93. Seah, M.P., ***Grain boundary segregation and the T-t dependence of temper brittleness.*** Acta Metallurgica, 1977. **25**(3): p. 345-357.

94. Hondros, E.D. and M.P. Seah, ***Theory of grain boundary segregation in terms of surface adsorption analogues.*** Metallurgical Transactions A (Physical Metallurgy and Materials Science), 1977. **8A**(9): p. 1363-1371.

95. Seah, M.P. and C. Lea, ***Surface segregation measurements by AES and their relation to metallurgical problem.*** Scripta Metallurgica, 1984. **18**(10): p. 1057-1062.

96. Seah, M.P., ***Grain boundary segregation.*** Journal of Physics, 1980. **10**(1659): p. 1043-1064.

97. Basu, S.N., H. Wu, V. Gupta, and V. Kireev, ***The effect of structure and chemistry on the strength of FeCrAl(Y)/sapphire interfaces: I. Structure and chemistry of interfaces.*** Materials Science and Engineering A, 2003. **349**(1-2): p. 248-255.

98. Chevalier, S., K. Przybylski, G. Borchardt, and J.P. Larpin. ***Role of minor element addition in the formation of thermally grown alumina scales.*** *Proceedings of the 6th International Symposium on High Temperature Corrosion and Protection of Materials, May 16-21 2004*. 2004. Les Embiez, France: Trans Tech Publications Ltd, Zurich-Ueticon, CH-8707, Switzerland.

99. Chevalier, S., A.P.D. Tankeu, H. Buscall, C. Issartel, G. Borchardt, and J.P. Larpin, ***Influence of the mode of introduction of a reactive element on the high temperature oxidation behavior of an alumina-forming alloy part II: Cyclic oxidation tests.*** Materials and Corrosion, 2004. **55**(8): p. 610-616.

100. Cueff, R., H. Buscail, E. Caudron, C. Issartel, and F. Riffard, ***Oxidation behaviour of alumina formers at 1173 K: Influence of yttrium alloying addition.*** Annales de Chimie: Science des Materiaux, 2003. **28**(SUPPL 1): p. 207-214.

101. Cueff, R., H. Buscail, E. Caudron, C. Issartel, and F. Riffard, ***Oxidation behaviour of Kanthal A1 and Kanthal AF at 1173 K: effect of yttrium alloying addition.*** Applied Surface Science, 2003. **207**(1-4): p. 246-254.

102. Cueff, R., H. Buscail, E. Caudron, C. Issartel, and F. Riffard, ***Oxidation behaviour of Kanthal APM and Kanthal AF at 1173 K: Effect of yttrium alloying addition.*** Surface Engineering, 2003. **19**(1): p. 58-64.

103. Cueff, R., H. Buscail, E. Caudron, C. Issartel, and F. Riffard, ***Oxidation of alumina formers at 1173 K: Effect of yttrium ion implantation and yttrium alloying addition.*** Corrosion Science, 2003. **45**(8): p. 1815-1831.

104. Curtis, C.E., ***Properties of Yttrium Oxide Ceramics.*** Journal of the American Ceramic Society, 1957. **40**(8): p. 274-278.

105. El Kadiri, H., R. Molins, and Y. Bienvenu. ***Phase transformation and growth of alumina on a thin FeCrAl-RE foil at around 900°C.*** *Proceedings of the 6th International Symposium on High Temperature Corrosion and Protection of Materials, May 16-21 2004*. 2004. Les Embiez, France: Trans Tech Publications Ltd, Zurich-Ueticon, CH-8707, Switzerland.

106. Elsasser, C. and A.G. Marinopoulos, ***Substitutional cation impurities in [alpha]-Al2O3: ab-initio case study of segregation to the rhombohedral twin boundary.*** Acta Materialia, 2001. **49**(15): p. 2951-2959.

107. Fabris, S. and C. Elsasser, ***First-principles analysis of cation segregation at grain boundaries in α-Al2O3***. Acta Materialia, 2003. **51**(1): p. 71-86.

108. Glazkov, A., M. Gobel, J. Jedlinski, J. Schimmelpfennig, G. Borchardt, S. Weber, S. Scherrer, and J. Le Coze, ***On the influence of yttrium and sulphur on the high temperature oxidation behaviour of alumina-forming high purity FeCrAl alloys.*** Proceedings of the 1995 2nd International Conference on Ultra High Purity Base Metals, UHPM-95, Jun 13-16 1995. Journal De Physique, 1995. **5**(7): p. 7-381.

109. Hou, P.Y., Z.R. Shui, G.Y. Chuang, and J. Stringer, ***Effect of reactive element oxide coatings on the high temperature oxidation behavior of a FeCrAl alloy.*** Journal of the Electrochemical Society, 1992. **139**(4): p. 1119-1126.

110. Ikuhara, Y., H. Yoshida, and T. Sakuma, ***Impurity effects on grain boundary strength in structural ceramics.*** Materials Science and Engineering A, 2001. **319-321**: p. 24-30.

111. Lartigue-Korinek, S., C. Carry, and L. Priester, ***Multiscale aspects of the influence of yttrium on microstructure, sintering and creep of alumina.*** Journal of the European Ceramic Society, 2002. **22**(9-10): p. 1525-1541.

112. Mendis, B.G., K.J.T. Livi, and K.J. Hemker, ***Observations of reactive element gettering of sulfur in thermally grown oxide pegs.*** Scripta Materialia, 2006. **55**(7): p. 589-592.

113. Mennicke, C., E. Schumann, M. Ruehle, R.J. Hussey, G.I. Sproule, and M.J. Graham, ***Effect of yttrium on the growth process and microstructure of α- Al_2O_3 on FeCrAl.*** Oxidation of Metals, 1998. **49**(5-6): p. 455-466.

114. Mennicke, C., E. Schumann, C. Ulrich, and M. Ruehle, ***Effect of yttrium and sulfur on the oxidation of FeCrAl.*** Proceedings of the 1996 4th International Symposium on High Temperature Corrosion and Protection of Materials. Part 1 (of 2), May 20-24 1996. Materials Science Forum, 1997. **251-254**(pt 1): p. 389-396.

115. Nanni, P., C.T.H. Stoddart, and E.D. Hondros, ***Grain boundary segregation and sintering in alumina.*** Materials Chemistry, 1976. **1**(4): p. 297-320.

116. Pint, B.A., ***Optimization of Reactive-Element Additions to Improve Oxidation Performance of Alumina-Forming Alloys.*** Journal of the American Ceramic Society, 2003. **86**(4): p. 686-95.

117. Pint, B.A., A.J. Garratt-Reed, and L.W. Hobbs, ***Reactive element effect in commercial ODS FeCrAl alloys.*** Materials at High Temperatures, 1995. **13**(1): p. 3-16.

118. Pint, B.A., A.J. Garratt-Reed, and L.W. Hobbs, ***Analytical Electron-Microscopy Study of the Breakdown of α-Al_2O_3 Scales Formed on Oxide Dispersion-Strengthened Alloys.*** Oxidation of Metals, 2001. **V56**(1): p. 119-145.

119. Pint, B.A., J.R. Martin, and L.W. Hobbs, ***18O/SIMS characterization of the growth mechanism of doped and undoped α-Al_2O_3.*** Oxidation of Metals, 1993. **V39**(3): p. 167-195.

120. Przybylski, K., ***The influence of implanted yttrium on the oxidation properties of a Co-25Cr---1Al alloy.*** Materials Science and Engineering A, 1989. **120-121**(Part 2): p. 509-517.

121. Quadakkers, W.J., D. Naumenko, M. Dani, A. Dimiaty, J. Mayer, and L. Singheiser. ***Importance of reactive element interaction with C- and N-impurities for alumina scale growth and adherence on FeCrAl alloys.*** *John Stringer Symposium on High Temperature Corrosion, Nov 5-8 2001.* 2001. Indianapolis, IN, United States: ASM International, 9639 Kinsman Road, OH 44073-0002, United States.

122. R. Cueff, H.B., E. Caudron, C. Issartel, and F. Riffard, ***Influence of Yttrium-Alloying Addition on the Oxidation of Alumina Formers at 1173 K.*** Oxidation of Metals, 2002. **Vol. 58**(Nos. 5/6): p. 439 - 455.

123. Riffard, F., H. Buscail, E. Caudron, R. Cueff, C. Issartel, and S. Perrier, ***The influence of implanted yttrium on the cyclic oxidation behaviour of 304 stainless steel.*** Applied Surface Science, 2006. **252**(10): p. 3697-3706.

124. S. Chevalier, G. Strehl, H. Buscail, G. Borchardt, and J.P. Larpin, ***Influence of the mode of introduction of a reactive element on the high temperature oxidation behavior of an alumina-forming alloy. Part I: Isothermal oxidation tests.*** Materials and Corrosion, 2004. **55**(5): p. 352-357.

125. Sakka, Y., Y. Oishi, K. Ando, and S. Morita, ***Cation Interdiffusion and Phase Stability in Polycrystalline Tetragonal Ceria-Zirconia-Hafnia Solid Solution.*** Journal of the American Ceramic Society, 1991. **74**(10): p. 2610-2614.

126. Stacy, D.W. and D.R. Wilder, ***Thermal Expansion in the System Y_2O_3-HfO_2.*** Journal of the American Ceramic Society, 1973. **56**(4): p. 224-224.

127. Stott, F.H., G.C. Wood, and F.A. Golightly, ***The isothermal oxidation behaviour of Fe-Cr-Al and Fe-Cr-Al-Y alloys at 1200°C.*** Corrosion Science, 1979. **19**(11): p. 869-887.

128. Tawancy, H.M., N.M. Abbas, and A. Bennett, ***Role of Y during high temperature oxidation of an M-Cr-Al-Y coating on an Ni-base superalloy.*** Surface and Coatings Technology, 1994. **68-69**: p. 10-16.

129. Tolpygo, V.K. and D.R. Clarke, ***Microstructural study of the theta-alpha transformation in alumina scales formed on nickel-aluminides.*** Materials at High Temperatures, 2000. **17**(1): p. 59-70.

130. Tolpygo, V.K. and D.R. Clarke, ***Microstructural evidence for counter-diffusion of aluminum and oxygen during the growth of alumina scales.*** Materials at High Temperatures, 2003. **20**(3): p. 261-271.

131. Deakin, J., V. Prunier, G.C. Wood, and F.H. Stott, ***High temperature oxidation of Fe-Cr-Al alloys containing reactive elements.*** Materials Science Forum, 1997. **251-254**(pt 1): p. 41-48.

132. S. Chevalier, K. Przybylski, G. Borchardt, and J.P. Larpin. ***Role of minor element addition in the formation of thermally grown alumina scales***. 2004. Les Embiez, France: Trans Tech Publications Ltd, Zurich-Ueticon, CH-8707, Switzerland.

133. Li, B., S. Wu, G.e. Meng, L. Jiang, and W. Pang, ***Effect of yttrium on mechanical properties of Fe-20Cr-4Al-Y alloy***. Jinshu Xuebao/Acta Metallurgica Sinica, 1990. **26**(5): p. 328-333.

134. Mennicke, C., E. Schumann, C. Ulrich, and M. Ruehle, ***Effect of yttrium and sulfur on the oxidation of FeCrAl***. Materials Science Forum, 1997. **251-254**(pt 1): p. 389-396.

135. Naumenko, D., V. Kochubey, J. Le-Coze, E. Wessel, L. Singheiser, and W.J. Quadakkers. ***Effect of combined yttrium and zirconium additions on protective alumina scale formation on high purity FeCrAl alloys during oxidation in the temperature range of 1200 to 1300°C***. 2004. Les Embiez, France: Trans Tech Publications Ltd, Zurich-Ueticon, CH-8707, Switzerland.

136. Jedlinski, J., ***Oxidation behaviour of FeCrAl `alumina forming' alloys at high temperatures***. Solid State Ionics, 1997. **101-103**(pt 2): p. 1033-1040.

137. Basu, S.N., H. Wu, V. Gupta, and V. Kireev, ***The effect of structure and chemistry on the strength of FeCrAl(Y)/sapphire interfaces: II. Strength of interfaces***. Materials Science and Engineering A, 2003. **349**(1-2): p. 265-271.

138. B.A.Pint, ***Optimization of reactive element additions to improve oxidation performance of alumina forming alloys***. Journal of the American Ceramic Society, 2003. **86**(4): p. 686 - 695.

139. Ram, D.L., G.J. Tatlock, and U. Falke, ***Segregation of reactive elements at oxide grain boundaries in FeCrAlRE alloys***. Materials at High Temperatures, 2005. **22**(3-4): p. 497-503.

140. Wang, C.M., G.S. Cargilllii, H.M. Chan, and M.P. Harmer, ***Structural features of Y-saturated and supersaturated grain boundaries in alumina***. Acta Materialia, 2000. **48**(10): p. 2579-2591.

141. Wang, C.M., G.S. Cargilllii, M.P. Harmer, H.M. Chan, and J. Cho, ***Atomic structural environment of grain boundary segregated Y and Zr in creep resistant alumina from EXAFS***. Acta Materialia, 1999. **47**(12): p. 3411-3422.

142. D.B.Williams and C.B.Carter, ***Transmission Electron Microscope***. Vol. 1-4. 1996, New York: Plenum Press. ISBN: 0-306-45247-x

143. Egerton, R.F., ***Electron energy loss spectroscopy in the electron microscope***. 1986, New York: Plenum Press.

144. ***EDAX microanalysis course***, in *Module 1*. March 15-18 2004: EDAX Europe, Tilburg, The Netherlands. p. 1-32.

145. ***EDAX microanalysis course***, in *Module 2*. March 15-18 2004: EDAX Europe, Tilburg, The Netherlands. p. 1-5.

146. Williams, D.B. and C.B. Carter, ***Transmission electron microscopy***. Spectrometry. 1996, New York: Plenum Press. p. 613-635. ISBN: 0-306-45247-x

147. ***EDAX microanalysis course***, in *Module 3*. March 15-18 2004: EDAX Europe, Tilburg, The Netherlands. p. 1-15.

148. Williams, D.B. and C.B. Carter, ***Transmission electron microscopy***. Basics. 1996, New York: Plenum Press. 613-635.

149. Kirkland, E.J., ***Advanced computing in electron microscopy***. 1998, New York Plenum Press. ISBN: 0-306-45936-1

150. Deakin, J., V. Prunier, G.C. Wood, and F.H. Stott, ***Effects of reactive elements on the oxidation of alumina-forming iron-chromium-aluminum alloys at high temperature.*** Journal De Physique, 1995. **5**(7): p. 7-357.

151. Stott, F.H., F.A. Golightly, and G.C. Wood, ***The influence of thermal cycling on the oxidation behaviour of Fe-Cr-Al and Fe-Cr-Al-Y alloys at 1200°C.*** Corrosion Science, 1979. **19**(11): p. 889-906.

152. V. Kochubey, H. Al-Badairy, G. Tatlock, J. Le-Coze, D. Naumenko, and W.J. Quadakkers, ***Effects of minor additions and impurities on oxidation behaviour of FeCrAl alloys. Development of novel surface coatings compositions.*** Materials and Corrosion, 2005. **56**(12): p. 848-853.

153. Wessel, E., V. Kochubey, D. Naumenko, L. Niewolak, L. Singheiser, and W.J. Quadakkers, ***Effect of Zr addition on the microstructure of the alumina scales on FeCrAlY-alloys.*** Scripta Materialia, 2004. **51**(10): p. 987-992.

154. Pint, B.A., J.R. Martin, and L.W. Hobbs, ***18/SIMS characterization of the growth mechanism of doped and undoped α- Al_2O_3.*** Oxidation of Metals, 1993. **39**(3-4): p. 167-195.

155. S. Chevalier, C.Issartel, R.Cueff, H Buscaif, G.Strehl, and G Borchardt, ***Influence of the mode of introduction of a reactive element on the high temperature oxidation behavior of an alumina-forming alloy. Part III: The use of two stage oxidation experiments and in situ X-ray diffraction to understand the oxidation mechanisms.*** Materials and Corrosion, 2006. **57**(6): p. 476-483.

156. Chevalier, S., G. Strehl, H. Buscail, G. Borchardt, and J.P. Larpin, ***Influence of the mode of introduction of a reactive element on the high temperature oxidation behavior of an alumina-forming alloy part I: Isothermal oxidation tests.*** Materials and Corrosion, 2004. **55**(5): p. 352-357.

157. Hou, P.Y. ***Impurity segregation to scale/alloy interfaces and its effect on interfacial properties***. *Materials Science Forum*, v 369-372, n I, 2001, p 23-38. Les Embiez: Trans Tech Publications Ltd.

158. More, K.L., B.A. Pint, P.F. Tortorelli, and D.W. Coffey. ***The fundamental role of microstructural and microchemical analysis in high-temperature oxidation science***. *2004 Joint International Meeting - 206th Meeting of the Electrochemical Society/2004 Fall Meeting of the Electrochemical Society of Japan, MA 2004-02*, 2004, p 1756. Honolulu, HI, United States: Electrochemical Society Inc., Pennington, NJ 08534-2896, United States.

159. Andrievskaya, E.R. and L.M. Lopato, ***Phase Equilibria in the System HfO_2-$Y2O_3$-CaO***. Journal of the American Ceramic Society, 1992. **75**(11): p. 3026-3032.

160. Andrievskaya, E.R. and L.M. Lopato, ***Phase Equilibria in the Hafnia-Yttria-Lanthana System***. Journal of the American Ceramic Society, 2001. **84**(10): p. 2415-2420.

161. Fabrichnaya, O. and C. Mercer, ***Phase relation in the HfO_2-Y_2O_3-Al_2O_3 system***. Computer Coupling of phase Diagram and Thermochemistry, 2005. **29**: p. 239-246.

162. Pint, B.A., B.M. Banks, J.C. Duncan, A.J. Garratt-Reed, and L.W. Hobbs. ***Characterization of the oxidation-sulfidation of a preoxidized ODS FeCrAl alloy***. *Proceedings - Annual Meeting, Microscopy Society of America*, 1993, p 1146-1147. Cincinnati, OH, USA: Publ by San Francisco Press Inc, San Francisco, CA, USA.

163. Pint, B.A. and L.W. Hobbs, ***Formation of α- Al_2O_3 scales at 1500°C***. Oxidation of Metals, 1994. **41**(3-4): p. 203-233.

164. Pint, B.A. and L.W. Hobbs, ***Limitations on the use of ion implantation for the study of the reactive element effect in β-NiAl***. Journal of the Electrochemical Society, 1994. **141**(9): p. 2443-2453.

165. Pint, B.A., J. Leibowitz, and J.H. DeVan, ***Effect of an oxide dispersion on the critical Al content in Fe-Al alloys***. Oxidation of Metals, 1999. **51**(1): p. 181-197.

166. Pint, B.A., K.L. More, P.F. Tortorelli, W.D. Porter, and I.G. Wright. ***Optimizing the imperfect oxidation performance of iron aluminides***. *Materials Science Forum*, v 369-372, n I, 2001, p 411-418. Les Embiez: Trans Tech Publications Ltd.

167. Calderon, H.A., P.W. Voorhees, J.L. Murray, and G. Kostorz, ***Ostwald Ripening in Concentrated Alloys***. Acta Materialia, 1994. **42**(3): p. 991-1000.

168. Li, C.-Y., J.M. Blakely, and A.H. Feingold, ***Mass transport Analysis for Ostwald Ripening and Related Phenomenon***. Acta Materialia, 1966. **14**: p. 1397-1402.

Appendix 1

Scripts used for cleaning HAADF image.

- **Hi – Low filter***

```
Image ILLowPass( Image image )
{
    number width, height

    GetSize( image, width, height )

    // This is inefficient in that it copies the
    // data, but it allows me to match the data
    // type easily.

    Image result = image

    SubArea imageS := image[ 1, 1, height - 2, width - 2 ]

    number nf = 1/9

    result[ 1, 1, height - 2, width - 2 ] = nf * ( \
        offset( imageS, -1, -1 ) + \
        offset( imageS, -1, 0 ) + \
        offset( imageS, -1, 1 ) + \
        offset( imageS, 0, -1 ) + \
        offset( imageS, 0, 0 ) + \
        offset( imageS, 0, 1 ) + \
        offset( imageS, 1, -1 ) + \
        offset( imageS, 1, 0 ) + \
        offset( imageS, 1, 1 ) )

    return result
}

//
// This function performs a 3x3 sharpen (high pass filter)
// on the given real image and returns a new image that is
// filtered.
//
Image ILHighPass( Image image )
{
    number width, height

    GetSize( image, width, height )

    // This is inefficient in that it copies the
    // data, but it allows me to match the data
    // type easily.
```

```
    Image result = image

    SubArea imageS := image[ 1, 1, height - 2, width - 2 ]

    result[ 1, 1, height - 2, width - 2 ] = \
        9 * offset( imageS, 0, 0 ) - \
        offset( imageS, -1, -1 ) - \
        offset( imageS, -1, 0 ) - \
        offset( imageS, -1, 1 ) - \
        offset( imageS, 0, -1 ) - \
        offset( imageS, 0, 1 ) - \
        offset( imageS, 1, -1 ) - \
        offset( imageS, 1, 0 ) - \
        offset( imageS, 1, 1 )

    return result
}
Image ILSharpen( Image image )
{
    return ILHighPass( image )
}

// Examples of use:

Image front := GetFrontImage()

ShowImage( ILLowPass( front ) )

ShowImage( ILHighPass( front ) )

ShowImage( ILSharpen( front ) )
```

- **Reduced stripes***

```
string prompt = "pick two images, the image to be cleaned and its profile"
string title = "reduce images strips"
string img_title = " reduced strips"

image image_a
image image_b
image image_c = RealImage("Average Profile 2 ", 4, 1024, 1)
image image_d
NUmber width_a, hight_a, width_b, hight_b, x, y, value
String name

GetTwoImagesWithPrompt( prompt, title, image_a, image_b)


GetSize(image_a, width_a, hight_a)
GetSize(image_b, width_b, hight_b)
```

```
IF (hight_a == 1)
{
    value = mean(image_a)

    image_c = image_a / value
    SetName (image_c, "Average Profile")
    ShowImage(image_c)

    image_d := image_b.ImageClone()
    name = GetName(image_b)


    For(x = 0; x < width_b; x++)
    {
        For(y = 0 ; y < hight_b ; y++)
        {

            if (spacedown())
                {
                    Throw("Procedure aborted")
                    exit(0)
                }

            Number value = GetPixel(image_b, x, y)
            Number shift = GetPixel(image_c, x, 0)
            SetPixel(image_d, x, y, value/shift)

        }
    }

}


ELSE

{

    value = mean(image_b)


    image_c = image_b / value
    SetName (image_c, "Average Profile")
    ShowImage(image_c)


    image_d := image_a.ImageClone()
    name = GetName(image_a)


    For(x = 0; x < width_a; x++)
```

```
    {
        For(y = 0 ; y < hight_a ; y++)
        {

            if (spacedown())
                {
                    Throw("Procedure aborted")
                    exit(0)
                }

            Number value = GetPixel(image_a, x, y)
            Number shift = GetPixel(image_c, y, 0)
            SetPixel(image_d, x, y, value/shift)

        }
    }
}

SetName (image_d, name + img_title)
ShowImage(image_d)
```

*www.gatan.com/scripting

Appendix 2

Calculation of numbers of atoms

1) Assuming a fixed area and thickness of the sample, approximate number of unit cells can be calculated.

$$\text{No. of unit cells} = \frac{\text{Area analyzed} * \text{Thickness}}{4.75 * 4.75 * 12.98}$$

$$\text{No. of unit cells} = \frac{200 * 200 * 600}{4.75 * 4.75 * 12.98}$$

No. of unit cells ≈ 81950

2) From number of unit cells the approximate number of Al and O ions present can be calculated. As each alumina cell has 12 Al^{3+} and 18 O^{2-} ions.

3) As we know the atomic percent of each element present in the fixed volume. It could be used to calculate number of ions present in that fixed volume.

   For example if we assume only 3 elements are present (Al, O and Hf) and we can form three quadratic equations if atomic percents are known,

   For Al,

   $27\ (x) = (\text{Al At. \%})\ [\ 178.5\ (z) + 27\ (x) + (16\ (y)\ ]$

   For O

   $16\ (y) = (\text{O At. \%})\ [\ 178.5\ (z) + 27\ (x) + (16\ (y)\ ]$

   For Hf

   $178.5\ (z) = (\text{Hf At. \%})\ [\ 178.5\ (z) + 27\ (x) + (16\ (y)\ ]$

   Solving the above equation for the variables x, y and z would result in number of respective ions.

   Similar calculation were carried out for the elemental compositions obtained from the fixed volume during GB analysis.

Appendix 3

Multislice simulations.

Slices used for α-Al_2O_3 calculation

- Slice 1

4.7600 3.1800 4.3300
0
8
0.5000 0.3333 0.0000
0.5000 0.6666 0.0000
1.0000 0.1666 0.5000
1.0000 0.8332 0.5000
0.5000 0.3333 1.0000
0.5000 0.6666 1.0000

- Slice 2

4.7600 3.1800 4.3300
0
13
0.2500 0.0000 0.0000
0.2500 1.0000 0.0000
0.2500 0.0000 1.0000
0.2500 1.0000 1.0000
1.0000 0.5000 0.5000

8
0.5000 0.6666 0.0000
1.0000 0.1666 0.5000
0.5000 0.6666 1.0000

- Slice 3

```
 4.7600  3.1800  4.3300
0
13
 0.2500  0.0000  0.0000
 0.2500  1.0000  0.0000
 0.2500  0.0000  1.0000
 0.2500  1.0000  1.0000
 1.0000  0.5000  0.5000

8
 0.5000  0.3333  0.0000
 1.0000  0.8336  0.5000
 0.5000  0.3333  1.0000
```

- Slice 4 (An Al site substituted by Hf)

```
 4.7600  3.1800  4.3300
0
13
 0.2500  0.0000  0.0000
 0.2500  1.0000  0.0000
 0.2500  0.0000  1.0000
 0.2500  1.0000  1.0000

72
 1.0000  0.5000  0.5000

8
 0.5000  0.6666  0.0000
 1.0000  0.1666  0.5000
 0.5000  0.6666  1.0000
```

Parameter used in calculation

Type in the stacking sequence :
20(abc)

Type in the name of 3 atomic potential layers :

Name of file with input atomic potential a :
1.tiff
Name of file with input atomic potential b :
2.tiff
Name of file with input atomic potential c :
3.tiff
STEM probe parameters, V0(kv), Cs(mm) df(Angstroms), apert1,2(mrad) :
100 0 0 0 24
Magnitude and angle of 2-fold astigmatism (in Ang. and degrees):
0 0
Magnitude and angle of 3-fold astigmatism (in Ang. and degrees):
0 0
wavelength = 0.037014 Angstroms
Size of probe wavefunction Nx,Ny in pixels :
512 512
Crystal tilt x,y in mrad. :
0 0
Do you want to calculate a 1D line scan (y/n) :
n
Number of detector geometries :
2
Detector 1: Type, min,max angles(mrad) of collector :
0 30
Name of file to get output of result for this detector:
bf.tiff
Detector 2: Type, min,max angles(mrad) of collector :

70 210

Name of file to get output of result for this detector:

haadf.tiff

xi,xf,yi,yf, nxout,nyout :

0 30 0 30 512 512

layer a, cz = 2.000000

layer b, cz = 2.000000

layer c, cz = 2.000000

Size in pixels Nx x Ny = 1024 x 1024 = 1048576 total pixels,

lattice constants a,b = 47.599998 x 31.799999

Total specimen thickness = 120 Angstroms

Number of symmetrical anti-aliasing beams in trans. function = 244523

with a resolution of 0.139453 Angstroms.

Number of symmetrical anti-aliasing beams in probe = 61121

output file size in pixels is 512 x 512